The channel from k(⁻)preactionsinthe(1690)region

Edwin Robert Hancock

THE $\pi\pi\Lambda$ CHANNEL FROM

K^-p REACTIONS IN THE $\Lambda(1690)$ REGION

by

Edwin Robert Hancock, B.Sc., Dunelm.

A Thesis submitted for the Degree of Doctor of Philosophy

in the University of Durham

MAY, 1981

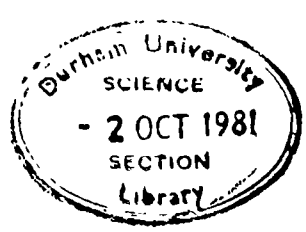

CONTENTS

ABSTRACT

This work represents a study of the $\Lambda\pi\pi$ final state of $\bar{k}N$ interactions between 0.620 and 0.870 GeV/c incident laboratory momentum. Data obtained from a Hydrogen Bubble Chamber exposure has been used to obtain channel cross-sections for the reaction $k^- p \rightarrow \Lambda\pi^+\pi^-$. Study of the $\Lambda\pi^+\pi^-$ Dalitz plot reveals that in addition to $\Sigma^+(1385)$ and $\Sigma^-(1385)$ isobar production, a final state $\pi\pi$ S-wave interaction ('ε') is present. Assuming a model of incoherent addition, quasi-two body descriptions for each of the $\pi^+\Sigma^-(1385)$, $\pi^-\Sigma^+(1385)$ and 'ε'Λ channels are extracted.

Subsequent consideration of the $\pi\Sigma(1385)$ quasi two-body channels reveals evidence for strong $\Lambda(1690)$ formation. Combining the newly obtained data with that previously published for the $\pi\Sigma(1385)$ channels, an energy dependent partial wave analysis is performed. Resonant amplitudes of the SO1(1670), D13(1678) and DO3(1690) states are determined. Consideration of the DDO3 and DSO3 partial wave amplitudes for the DO3(1690) state, indicates substantial $\Lambda^4 8_3 - \Lambda^2 8_3$ mixing within SU(6)w ⊗ O(3). In addition, a comparison is given between the amplidues Y^* states observed in the partial wave analysis and those predicted by the Isgur-Karl Model.

ACKNOWLEDGMENT

I would like to express my thanks to the following, who have made the completion of this thesis possible :-

(i) Professors B.H.Bransden and A.W.Wolfendale who made available the facilities of the Physics Department at Durham University, where in addition to the period of work for this thesis, I spent three most enjoyable undergraduate years.

(ii) Drs. John Major and Desmond Evans who as leader of the High Energy Physics Research Group and my supervisor, respectively, provided much essential encouragement and guidance throughout my research. I would also like to thank other members of the High Energy Physics Research Group at Durham University, in particular Alan Lotts, for help with the many computational problems which presented themselves during this work.

(iii) Drs. George Kalmus, Bill Cameron, Jon Guy, Bodé Franek and Gian Gopal of the Rutherford Laboratory for initiating me into the mystique of $\bar{k}N$ physics.

(iv) The Science Research Council for the award of a research studentship.

(v) Ann Diggory and Sylvia Mellanby for providing the superb technical where-with-all to produce this thesis.

(vi) Dame Enid, Charlotte, Simon and Cynthia Cereopsis for aleviating some of the side effects of low-energy $\bar{k}N$ physics.

CHAPTER 1

1.1 INTRODUCTION

What was later referred to by de Rujula et al (Ref.1.1) as the 'teeming democracy of hadrons', lead Gell-Mann to propose 'The Eightfold Way' in the 1961 (Ref.1.2). So, with the SU(3) quark model, was started the trend in particle physics for symmetry groups. Gell-Mann's rather ephemeral quarks have now become the partons of Quantum Chromodynamics (Q.C.D) and the fundamental objects required of SU(5) Grand Unified Theories outnumber the hadrons known in 1961. Whatever the success of asymptotically free field theories, such as Q.C.D, in describing scaling violations and jet production, the hadronic bound state problem remains. Isgur, Karl and Koniuk, in a monumental series of papers (Refs. 1.3 to 1.7) have determined the baryonic masses, wavefunctions and branching fractions with great economy of phenomenological parameters. This model embodies features expected of Q.C.D, including a long range quark confining potential and a short range vector particle exchange, which mediates quark-quark hyperfine interactions.

Even now, twenty years after the proposition of the Eightfold Way, data to test hadronic symmetries and quark models remains incomplete. Two-body reactions such as $\bar{k}N \rightarrow \bar{k}N$, $\bar{k}N \rightarrow \pi\Lambda$ and $\bar{k}N \rightarrow \pi\Sigma$ explore the SU(3) $\tilde{8} \otimes \tilde{8}$ final state couplings of negative strangeness baryons (Y^* states) and have been well observed. However, determination of $\tilde{8} \otimes \tilde{10}$ couplings is more difficult, requiring study of the $\pi\Sigma$ (1385) quasi-two-body final state. Since the $\Sigma(1385)$ undergoes strong decay, with lifetime $\sim 10^{-14}$s to $\Lambda\,\pi$, Y^* couplings are found by extracting the process

$$\bar{k}N \rightarrow \pi\ \Sigma(1385) \hookrightarrow \Lambda\,\pi \qquad (1.1)$$

seen in the reaction $\bar{k}N \rightarrow \pi\pi\Lambda$. Although complicated, the results of this form of analysis are rewarding ; comparisons of $\pi\Sigma$ (1385) and $\pi\Delta(1232)$ couplings

within the framework of SU(3) and tests of the baryonic composition found by Isgur et al are possible. The object of this thesis is to examine the reaction $k^- p \to \pi^+ \pi^- \Lambda$, seen in experimental data, and determine the underlying s-channel $\pi\Sigma(1385)$ dynamics.

1.2 S-CHANNEL PARTIAL WAVES

To describe s-channel dynamics for the reaction $k^- p \to \pi^{\pm} \Sigma(1385)^{\mp}$, partial wave formalism will be used throughout this thesis. Each $\pi\Sigma(1385)$ final state is decomposed in terms of isospin content and the allowed initial and final state orbital angular momentum for given s-channel angular momentum. The isospin composition of the s-channel will be discussed in section 1.4 ; this section gives the angular momentum content of the partial waves.

If the initial $k^- p$ system has relative orbital angular momentum $\vec{L}$ and the final state $\pi\ \Sigma(1385)$ system has relative orbital angular momentum $\vec{L}'$, conservation of total angular momentum ($\vec{J}$) gives :-

$$\vec{J} = \vec{L} + \frac{\vec{1}}{2} = \vec{L}' + \frac{\vec{3}}{2} \qquad (1.2)$$

Parity conservation gives $(-1)^L = (-1)^{L'}$ and $\Delta L = |L-L'| = 0,2$. The permitted s-channel partial waves are given in the $LL'(2J)$ spectroscopic notation :-

S D 1 D S 3 D D 3 D D 5 D G 5 G D 7 G G 7
with parity = -1

P P 1 P P 3 P F 3 F P 5 F F 5 F F 7 F H 7
with parity = + 1

Throughout the rest of this thesis the $LL'(I)(2J)$ notation is used to include isospin. Since only isoscalar and isovector amplitudes may couple to the $k^- p$ system, I=0 and 1 partial waves exist for each spin parity sector above.

LI2J	Mass (in MeV)	Width (in MeV)	Elasticity	Amplitude at Resonance (t) $\pi\Sigma$	$\pi\Lambda$	$\pi\Sigma^*(L')$	$\bar{k}^*N(L'2S')$	Status
S11	1768 ± 10 1925 ± 20	105 ± 15 200 ± 20	0.18 ± .05 0.48 ± .03	(+)0.08 ± .03 0.20 ± .04	-0.10 ± .02 (+)0.08 ± .03	≲0.03(D) ≲0.03(D)	- {-0.10 ±.02(S1) {-0.07 ±.03(D3)	*** **
P11	1673 ± 10 1870 ± 10	140 ± 20 140 ± 20	0.10 ± .03 0.19 ± .05	-0.13 ± ..02 0.30 ± 0.10	≲0.03 -0.24 ± .08	-	- { 0.05 ±.03(P1) { 0.11 ±.03(P3)	*** **
D13	1670 ± 5 1920 ± 20	60 ± 5 215 ± 25	0.09 ± .02 0.10 ± .04	0.20 ± .02 -0.13 ± .03	0.07 ± .02 -0.08 ± .03	- {-0.07±.03(S) { ≲0.03(D)	- {-0.09 ±.03(S3) {≲0.03(D1+D3)	**** ***
D15	1775 ± 2 2270 ± 5	120 ± 5 100 ± 5	0.38 ± .02 0.06 ± .02	0.10 ± .02 0.0½ ± .02	-0.28 ± .02 0.12 ± .02	{0.17±.03(D) { ≲0.03(G) -	- -	**** *
F15	1930 ± 10 2060 ± 15	120 ± 15 225 ± 25	0.06 ± .02 0.08 ± .03	-0.18 ± .03 0.12 ± .04	-0.09 ± .02 -	{ ≲0.03(P) {-0.04±.02(F) -	≲0.03(P3,F1&F3) -	**** **
F17	2040 ± 5	165 ± 10	0.22 ± .02	-0.13 ± .02	0.19 ± .02	{-0.15±.03(F) { ≲0.03(H)	{-0.06 ±.03(F1) { 0.04 ±.03(F3) ≲0.03(H3)	****
G19	2210 ± 10	70 ± 10	0.22 ± .01	-0.03 ± .02	0.09 ± .02	-	-	*
S01	1670 ± 4 1810 ± 25	36 ± 5 215 ± 20	0.19 ± .03 0.33 ± .05	-0.26 ± .03 -0.08 ± .05	-	-0.06 ± .03(D)	{-0.17 ± .03(S1) {-0.13 ± .04(D3)	**** ***
P01	1588 ± 15	187 ± 50	0.25 ± .04	-0.25 ± .07	-	-	{ 0.14 ± .03(P1) { 0.35 ± .06(P3)	***
P03	1896 ± 10	104 ± 20	0.25 ± .04	0.12 ± .03	-	{ ≲0.03(P) {+ 12 ± .04(F)	{ 0.07 ± .03(P1) {≲0.03(P3 & F3)	****
D03	1520 ± 1 1690 ± 5 2325 ± 20	16 ± 1 62 ± 5 170 ± 30	0.46 ± .02 0.23 ± .02 0.19 ± .06	0.46 ± .02 -0.26 ± .02 -	- - -	- - -	- - -	**** ****
D05	1823 ± 5	90 ± 15	0.04 ± .02	-0.17 ± .02	-	{-0.14 ± .03(D) { ≲0.03(G)	≲0.03(D1,D3&G3)	****
F05	1820 ± 2 2115 ± 15	80 ± 5 190 ± 30	0.58 ± .02 0.07 ± .02	-0.27 ± .02 0.15 ± .03	- -	{ 0.15 ± .03(P) {-0.05 ± .03(F) {-0.06 ± .03(P) { ≲0.03(F)	≲0.03(P3,F1&F3) ≲0.03(P3&F3) 0.17 ± .04(F1)	**** ***
G07	2110 ± 10	190 ± 30	0.27 ± .02	0.12 ± .03	- -	≲0.03(D&G) ≲0.03(D&G)	{ 0.21 ± .04(D3) { 0.04 ± .03(G1) { ≲0.03(G3)	****
H09	2365 ± 25	160 ± 20	0.12 ± .04	-0.10 ± .02	-	-	-	

TABLE 1.1 : Amplitudes at resonance for Y* states observed in $\bar{k}N$ formation experiments.

1.3 RESONANCE FORMATION

Major contributions to the s-channel partial waves in $\bar{k}N$ reactions have been shown to come from Y^* resonance formation (ref 1.13). This section will consider the resonances known to be present in the centre of mass energy range 1.640 to 2.040 GeV/c, which is explored in this thesis. The bulk of such knowledge comes from global, energy dependant, partial wave analyses of two body final states of $\bar{k}N$ interactions (Refs. 1.8 to 1.12). At the 1980 Toronto conference, the current situation concerning Y^* states was reviewed by G.Gopal, (Ref. 1.18), from which Table 1.1 is taken. States receiving a (* * * *) status are considered well established and have been verified by many analyses ; 11 such states exist. Those remaining states are less well established and are not seen with consistent parameters in different analyses. Table 1.1 also lists the observed couplings of the Y^*'s to two-body final states of $\bar{k}N$ interactions ($\bar{k}N$, $\pi\Lambda$ and $\pi\Sigma$)together with the quasi two-body couplings (k^* (890)N and $\pi\Sigma(1385)$).

The object of this thesis is to extend the energy range of data available for a partial wave analysis of the $\pi\Sigma(1385)$ channels, which was performed over the 1.775 to 2.170 GeV range by the RL/IC group in 1977 (ref 1.13). Since this previous analysis was completed, new high statistics data for two-body final states has clarified certain features of the Y^* spectrum (references 1.15 to 1.17). In particular, an update of the partial wave analysis of elastic scatter and charge exchange channels, (reference 1.18) has been undertaken and resolves many of the previously features found previously. Table 1.2 gives the results of this reanalysis and will be used as input to a new study of the $\pi\Sigma(1385)$ final state over an extended energy range.

Above all, new data presented in this thesis for the 0.630 to 0.870 GeV/c interval, will permit the $\pi\Sigma(1385)$ couplings of DO3(1690), D13(1670), and SO1(1670) states to be determined. A substantial branching fraction for each resonance remains unaccounted for in Table 1.1. Inclusion of these rather narrow states in the $\pi\Sigma(1385)$ analysis will constrain greatly the

Wave	Mass (MeV)	Width (MeV)	Elasticity	Status
S01	1667 ± 5	29 ± 5	0.18 ± .03	****
	1841 ± 10	228 ± 20	0.36 ± .04	**(*)
S11	1756 ± 10	64 ± 10	0.14 ± .03	***
	1944 ± 15	215 ± 25	0.51 ± .05	**(*)
P01	1568 ± 20	116 ± 20	0.23 ± .04	**
	1841 ± 20	164 ± 20	0.24 ± .04	**
P11	1670 ± 10	152 ± 20	0.12 ± .03	***
	1826 ± 20	86 ± 15	0.06 ± .02	**
P03	1897 ± 5	74 ± 10	0.20 ± .02	***(*)
D03	1519 ± 1	16 ± 1	0.47 ± .02	****
	1690 ± 5	61 ± 5	0.23 ± .02	****
	1895 ± 30	175 ± 25	0.03 ± .02	(*)
D13	1682 ± 5	79 ± 10	0.10 ± .03	****
D05	1831 ± 10	100 ± 10	0.08 ± .03	****
D15	1778 ± 5	137 ± 10	0.40 ± .02	****
F05	1823 ± 3	77 ± 5	0.58 ± .02	****
	2092 ± 25	245 ± 25	0.07 ± .03	**(*)
F15	(1920) [a]	(130)	0.03 ± .02	****
	2051 ± 25	300 ± 30	0.08 ± .03	* (*)
F17	2036 ± 5	172 ± 10	0.19 ± .03	****
G07	2104 ± 10	(250)	0.34 ± .03	****
G09	(1808)	(27)	0.03 ± .03	(*)

a) Masses and widths in parenthesis were kept fixed.

TABLE 1.2 : Parameters for Y* states from the new $\bar{k}N$ analysis.

SDO1, DSO3, DS13, DDO3 and DD13 amplitudes which previously contained no established resonance structure.

In particular, the new analysis of $\bar{k}N$ final states has clarified the position concerning the poorly understood $J^P = \frac{1}{2}^+$ Y^* states. Two rather wide structures are observed in both the I = 1 and I = 0 sectors. Both the PO1(1850) and P11(1870) lay in the energy range of the previous $\pi\Sigma(1385)$ analysis ; however, no resonant structure was included in either the PPO1 or PP11 amplitudes. In the new energy range, both the PO1(1580) and P11(1673) may be expected to contribute. An FO5(2100) state required in the $\pi\Sigma(1385)$ channels has now been confirmed by $\bar{k}N$ analyses, but the values for its width are not well determined. Structure in the SD11 amplitude due to the poorly established S11(1925) could previously be replaced by a non-resonant background. However, the mass and width of this state are now known with greater certainty and the new values will be used.

1.4 ISOSPIN DECOMPOSITION

Three sources of data are available concerning the reaction $\bar{k}N \to \Lambda\pi\pi$:-

$$\left.\begin{array}{l} k^- p \to \pi^+\pi^- \Lambda \\ k_L^o\, p \to \pi^+\pi^o \Lambda \end{array}\right\} \quad \text{(hydrogen target experiments)}$$

$$k^- n \to \pi^-\pi^o \Lambda \qquad \text{(from deuterium target experiments)}$$

Cross-sections for these processes may be related using SU(2) invariance of the s-channel isospin amplitudes in the strong interaction. This principle has its origin in the observed charge independence of the strong interaction from Nuclear Physics. In the isospin basis, the initial states are :-

$$|1\ k^- p\rangle = \left|\tfrac{1}{2} - \tfrac{1}{2}\right\rangle \otimes \left|\tfrac{1}{2} - \tfrac{1}{2}\right\rangle = \frac{-1}{\sqrt{2}} \left|1,0\right\rangle + \left|0,0\right\rangle \qquad (1.3)$$

$$|1\ k^- n\rangle = \left|\tfrac{1}{2} - \tfrac{1}{2}\right\rangle \otimes \left|\tfrac{1}{2} - \tfrac{1}{2}\right\rangle = \left|1 - 1\right\rangle \qquad (1.4)$$

Complication arises for the k_L^o induced reaction from weak interaction effects which mix k^o and $\bar{k}^o$, leading to strangeness non-conservation in the beam. Charge conjugation-parity (CP) is conserved in the weak interaction and the following eigenstates may be constructed : -

$$\left|k^o_s\right> = \frac{1}{\sqrt{2}}\left[\left|k^o\right> + \left|\bar{k}^o\right>\right] \quad \text{with lifetime } \sim 10^{-10}\ \text{s}$$

and CP eigenvalue = +1 (1.5)

$$\left|k^o_L\right> = \frac{1}{\sqrt{2}}\left[\left|k^o\right> - \left|\bar{k}^o\right>\right] \quad \text{with lifetime } \sim 10^{-8}\ \text{s}$$

and CP eigenvalue = -1 (1.6)

Given the greater lifetime of k^o_L, it is this which is seen to undergo strong interaction. However, only the negative strangeness (i.e. $\bar{k}^o$) component may produce $\Lambda\ \pi\ \pi$ final states :-

$$\left|k^o_L p\right>_{s=-1} = \sqrt{\frac{1}{2}}\ \left|\frac{1}{2}, \frac{1}{2}\right>\left|\frac{1}{2}, \frac{1}{2}\right> = \sqrt{\frac{1}{2}}\ \left|1, 1\right> \qquad (1.7)$$

Similarly, the final states produced decompose as follows :-

$$\left|\pi^+\pi^-\ \Lambda\right> = \sqrt{\frac{1}{6}}\ \left|2,0\right> + \sqrt{\frac{1}{2}}\ \left|1, 0\right> + \sqrt{\frac{1}{2}}\ \left|0, 0\right> \qquad (1.8)$$

$$\left|\pi^+\pi^o\ \Lambda\right> = \sqrt{\frac{1}{2}}\ \left|2,1\right> + \sqrt{\frac{1}{2}}\ \left|1, 1\right> \qquad (1.9)$$

$$\left|\pi^-\pi^o\ \Lambda\right> = \sqrt{\frac{1}{2}}\ \left|2, -1\right> - \sqrt{\frac{1}{2}}\ \left|1, -1\right> \qquad (1.10)$$

Since no $I = 2$ component exists in the initial state, isospin conservation forbids transitions to the $I = 2$ component of the final state. Further, if T is the operator describing transformations to the

final state, the cross-section for the reaction $\bar{k}N \rightarrow \pi\pi\Lambda$ may be written as :-

$$\sigma(\bar{k}N \rightarrow \pi\pi\Lambda) \sim \left| \langle \bar{k}N \,|T|\, \pi\pi\Lambda \rangle \right|^2 \qquad (1.11)$$

Invariance of the isospin amplitudes, isospin conservation and charge conservation allow the cross-sections to be written :-

$$\sigma(k^- p \rightarrow \pi^+ \pi^- \Lambda) = \frac{1}{4}\sigma(I = 1) + \frac{1}{6}\sigma(I = 0) \qquad (1.12)$$

$$\sigma(k^- n \rightarrow \pi^0 \pi^- \Lambda) = \frac{1}{2}\sigma(I = 1) \qquad (1.13)$$

$$\sigma(k^0_L p \rightarrow \pi^+ \pi^0 \Lambda) = \frac{1}{4}\sigma(I = 1) \qquad (1.14)$$

where

$$\sigma(I = 0) \sim \left| \langle 0,0 \,|T|\, 0,0 \rangle \right|^2 \qquad (1.15)$$

$$\sigma(I = 1) \sim \left| \langle 1,-1|T|\, 1,-1\rangle \right|^2 = \left| \langle 1+1|T|1+1 \rangle \right|^2 \qquad (1.16)$$

are the pure $I = 0$ and $I = 1$ cross-sections.

It is now possible to make some conclusions concerning the s-channel isospin composition from published cross-sections for $\pi\pi\Lambda$ final states. Figure 1.1 shows a compilation of cross-sections for the reaction $k^- p \rightarrow \pi^+ \pi^- \Lambda$ in the incident momentum range 0.280 to 1.450 GeV/c. This data shows the following features :-

1. A strong resonant feature in the D03(1520) region at 0.395 GeV/c in the data of Mast et al (Ref. 1.21).

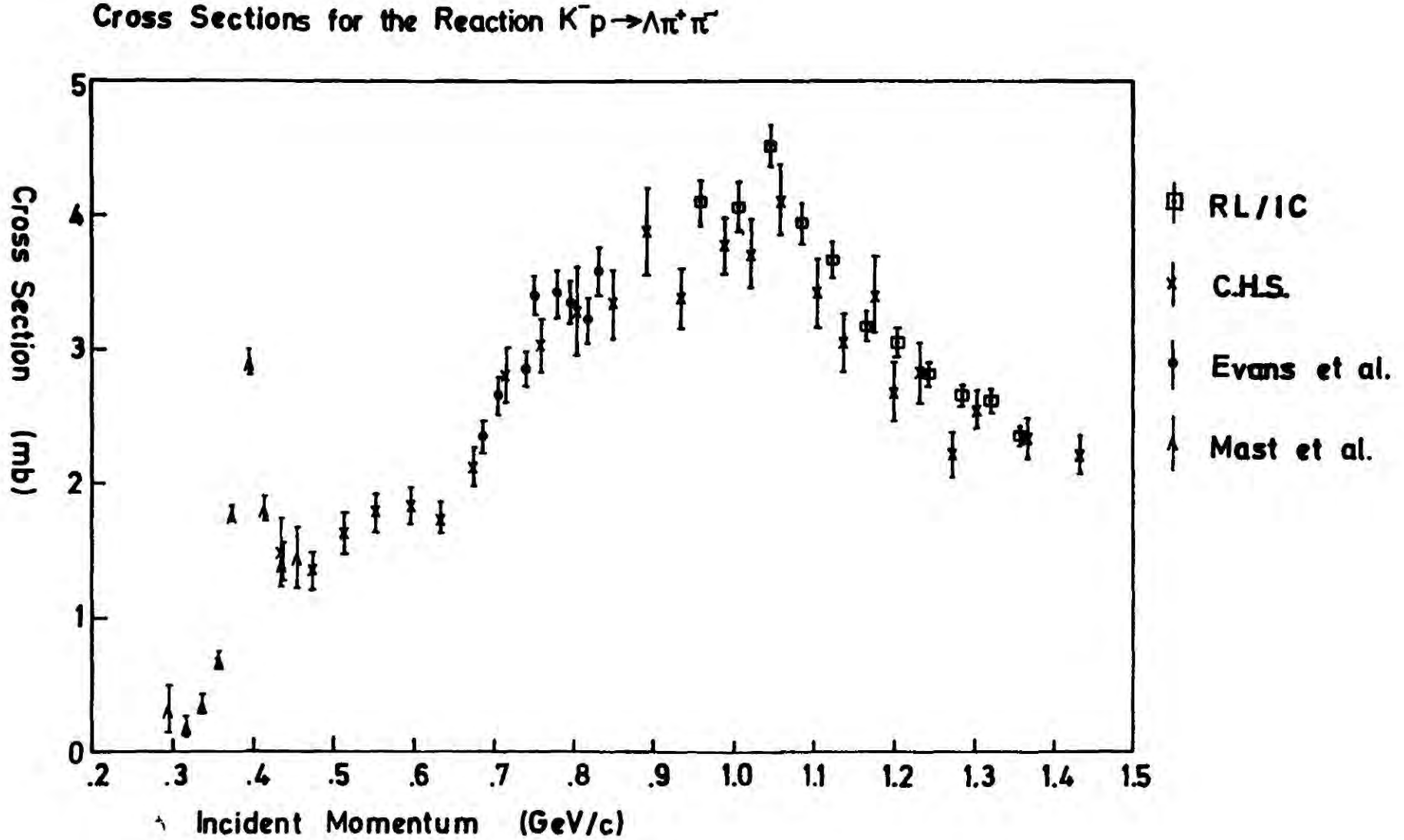

Figure 1.1 : Compilation of cross-sections for the reaction $k^- p \rightarrow \pi^+ \pi^- \Lambda$ between 0.280 and 1.450 GeV/c Incident Momentum.

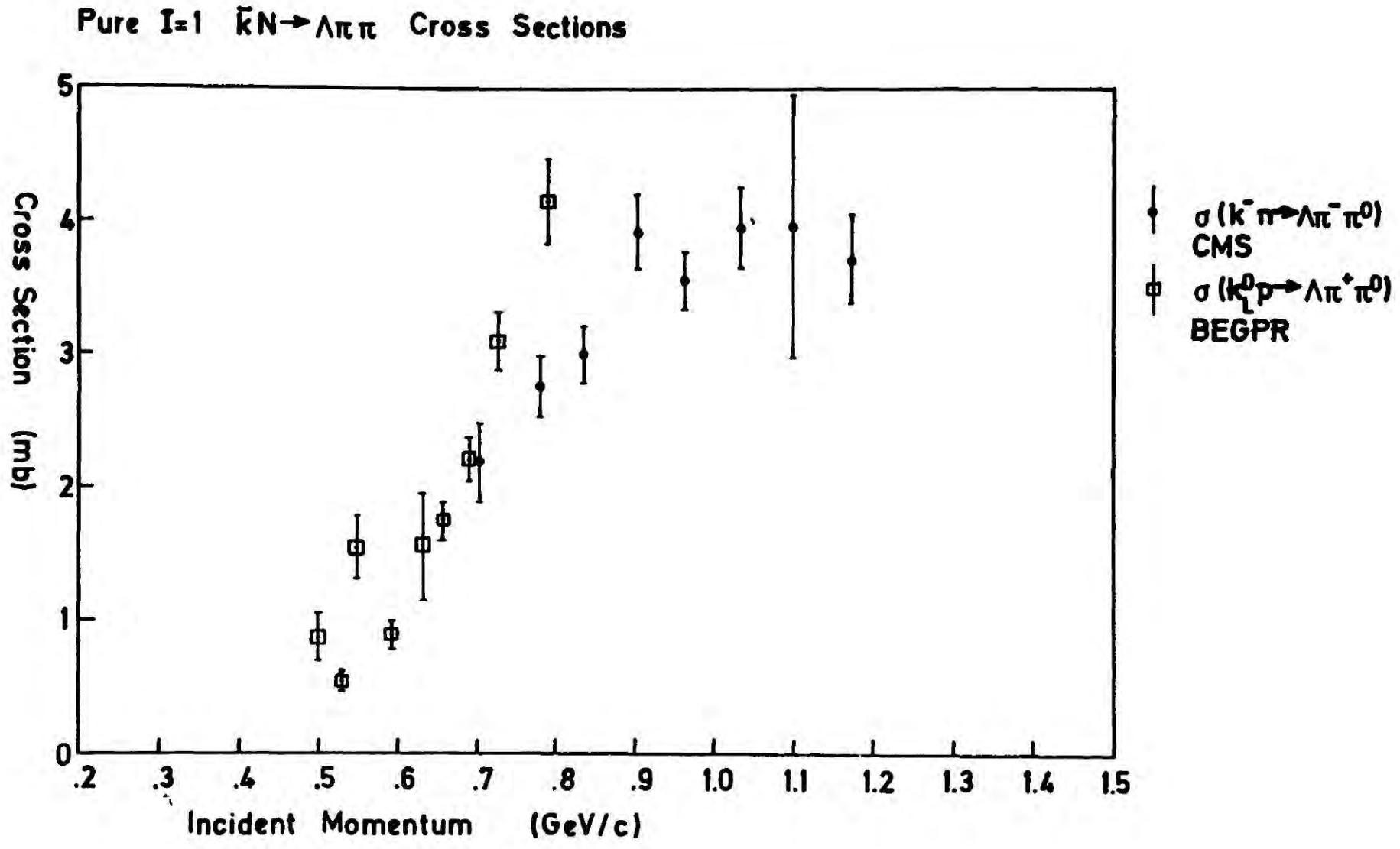

Figure 1.2 : Pure I = 1 cross-sections for the reaction $\bar{k}N \to \pi\ \pi\ \Lambda$.

2. A broad shoulder between 0.650 and 0.800 GeV/c in both the data of CERN-Heidelberg-Saclay (Ref. 1.22) and Evans et.al. (Ref. 1.23). This corresponds to the rather complex region of resonance formation dominated by the DO3(1690),D13(1670) and SO1(1670).

3. A broad enhancement in the cross-section between 0.800 and 1.200 GeV/c. This structure is seen in the data of RL/IC (Ref. 1.13) and C.H.S, but with different normalization. Four spin 5/2 resonances exist in the region, these are DO5(1830), D15(1775), FO5(1815) and F15(1915).

Pure $I = 1$ data comes from two sources. Cameron et al (BEGPR, Ref. 1.24) have published data in the 0.480 to 0.780 GeV/c range from a k^o_L bubble chamber exposure ; Prevost et al (Ref. 1.25) report data obtained by the CERN-Munich-Saclay group for $k^- n \rightarrow \pi^o \pi^- \Lambda$ using a deuterium filled bubble chamber in the 0.720 to 1.200 GeV/c interval. Figure 1.2 shows a plot of $\sigma(k^- n \rightarrow \pi^- \pi^o \Lambda)$ and $2\sigma(k^o_L p \rightarrow \pi^+ \pi^o \Lambda)$ for comparison. Reasonable agreement exists between the two sets of data ; however, some divergence is evident at the highest energy of Cameron. A rapid rise in cross-section is seen up to 0.800 GeV/c, covering the D13(1670) region. A broad enhancement, which may be indicative of D15(1775) and F15(1915) formation, is seen between 0.950 and 1.200 GeV/c.

In addition, Prevost in reference 1.25 has separated pure $I = 0$ cross-sections from the reaction $k^- p \rightarrow \pi^+ \pi^- \Lambda$, represented by the data of C.H.S., using equation 1.12 and extrapolating the C.M.S. pure $I = 1$ data. This analysis indicates that pure isosinglet dynamics dominates the interval devoid of resonances between 0.450 and 0.650 GeV/c. Above 1.2 GeV/c, the pure $I = 1$ cross-section is dominant which is suspected of being due to $\rho\Lambda$ formation.

1.5 PREVIOUS STUDIES

Previous studies of the $\pi\Sigma(1385)$ channel use two rather different methods of analysis. Deller and Valladas (Ref. 1.26) have proposed a set

of paramatrizations which allow isobar model analysis of the data for three body final states to be performed. The isobar model permits possible interference between $\Sigma^+(1385)$ and $\Sigma^-(1385)$ bands in the Dalitz plot. Quasi two-body methods, which are used in this thesis and Ref. 1.13, are somewhat different in nature. No interference is permitted in the Dalitz plot and each $\pi\Sigma(1385)$ channel contributes incoherently to the $\Lambda\,\pi^+\pi^-$ final state.

Prevost (Ref. 1.25) uses Deller and Valladas formalism, with about 300 corrected events per 0.020 GeV/c incident momentum interval,over the 0.600 to 1.200 GeV/c range. Both $k^-p \rightarrow \pi^+\pi^-\Lambda$ and $k^-n \rightarrow \pi^o\pi^-\Lambda$ channels are analysed. Couplings of SO1(1670), S11(1750), DO3(1690), D13(1660), DO5(1830), D15(1765) and FO5(1815) states to the lower accessible final state angular momentum are observed. Non-resonant PPO1, PP11, PPO3, PP13 and FP15 amplitudes are also included. The PO3(1900) and F15 (1915) states lay just outside the energy range of the analysis, but are not included as resonant amplitude contributions. As a final check on the model used, the partial wave amplitudes obtained are used to calculate the forms expected of $\Lambda\pi^+$, $\Lambda\pi^-$ and $\pi^+\pi^-$ effective mass distributions. Although good account is given of the $\Lambda\pi^+$ and $\Lambda\pi^-$ distributions, the $\pi^+\pi^-$ spectrum is poorly described.

The RL/IC (Ref.1.13) analysis is based on the quasi two-body model. Contributions from $\pi^+\Sigma^-$ (1385), $\pi^-\Sigma^+(1385)$, $\rho\Lambda$ and Lorentz Invariant Phase Space (LIPS) are included to account for the Dalitz plot density in the 1.775 to 2.170 GeV centre of mass energy range. An energy dependant partial wave analysis of the $\pi^+\Sigma^-$ (1385) and $\pi^-\Sigma^+$ (1385) channels is performed and resonance couplings observed for SO1(1825), PO3(1900), D13(1920), DO5(1830), D15(1775), FO5(1820), FO5(2100) and F17(2040) to all permitted final state angular momenta. The results of this analysis are summarized in Table 1.1. Non-$\pi\Sigma$ (1385) processes are found to become increasingly important at higher energies. At the lowest momentum analysed, $\rho\Lambda$ (pure I = 1) and LIPS account for less than 20% of the Dalitz plot density, while at the highest momentum

the fraction is 35%. This supports the assertion of Prevost (Ref.1.25) concerning the large isovector component of the $\Lambda\pi\pi$ cross-section above 1 1.2 GeV/c. Statistics of the RL/IC analysis at each energy analysed number about 1500 corrected events.

Mast et al (Ref. 1.21) present very high statistics data in the region of the DO3(1520). An energy independant analysis, based on Deller and Valladas formalism, is performed in which $\Sigma(1385)$, $\pi\pi$ S-wave(ε) and $\pi\pi$ P-wave (ρ) isobars are included. The important s-channel partial wave amplitudes are found to be a resonant $\pi\Sigma(1385)$DSO3 and a non-resonant $\varepsilon\Lambda$DPO3, but the $\pi\,\Sigma(1385)$ DDO3 amplitude which is expected to couple to the DO3(1520) is not included. The presence of the strong non-resonant $\varepsilon\Lambda$ DPO3 amplitude may give credence to the large I = O cross-section in the 0.450 to 0.650 GeV/c interval observed by Prevost. That S-wave $\pi\pi$ isobars become important in the $\Lambda\pi\pi$ final state at low energy will be discussed further in Chapter 5 of this thesis.

In conclusion, the reaction $k^- p \rightarrow \Lambda\pi^+\pi^-$ has been found to be dominated by $\Sigma(1385)$ isobar formation and evidence is seen for Y^* states coupling to $\pi\ \Sigma(1385)$. However, $\pi\pi$ isobar formation may also be important, the production of $\pi\pi$ a S-wave resulting in the dominance of the I = O cross-section at low energies and the P-wave $\rho(770)$ being observed above 1.2 GeV/c incident momentum.

1.6 THESIS OUTLINE

The objective of this thesis is to determine the couplings of SO1(1670), DO3(1690) and D13(1670) resonances to the $\pi\Sigma$ (1385) quasi two-body-final state, for which predictions exist from models of the baryon spectrum. To this end,the outline the rest of this thesis will be

Chapter 2 : Processing and cleaning of the data sample used in the analysis.

Chapter 3 : Formalism required in the analysis.

Chapter 4 : Qualitative description of the Dalitz plot and a discussion of the features seen.

Chapter 5 : The role of $\pi\pi$ S-wave isobars in the Dalitz plot. Extraction of parameters of the $\pi\Sigma(1385)$ quasi two-body final states.

Chapter 6 : Partial Wave Analysis of $\pi\Sigma(1385)$ final states.

Chapter 7 : Comparison of the coupling found for Y^* states with theory.

Chapter 8 : Conclusions and outlook for future work.

CHAPTER 1

REFERENCES

1.1 A. De Rujala et al, Phys. Rev. D12 (1975) 147.

1.2 M. Gell-Mann, Phys. Rev. 125 (1962) 1067.

1.3 N.Isgur and G. Karl, Phys. Rev. D18 (1978) 4187.

1.4 N.Isgur and G.Karl, Phys. Rev. D19 (1979) 2653.

1.5 N.Isgur and G.Karl, Phys. Rev. D20 (1979) 1191.

1.6 R. Koniuk and N.Isgur, Phys. Rev. D21 (1980), 1868.

1.7 R.Koniuk and N.Isgur, Phys. Rev. Lett 44 (1980) 845.

1.8 B.R.Martin et al, Nucl.Phys. B127 (1977) 349.

1.9 M.Alston-Garnjost et al, Phys.Rev. D18 (1978) 182.

1.10 A de Bellefor et al, Nuovo Cimento 42A (1977) 403.

1.11 A.J. Van Horn, Nucl.Phys. B87 (1975) 145.

1.12 G.Gopal et al, Nucl.Phys. B119(1977) 362.

1.13 W.Cameron et al, Nucl.Phys. B143 (1978) 189.

1.14 M.Alston-Garnjost et al, Phys.Rev.D17 (1978) 2226.

1.15 W.Cameron et al, Rutherford Laboratory Report, RL-80-73.

1.16 R.D.Ehrlich et al, Phys.Lett 71B (1977) 455.

1.17 C.J.S.Damerell et al, Nucl.Phys. B155 (1979) 13.

1.18 G.Gopal, Proceedings, 1980 Toronto Baryon Conference (N.Isgur, Editor) page 159.

1.19 R.A.Stern, Ph.D.Thesis, University of London, (unpublished).

1.21 T.S.Mast et al, Phys.Rev D7 (1973) 5.

1.22 R.Arm enteros et al, Nucl.Phys. B21 (1970) 15.

1.23 D.A.Evans et al, Nucl.Phys. B119 (1977) 315.

1.24 L. Berlanza et al, Nucl.Phys. B110(1976) 1

1.25 J. Prevost et al, Nucl.Phys. B69 (1974) 246.

1.26 B.Deller and G.Valladas, Nuovo Cimento 45A (1966) 559.

CHAPTER 2

2.1 INTRODUCTION

The data analysed in this thesis comes from a k^- beam exposure in the Saclay 81 cm Hydrogen Bubble Chamber at CERN, performed by the CERN-Heidelberg-Munich collaboration. A quantity of the film obtained was made available to the Rutherford Laboratory as part of a program to study $k^- p$ interactions, with high statistics, in the resonance region. This work has been conducted in collaboration with Imperial College, London, and lately with Durham University. The author of this thesis has undertaken a study of the reaction $k^- p \rightarrow \Lambda\pi^+\pi^-$ observed in this data as part of the work for the degree of Ph.D. at Durham University. As such, the author's contribution to this effort began with the problems associated with track reconstruction and data assessment for film obtained using a Track Sensitive Target (T.S.T) in the 0.480 to 0.600 GeV/c incident momentum range. The rest of this chapter will be devoted to a description of the methods used to process events measured in the 0.620 to 0.870 GeV/c interval from the so called SURVEY-81 experiment and the quality of such data.

2.2 DATA PROCESSING

Figure 2.1 shows the data processing chain used in the SURVEY-81 experiment. This is given since it clarifies some of the corrections, which will be employed in Section 2.10, concerning the scanning and throughput efficiences for events.

The entire film available (some rolls were lost because of poor quality) was scanned for strong interactions of all topologies* and the weak decay $k^- \rightarrow \pi^+\pi^-\pi^-$, which is the normalizing process. Each event was then coded according to its measurability. Events which were outside the agreed scanning area or considered too obscured by overlapping tracks for measurement, were coded as not-measurable. Measurable events, following

Figure 2.1 : Flow diagram for the Data Processing Chain
Circular elements indicate scan-time decision recorded on MASTERLIST, rectangular elements refer to analysis programs and triangular blocks to operations performed.

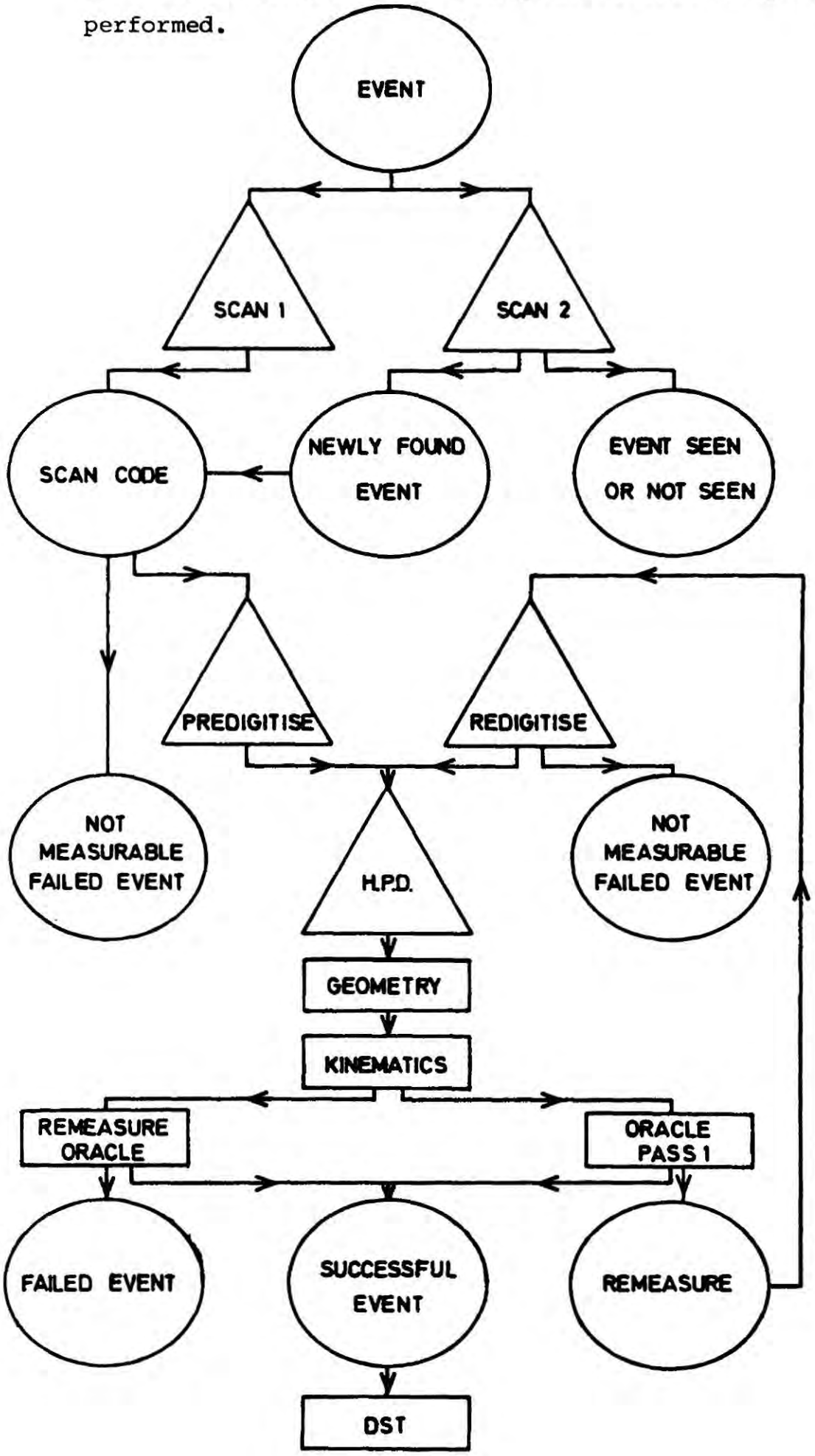

a predigitisation procedure, were sent for automatic measurements on the Rutherford Laboratory H.P.D. system. About 25% of the film was scanned a second time in order to determine scanning efficiency. Again, all events seen were recorded. Those seen for the first time on this second scan were subsequently predigitized for measurement on the H.P.D.(Hough-Powell Device).

Post H.P.D processing for events is performed sequentially by the programs GEOMETRY, KINEMATICS and ORACLE, the functions of which are described below :-

GEOMETRY : This program reconstructs the digital information from each of the three film images of an event, obtained by the H.P.D., into particle track paths in the bubble chamber. As such , it contains detailed information concerning the optics of the bubble chamber camera system and other refracting surfaces through which events are seen. Output from this program consists of the directions and curvatures of charged particle tracks.

KINEMATICS : This interprets track data from GEOMETRY in terms of kinematic hypotheses concerning the observed reactions. A set of fitted momenta for each event are returned together with a χ^2 probability for each successful hypothesis tried.

ORACLE : Several kinematic hypotheses may be simultaneously satisfied by each event. Criteria for the resolution of such ambiguity are contained within ORACLE. These include :-

(i) The use of bubble density information from the H.P.D to resolve, on the basis of ionization, different particle assignments to a given track.

(ii) The relative rarity of channels and the relative χ^2 probabilities.

Two versions of ORACLE are used. A first-pass version returns events for remeasurement which are ambiguous, have poor KINEMATICS χ^2 probability, or which have failed track reconstruction in GEOMETRY.

The second-pass version, for remeasured events, accepts events which

have ambiguous kinematic fits or poor χ^2. Successful events are written to final Data Summary Tape (D.S.T).

At all times during this process, the status of events seen at scan time has been monitored by a book-keeping system called MASTERLIST. This keeps records of scantime coding of events and the outcome of GEOMETRY, KINEMATICS and ORACLE. Hence, throughput of the measurement system, according to event topology, may be determined and correction for failure of events to appear on final D.S.T. found.

* Throughout this thesis the notation I J K will be used for topology, where I is the number of charged tracks leaving the production vertex, J is the number of charged particle decays seen, and K is the number of neutral particle decays seen.

2.3 BEAM DEFINITION

In this experiment the beam line optics has been set to select a series of narrowly defined momenta at entrance to the bubble chamber. Defocussing effects caused by the beam optics result in the envelope of the beam tracks being conical in shape (ref. 2.1). At incident k^- momenta in excess of 1 GeV/c (e.g. ref. 2.2), the curvature of the beam in the chamber magnetic field is small and beam momenta are known more reliably from beam optics than from geometrical reconstruction of tracks. Contamination of the otherwise monoenergetic beam is a result of scattering of k^- mesons from the beam pipes. Elastic scattering results in degradation of the momentum spectrum, whilst inelastic reactions produce other hadrons, mainly π^- Leptonic beam components, which will not undergo strong interaction in the chamber, result from weak decays of k^- mesons. Whatever the mechanism involved, these beam impurities are expected to be scattered outside the beam envelope. This property may be exploited to define a pure beam. At each beam optics setting, a set of angles were used to paramatrize the envelope of the beam at the entrance to the chamber field. Here, the

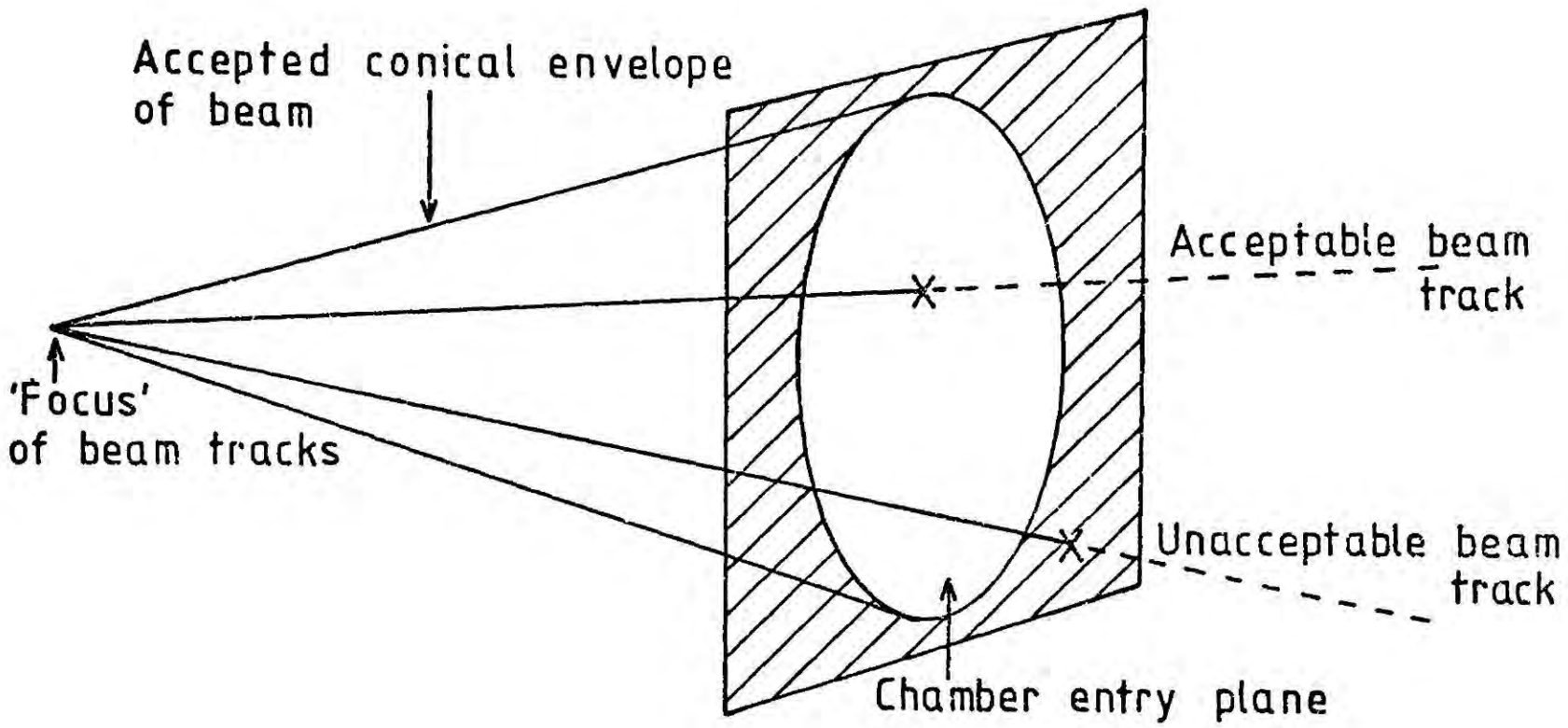

Imposition of Beam Cuts

Figure 2.2 : Schematic diagram showing how beam cuts are imposed.

cross-section of the beam is elliptical. All beam tracks which intercept the chamber entry plane outside this ellipse are rejected (Figure. 2.2).

The application of such beam cuts has been carried over from other experiments, although they are not significant in the 0.650 to 0.850 GeV/c momentum range, where beam tracks have measurable curvature. Furthermore, backgrounds from non-k^- meson interactions, which are topologically equivalent to the reaction $k^- p \to \Lambda\pi^+\pi^-$, are not expected since the highest energy of this experiment is below threshold for strange particle production in pion induced reactions.

Figure 2.3 shows the distribution of entrance beam momentum for events fitting the reaction $k^- p \to \Lambda\pi^+\pi^-$. The dip in statistics between 0.680 and 0.720 GeV/c is due to poor picture quality, which prevented the measurement of several rolls of film exposed in this energy range. A typical entrance momentum distribution for one of the beam optics settings is shown in Figure 2.4.

A fiducial volume cut has also been imposed on events of all topologies. This was chosen to give reasonable scanning efficiency and measurability of events. The cuts on interaction vertex co-ordinates are

$$-6.0 < x < 28.0 \text{ cm.}$$

$$-7.0 < y < 7.0 \text{ cm.}$$

$$-28.0 < z < -8.0 \text{ cm.}$$

The choice of beam cuts and fiducial volume are discussed in Ref. 2.1.

2.4 RESOLUTION OF AMBIGUITIES

Reliance is placed in bubble chamber technique on the determination of curvature and direction in space, for charged particle tracks, by geometrical reconstruction of points measured along their length. Subsequently, these quantities are interpreted as 3-vector momenta and are

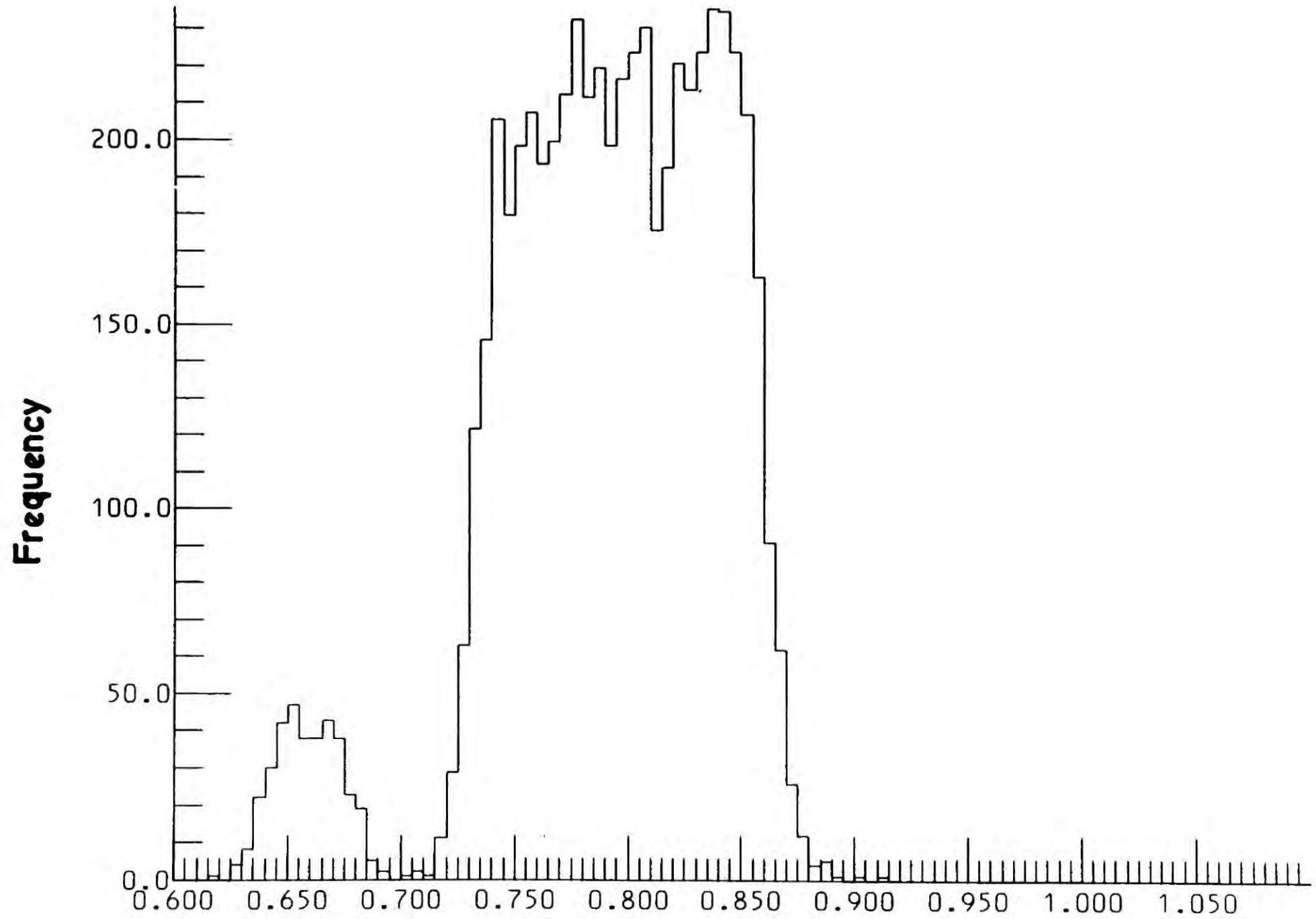

Figure 2.3 : Distribution of Entrance Beam Momentum.

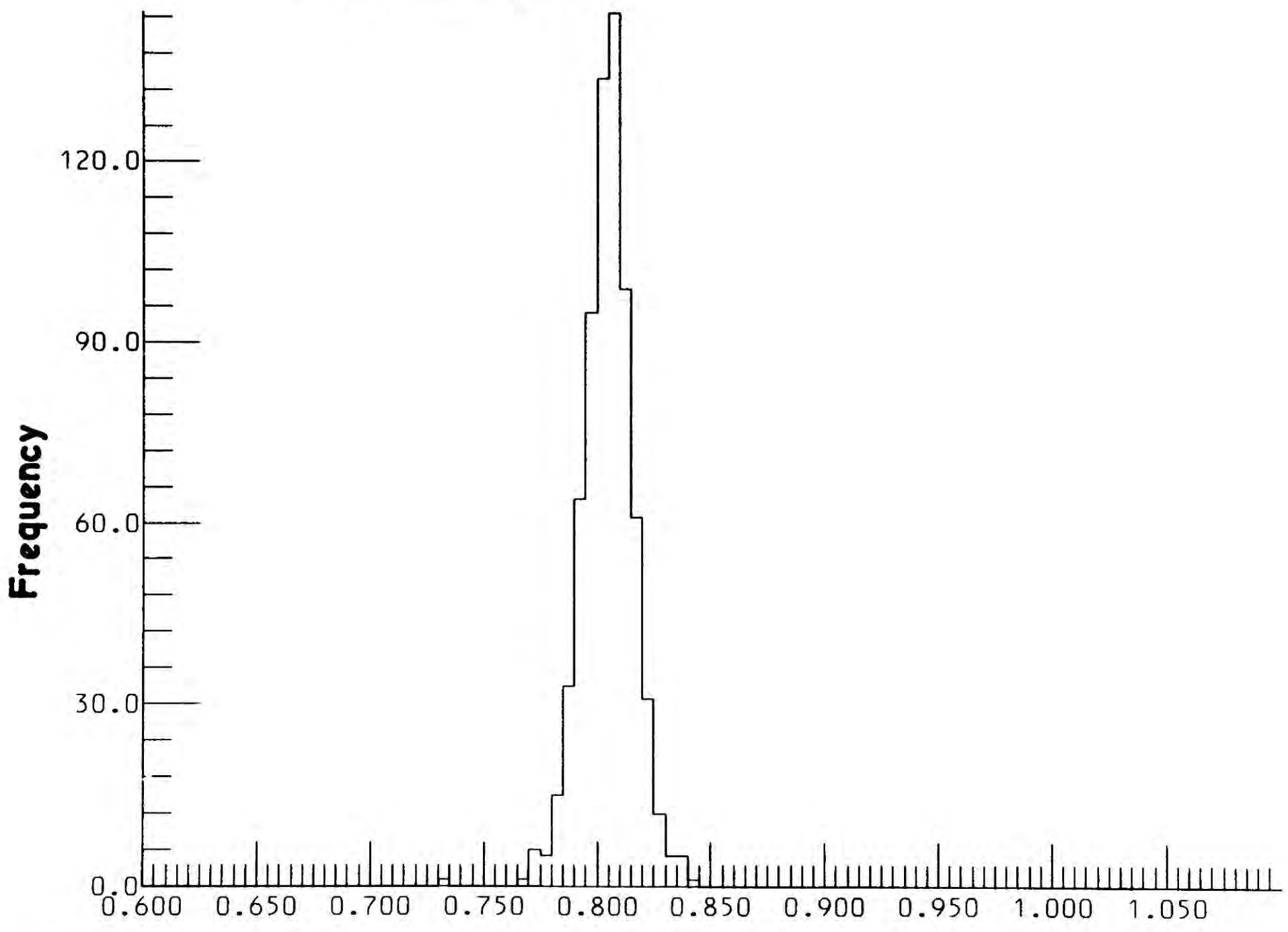

Figure 2.4 : Typical Beam Momentum Bite.

fitted to kinematical hypotheses concerning the origin of the charged tracks. As such, reactions which result in topologically equivalent configurations of tracks may satisfy several kinematic hypotheses ambiguously.

The reaction studied in this thesis is

$$k^- p \rightarrow \Lambda \pi^+ \pi^- \qquad (2.1)$$

$$\Lambda \rightarrow p \pi^-$$

which is characterized, in the final state, by two charged tracks leaving the interaction vertex, together with π^- and p tracks leaving the vertex associated with the Λ^o decay. Topologically equivalent with this reaction are the reactions,

$$k^- p \rightarrow \Sigma^o \pi^+ \pi^-$$

$$\Sigma^o \rightarrow \Lambda^o \gamma \qquad (2.2)$$

$$\Lambda \rightarrow \pi^- p$$

$$k^- p \rightarrow \bar{k}^o p \pi^-$$

$$\bar{k}^o \rightarrow \pi^+ \pi^- \qquad (2.3)$$

$$k^- p \rightarrow \Lambda \pi^+ \pi^- \pi^o \qquad (2.4)$$

$$\Lambda \rightarrow \pi^- p$$

Events in which the decay $\Lambda^o \rightarrow p \pi^-$ is not observed, were also measured. These events are seen as two oppositely charged pion tracks emerging from a production vertex and are found to be highly kinematically ambiguous with other reactions of the same topology. For this reason, only events with a fitted $\Lambda^o \rightarrow p\pi^-$ decay are used in this work. Later in this chapter, the

corrections for losses of events with unseen Λ^{o} decay, i.e. those of 200 topology, will be discussed.

No events represented by reaction 2.3 are found to fit ambiguously with reaction 2.1. This is due to the availability of ionization information from the H.P.D. Reaction 2.4 is expected to contain a significant contribution, above threshold (0.720 GeV/c), from the reaction

$$\begin{aligned} k^{-} p &\rightarrow \Lambda \eta \\ \eta &\rightarrow \pi^{+}\pi^{-}\pi^{o} \\ \Lambda &\rightarrow \pi \bar{p} \end{aligned} \qquad (2.5)$$

Previous studies of reaction (2.5) (Ref. 2.3) show a large cross-section at threshold which falls rapidly with increasing energy. As such, this fact underlies the importance of correct assignment of ambiguities. Mis-assignment of events fitting reaction 2.5 would result in large, momentum dependant, errors in the determination of the cross-section for reaction 2.1.

Both reactions 2.2 and 2.4 give rise to the same final state particles as reaction 2.1. The only basis for discrimination comes from the missing-mass recoiling against the $\pi^{+}\pi^{-}$ system in the final state. In the case of reaction 2.1 this is expected to correspond to a Λ^{o} (1.115 GeV/c^{2}, in the case of reaction 2.2 a Σ^{o} (1.192 GeV/c^{2}), whilst for reaction 2.4, it is a $\Lambda\pi^{o}$ system of minimum effective-mass 1.254 GeV/c^{2}. If the recoiling missing-mass is calculated from the measured momenta of charged tracks entering and leaving the production vertex, which are reconstructed by the program GEOMETRY, resolution of ambiguities may be attempted on the basis of missing-mass cuts. In reality, the determination of recoiling missing-mass is subject to error due to measurement errors in track trajectories by the H.P.D. Assuming a simple propagation of errors, one expects the missing-mass squared distributions for reactions (2.1), (2.2) and (2.4.) to be

convolved with Gaussian resolution functions.

The missing-mass to the $\pi^+\pi^-$ system is shown in Figure 2.5 for unique fits to reactions (2.1) and (2.2) together with those events fitting both reactions ambiguously. A total of 5397 unique fits exist to reaction 2.1 and 959 events fit ambiguously with reaction 2.2. Ambiguities with reaction 2.4 have been ignored since the Gaussian width of the Λ^o contribution is $0.05\ (GeV/c^2)^2$, whilst the minimum difference in missing mass squared for reactions (2.1) and (2.4) is expected to be $0.177\ (GeV/c^2)^2$. On the basis of Figure 2.5, all ambiguous events have been assigned to reaction 2.1.

2.5 INVESTIGATION OF BIASSES

Events selected after fiducial volume and beam cuts, which satisfy the missing-mass criteria described in the previous section, may be subject to losses resulting from poor visibility for certain geometries in the bubble chamber, which in turn are correlated to the underlaying kinematics. Hence, the experimental inaccessibility of certain event geometries may bias conclusions concerning the dynamics of the reaction $k^- p \to \Lambda\pi^+\pi^-$.

Steep tracks are both difficult to see and measure in the bubble chamber. To identify any such loss for the reaction $k^- p \to \Lambda\pi^+\pi^-$, $\Lambda \to \pi^- p$ two angles were utilized :-

(a) The rotation of the Λ about the beam direction, ϕ_p.

If $\hat{3}$ is a unit vector along the chamber z axis (i.e. in the direction from which the chamber is viewed by the camera optics), $\bar{k}$ is the vector defining the incident k^- direction and $\bar{\Lambda}$ is the vector defining the Λ^o motion in the laboratory, then :-

$$\phi_p = \cos^{-1} \frac{(\bar{k}\hat{\wedge}\hat{3}) \cdot (\bar{k} \wedge \bar{\Lambda})}{|\bar{k}\hat{\wedge}\hat{3}|\ |\bar{k} \wedge \bar{\Lambda}|} \qquad (2.6)$$

When the $(\bar{k} \wedge \bar{\Lambda})$ plane is normal to the chamber X-Y plane, $\phi_p = 0$ or π radians.

Distribution of Missing Mass Squared for Events of 201 Topology

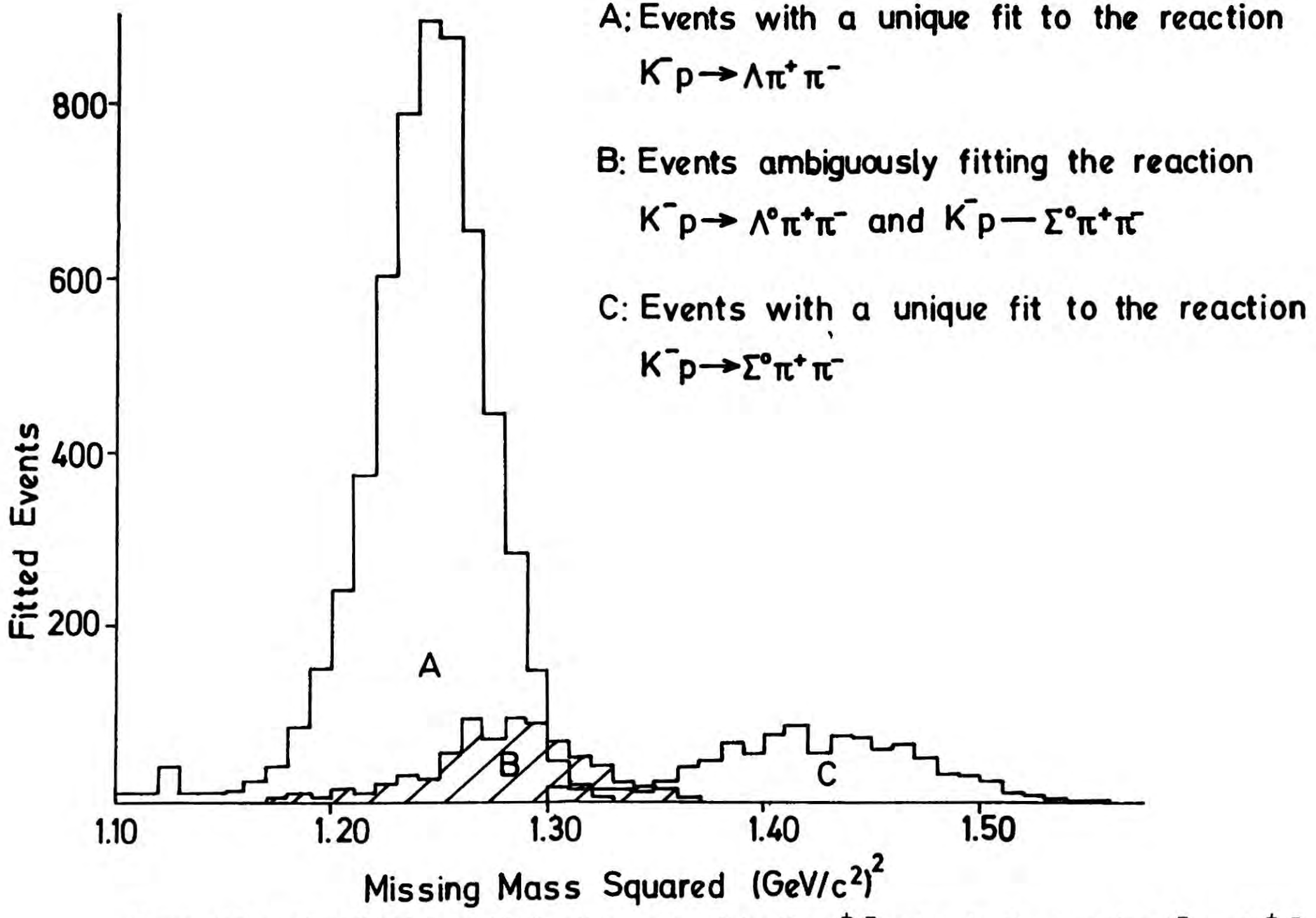

Figure 2.5 : Distribution of Missing-Mass squared to the $\pi^+\pi^-$ system in the reaction $k^-p \rightarrow \Lambda\pi^+\pi^-$.

(b) The angle giving the rotation of the decay plane, defined by the normal to the π^- and p tracks, about the Λ^o direction in the laboratory. If $\bar{\Lambda}$ is the Λ^o direction and $\bar{D}_1$ and $\bar{D}_2$ are the π^- and p directions, this angle is defined as :-

$$\phi_d = \cos^{-1} \frac{(\bar{\Lambda}\hat{\wedge}\hat{3}) \cdot (\bar{D}_1 \wedge \bar{D}_2)}{|\bar{\Lambda} \wedge \hat{3}| \, |D_1 \wedge D_2|} \qquad (2.7)$$

If steep track losses are absent from the data, both of these angles should be uniformly distributed. Steep track losses will be signified by absence of events when ϕ_p, or $\phi_d = 0$ and π. Figure 2.6 shows the distribution of these quantities for the data and no such losses are apparent.

Events with short pion tracks or Λ^o decays without visible gaps to the production vertex, are subject to losses which are directly related to the centre of mass production kinematics. Since in Chapter 5 a dynamic interpretation of these properties will be given, it is essential to show that such losses do not remove specific production kinematical regions from experimental investigation.

If the total centre of mass energy of the initial k^-p system is $\sqrt{s}$ and a two-body system of effective-mass m recoils against a third particle particle of mass m_3, then the centre of mass momentum, q, of particle m_3 is given by,

$$q^2 = \frac{(s-(m_3 + m)^2)(s-(m_3-m)^2)}{4s} \qquad (2.8)$$

Hence, for given $\sqrt{s}$, q^2 takes on its maximum value when m takes on its minimum value, $m = m_1 + m_2$, where m_1 and m_2 are the masses of the particles forming the two particle subsystem. The minimum value of the laboratory momentum for the third particle occurs when it is produced backwards in the

Distribution of Production Azimuth Angle for Λ^o (ϕ_p)

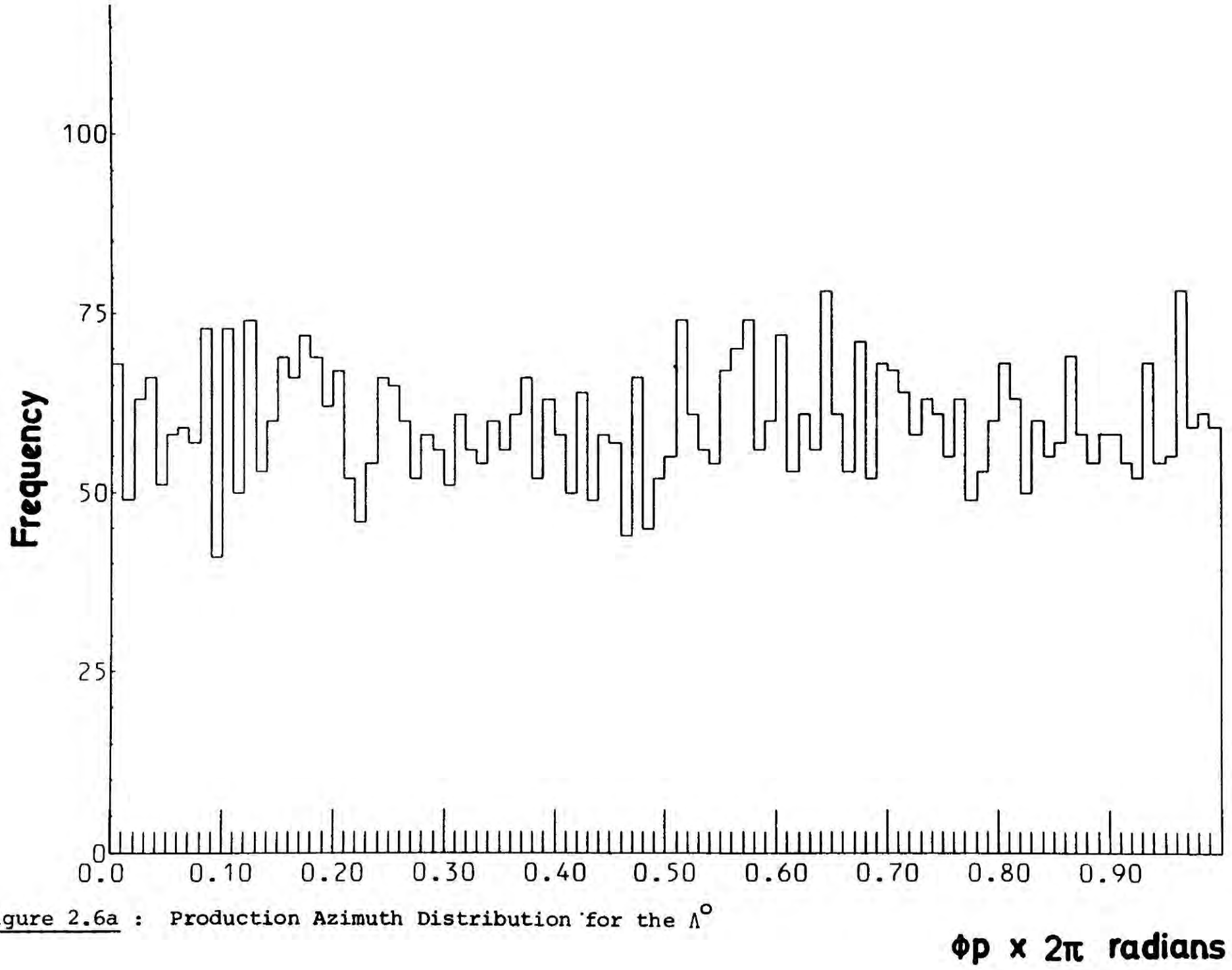

Figure 2.6a : Production Azimuth Distribution for the Λ^o

Distribution of Decay Azimuthal Angle for Λ° (ϕd)

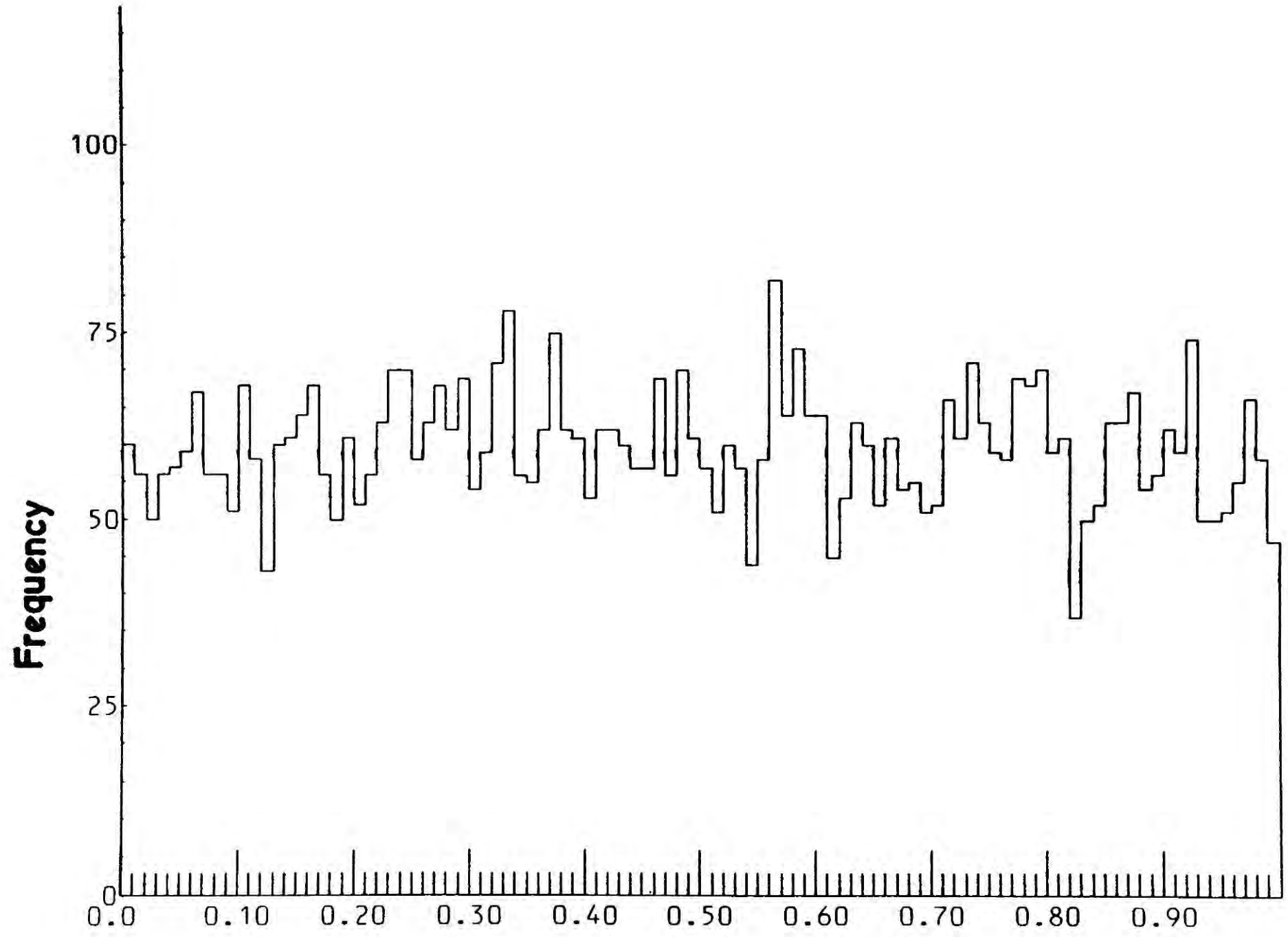

Figure 2.6b : Decay Azimuth Distribution for the Λ^{o}

centre of mass and if $C\beta$ is the boost velocity from the laboratory system to the centre of mass system, this is given by

$$p_{LAB} = \gamma q - \gamma \beta E \quad , \quad \gamma = (1-\beta^2)^{-\frac{1}{2}}$$

where $E = \sqrt{q^2 + m_3^2}$

Minimum momenta of the production vertex pions and Λ^o calculated in this way are given in Table 2.1.

Slow pions become difficult to detect when their range falls below 1 cm. in the liquid hydrogen of the bubble chamber. The minimum pion momentum from Table 2.1 is found to be 56 MeV/c which corresponds to a range of 5 cm. No slow pion loss at the production vertex is therefore anticipated.

The proper Λ^o time of flight, τ, is given in terms of its measured decay length in the laboratory ℓ , its laboratory momentum p_Λ and its mass m_Λ by :-

$$C\tau = \frac{m_\Lambda}{p_\Lambda} \cdot \ell \qquad (2.9)$$

The distribution of Λ^o lifetime follows the exponential decay law :-

$$\frac{dN(\tau)}{d\tau} = N_o \, e^{-\tau/\tau_c} \qquad (2.10)$$

where $N(\tau)$ is the number of Λ^o surviving after time τ.

and τ_c is the mean Λ^o lifetime ($C\tau_c = 7.89$ cm). If events with decay lengths less than 0.5 cm are lost, then at the lowest Λ^o momenta, the minimum accessible value of $C\tau$ is 7.0 cm. The slowest Λ^o will have the lowest detection efficiency due to short gap losses

$$= \left[1 - e^{-\tau/\tau_c} \right] = 40\%$$

Incident k^- momentum p_k/(GeV/c)	Minimum pion momentum p_π/(GeV/c)	Minimum Λ^o momentum p_Λ/(GeV/c)
.65	.056	.079
.70	.059	.083
.75	.062	.089
.80	.066	.094
.85	.069	.098

TABLE 2.1 : Minimum Momenta of the Production Vertex Pions and Λ^o

One therefore feels confident to proceed and correct for losses which result from visibility resolution for the observed Λ^o decay gap, since no production kinematics will be completely absent from the data.

The detection probability for a Λ^o to be seen to decay between distances ℓ_1 and ℓ_2 from its point of production is

$$P_D = e^{-\frac{m\,\ell_1}{p_\Lambda c\tau_o}} - e^{-\frac{m\,\ell_2}{p_\Lambda c\tau_o}} \qquad (2.11)$$

If the Λ^o subtends an angle δ to the chamber X-Y plane, it will be seen to have a projected decay length = $\ell \cos\delta$. In order to correct for the unseen decays of Λ^o below a minimum projected decay length $\ell min = \ell \cos\delta$ or outside the interaction fiducial volume, within which the Λ^o has potential length for decay $\ell_{(pot)}$, each event is weighted by the inverse of its detection probability :-

$$wt = \frac{1}{\left[\exp\left[\frac{-m\ell_{min}}{p\,c\tau_o\cos\delta}\right] - \exp\left[\frac{-m\ell_{pot}}{p\,c\tau_o}\right]\right]} \qquad (2.12)$$

To decide the most economical projected length cut (ℓ min), all events with projected length greater than ℓmin and decaying within the fiducial volume are weighted according to various values of ℓmin. The total weight of the event sample is plotted as a function of ℓmin. Stability of the total weight indicates that further increase of ℓmin, beyond the most economical value, reweights for removed events. On this basis a value ℓmin = 0.15 cm has been chosen (Figure 2.7). For events of the lowest Λ^o momenta this gives a detection efficiency of 78%.

Fig. 2.7 : Total Event Weight as a Function of Projected Length Cut

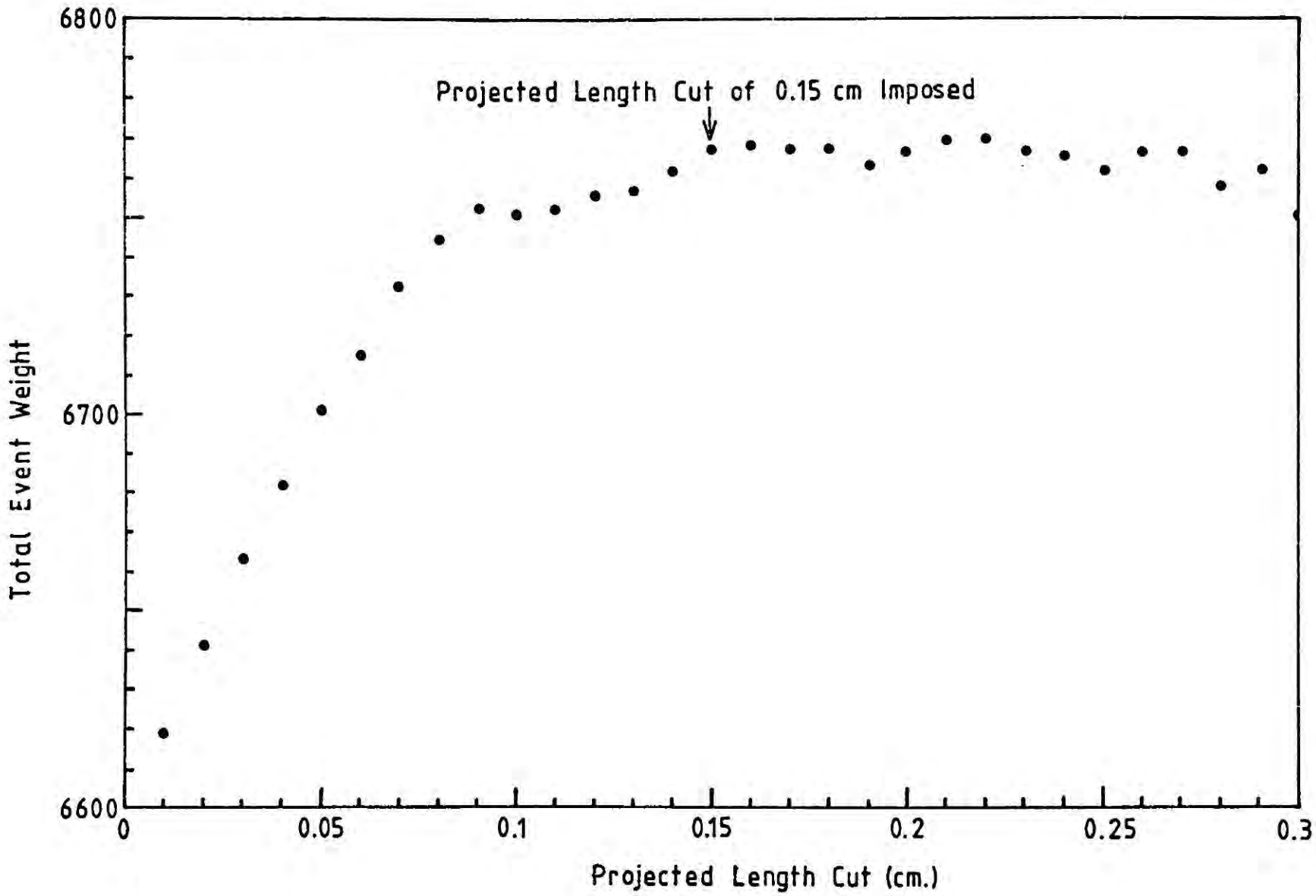

2.6 Λ^o DECAY LOSSES

Having observed that restrictions on visibility of $\pi^+\pi^-$ and Λ^o final state particles due to steepness or shortness of tracks, do not completely remove any portion of the production vertex kinematics, the Λ^o decay vertex kinematics will be considered.

Consider the decay $\Lambda^o \rightarrow p\,\pi^-$ in the rest frame of the Λ^o. If $\vec{D}$ is the momentum of the π^- in the rest frame of the Λ^o and $\vec{\Lambda}$ is the momentum of the Λ^o in the laboratory, then

$$\cos\Theta^*_d = \frac{\bar{\Lambda}\,.\vec{D}}{|\bar{\Lambda}|.|D|} \qquad (2.13)$$

is known to be uniformly distributed between -1 and +1. Figure 2.10 shows the experimental distribution of this quality. A clear loss is visible for $0.94 \lesssim \cos\Theta^*_d \lesssim +1.0$.

The recoil momentum of the π^- and p in the Λ^o rest frame is $q = 0.1$ GeV/c. For the Lorentz boost from the Λ^o rest frame to the laboratory $\beta = p_\Lambda/E_\Lambda$, where p_Λ and E_Λ are the Λ momentum and energy in the laboratory. Hence, the π^- has energy $E = \gamma E^* - \gamma\beta\, q \cos\Theta^*_d$ in the laboratory, with $E^* = \sqrt{q^2 + m_\pi^2}$. In the laboratory, the π^- has a momentum component parallel to the Λ direction,

$$p'' = \gamma q \cos\Theta^*_d - \gamma\beta E^* \qquad (2.14)$$

and a component perpendicular to the Λ direction, $p^\perp = q \sin\Theta^*_d$ (2.15)

So the angle subtended by the π^- to the Λ direction in the laboratory Θ_L is given by

$$\text{Tan}\,\Theta_L = \frac{p^\perp}{p''} = \frac{q \sin\Theta^*_d}{\gamma q \cos\Theta^*_d - \gamma\beta E^*} \qquad (2.16)$$

Provided $\frac{q}{E^*}\cos\Theta^*_d \gtrsim \beta$, the π^- is produced in the forward direction with respect to the Λ^o in the laboratory. Considering the motion of the π^- parallel to the Λ^o, when $\cos\Theta^*_d = +1$:-

$p'' = 0$ when $\beta = \frac{q}{E^*}$ i.e. the π^- is produced at rest in the

laboratory when its velocity in the Λ^o rest frame is equal and opposite to the boost velocity from the laboratory system. This occurs when p_Λ= 0.8 GeV/c. At this point also, the π^- is produced backwards in the laboratory system. Similar expressions for the proton give the Λ momentum at which the proton is produced at rest in the laboratory as 0.1 GeV/c. Above this momentum the proton is produced forward in the laboratory when $\cos\theta^*_d = 1$. In particular, the energy of the proton in the laboratory is :-

$$E_p = \gamma E^*_p + \cos\theta^*_d . \gamma\beta \; q \qquad (2.17)$$

Hence, provided $p_\Lambda > 0.1$ GeV/c, the region near $\cos\theta^*_d = 1$ corresponds to production of slow pions, which may be subject to short range losses, and fast protons in the laboratory. If $p < 0.8$ GeV/c the laboratory angle between proton and pion θ_V, i.e. the opening angle of the V^o, will be small; when $p_\Lambda > 0.8$ GeV/c, the opening angle is close to 180^o. Both of these geometries are potentially subject to loss :-

(i) If $\theta_V \sim 0$ the π^- and p tracks may obscure each other and provide measurement difficulties (Fig. 2.8).

(ii) If $\theta_V \sim \pi$ the Λ^o decay vertex may be difficult to locate, causing the vector describing the Λ^o trajectory in the laboratory to be misdetermined, (Fig. 2.9). To investigate short pion range and opening angle losses, a Monte-Carlo technique has been developed.

2.7 MONTE-CARLO STUDIES

Strictly, a Monte-Carlo technique is one which allows the consequences of a physical model to be examined in a regime where finite statistical precision is the limiting factor. In this thesis the technique will be used to investigate the relationship between geometrical and

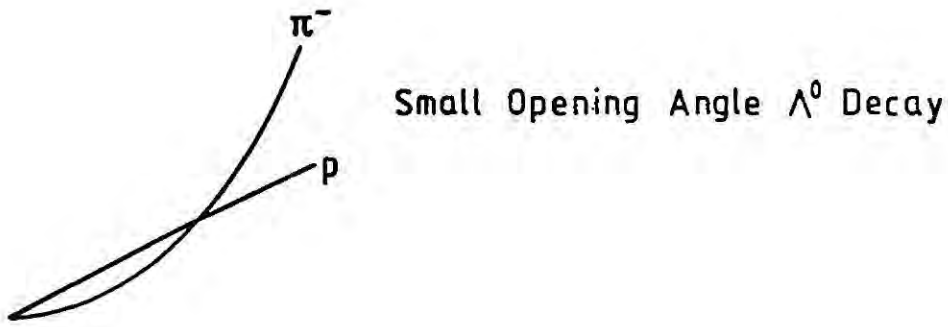

Figure 2.8 : Small opening angle Λ^{o} decay.

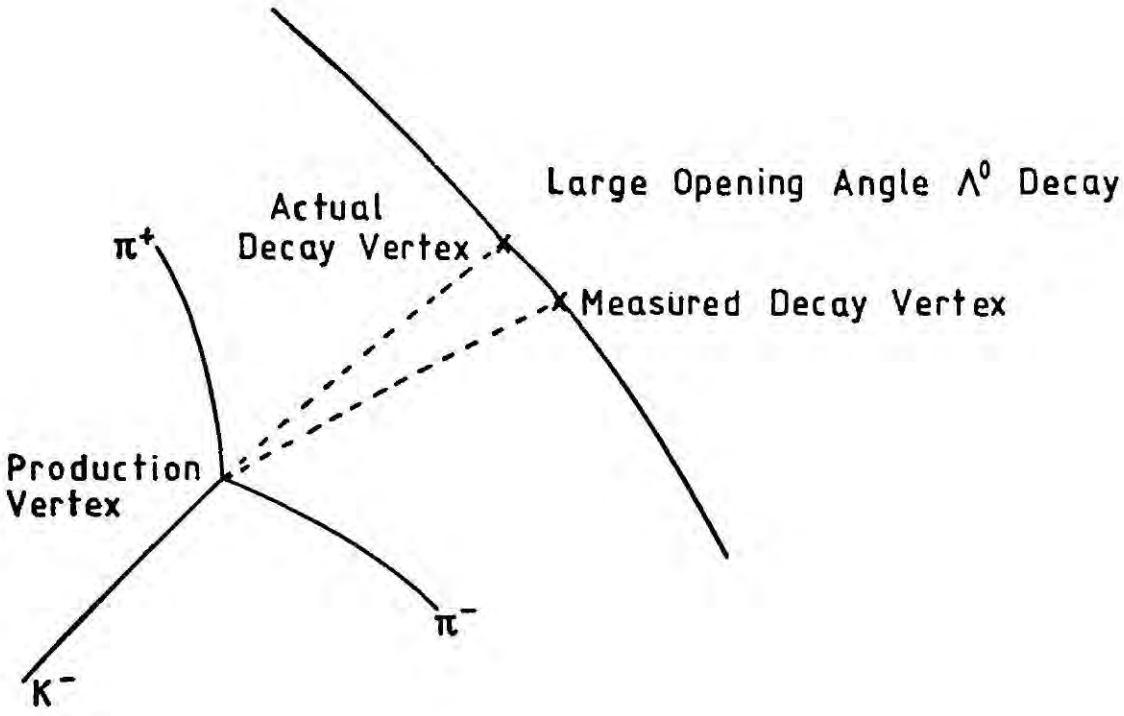

Figure 2.9 : Large opening angle Λ^{o} decay.

kinematic quantities for the Λ^o decay. As such the model for the production properties of the Λ comes from the event sample itself, the Monte-Carlo input comes from the randomisation of the decay properties of the Λ^o.

To generate an interaction vertex and k^- 3-vector momentum for events requiresa detailed knowledge of the incident beam profile in both configuration and momentum space. This would demand a detailed knowledge of the beam line optics and is beyond the scope of this thesis. Since the k^-beam envelope is conical at entry to the chamber and subsequently develops curvature in the chamber field, it is clear that the k^- direction and position at interaction in the chamber are highly correlated. This effect has been embodied in the Monte-Carlo by randomly selecting interaction vertex and k^- direction from those for 100 real events. These values are randomly overwritten by new values throughout the procedure. Only events passing fiducial volume and beam cuts are used.

Similar problems arise in the generation of Λ^o momentum. The Λ^o momentum depends on its centre of mass production angle and the incident k^- momentum. A description of the variation of centre of mass production angle with incident momentum requires a detailed knowledge of s-channel dynamics. But, since it is clear that no Λ^o production kinematics occurs with a detection probability less than 78%, see section 2.5, one may use the centre of mass production angle and incident momentum from the real event sample.

Randomization of other event quantities is more straight forward. As discussed in section 2.4, the distributions of ϕ_p, ϕ_d and $\cos\Theta^*_d$ are known to be uniform. The distribution of Λ^o lifetimes follows an exponential decay law.

Programatically, the Monte-Carlo randomization from the Λ^o production kinematics flows as follows :-

(a) For each event of given angle, one hundred Monte-Carlo events are generated according to the randomization criteria : -

(i) Interaction vertex and direction are selected randomly from 100 values for real events.

(ii) The Λ^o direction in space is randomized by choosing a value of ϕ_p between 0 and 2π .

(iii) The position of the Λ^o decay vertex is now obtained by randomly selecting a Λ^o lifetime according to the exponential decay law and using the decay length vector :-

$$\vec{\ell} = \frac{\vec{p}_\Lambda}{m} c\tau \qquad (2.18)$$

relative to the production vertex.

(iv) The directions and momenta for π^- and p tracks emerging from the Λ^o decay vertex are obtained from ϕ_d selected uniformly between 0 and 2π and $\cos\theta^*_d$ selected uniformly between -1.0 and +1.0.

All kinematic and geometrical properties of the 100 generated events are now specified.

(b) Cuts, where required, are applied to the generated event samples and various quantities are histogrammed for comparison with the later sample.

(c) One of the 100 sets of interaction quantities is randomly overwritten by those for the current event.

(d) A new event is read from Data Summary Tape and steps (a) to (c) are repeated.

(e) When all events are read and randomized, comparison is made between generated events and real events subject to the same set of cuts.

The results obtained using this method will be discussed in the next section.

2.8 CALCULATION OF CORRECTIONS

Before any investigations were performed concerning the origin of the loss observed in $\cos\theta^*_d$ near + 1.0, events with projected length less than 0.15 cm or decaying outside the fiducial volume for interaction were removed from both event and Monte-Carlo samples. Comparison was then made between

the $\cos\theta^*_d$ distributions from both samples. No loss was apparent in the generated $\cos\theta^*_d$ distribution. Distributionsof laboratory momenta of pion and proton coming from Λ^o decay and of Λ^o opening angle were also compared. The most striking difference was observed in the pion laboratory momentum below 45 MeV/c. This momentum corresponds to a pion range of 2 cm in liquid hydrogen. With a pion momentum cut of 45 MeV/c imposed on both samples of events, the $\cos\theta^*_d$ distribution of Fig. 2.10a was obtained, which shows good agreement with the $\cos\theta^*_d$ distribution of the data (Figure 2.1C b). Figure 2.11 shows a comparison of Monte-Carlo and pion momentum distribution with that of the data. No additional systematic losses are evident. For events surviving the cuts on projected length, decay fiducial volume and pion momentum , the probability of detection for a given incident momentum and centre of mass production angle is

$$P_d = \frac{\text{Number of Monte-Carlo events surviving cuts}}{\text{Total number of events generated}} \qquad (2.19)$$

and each event is weighted by

$$w_\varepsilon = 1/P_d \qquad (2.20)$$

Figure 2.12 shows a scatter plot of $w\varepsilon$ as a function of cosine of the Λ^o production angle in the centre of mass. The largest weight calculated is 1.5, which corresponds to a detection efficiency of 66%.

2.9 NORMALIZATION

In order to calculate absolute cross-sections for the reaction $k^- p \to \pi^+\pi^-\Lambda$, a normalizing process is required. To this end, use has been made of the weak τ decay mode of the k^- meson :-

$$k^- \to \pi^+\pi^-\pi^- \qquad (2.21)$$

This process is topologically unambiguous with any other k^- decay or strong

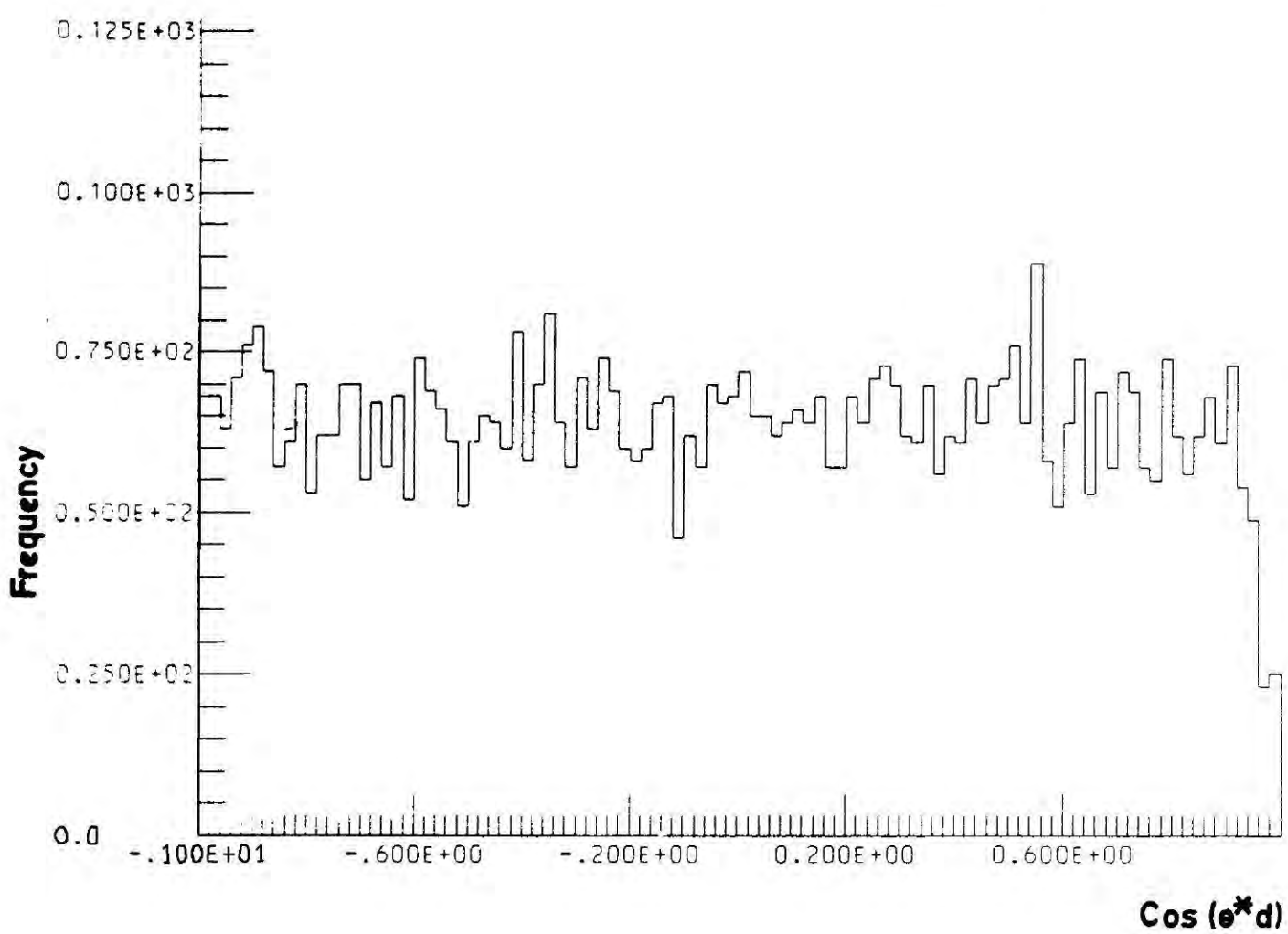

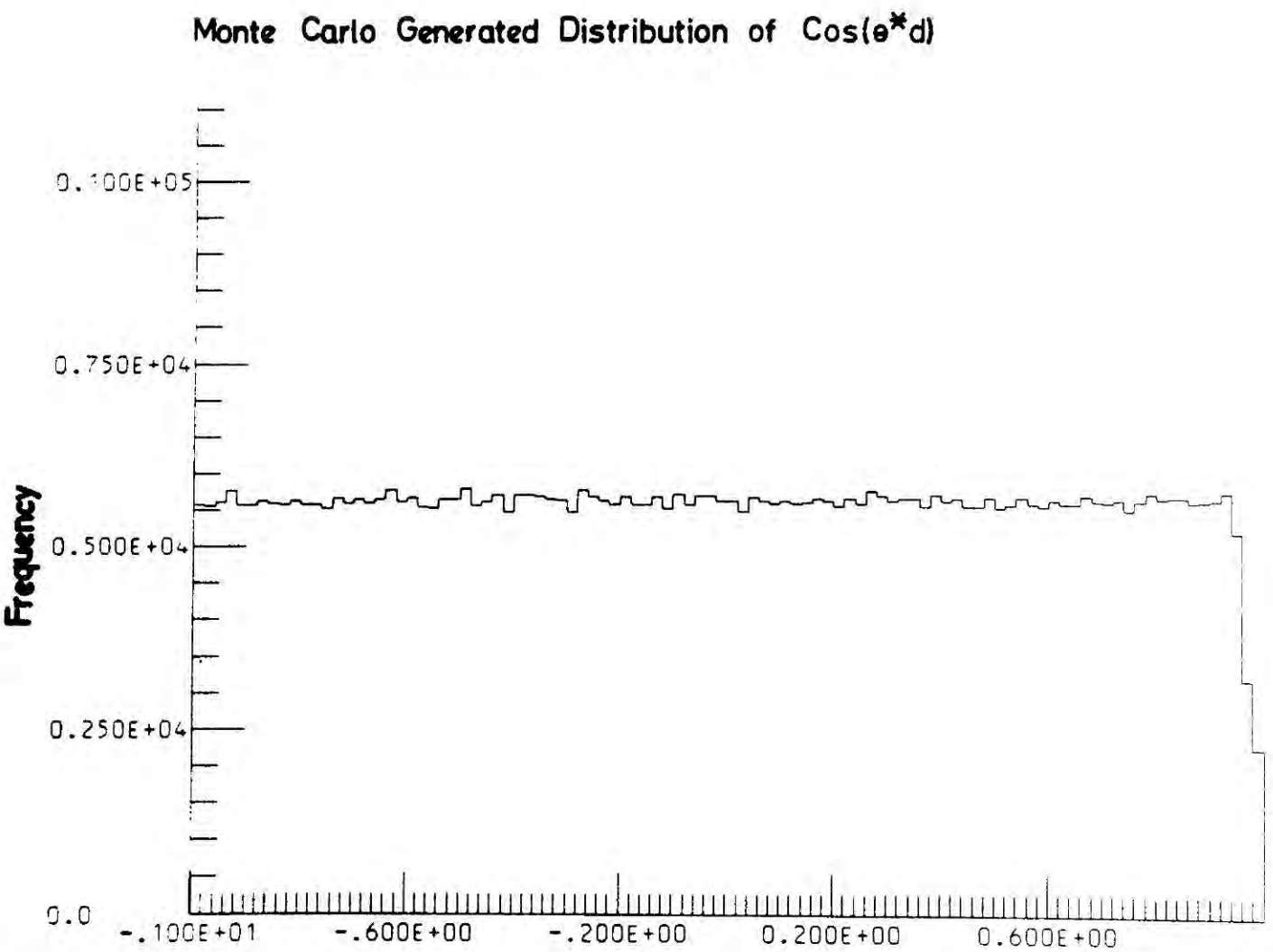

Figure 2.10 : Comparison of Monte-Carlo and event sample $\cos\theta^*_d$ distributions.

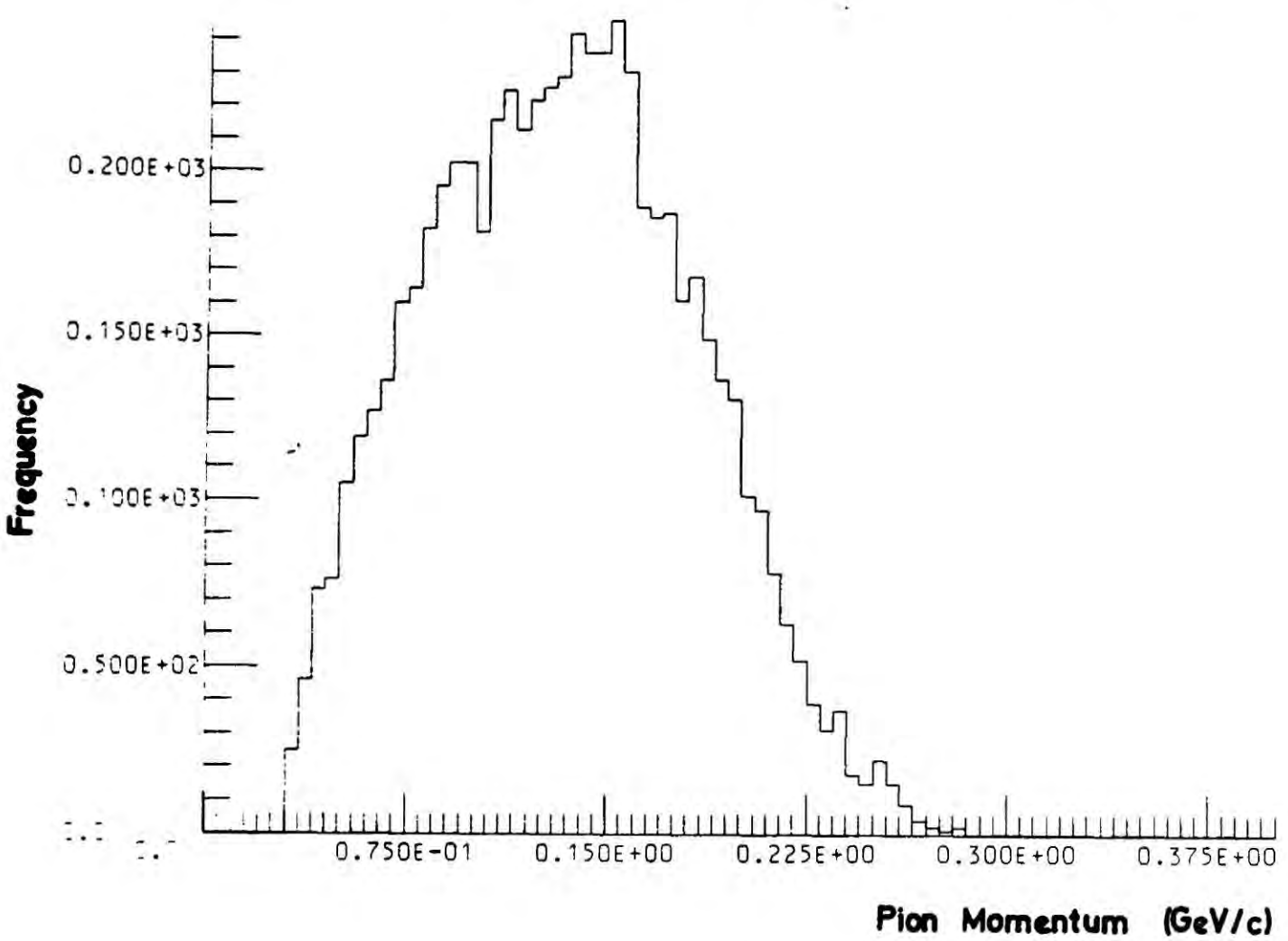

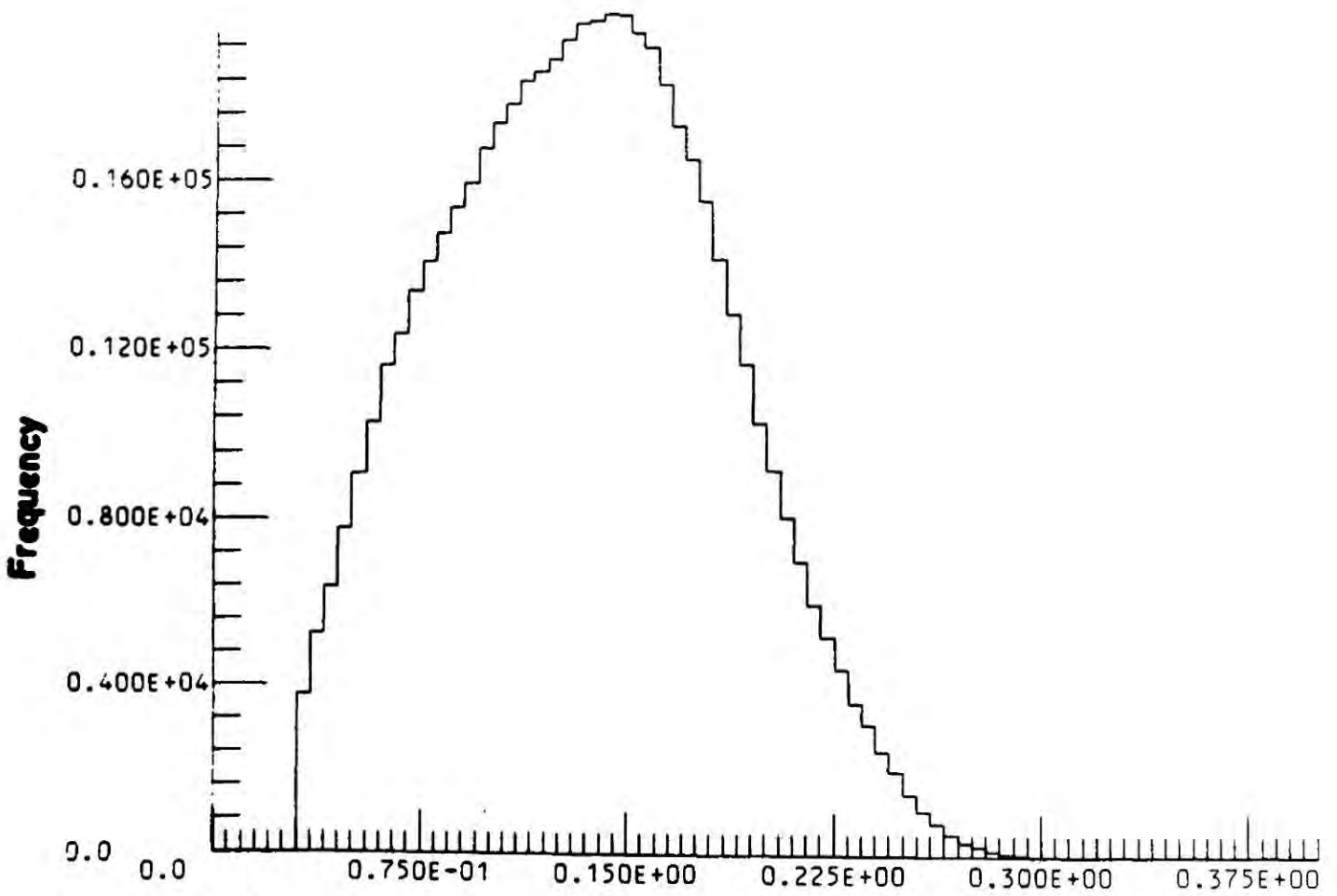

Figure 2.11 : Comparison of pion momentum distribution for Monte-Carlo and data samples.

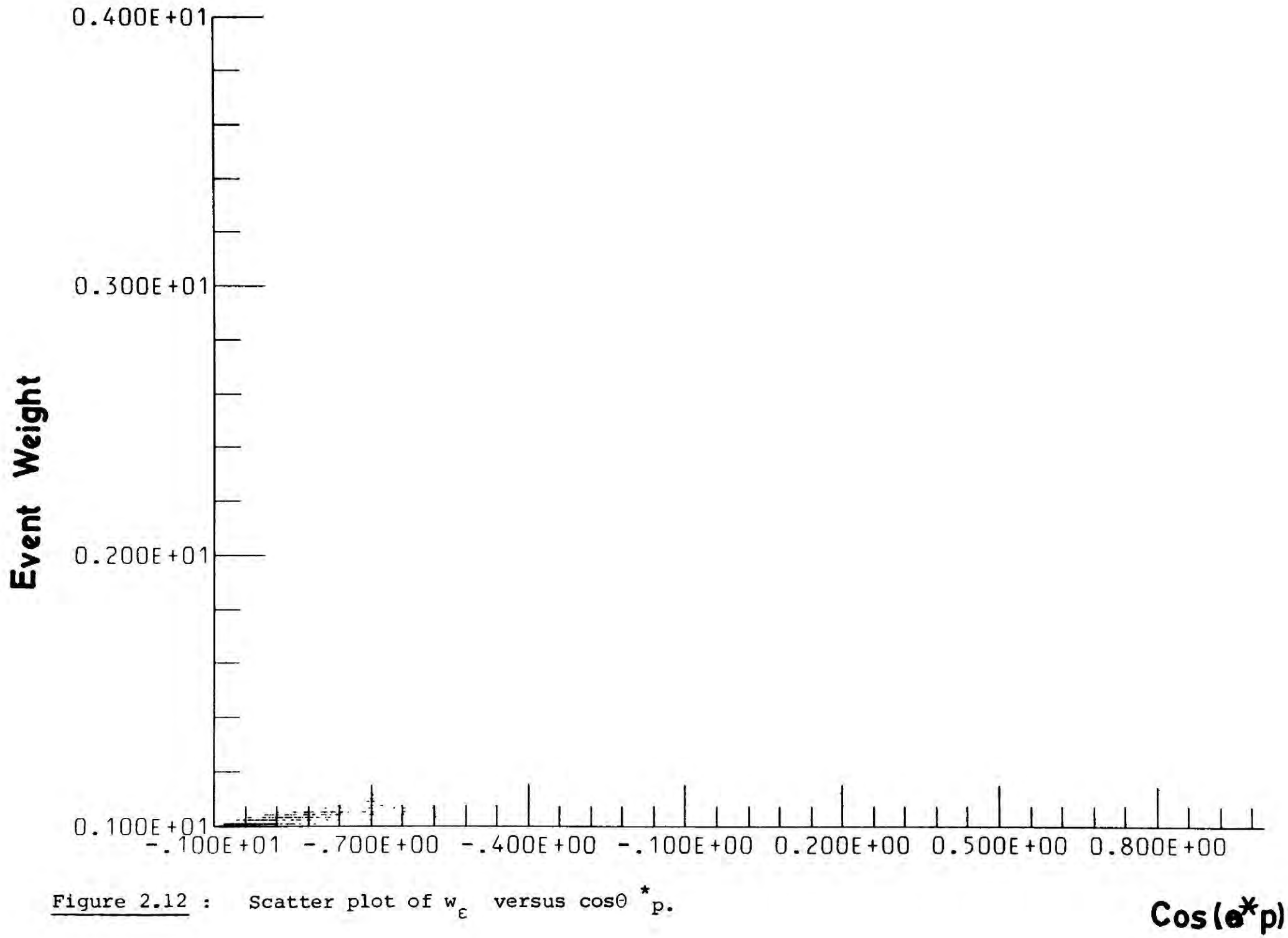

Figure 2.12 : Scatter plot of w_ε versus $\cos\Theta^*_p$.

interaction in liquid hydrogen. The only losses which may be anticipated are those of short stopping pions. Using an approach similar to that of section 2.4, the minimum pion momentum in the laboratory may be calculated. When the effective mass of the dipion system is minimum, the centre of mass momentum of the recoiling single pion takes on its maximum value. If the direction of motion for this pion, in the k^- meson rest frame, is opposite to that of the k^- in the laboratory, the laboratory momentum of the pion takes on its minimum value. Minimum pion momenta in the laboratory as a function of incident k^- meson momenta are given in Table 2.2. The lowest incident k^- momentum in this experiment is 0.650 GeV/c, at which the slowest possible pion produced by τ decay has momentum 0.55 GeV/c. This corresponds to a range in liquid hydrogen 5 cm. which should be easily detectable.

2.10 CROSS-SECTIONS

The cross-section for the reaction $k^- p \rightarrow \Lambda \pi^+ \pi^-$ is defined to be

$$\sigma = \frac{1}{N\lambda} \qquad (2.22)$$

where N is the number of scattering centres per unit volume and λ is the mean free path for interaction in a particular incident momentum interval. If the total path length for strong interactions is ℓ and N_c strong interactions are observed

$$\lambda = \ell/N_c \qquad (2.23)$$

Similarly the mean free path for weak decay is

$$\lambda_d = \ell/N_d \quad \text{where } N_d \text{ is the total} \qquad (2.24)$$

number of decays observed. If τ is the lifetime for k^- decays,

$$\lambda_d = \frac{p}{m_k} c\tau \qquad (2.25)$$

where p is the incident laboratory momentum of the k^- mesons and m_k is the k^- mass.

Assuming the potential pathlength for strong interaction and decay are identical at each momentum

$$\sigma = \frac{N_c}{N_\tau} \cdot f. \cdot \frac{m_k}{p} \cdot \frac{1}{c\tau} \cdot \frac{1}{N_A \rho} \qquad (2.26)$$

where f is the branching fraction for the τ decay mode, ρ is the density of liquid hydrogen and N_A is Avogadro's number.

The number of interactions for $k^- p \rightarrow \Lambda\pi^+\pi^-$ is determined from the total number of events in this channel, surviving cuts, weighted by the correction factors calculated in section 2.7, multiplied by a factor to account for the branching fraction of the Λ^o hyperon into the visible $\pi^- p$ mode. Both the number of τ mode decays and strong interactions have been corrected for throughput efficiency and scanning efficiency.

All the film has been scanned once. Some of it has been scanned twice. For events of a given topology in the sample scanned twice, a scanning efficiency may be calculated. If N_1 events are seen on the first scan, N_2 are seen on the second scan and N_{12} are seen on both scans,

$$\begin{aligned} \varepsilon_1 &= \frac{N_{12}}{N_2} && \text{: first scan efficiency} \\ \varepsilon_2 &= \frac{N_{12}}{N_1} && \text{: second scan efficiency} \qquad (2.27) \\ \varepsilon_{12} &= \frac{N_{12}(N_1 + N_2 - N_{12})}{N_1 N_2} && \text{: double scan efficiency} \end{aligned}$$

The events are weighted according to the inverse of the appropriate scanning efficiency, depending into which category they fall.

Separate scanning efficiencies exist for 300 topology events which include the τ decay mode and 201 topology events which include the reaction $k^- p \rightarrow \Lambda\pi^+\pi^-$. These have been determined by G. Gopal (Ref. 2.4), and are

Energy Number	1	2	3	4	5	6	7	8	9
Scan 1 Efficiency (τ's)	.932	.957	.938	.956	.944	.948	.945	.935	.909
Scan 1 Efficiency ($\Lambda\pi^+\pi^-$)	1.0	.926	.973	.961	.948	.953	.959	.925	.933
Scan 2 Efficiency (τ's)	.932	.941	.957	.942	.957	.919	.911	.946	.940
Scan 2 Efficiency ($\Lambda\pi^+\pi^-$)	.988	.926	.955	.931	.962	.921	.971	.946	.913
Double Scan Efficiency (τ's)	.995	.997	.997	.997	.998	.996	.995	.996	.995
Double Scan Efficiency ($\Lambda\pi^+\pi^-$)	1.00	.995	.999	.997	.998	.996	.999	.996	.994
Scan 1 Throughput (τ's)	.798	.806	.851	.825	.866	.844	.854	.836	.822
Scan 1 Throughput ($\Lambda\pi^+\pi^-$)	.921	.886	.909	.874	.883	.884	.879	.879	.878
Scan 2 Throughput (τ's)	.902	.759	.855	.825	.849	.871	.814	.831	.771
Scan 2 Throughput ($\Lambda\pi^+\pi^-$)	.901	.878	.849	.856	.871	.885	.849	.855	.857

TABLE 2.2 : Scanning and Throughput Efficiencies.

given in Table 2.2 as a function of beam optics setting. A certain amount of overweighting may occur in the calculation of cross-sections. Although losses of events with short pions and Λ^{o} decay lengths result in events not being seen as $\pi\pi\Lambda$ events, it is possible that these effects result in poor measurability and geometrical reconstruction or simply poor scanning. No possibility exists for investigation of these effects given the systematic procedure adopted in this experiment.

Cross-sections for the reaction $k^{-} p \rightarrow \Lambda\pi^{+}\pi^{-}$ as a function of momentum bin are given in Table 2.3 together with the total weighted and unweighted numbers of τ decays and interactions in these bins. Errors are determined from the Poisson error of the bin contents.

Figure 2.13 shows the cross-sections together with those found by the C.H.S. collaboration (Ref. 2.3) and Evans et al (Ref. 2.5). All three data sets agree well. The statistics of Evans et al are comparable with those of this experiment at each energy, whilst C.H.S. has only about 350 corrected events per momentum bin.

Incident Momentum (GeV/c) (20 MeV/c bins)	Number of $k^- p \to \Lambda\pi^+\pi^-$ Events	Total Weighted $k^- p \to \Lambda\pi^+\pi^-$	Number of τ Decays	Total Weighted of τ Decays	Cross-Section (mb)	Error (mb)
0.660	291	417.4	1010	1175.9	1.64	0.11
0.730	347	477.4	530	622.5	3.21	0.22
0.750	774	1077.5	1244	149.6	2.99	0.14
0.770	823	1148.3	1281	1525.1	2.99	0.13
0.790	803	1110.4	1078	1283.7	3.35	0.136
0.810	789	1109.4	973	1165.4	3.60	0.17
0.830	864	1261.0	1113	1346.6	3.46	0.16
0.850	811	1200.7	1095	1353.6	3.20	0.15

TABLE 2.3 : Cross-Sections for the Reaction $k^- p \to \Lambda\pi^+\pi^-$

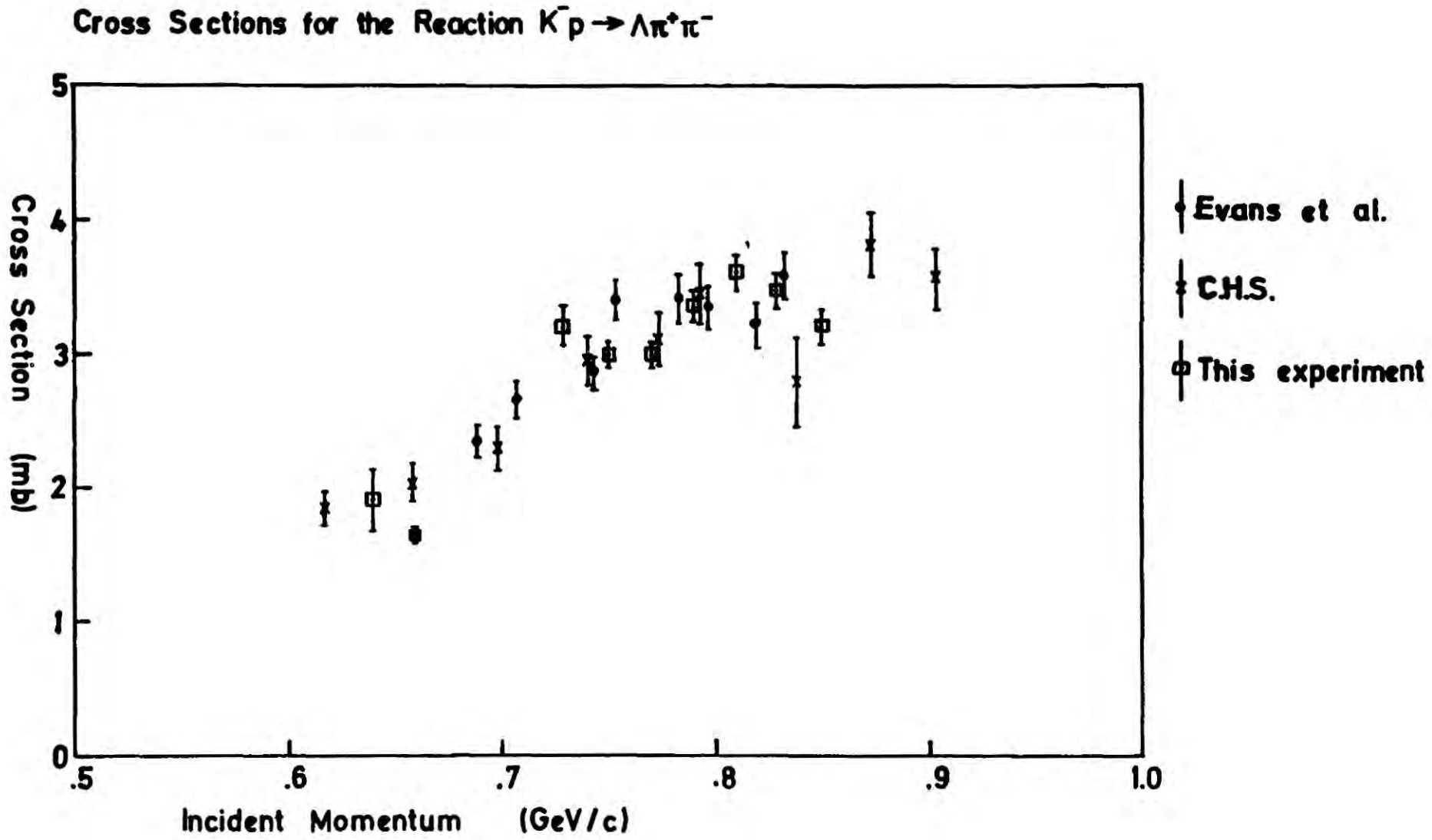

Figure 2.13 : Comparison of cross-sections found in this experiment with those found by previous studies of the reaction $k^-p \rightarrow \pi^+\pi^-\Lambda$.

CHAPTER 2

REFERENCES

2.1 R.M.W.Hughes, Rutherford Laboratory Bubble Chamber Note 91 (unpublished).

2.2 B.Conforto et al, Nucl.Phys. B105(1976) 189.

2.3 R. Armenteros et al, Nucl.Phys. B21 (1970) 15.

2.4 G.Gopal (Rutherford Laboratory), Private communication.

2.5 D.A. Evans et al, Nucl.Phys. B119 (1977) 315.

2.6 J.Prevost, Nucl.Phys. B69 (1974) 246.

CHAPTER 3

3.1 INTRODUCTION

The formulation, in terms of spin, of two body scattering processes and decays has been investigated and reviewed by several authors (references 3.1, 3.2, 3.3). This chapter will not present any new results concerning spin formalism, but will present results merely as they relate to the method of analysis used in Chapters 5 and 6. As such, the aim of this thesis is to extract $\pi\Sigma(1385)$ final states from the $\Lambda\pi^+\pi^-$ Dalitz plot and to decompose the scattering process $k^-p \rightarrow \pi\Sigma(1385)$ in terms of partial wave amplitudes.

Fig 3.1 shows a schematic representation of the basic scattering process used in isobar analyses. The $\pi\Sigma(1385)$ final state couples to the k^-p initial state via a set of s-channel partial wave amplitudes. Subsquently, the $\Sigma(1385)$ isobar undergoes decay. This decay is independent of all production properties, with the exception of the $\Sigma(1385)$ helicity. As a measure of the statistical mixture of spin eigenstates, the spin density matrix will be used. In fact the angular distribution of the $\Sigma(1385)$ decay fragments may be used to deduce the elements of the spin density matrix.

The following processes are expected to contribute to the $\Lambda\pi^+\pi^-$ Dalitz plot :-

$$k^-p \rightarrow \pi^-\Sigma^+(1385) \qquad (3.1)$$
$$\hookrightarrow \Lambda\pi^+$$

$$k^-p \rightarrow \pi^+\Sigma^-(1385) \qquad (3.2)$$
$$\hookrightarrow \Lambda\pi^-$$

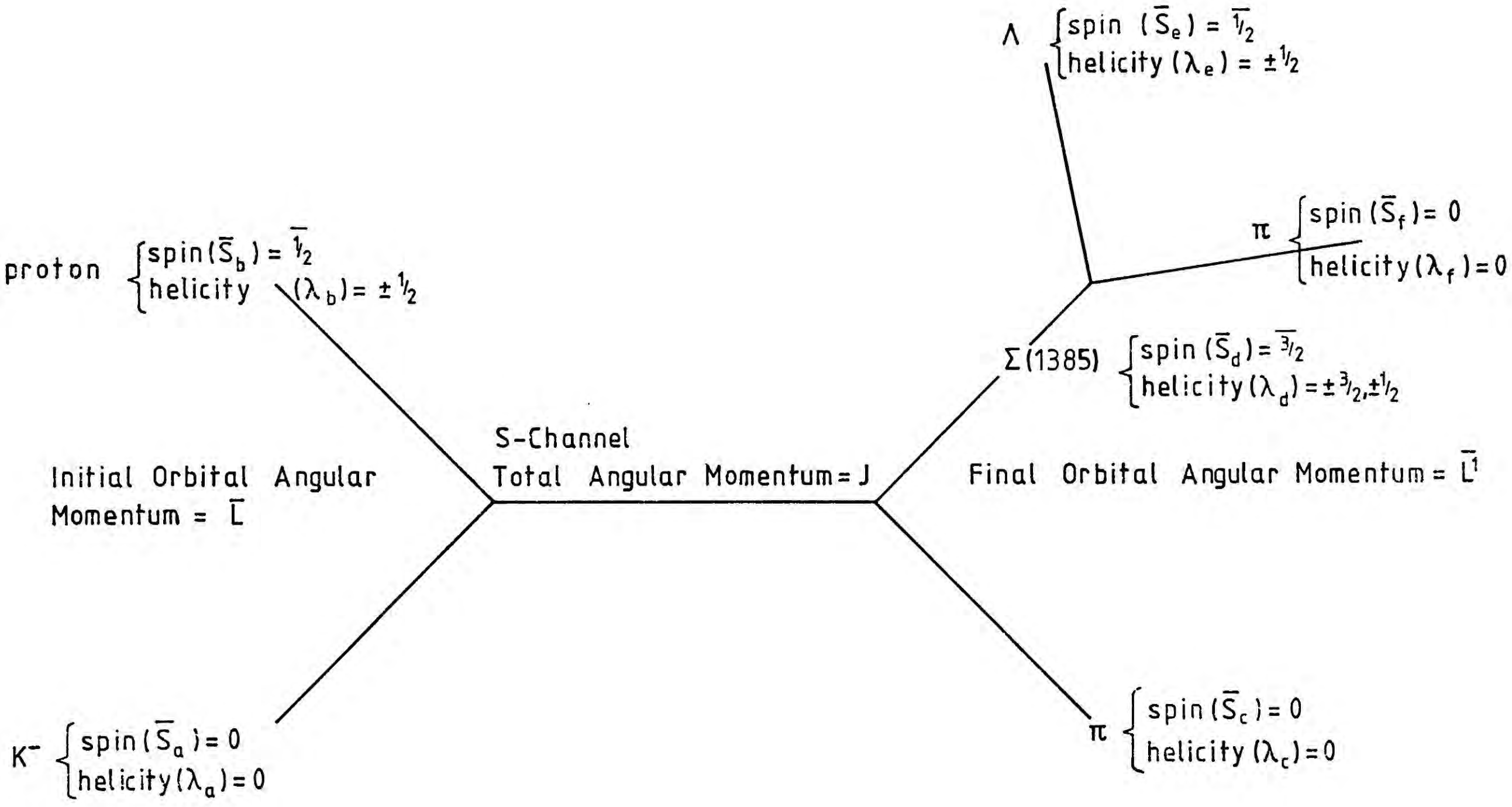

Fig. 3.1 Quantum Numbers in the Reaction $K^- p \rightarrow \pi \Sigma(1385)$

Consider the kinematics of reactions 3.1 and 3.2 expressed in terms of the Dalitz plot variables m_1^2 and m_2^2, which are the effective masses of the $\Lambda\pi^+$ and $\Lambda\pi^-$ systems respectively. The spatial configuration of final state particles may be described in terms of three angles :

(i) The production angle, θ^*, for the appropriate $\Lambda\pi^+/\Lambda\pi^-$ system in the overall centre of mass, measured with respect to the direction of motion for the incident proton.

(ii) The angle θ of the Λ to the initial direction of motion of the $\Sigma(1385)$ in the $\Lambda\pi^+/\Lambda\pi^-$ rest frame.

(iii) The azimuthal angle ϕ of the Λ about the $\Sigma(1385)$ direction of motion in the $\Lambda\pi^{\pm}$ rest system.

Both m_1^2 and m_2^2 are independent of centre of mass production angles and decay azimuthal angles. Hence, the distribution of events in the $\Lambda\pi^+\ \pi^-$ Dalitz plot depends only on effective mass and decay polar angle, Θ. However, dependence on the $\pi\Sigma(1385)$ production mechanism is introduced by virtue of the fact that the angular distribution for decay of the $\Sigma(1385)$ depends on the population of its helicity states. In Section 3.2 of this chapter, it is shown that given a set of s-channel partial wave amplitudes, the spin density matrix elements are a function of centre of mass production angle for the appropriate $\Sigma(1385)$ system. The density of events in the Dalitz plot may be used to determine the diagonal elements of the spin density matrix integrated over centre of mass production angle $\cos\theta^*$. To determine the off diagonal elements, the distribution of ϕ must also be used.

If the amplitudes for reactions 3.1 & 3.2, which contribute to the $\Lambda\pi^+\pi^-$ Dalitz plot density, are T_1 and T_2, the total amplitude for pure $\pi\Sigma(1385)$ production is

$$T(m_1, m_2, \Theta_1, \Theta_2) = T_1(m_1, \Theta_1) + T_2(m_2, \Theta_2).$$

The density of events in the Dalitz plot is proportional to

$$|T|^2 = |T_1(m_1,\Theta_1)|^2 + |T_2(m_2,\Theta_2)|^2 + 2\,\mathrm{Re}\left\{ T_1(m_1,\Theta_1)^* \; T_2(m_2,\Theta_2) \right\} \qquad (3.3)$$

The dependence of amplitudes T_1 and T_2 on effective masses m_1 and m_2 will be given by Breit Wigner functions of m_1 and m_2 respectively, whilst the dependence on Θ_1 and Θ_2 will integrate over m_1 and m_2.
This leads one to expect that the interference term in equation 3.3 will only be appreciable in zones of overlap between bands representing reactions 3.1 and 3.2 in the Dalitz plot. In Chapter 4 it will be shown that even in regions of kinematic overlap this term may be ignored, since the density of events in the overlap region is just the sum of $\Sigma(1385)$ bands in non-overlap regions. Assuming the cross term may be neglected, the Dalitz plot density becomes an incoherent sum of the quasi two-body final states of reactions 3.1 and 3.2. The formalism required for extracting descriptions of the differential cross section and spin density matrix elements for the corrected data sample, described in Chapter 2, will be given in the remainder of this chapter.

3.2 PRODUCTION PROPERTIES

Reference 3.3 gives the differential cross section $\frac{d\sigma}{d\Omega}$ as a Legendre polynomial expansion in terms of products of partial waves for the process :-

$$a + b \rightarrow c + d$$

in which particles a,b, c and d have general spins. In brief, this result is obtained from the definition of the scattering amplitude with λ as the helicity label :-

$$f(\cos\theta^*) = \frac{1}{p^2\sqrt{(2s_a+1)(2s_b+1)}} \sum_{\text{all } \lambda} \langle \lambda_c \lambda_d |T| \lambda_a \lambda_b \rangle \qquad (3.4)$$

given that :-

$$\frac{d\sigma}{d\Omega} = |f(\cos\theta^*)|^2 \qquad (3.5)$$

The final form for $d\sigma/d\Omega$ is expressed in the angular momentum basis, whereas 3.4 is written in the helicity basis. To perform this transformation the following results are used :-

(i) The T matrix, which describes the transition between different initial and final states, is expanded in terms of angular momentum eigenstates T^J :-

$$\langle\lambda_c\lambda_d\,|T|\,\lambda_a\lambda_b\rangle = \sum_J (J+\tfrac{1}{2})\langle\lambda_c\lambda_d\,|T^J|\,\lambda_a\lambda_b\rangle d^J_{\lambda\lambda'}(\theta^*) \qquad (3.6)$$

where $\lambda = \lambda_a - \lambda_b$, $\lambda' = \lambda_c - \lambda_d$. and θ^* is the centre of mass scattering angle of the final state particles measured with respect to the initial state particles. A choice of initial state scattering plane with y axis as normal and z axis in the $\bar{k}$ direction has been made(see Figure 3.2).

(ii) The transformation coefficient between two particle helicity states $|J\ m\ \lambda_c\lambda_d\rangle$ and orbital angular momentum states $|J\ m\ \ell\ s\rangle$:-

$$\langle J\ m\ \ell\ \ s\ |J\ m\ \lambda_c\lambda_d\rangle = \left[\frac{2\ell+1}{2J+1}\right]^{\frac{1}{2}} C(\ell os\lambda|J\lambda)C(s_c\lambda_c s_d-\lambda_d|s,\lambda_c-\lambda_d) \quad (3.7)$$

where $\bar{s} = \bar{s}_a + \bar{s}_b$ and $\bar{J} = \bar{\ell} + \bar{s}$ with $\bar{\ell}$ the relative orbital angular momentum of particles c and d.

(iii) The multiplicative properties of d functions :-

$$d^{J_1}_{\lambda_1\lambda_1'}(\theta^*)\, d^{J_2}_{\lambda_2\lambda_2'}(\theta^*) = \sum_{\ell=|J_1-J_2|}^{J_1+J_2} C(J_1\lambda_1 J_2-\lambda_2|\ell,\lambda_1-\lambda_2)C(J_1\lambda_1' J_2-\lambda_2'|\ell,\lambda_1'-\lambda_2')$$

$$* (-1)^{\lambda_2-\lambda_2'}\, d^{\ell}_{\lambda_1-\lambda_2,\lambda_1'-\lambda_2'}(\theta^*) \quad (3.8)$$

and their relationship to Legendre polynomials :-

$$d^{\ell}_{om}(\theta^*) = (-1)^m d_{mo}(\theta^*) = \left[\frac{(\ell-m)!}{(\ell+m)!}\right] p_\ell^m (\cos\theta^*) \qquad (3.9)$$

Finally, the result for unpolarized initial particles is :-

$$\frac{d\sigma}{d\Omega} = \frac{1}{p^2(2s_a+1)(2s_b+1)} \cdot \sum (-1)^{(\lambda_2-\lambda_2')} \sqrt{(\ell_1'+\tfrac{1}{2})(\ell_1+\tfrac{1}{2})(\ell_2'+\tfrac{1}{2})(\ell_2+\tfrac{1}{2})}$$

$$* \prod_{i=1}^{10} C_i \; R_e \left\{ \langle \ell_1' s_1' | T^{J1} | \ell_1 s_1 \rangle \langle \ell_2' s_2' | T^{J2} | \ell_2 s_2 \rangle^* \right\} P_\ell (\cos\theta^*) \qquad (3.10)$$

Here the subscripts 1 and 2 refer to the partial wave amplitudes $\langle \ell_1' s_1' | T^{J1} | \ell_1 s_1 \rangle$ and $\langle \ell_2' s_2' | T^{J2} | \ell_2 s_2 \rangle$; the primed and unprimed quantities are associated with final and initial state particles respectively. Table 3.1 lists the ten Clebsch-Gordan coefficients which appear in the product $\prod_{i=1}^{10} C_i$. The summation runs over ℓ such that $|J_1-J_2| < \ell < |J_1+J_2|$, J_1, J_2, ℓ_1', ℓ_1, ℓ_2', ℓ_2 $s_1 (= s_2)$, $s_1' (= s_2')$ and the particle helicities $\lambda_a, \lambda_b, \lambda_c$ and λ_d.

Starting from the definition of the elements of the spin density matrix for particle d :-

$$\rho_{mm'} = \frac{\frac{1}{p^2(2s_a+1)(2s_b+1)} \sum_{\lambda_a,\lambda_b,\lambda_c} \langle \lambda_c \tfrac{m}{2} | T | \lambda_a \lambda_b \rangle \langle \lambda_c \tfrac{m'}{2} | T | \lambda_a \lambda_b \rangle^*}{\frac{1}{p^2(2s_a+1)(2s_b+1)} \sum_{\text{all } \lambda} | \langle \lambda_c \lambda_d | T | \lambda_a \lambda_b \rangle |^2}$$

$$\text{where } \lambda_d = \frac{m}{2} \text{ and } \lambda_d' = \frac{m'}{2} \qquad (3.11)$$

1	$C\left(\ell_1 0\ s_1\ \lambda_1' \mid J_1\ \lambda_1'\right)$
2	$C\left(s_c\ \lambda_c\ s_d - \lambda_d \mid s_1'\ ,\ \lambda_c - \lambda_d\right)$
3	$C\left(\ell_1 0\ s_1 \lambda_1 \mid J_1 \lambda_1\right)$
4	$C\left(s_a \lambda_a\ s_b - \lambda_b \mid s_1,\ \lambda_a - \lambda_b\right)$
5	$C\left(\ell_2\ 0\ s_2'\ \lambda_2' \mid J_2\ \lambda_2'\right)$
6	$C\left(s_c\ \lambda_c s_d,\ -\lambda_d \mid J_2',\ \lambda_c - \lambda_d\right)$
7	$C\left(\ell_2\ 0\ s_2 \lambda_2 \mid J_2 \lambda_2\right)$
8	$C\left(s_1\ \lambda_a\ s_b - \lambda_b \mid s_2 \lambda_a - \lambda_b\right)$
9	$C\left(J_1 \lambda_1\ J_2 - \lambda_2 \mid \ell,\ \lambda_1 - \lambda_2\right)$
10	$C\left(J_1 \lambda_1'\ J_2 - \lambda_2' \mid \ell, \lambda_1' - \lambda_2'\right)$

TABLE 3.1 : Clebsch-Gordan Coefficients

In this expression the denominator is simply the definition of the differential cross-section and the numerator may be transformed to the angular momentum basis using equations 3.6, 3.7, 3.8 and 3.9. The result is :-

$$\rho_{mm'} \quad \frac{d\sigma}{d\Omega} = \frac{1}{p^2(2a+1)(2sb+1)} \sum (-1)^{\lambda_2 - \lambda_2'} \prod_{2=1}^{10} C_i \sqrt{(\ell_1'+\tfrac{1}{2})(\ell_1+\tfrac{1}{2})(\ell_2'+\tfrac{1}{2})(\ell_2+\tfrac{1}{2})}$$

$$\left[\frac{\ell - \frac{1}{2}(m-m')}{\ell + \frac{1}{2}(m-m')} \right]^{\frac{1}{2}} \langle \ell_1' s_1' | T^{J1} | \ell_1 s_1 \rangle \langle \ell_2' s_2' | T^{J_2} | \ell_2 s_2 \rangle^* \; P_\ell^{\frac{1}{2}(m-m')}(\cos\Theta^*) \tag{3.12}$$

Again, $\prod_{i=1}^{10} C_i$ is a product of ten Clebsch-Gordan coefficients and the summation extends over the same variables as equation 3.10, with the exception of λ_a. The results given in this section are taken from reference 3.3, but similar developments are also given in references 3.1 and 3.2.

3.3 DECAY PROPERTIES

The decay angular distribution of the $\Sigma(1385)$, which is produced as a statistical mixture of different helicities, is given by reference 3.2 as :-

$$w(\Theta,\phi) = \sum_{mm'} \sum_{\lambda_e \lambda_f} A_m(\lambda_e \lambda_f)\, \rho_{mm'}\, A_{m'}(\lambda_e \lambda_f) \cdot N$$

where N is a normalizing factor and :-

$$A_m(\lambda_e \lambda_f) = \langle \lambda_e \lambda_f \; |T| \; J \; m \rangle \tag{3.14}$$

with λ_e and λ_f the Λ and π^- particle helicities.

Again, a choice of axis system is possible, here it is taken as the helicity frame, in which the decay polar angle θ is measured with respect to the incoming $\Sigma(1385)$direction and the azimuthal angle ϕ is measured with respect to the x-axis, the y-axis being defined as the normal to the plane which includes the initial state k^- direction and the $\Sigma(1385)$ direction in the overall centre of mass (Fig.3.2). It is then possible to write (c.f.of equation 3.6)

$$| \lambda_e \lambda_f > = \sum_m |s_d m > \sqrt{\frac{2s_d+1}{4\pi}} \quad D_{m\mu}^{s_d} \ (\phi,\theta,0) \qquad (3.15)$$

$$\mu = \lambda_e - \lambda_f$$

Considerable simplification arises from the following relationships between the spin density matrix elements :-

(i) $\rho_{mm'} = \rho_{m'm}^*$, i.e. ρ is hermitian from the definition of equation 3.11 since it is an observable.

(ii) $T_r\left[\rho\right] = \sum_m \rho_{mm} = 1.$

(iii) With this choice of axes, parity conservation gives :-

$$\rho_{mm'} = \rho_{m-m'} (-1)^{m-m'}$$

Hence,

$$\rho_{1\,1} = \rho_{-1\,-1} \quad \rho_{3\,3} = \rho_{-3\,-3} \text{ (parity conservation)}$$

and $$2(\rho_{1\,1} + \rho_{3\,3}) = 1 \quad \text{(trace condition)}$$

$\rho_{1\,1}$ and $\rho_{3\,3}$ are pure real.

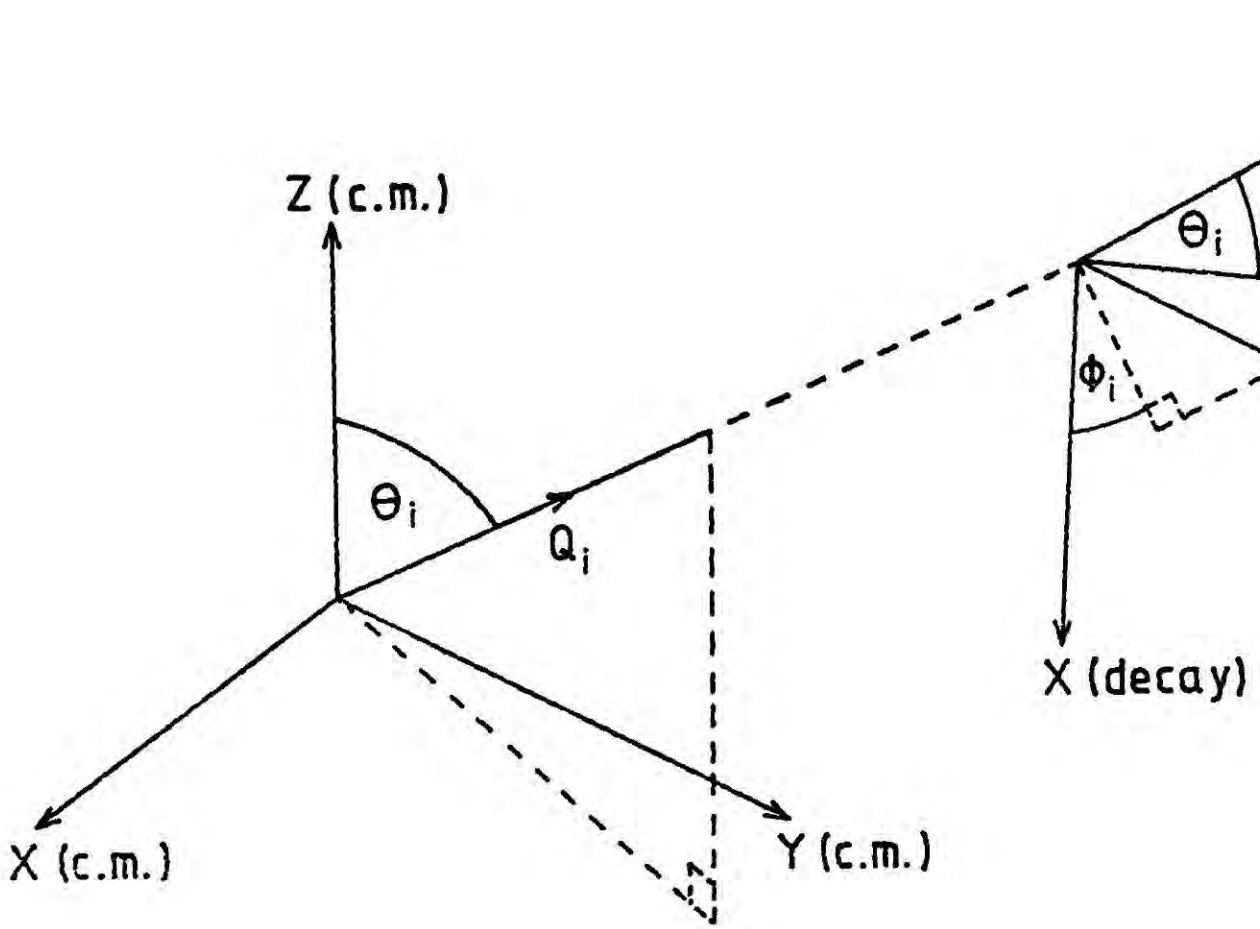

Axis definitions

$$Z\,(c.m.) = \frac{\overline{P_a}}{|P_a|}$$

$$Z\,(decay) = \frac{\overline{Q_i}}{|Q_i|}$$

$$Y\,(decay) = \frac{\overline{P_a} \wedge |\overline{Q_i}|}{|\overline{P_a}| \cdot |\overline{Q_i}|}$$

$$X(decay) = Y(decay) \wedge Z(decay)$$

Fig. 3.2 Axic System Used in this Thesis

$\rho_{3-3} = \rho_{-3,3}$ (hemiticity) $= \rho_{3-3}^{*}$ (parity) : are pure imaginary

$\rho_{1-1} = \rho_{-1,1} = \rho^{*}_{1-1}$: are pure imaginary

$\rho_{3\ 1} = \rho^{*}_{1\ 3} = \rho^{*}_{-1-3} = -\rho_{-3-1}$: complex

$\rho_{3-1} = \rho^{*}_{-1\ 3} = \rho^{*}_{1-3} = \rho_{3\ 1}$: complex

So, the spin density matrix has seven independent parameters, $\rho_{3\ 3}$, Im ρ_{3-3}, Im ρ_{-1-}, Re $\rho_{3\ 1}$, Re ρ_{3-1}, Im $\rho_{3\ 1}$ and Im ρ_{3-1}, of which it is only possible to measure the real parts if polarization information is lacking.

Finally, on insertion of the values $J^{P} = 3/2^{+}$ for $\Sigma(1385)$, $\frac{1}{2}^{+}$ for Λ and 0^{-} for π, the angular distribution for decay is :-

$$W(\theta,\phi) = \frac{3}{4\pi}\frac{1}{\sigma}\left[\frac{1}{2}\left(\frac{1}{3}+\cos^2\theta\right)+2\left(\frac{1}{3}-\cos^2\theta\right)\rho_{33}\right.$$
$$\left.-\frac{2}{\sqrt{3}}\sin 2\theta\cos\phi\ \mathrm{Re}\ \rho_{31}-\frac{2}{\sqrt{3}}\sin^2\theta\cos 2\phi\ \mathrm{Re}\ \rho_{3-1}\right] \qquad (3.16)$$

where the ρ_{mm}' have been averaged over the centre of mass production angle θ^{*}. In the next section this result will be used to obtain :-

(i) a density function for events in the Dalitz plot which depends on the $\Lambda\pi^{\pm}$ effective masses and the decay polar angle θ only.

(ii) a probability function which depends on production centre of mass angle, decay polar and azimuthal angles and also on $\Lambda\pi^{\pm}$ effective masses.

3.4 DENSITY FUNCTIONS IN THE DALITZ PLOT

It was stated in Section 3.1 that the density of events in the Dalitz plot depends only on the $\Lambda\pi^{+}$ and $\Lambda\pi^{-}$ effective masses (m_1 and m_2) and the polar decay angles for these systems (θ_1 and θ_2). Both effective mass

projections from the Dalitz plot are expected to be determined by Breit-Wigner functions :-

$$B(m^2) = \frac{m_o \Gamma}{(m_o^2 - m^2)^2 + m_o^2 \Gamma^2}$$

where Γ is the $\Sigma(1385)$ width and m_o its mass. The decay polar angular dependence of the Dalitz plot is obtained by integrating equation 3.16 over decay azimuthal angle :-

$$W(\Theta) = \int_0^{2\pi} W(\Theta,\phi)\ d\phi$$

$$= \frac{3}{2}\left[\frac{1}{2}\left(\frac{1}{3} + \cos^2\Theta\right) + 2\left(\frac{1}{3} - \cos^2\Theta\right)\rho_{33}\right] \qquad (3.17)$$

Hence, the only factors determining the Dalitz plot density are the relative fractions and the values of ρ_{33} for the $\pi^{\pm}\ \Sigma^{\mp}$ (1385) final states.

To obtain information which may be related to the partial wave expansions of Section 3.2 the production angular distribution must be investigated. Since angular dependence of Re ρ_{3-1} and Re ρ_{31} constrain the values of partial waves, in addition to $d\sigma/d\Omega$ and ρ_{33}, the decay azimuthal angle will also be included. Production and decay angular dependence are now represented as

$$W(\Theta^*,\Theta,\phi) = \frac{3}{4\pi}\left[\frac{1}{2}\left(\frac{1}{3} + \cos^2\Theta\right) + 2\left(\frac{1}{3} - \cos^2\Theta\right)\rho_{33}\ (\Theta^*)\right.$$

$$\left. - \frac{2}{\sqrt{3}}\ \sin 2\Theta\ \cos\phi\ \text{Re}\ \rho_{31}\ (\cos\Theta^*) - \frac{2}{\sqrt{3}}\sin^2\Theta\ \cos 2\phi\ \text{Re}\rho_{3-1}\ (\cos\Theta^*)\right]\frac{d\sigma}{d\Omega}$$

(3.18)

For fitting purposes, a production angle dependant paramatrization, consistent with partial wave expansions given in Section 3.2, must be chosen for $d\sigma/d\Omega$, $\rho_{33}\ (\cos\Theta^*)\ d\sigma/d\Omega$, Re $\rho_{3-1}(\cos\Theta^*)\ d\sigma/d\Omega$ and Re $\rho_{3\ 1}(\cos\Theta^*)\, d\sigma/d\Omega$.

Since $d\sigma/d\Omega$ is expanded in Legendre polynomials (eqn.3.10) and $\rho_{mm'}$ $d\sigma/d\Omega$ is expanded in terms of the associated Legendre polynomials $P_\ell^{\frac{1}{2}(m-m')}(\cos\theta^*)$, the following are used :-

$$\frac{1}{\sigma}\frac{d\sigma}{d\Omega} = 2\pi\lambda^2 \sum_{\ell=0}^{L} \frac{A_\ell}{A_o} P_\ell(\cos\theta^*)$$

$$\frac{1}{\sigma}\rho_{33}\frac{d\sigma}{d\Omega} = 2\pi\lambda^2 \sum_{\ell=0}^{L} \frac{B_\ell}{A_o} P_\ell(\cos\theta^*) \qquad (3.19)$$

$$\frac{1}{\sigma}\,\mathrm{Re}\,\rho_{3-1}\frac{d\sigma}{d\Omega} = 2\pi\lambda^2 \sum_{\ell=1}^{L} \frac{C_\ell}{A_o} P_\ell'(\cos\theta^*)$$

$$\frac{1}{\sigma}\,\mathrm{Re}\,\rho_{3-1}\frac{d\sigma}{d\Omega} = 2\pi\lambda^2 \sum_{\ell=2}^{L} \frac{D_\ell}{A_o} P_\ell^2(\cos\theta^*)$$

where L is the maximum order of expansion

λ is the wavenumber of the incident k^- in the overall centre of mass

which have the attractive feature that the paramatrizing coefficients A_ℓ/A_o, B_ℓ/A_o, C_ℓ/A_o and D_ℓ/A_o are related to expansions in the real parts of products of partial wave amplitudes. The coefficients of these partial wave expansions are the products of 10 Clebsch-Gordan coefficients and the angular momentum factors of equations 3.10 and 3.12.

If the relative populations of $\Sigma^+(1385)$ and $\Sigma^-(1385)$ bands in the Dalitz plot are known, then statistical estimates of the A_ℓ, B_ℓ, C_ℓ and D_ℓ coefficients may be obtained from distributions of $\cos\theta^*$, θ and ϕ, weighted by the appropriate Breit-Wigner function, using the following expressions, which are given in Ref. 3.3 :-

$$\frac{A_\ell}{A_o} = (2\ell+1) \langle P_\ell(\cos\theta^*) \rangle \qquad (3.20)$$

$$\frac{B_\ell}{B_o} = \frac{(2\ell+1)}{2} \langle (5\cos^2\theta - 1)\, P_\ell(\cos\theta^*) \rangle \qquad (3.21)$$

$$\frac{C_\ell}{A_o} = - \frac{5(2\ell+1)}{4\sqrt{2}\,\ell(\ell+1)} < \sin 2\Theta \cos\phi \; P_\ell' (\cos\Theta^*) > \qquad (3.22)$$

$$\frac{D_\ell}{A_o} = - \frac{(2\ell+1)(\ell-2)!}{(\ell+2)!} < \cos 2\phi \; P_\ell^2 (\cos\Theta^*) > \qquad (3.23)$$

Equations 3.20, 3.21, 3.22, and 3.23 are obtained by substituting the paramatrizations of equation 3.19 into $W(\Theta^*,\Theta,\phi)$ given by equation 3.18 and using the orthonormality conditions for Legendre and associated Legendre polynomials.

3.5 FITTING OF THE DALITZ PLOT DENSITY AND ANGULAR DISTRIBUTIONS

Although the density function $W(\Theta^*,\Theta,\phi)$ given in equation 3.18, together with the paramatrizations of $d\sigma/d\Omega$ and $\rho_{mm}' \, d\sigma/d\Omega$, can be used as the basis for a maximum likelihood fit to the variables M,Θ^*,Θ and ϕ for $\pi^+ \Sigma^-(1385)$ and $\pi^- \Sigma^+(1385)$ quasi two body final states, this proves expensive in computer time usage (Ref. 3.5). A more economical method, relying on the moments expressions given in equations 3.20 to 3.23, has been developed by B.Franek of the Rutherford Laboratory. The underlaying formalism and the programmatic procedure are described in Refs. 3.5 and 3.6, this section will be devoted to a brief description of the method. Chapter 5 contains a description of modifications which allow non-resonant effects to be included ; these are required to account for dynamic effects seen in the $\pi^+\pi^-$ system in the Dalitz plot.

One clear objection to using the moments expressions to calculate the A_ℓ, B_ℓ, C_ℓ and D_ℓ, is that the relative population of $\Sigma^+(1385)$ and $\Sigma^-(1385)$ bands in the Dalitz plot are required to weight the $\cos\Theta^*$, $\cos\Theta$ and ϕ distributions and obtain the statistical estimates. Equation 3.17 shows that to fit the Dalitz plot, or its effective mass projections, requires not only freedom of the fractions of $\pi^+\Sigma^-(1385)$ and $\pi^-\Sigma^+(1385)$ present (α_1 and α_2) but also of ρ_{33}. There are hence correlations between the determination of α_1,α_2 and the coefficients A_ℓ, B_ℓ, C_ℓ and D_ℓ. To obviate this problem an iterative method has been developed.

It is possible to describe the reaction $k^- p \rightarrow \Lambda \pi^+ \pi^-$ in terms of five independent variables, since each of the three final state particles has three components of momentum and conservation of 4 vector momentum imposes 4 constraint equations. If this set of variables is described by $\vec{x}$, the probability density for the reaction is given by :-

$$dw(\vec{x}) = F(\vec{x})\, d\,pH \qquad (3.24)$$

where $F(\vec{x}) = \sum_{j=1}^{2} \alpha_j f_j(\vec{x})$ is a

sum over $\Sigma^{\pm}(1385)\ \pi^{\mp}$ quasi two body final state contributions. The fraction of a particular quasi two-body contribution present is α_j and the single channel distribution functions $f_j(\vec{x})$ are given by :-

$$f_j(\vec{x}) = \frac{1}{Z_j} B(m_j^2) W(\Theta_j^*, \Theta_j, \phi_j) \qquad (3.25)$$

Each channel is normalized by a factor Z_j, which is given as an integral over the available three-body Lorentz Invariant Phase Space d PH, subject to the condition :-

$$1 = \int f_j(\vec{x})\ d\,PH$$

and

$$Z_j = \int_{(\sqrt{s} - m_\pi)^2}^{(m_\pi + m_\Lambda)^2} d\,m_j^2\, BW(m_j^2)\, \frac{Q_j q_j}{4\sqrt{s}\,.4m_j} \qquad (3.26)$$

where Q_j is the momentum of the quasi two-body $\Sigma(1385)$ system in the overall centre of mass, q_j is the momentum of the Λ in the $\Sigma(1385)$ helicity frame and $\sqrt{s}$ is the total centre of mass energy.

Each event in the Dalitz plot may be assigned a weight :-

$$\omega_j(\vec{x}) = \frac{\alpha_j f_j(\vec{x})}{F(\vec{x})} \qquad j = 1,2 \qquad (3.27)$$

for each of the two $\pi\Sigma(1385)$ final states, provided starting values exist for the α_j and the coefficients A_ℓ, B_ℓ, C_ℓ and D_ℓ. With the coefficients A_ℓ, B_ℓ, C_ℓ and D_ℓ fixed, it is possible to calculate an improved estimate of the channel fractions :-

$$\alpha_j' = \frac{1}{N} \sum_{k=1}^{N} \omega_j(\vec{x}_k) = \frac{\alpha_j}{N} \sum_{k=1}^{N} \frac{f_j(\vec{x}_k)}{F(\vec{x}_k)} \qquad (3.28)$$

where the sum over k is over all events in the sample and N is the total number of events. This is repeated until successive values of the α_j calculated in the iterative procedure are equal, to within rounding errors. Ideally, at this point, the final α_j are solutions of the equation :-

$$1 = \frac{\alpha_j}{N} \sum_{k=1}^{N} \frac{f_j(\vec{x}_k)}{F(\vec{x}_k)} \qquad (3.29)$$

Condon (Ref.3.7) shows that the values of α_j satisfying equation 3.29 correspond to a maximum of the likelihood function $\prod_{k=1}^{N} F(x_k)$.

Using the α_j found in this way, new statistical estimates of the A_ℓ, B_ℓ, C_ℓ and D_ℓ coefficients may be calculated. These are then used, together with the current α_j values, as input for a new channel fraction iteration. The process is deemed to have converged when the values of A_ℓ, B_ℓ, C_ℓ and D_ℓ coefficients, found after subsequent channel fraction iterations satisfy a stability condition. The criteria chosen for convergence of channel fraction iteration and stability of coefficients will be discussed in Chapter 4.

3.6 AXIS SYSTEMS

In Sections 3.2 and 3.3, angular variables were given which described the production and decay of quasi two-body systems. This section is devoted to a description of the conventions used in this thesis for analysis of the reaction $k^- p \to \Lambda\pi^+\pi^-$.

Throughout this work the meson first convention will be used. The angle defining the production of a particular quasi two body system will be measured between the incident k^- and the recoiling final state meson, in the case of $\Lambda\pi$ subsystems, or between direction of motion of the proton and the recoiling Λ for the $\pi^+\pi^-$ subsystem. Since $d\sigma/d\Omega$ and $\rho_{mm}\, d\sigma/d\Omega$ do not depend on the rotation of the reaction plane about the initial k^- direction, the choice of axis system used to describe production is not crucial.

For a description of the decay of a quasi two body system, the rotation of the decay plane about the initial direction of motion, does enter the angular distribution. The choice of axis system now becomes important ; the helicity frame is used in this thesis and results in the relationships between the spin density matrix elements given in section 3.3. In this system the decay polar angle Θ is measured between the initial direction of motion for the quasi two body system and one of the decay products. The azimuthal angle, ϕ, is measured as the rotation of the vector of this decay particle about the initial direction of motion of the quasi-two body system. Fig 3.2 shows the helicity system axis and the definition of angles Θ and ϕ.

The convention used to choose the decay particle, whose direction of motion in the helicity frame defines Θ and ϕ is as follows :-

(i) The particles $\pi^+\Lambda^o\pi^-$ are given labels 1, 2 and 3 respectively.

(ii) For the subsystem consisting of particles i and j, which recoils against particle k in the overall centre of mass, the angles are measured to particle i when i, j and k are taken in cyclic permutation. Hence, for $\pi^+\Lambda$ system the decay particle is π^+, for $\Lambda\pi^-$ it is Λ^o and for $\pi^-\pi^+$ it is π^-.

CHAPTER 3

REFERENCES

3.1 M. Jacob and G.C. Wick, Annals of Physics, 7, (1959) 404.

3.2 G.C.Wick, Annals of Physics 18, (1962) 65.

3.3 S.M.Deen, Rutherford Laboratory Preprint, RPP/H/68,(1968).

3.4 J.D.Jackson, Les Houches Proceedings 1965, (North Holland, Publishers), page 327.

3.5 R. Stern, Ph.D.Thesis, University of London (1978).

3.6 B. Franek,Rutherford Laboratory Note, RL-77-069 (1977).

3.7 Condon et al, Phys.Rev. D9 (1974) 2558.

CHAPTER 4

4.1 INTRODUCTION

Before any rigorous investigation of the Dalitz plot for $\Lambda\pi^+\pi^-$ final states is undertaken, it seems appropriate that certain statements concerning kinematic properties should be made. These will be specific to the 0.500 to 0.870 GeV/c incident momentum range. Furthermore, an attempt will be made to account for the salient features of $\Lambda\pi^+$, $\Lambda\pi^-$ and $\pi^+\pi^-$ quasi two-body variables in terms of $\Sigma(1385)$ production. Insight gained from this simple approach will form the basis for a more thorough analysis, which will be performed in Chapter 5 of this thesis.

4.2 KINEMATIC PROPERTIES OF THE DALITZ PLOT

If the effective masses of the $\Lambda\pi^+$, $\Lambda\pi^-$ and $\pi^+\pi^-$ systems are denoted by $m(\Lambda\pi^+)$, $m(\Lambda\pi^-)$, $m(\pi^+\pi^-)$ respectively, then conservation of momentum and energy leads to the result :-

$$m^2(\Lambda\,\pi^+) + m^2(\Lambda\pi^-) + m^2(\pi^+\pi^-) = S + 2m_\pi^2 + m_\Lambda^2 \qquad (4.1)$$

where $\sqrt{s}$ is the total centre of mass energy and m_Λ and m_π are the Λ and π rest masses. Available phase space for the $\Lambda\pi^+\pi^-$ final state, which is proportional to the area enclosed by the Dalitz plot boundary, is limited by,

$$(m_\pi + m_\Lambda)^2 \leq m^2(\Lambda\,\pi^\pm) \leq \left(\sqrt{s} - m_\pi\right)^2 \qquad (4.2)$$

$$4m_\pi^2 \leq m^2(\pi^+\pi^-) \leq \left(\sqrt{s} - m_\Lambda\right)^2 \qquad (4.3)$$

Table 4.1 gives the lower and upper limits of the effective mass for each two particle subsystem as a function of incident momentum. Since

Incident Momentum pk (GeV/c)	Total Centre of Mass Energy $\sqrt{s}$ (GeV)	Lower Limit of $m(\Lambda\pi^{\pm})^2$ $(GeV/c^2)^2$	Upper Limit of $m(\Lambda\pi^{\pm})^2$ $(GeV/c^2)^2$	Lower Limit of $m(\pi^+\pi^-)^2$ $(GeV/c^2)^2$	Upper Limit of $m(\pi^+\pi^-)^2$ $(GeV/c^2)^2$
0.300	1.563	1.567	2.02	0.077	0.200
0.600	1.607	1.367	2.15	0.077	0.242
0.700	1.653	1.567	2.29	0.077	0.289
0.800	1.699	1.567	2.43	0.077	0.341
0.900	1.747	1.567	2.59	0.077	0.400

TABLE 4.1 : Limits of $\Lambda\pi^{\pm}$ and $\pi^+\pi^-$ system effective masses as a function of incident momentum

the measured width of the $\Sigma(1385)$ is about 0.04 GeV/c^2 a substantial fraction of the $\Lambda\pi^+/\Lambda\pi^-$ Dalitz plot, i.e. phase space, will be available to production of $\pi\Sigma(1385)$ channels. It is also clear that the available phase space grows rapidly over the momentum range studied.

Another important kinematic property of the $\Lambda\pi^+/\Lambda\pi^-$ Dalitz plot is the proximity of cross-over between $\Sigma(1385)$ bands. This position is determined by equating $m(\Lambda\pi^+)$ and $m(\pi^-)$ to the $\Sigma(1385)$ mass in equation 4.1 and calculating the resulting value of $m(\pi\pi)$ as a function of incident momentum. Criteria for deciding the position of cross-over are :-

$m(\pi^+\pi^-) > \sqrt{s}-m_\Lambda$: cross-over lies below the lower kinematic boundary of the Dalitz plot and is non-physical. (4.4)

$2m_\pi < m(\pi^+\pi^-) < \sqrt{s} - m_\Lambda$: cross-over lies within the Dalitz plot boundary and is physical. (4.5)

$m(\pi^+\pi^-) < 2m_\pi$: cross-over lies above the upper kinematic boundary of the Dalitz plot and is non-physical. (4.6)

Condition 4.5 is satisfied provided $\sqrt{s} > 1.702$ GeV and condition 4.7 satisfied provided $\sqrt{s} < 1.622$ GeV. Hence, in the incident momentum range 0.64 GeV/c to 0.81 GeV/c, $\Sigma(1385)$ bands overlap within the boundary of the Dalitz plot.

4.3 EXPERIMENTAL DATA FOR THE $\Lambda\pi^+/\Lambda\pi^-$ DALITZ PLOT

Dalitz plots are shown in Figure 4.1 for the $\Lambda\pi^+\pi^-$ final state. Data in each plot corresponds to a 0.020 GeV/c incident momentum bite, the central values being 0.750, 0.770, 0.790, 0.810, 0.830 and 0.850 GeV/c. for which the kinematic boundaries are calculated. Also shown are the $m^2(\Lambda\pi^+)$ and $m^2(\Lambda\pi^-)$ projections. Figure 4.2 shows the distribution of $m^2(\pi^+\pi^-)$ in the same momentum intervals. For each of these plots, the $\Sigma(1385)$ bands overlap below the upper kinematic boundary. Data is

Figure 4.1 : Dalitz plots for the reaction $k^- p \rightarrow \Lambda \pi^+ \pi^-$ as a function of incident momentum in 20 MeV/c bins.

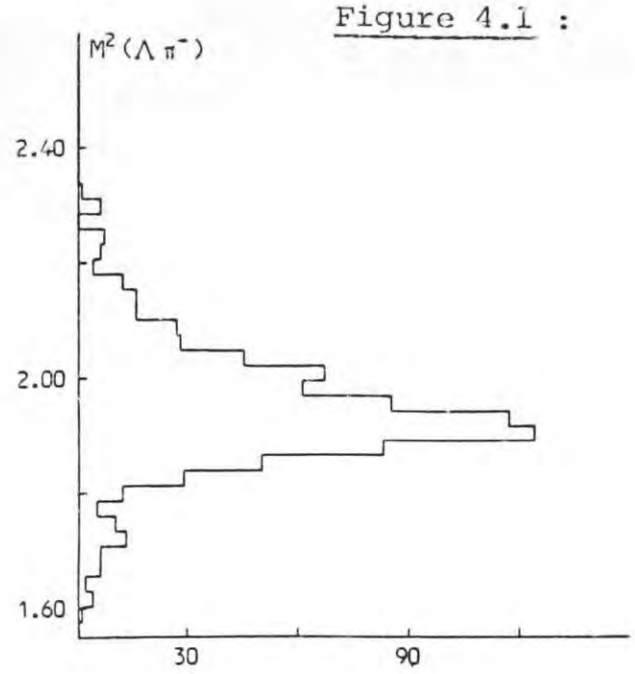

Dalitz Plot for the Reaction $K^-p \rightarrow \Lambda\pi^+\pi^-$

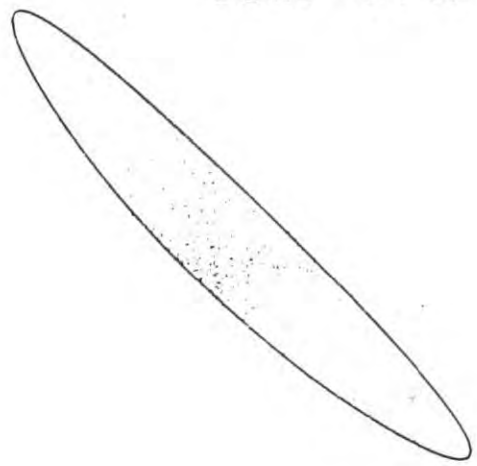

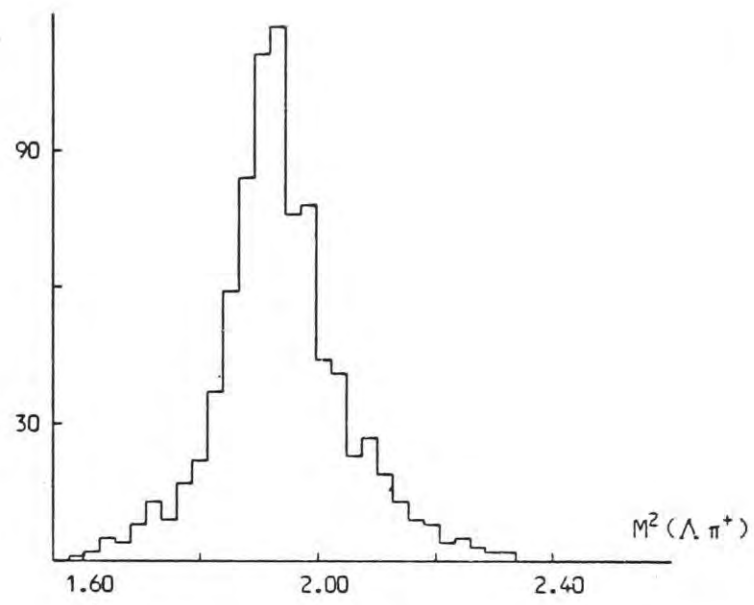

Inc. K^- Momentum = 0.750 GeV/c

$M^2(\Lambda\pi^-)$ .V. $M^2(\Lambda\pi^+)$

in $(GeV/c^2)^2$

843 Events

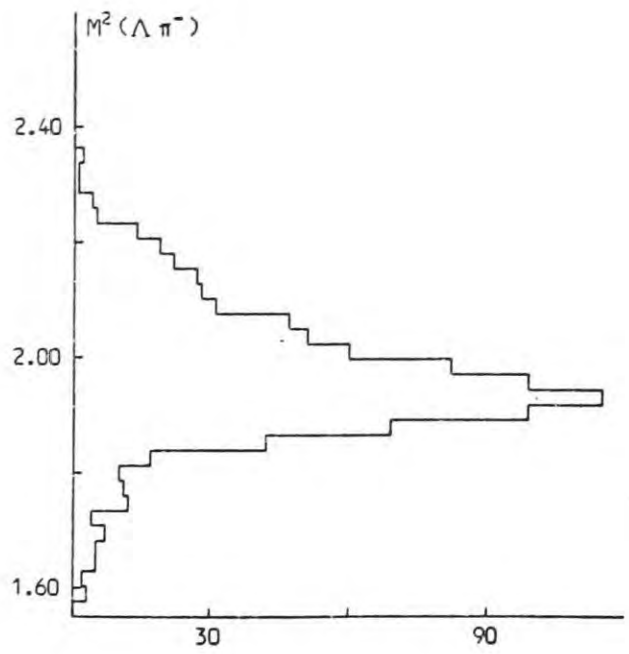

Dalitz Plot for the Reaction $K^-p \rightarrow \Lambda\pi^+\pi^-$

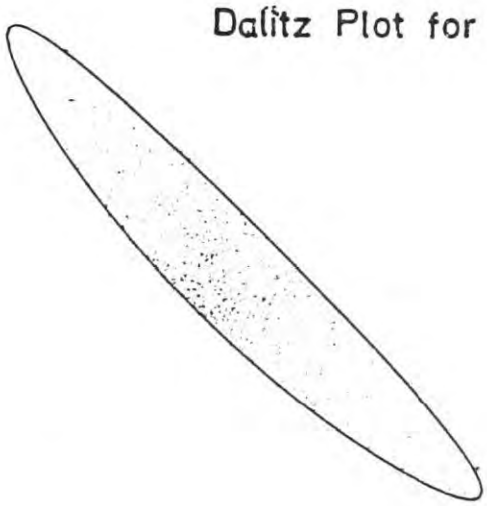

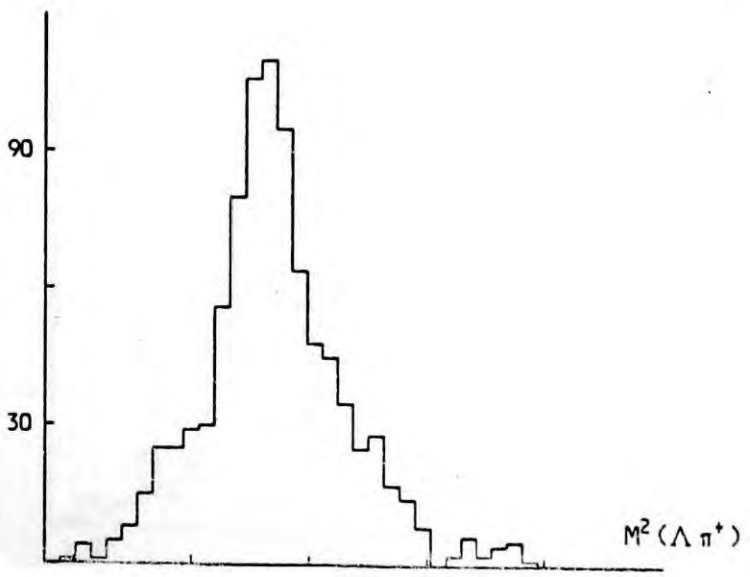

Inc. K^- Momentum = 0.770 GeV/c

$M^2(\Lambda\pi^-)$ .V. $M^2(\Lambda\pi^+)$

in $(GeV/c^2)^2$

894 Events

Figure 4.1 Cont'd..

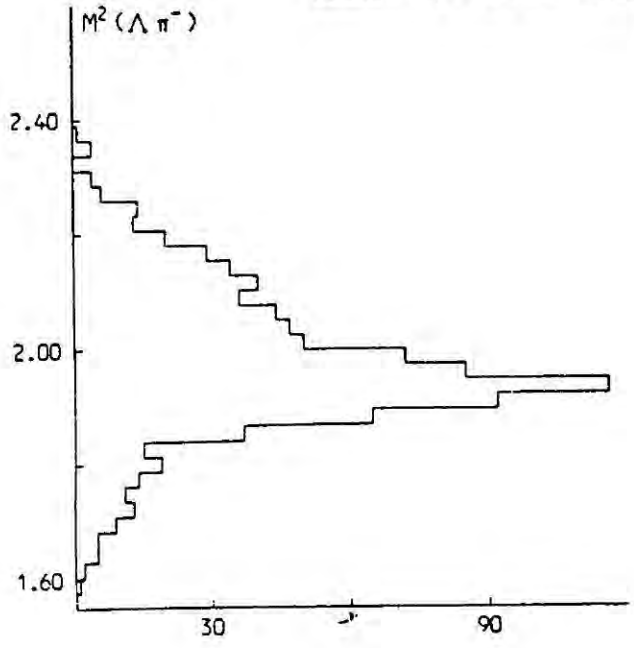

Dalitz Plot for the Reaction $K^-p \rightarrow \Lambda\pi^+\pi^-$

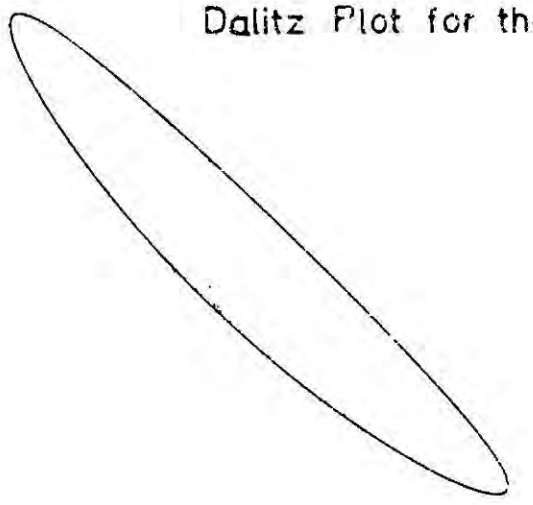

Inc. K^- Momentum = 0.790 GeV/c

$M^2(\Lambda\pi^-)$ .V. $M^2(\Lambda\pi^+)$

in $(GeV/c^2)^2$

903 Events

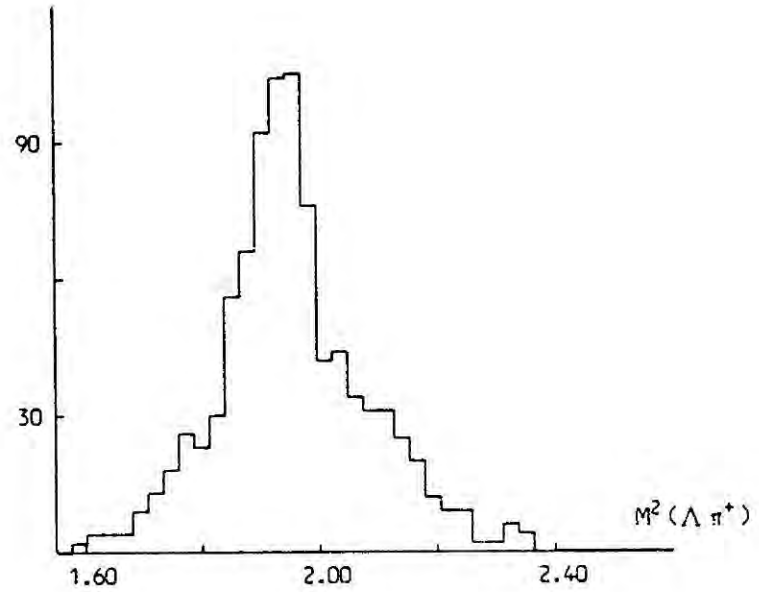

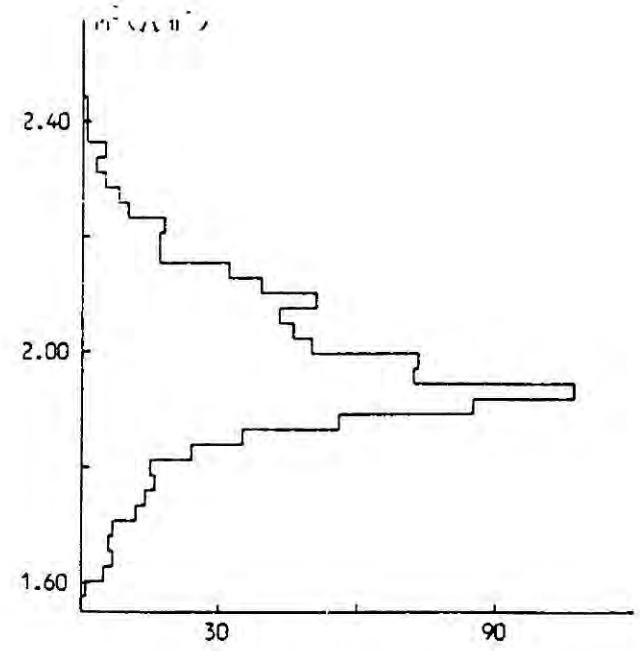

Dalitz Plot for the Reaction $K^-p \rightarrow \Lambda\pi^+\pi^-$

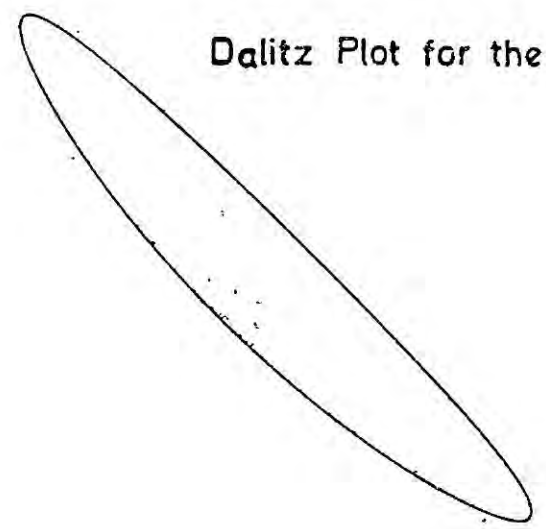

Inc. K^- Momentum = 0.810 GeV/c

$M^2(\Lambda\pi^-)$ .V. $M^2(\Lambda\pi^+)$

in $(GeV/c^2)^2$

882 Events

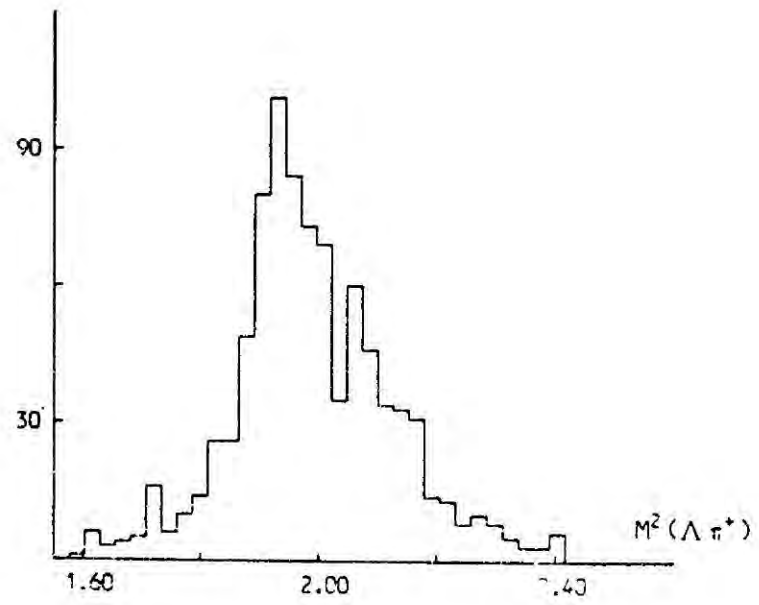

Figure 4.1 (Cont'd...

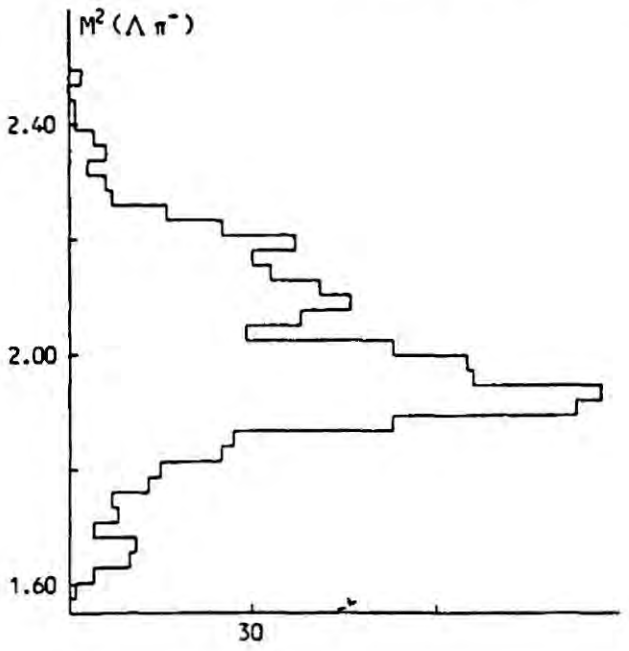

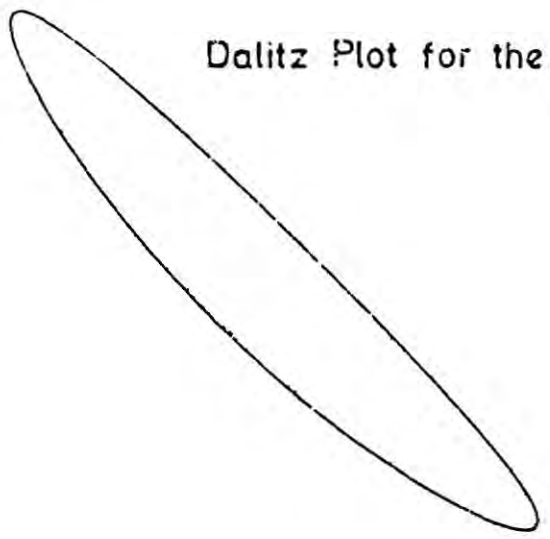

Inc. K^- Momentum = 0.830 GeV/c

$M^2(\Lambda\pi^-)$ .V. $M^2(\Lambda\pi^+)$

in $(GeV/c^2)^2$

857 Events

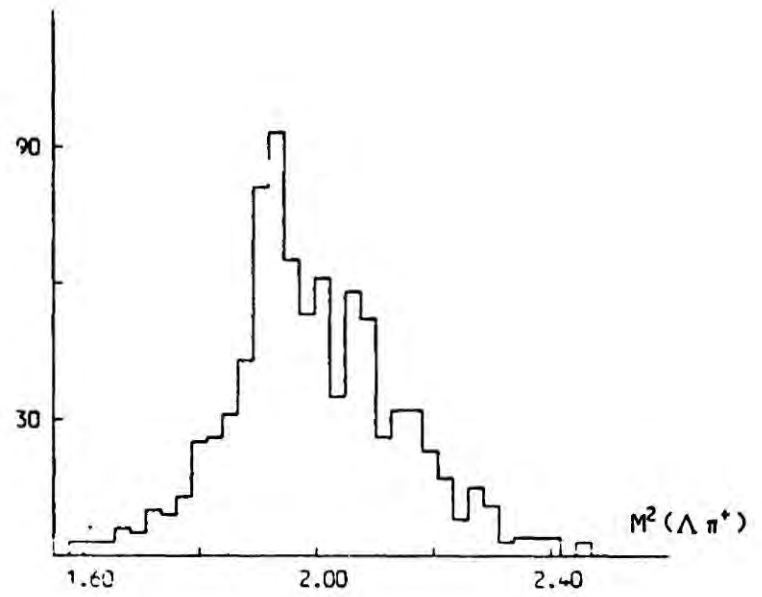

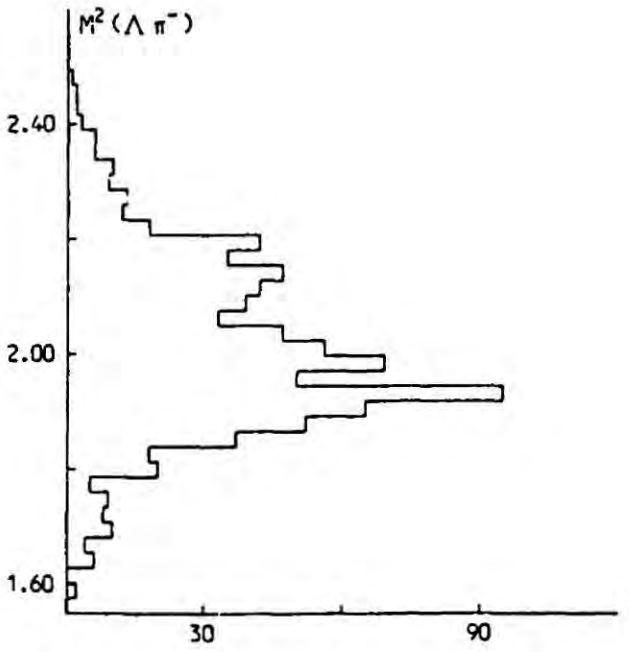

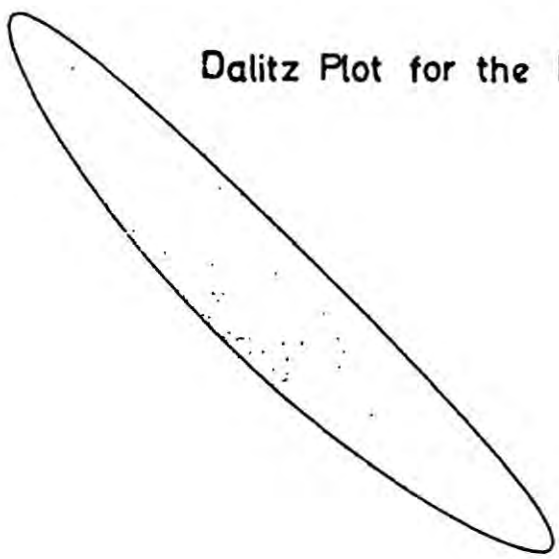

Inc. K^- Momentum = 0.850 GeV/c

$M^2(\Lambda\pi^-)$ .V. $M^2(\Lambda\pi^+)$

in $(GeV/c^2)^2$

873 Events

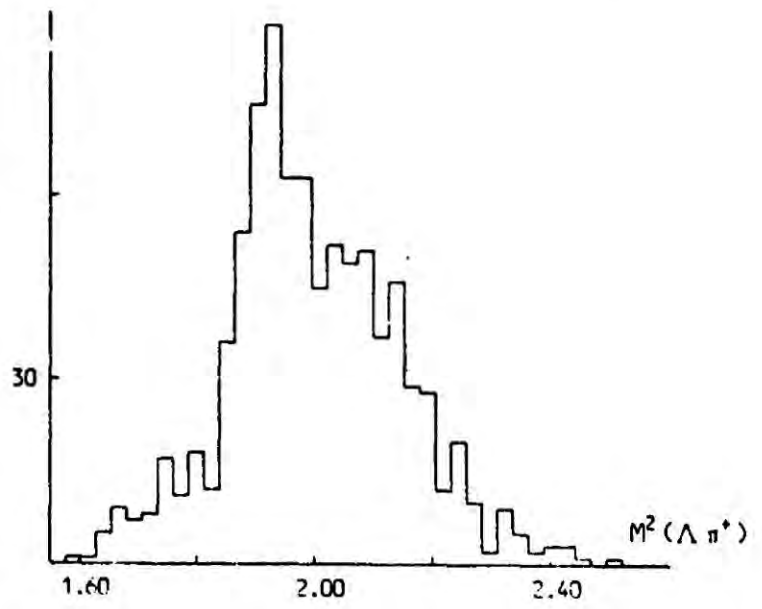

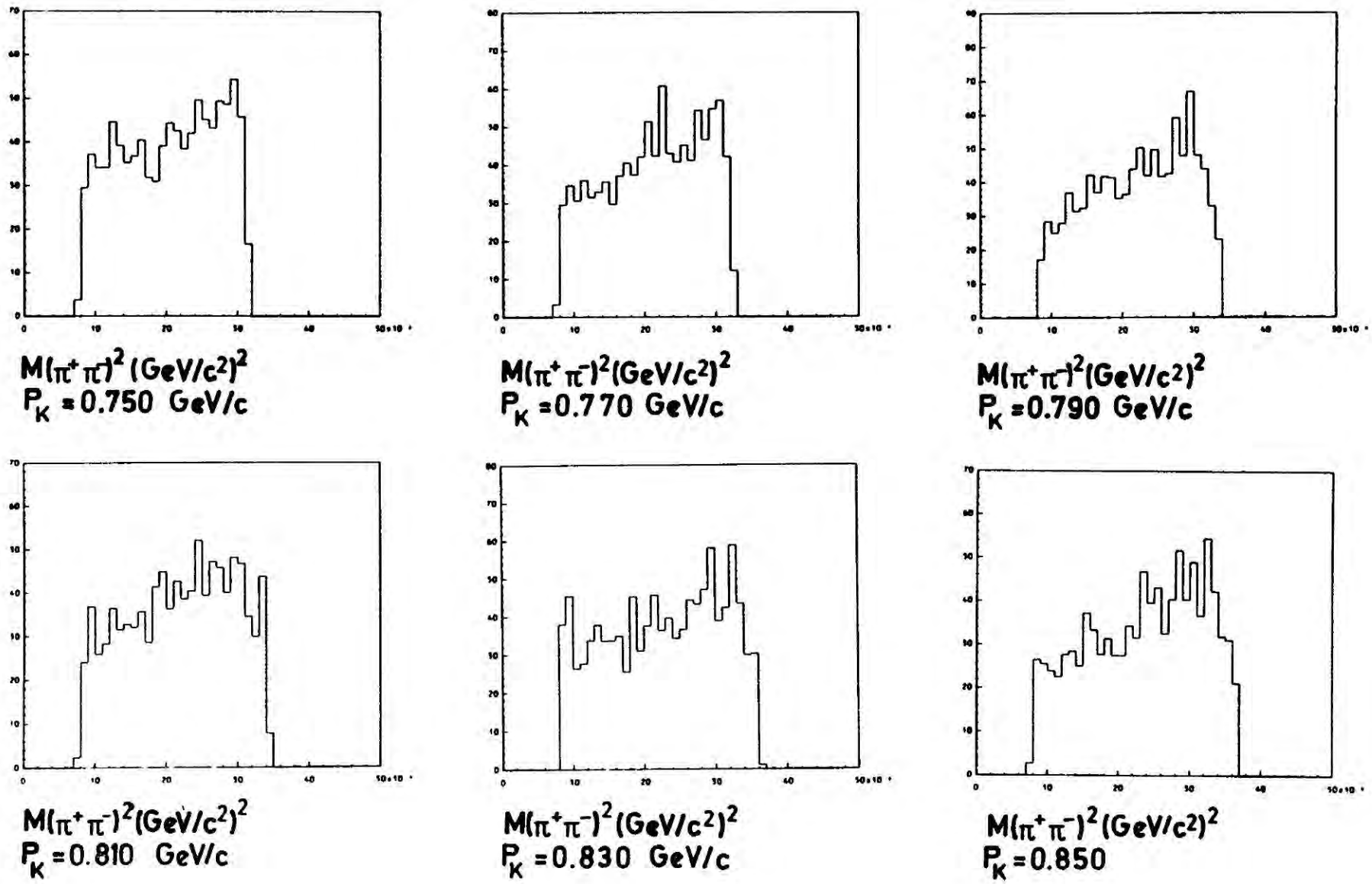

Figure 4.2 : Distributions of $M^2(\pi^+\pi^-)$ for the reaction $k^- p \Lambda \Lambda\pi^+\pi^-$, with the same binning as Figure 4.1.

available in the 0.500 to 0.580 GeV/c interval, from the Track Sensitive Target (T.S.T), experiment mentioned in Chapter 2 of this thesis, for which kinematic overlap occurs above the upper kinematic boundary. The Dalitz plot and $m^2(\pi^+\pi^-)$ distribution are shown in Figures 4.3 and 4.4 respectively.

Qualitative features present in this data are :-

(i) Strong $\Sigma(1385)$ production seen in both $m^2(\Lambda\pi^+)$ and $m^2(\Lambda\pi^-)$ distributions and apparent as broad bands of enhanced density centred on 1.92 $(GeV/c^2)^2$ in the Dalitz plot. This effect persists between 0.720 and 0.860 GeV/c, but is not evident in the T.S.T. data.

(ii) An enhancement in density of the Dalitz plot near the lower kinematic boundary, which is seen as a peaking at high dipion masses in the $m^2(\pi^+\pi^-)$ distribution. Furthermore, this effect persists with incident momentum and is independent of the position of kinematic overlap between $\Sigma(1385)$ bands. As such, the magnitude of this enhancement is most pronounced in the T.S.T. data.

Kinematically, these properties are reflected in the $\cos\theta$ distribution for $\Lambda\pi^+$ and $\Lambda\pi^-$ systems. Figures 4.5 and 4.6 show the distributions of these quantities in the momentum intervals chosen to display the Dalitz plot data. At all momenta, there is a marked peaking near $\cos\theta = +1$ for the $\Lambda\pi^+$ system and at $\cos\theta = -1$ for the $\Lambda\pi^-$ system. This feature corresponds to the enhancement of events at high $\pi^+\pi^-$ effective masses.

Equation 3.17, gives the decay angular distribution of the $\Sigma(1385)$ in its own rest frame as :-

$$W(\theta) = \frac{3}{2}\left[\frac{1}{3}\left(\frac{1}{2} + 2\rho_{33}\right) + \left(\frac{1}{2} - 2\rho_{33}\right)\cos^2\theta\right] \qquad (4.7)$$

As expected from parity conservation for the strong decay $\Sigma(1385) \rightarrow \Lambda\pi$, $W(\theta)$ is symmetrical. However, the form of this distribution depends on

Dalitz Plot for the Reaction $K^- p \rightarrow \Lambda \pi^+ \pi^-$

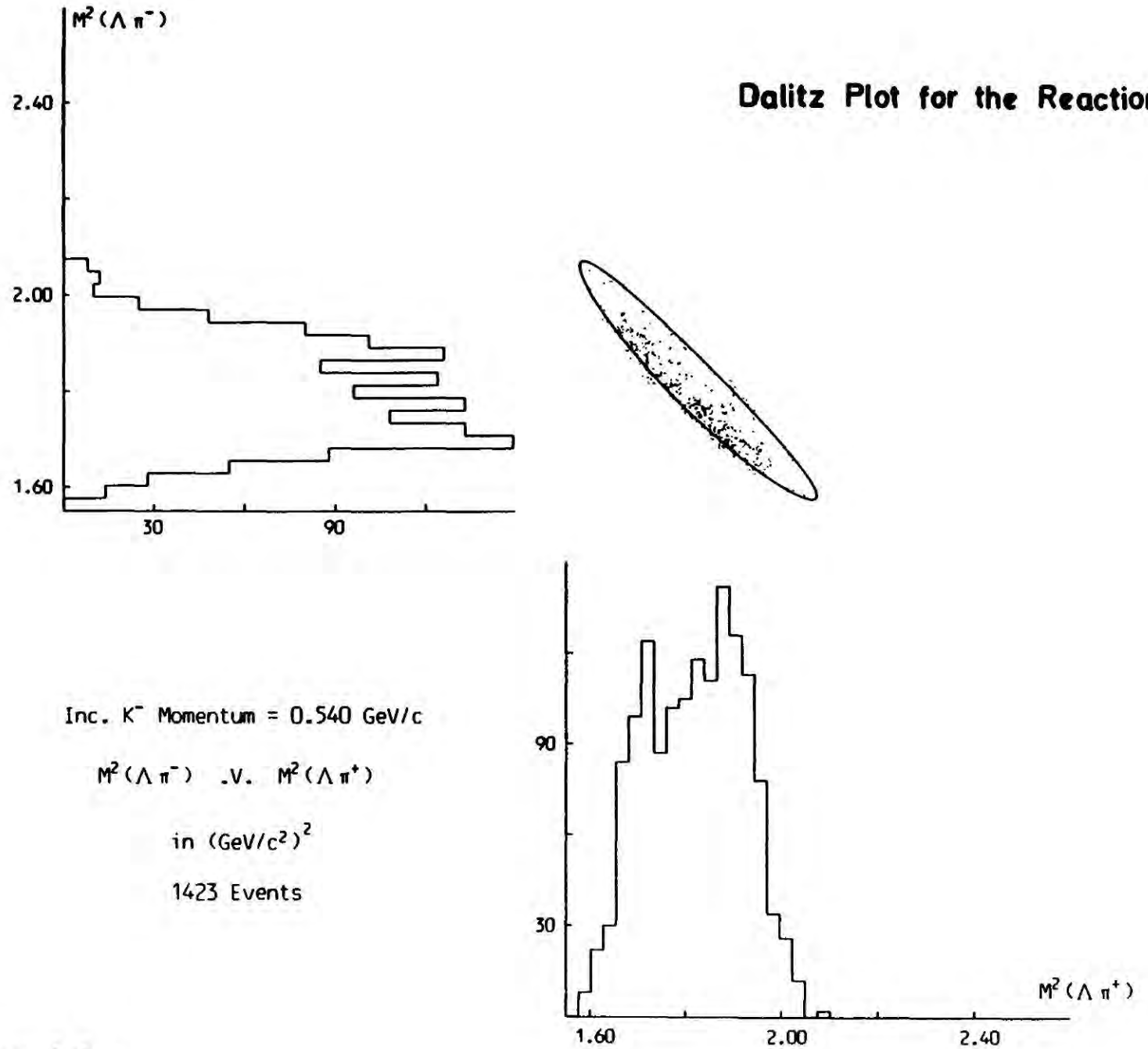

Inc. K^- Momentum = 0.540 GeV/c

$M^2(\Lambda \pi^-)$ .V. $M^2(\Lambda \pi^+)$

in $(GeV/c^2)^2$

1423 Events

Figure 4.3 :

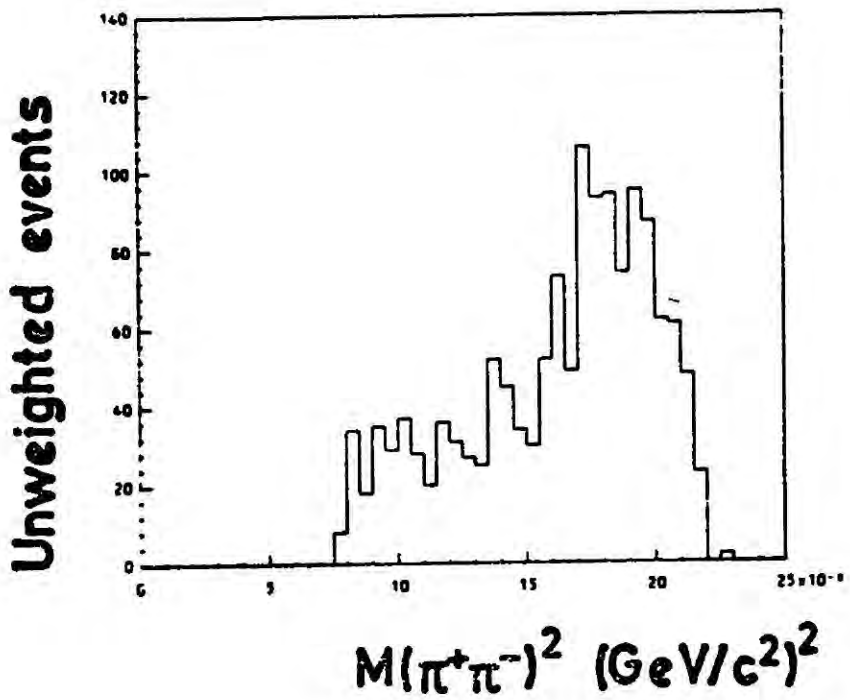

Distribution of $M^2(\pi^+\pi^-)$ for Events Fitting the Reaction $K^-p \rightarrow \Lambda\pi^+\pi^-$ in the 0.500 to 0.580 GeV/c Incident Momentum Interval

Figure 4.4 :

Distributions of Cos θ for $\Lambda\pi^+$ System as a Function of Incident Momentum (P_K)

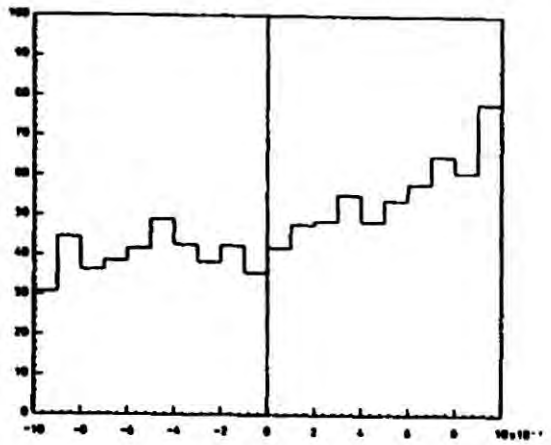

Cos θ for $\Lambda\pi^+$ system
P_K = 0.750 GeV/c

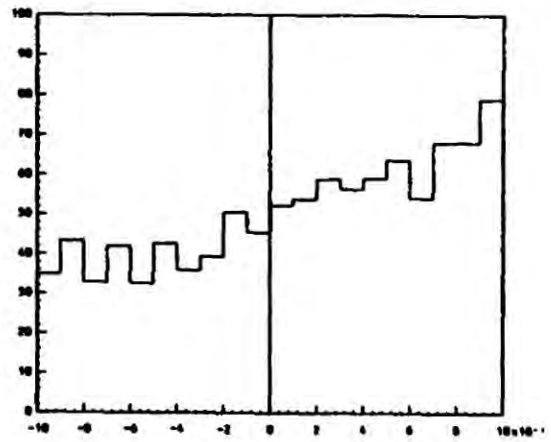

Cos θ for $\Lambda\pi^+$ system
P_K = 0.770 GeV/c

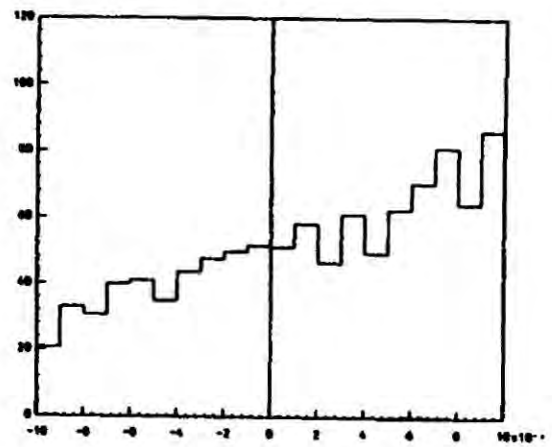

Cos θ for $\Lambda\pi^+$ system
P_K = 0.790 GeV/c

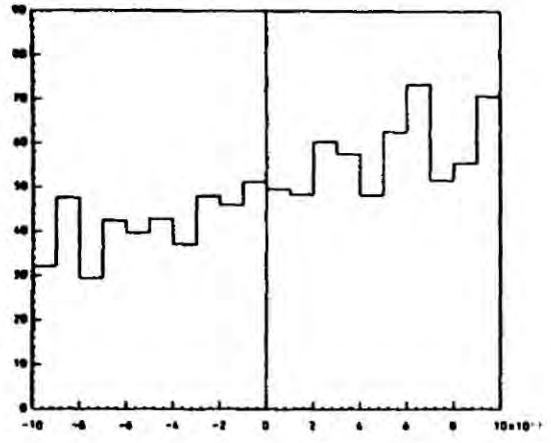

Cos θ for $\Lambda\pi^+$ system
P_K = 0.810 GeV/c

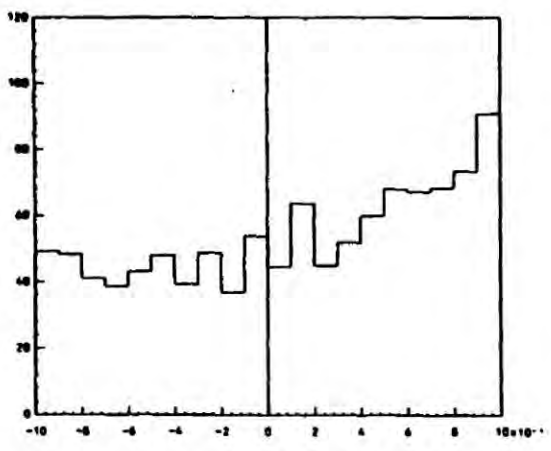

Cos θ for $\Lambda\pi^+$ system
P_K = 0.830 GeV/c

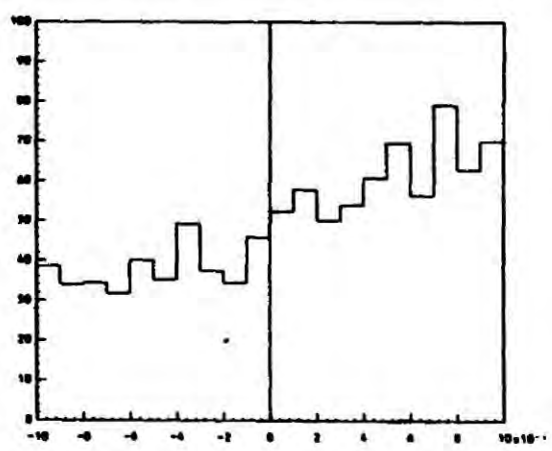

Cos θ for $\Lambda\pi^+$ system
P_K = 0.850 GeV/c

Figure 4.5 : Distributions of cosΘ for the $\Lambda\pi^+$ system as a function of incident momentum with the same binning as Figure 4.1.

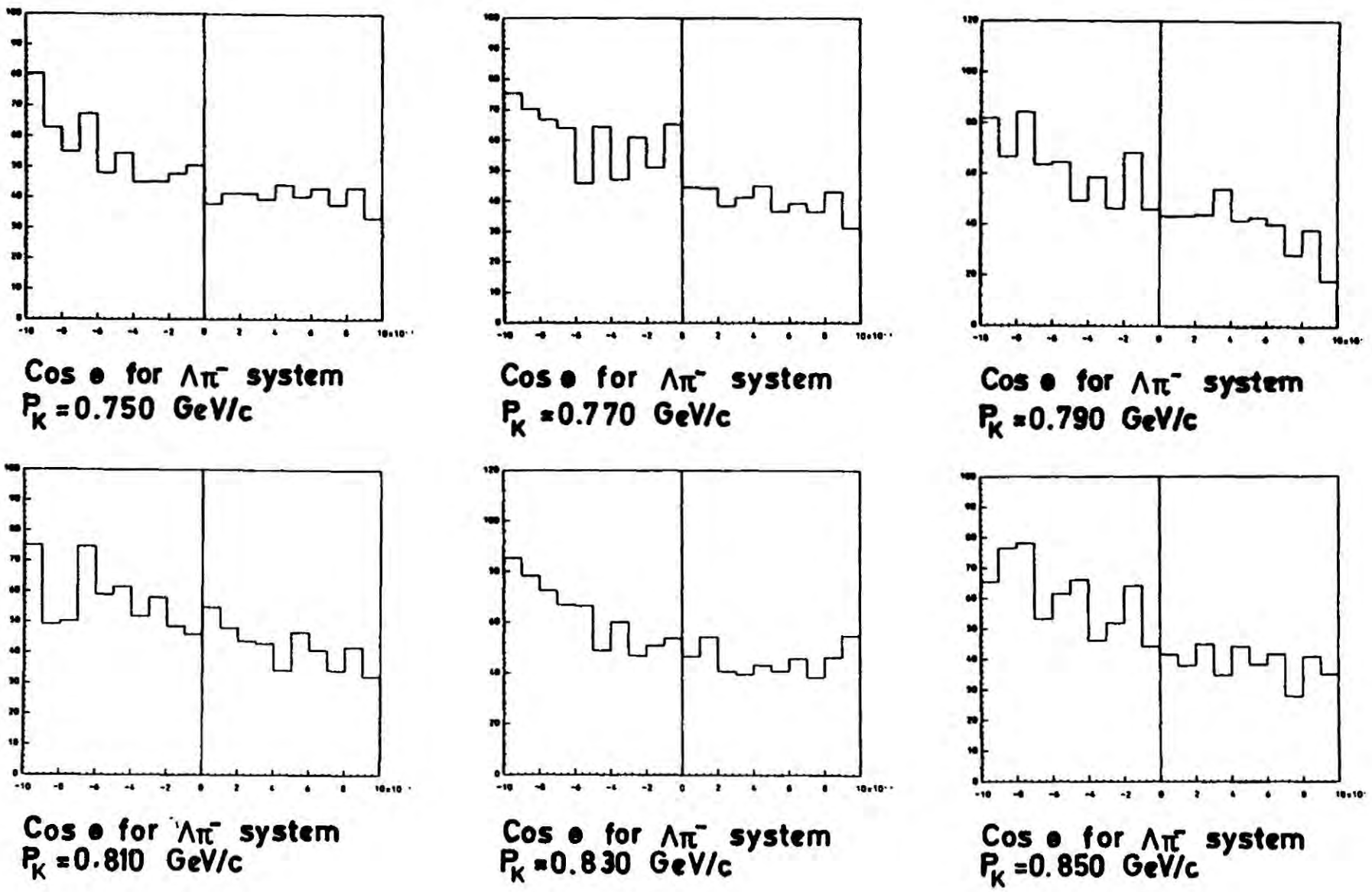

Figure 4.6 : Distribution of cosΘ for the $\Lambda\pi^-$ system as a function of incident momentum, with the same binning as Figure 4.1.

the value of ρ_{33} :-

(i) If $\rho_{33} > \frac{1}{4}$, $W(\Theta)$ peaks at $\cos\Theta = +1$ and $\cos\Theta = -1$

(ii) If $\rho_{33} < \frac{1}{4}$, $W(\Theta)$ peaks at $\cos\Theta = 0.0$.

Since the values of ρ_{33} appearing in $W(\Theta)$ are averaged over $\cos\Theta^*$, only the even $\left[B_\ell/A_o\right]$ coefficients determine this behaviour.

An asymmetry does appear in the $\cos\Theta$ distribution as a kinematic consequence of observing the decay of one $\Sigma(1385)$ system from the rest frame of another. However, this effect should move across the $\cos\Theta$ distribution as the $\Sigma(1385)$ overlap moves across the Dalitz plot. When the overlap is central in the Dalitz plot and the $\Sigma(1385)$bands fill the available phase space, the $\cos\Theta$ distribution will appear nearly symmetrical. This is a consequence of $\Sigma^+(1385)$ and $\Sigma^-(1385)$ being kinematically indistinguishable.

4.4 ORIGINS OF THE HIGH DIPION MASS ENHANCEMENT

Two previous experiments have also seen evidence for structure in the $m(\pi^+\pi^-)^2$ distribution. Both have obtained data for the reaction $k^-p \to \Lambda\pi^+\pi^-$ from hydrogen bubble chamber exposures at momenta similar to those explored in this experiment. Analysis was performed using the parametrizations due to Deller and Valladas [reference 4.1] , which allow for possible interference effects between $\Sigma(1385)$ isobars.

Prevost et al [references 4.2 and 4.3] have data in the 0.430 to 1.230 GeV/c incident momentum interval. Data below 0.600 GeV/c was rejected by the authors and a partial wave analysis was performed for $\pi\Sigma(1385)$ final states. However, the final results of this analysis which allowsfor possible interferences between $\Sigma^-(1385)$ and $\Sigma^+(1385)$ isobars within the Dalitz plot, do not account for the shape of the $\pi^+\pi^-$ effective mass distribution.

Possible $\Sigma(1385)$ isobar interference, as the origin of the structure has also been suggested by Evans et al [reference 4.4] . Only those incident momenta where $\Sigma(1385)$ overlap occurs below the upper kinematic boundary of the Dalitz plot were explored [0.690 to 0.830 GeV/c] . No convincing evidence is presented that the momentum dependence of the observed structure is consistent with an interference effect.

That the high $m^2(\pi^+\pi^-)$ enhancement is independent of incident momentum,is strong evidence that it is not the consequence of an interference effect. Equation 3.3 indicates that coherent production of $\Sigma^+(1385)$ and $\Sigma^-(1385)$ isobars will lead to an enhanced (or depleted) density of the Dalitz plot in the vicinity of the kinematic overlap. This would result in a movement of the structure from the lowest accessible $\pi\pi$ masses at 0.500 GeV/c to the highest $\pi\pi$ masses at 0.850 GeV/c. No such effect is observed, the enhancement is independent of the position of $\Sigma(1385)$overlap.

Throughout the rest of this thesis, it will be assumed that final state isobars are produced incoherently. Production of final state $\pi\pi$ isobars will be considered in Chapter 5 as the possible origin of the high $\pi^+\pi^-$ mass enhancement.

4.5 CONSEQUENCES OF PURE INCOHERENT $\Sigma(1385)$ PRODUCTION

A purely qualitative description of the role of $\Sigma(1385)$ production in determining the features of the Dalitz plot was given in sections 4.3 and 4.4. In order to establish a quantitative appreciation of the magnitude of non-$\Sigma(1385)$ effects, namely $\pi\pi$ isobar formation, this section will be devoted to a description of an attempt to account for the quasi two-body variables of the $\Lambda\pi^+\pi^-$ final state allowing only incoherent addition of $\pi\Sigma(1385)$ channels. This study was undertaken using the program EXTRA described in Chapter 3.

Table 4.2 gives the masses and widths used for $\Sigma^+(1385)$ and $\Sigma^-(1385)$ states. These are taken from reference 4.5 and were obtained by fitting a

State	Mass $(GeV/c^2)^2$	Width $(GeV/c^2)^2$
Σ^+ (1385)	1.3822 $\pm$ 0.0004	0.0375 $\pm$ 0.0021
Σ^- (1385)	1.3883 $\pm$ 0.0004	0.0440 $\pm$ 0.0020

TABLE 4.2 : Masses and Widths of the $\Sigma(1385)$

(Taken from reference 4.5)

polynomial background plus Breit-Wigner form to the $m^2(\Lambda\,\pi^+)$ and $m^2(\Lambda\pi^-)$ distributions. In determining the convergence of channel fraction iteration, the following criteria has been used :-

$$\sum_{j=1}^{NPRS} \left(\alpha_j - \alpha_j'\right)^2 \lesssim 0.0001 \qquad (4.8)$$

This implies residues between successive fraction iterations of less than 2%. Stability of coefficients has been found to occur to better than 5% after three iterations.

Once extraction of channel fractions and coefficients is complete, EXTRA generates a set of events uniformly in a set of five independent quasi-two-body variables. Each such event was weighted according to the available three body phase space and each fitted channel probability ω_j (see section 3.5). The weighted numbers of generated events were then normalized to the corrected event sample and comparison of distributions of the quasi two-body variables performed. As a measure of goodness of fit, a χ^2 value was calculated for each histogram bin fitted.

Figure 4.7 shows the distributions of quasi-two-body variables for events in the momentum bin centred on 0.830 GeV/c. The curves represent the results of Monte-Carlo integration, described above, for channel fractions and coefficients obtained with incoherent addition of $\pi^+\Sigma^-$ (1385) and $\pi^-\Sigma^+$(1385)processes. As anticipated, no account is given for the following features :-

(i) The high $m^2(\pi^+\pi^-)$ enhancement.

(ii) Peaking at $\cos\Theta = -1$ and $\cos\Theta = +1$ in the $\cos\Theta$ distribution for $\Lambda\pi^-$ and $\Lambda\pi^+$ systems respectively.

Good account is given of other quantities and the fitted $\bar{\Sigma}$(1385/Σ^+(1385) ratio is found to be 1.22.

Results of Quasi Two-Body Analysis for Pure Σ(1385) Production

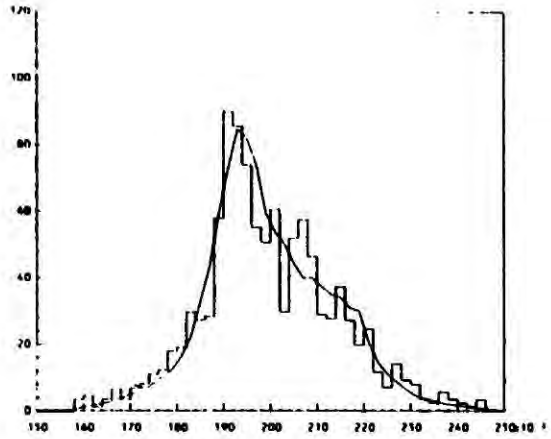

$M(\Lambda\pi^-)^2\,(GeV/c^2)^2$

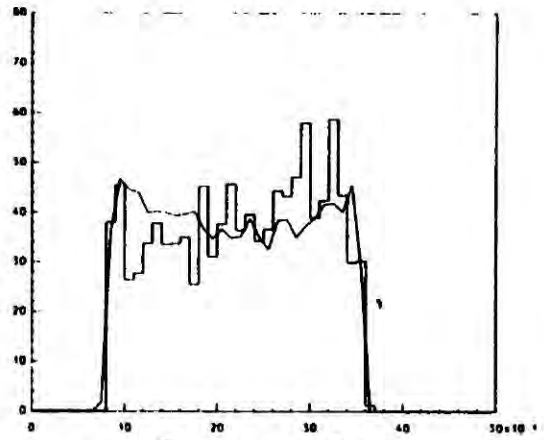

$M(\pi^+\pi^-)^2\,(GeV/c^2)^2$

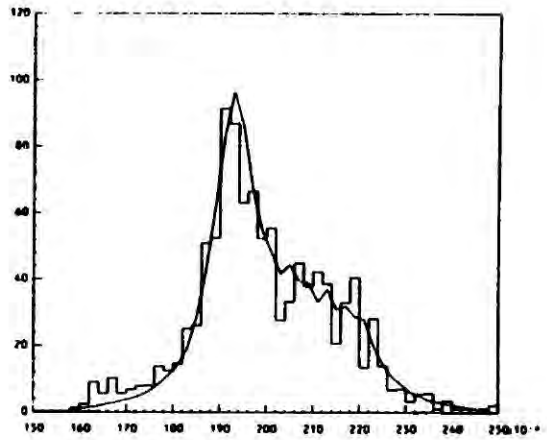

$M(\Lambda\pi^+)^2\,(GeV/c^2)^2$

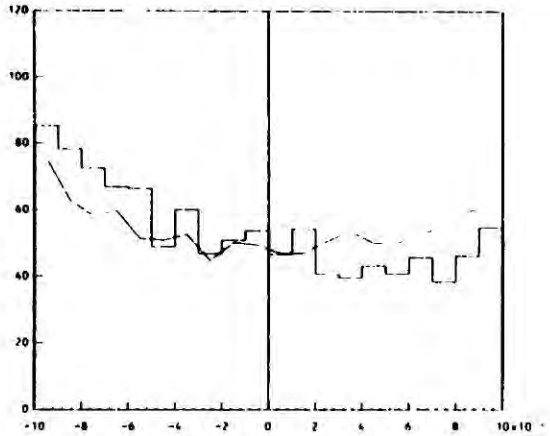

Cos θ for $\Lambda\pi^-$ system

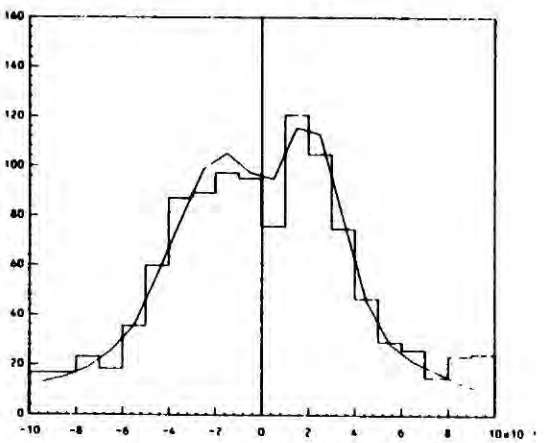

Cos θ for $\pi^+\pi^-$ system

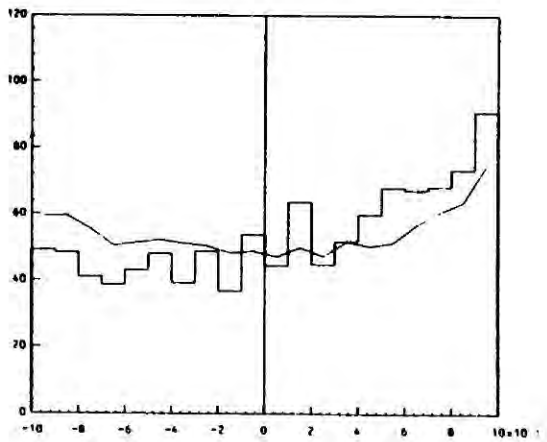

Cos θ for $\Lambda\pi^+$ system

Figure 4.7 : Results of Quasi-two-body analysis of the reaction $k^-p \rightarrow \Lambda\pi^+\pi^-$ in the incident momentum bin centred on 0.830 GeV/c and allowing only pure $\pi\Sigma(1385)$ channels.

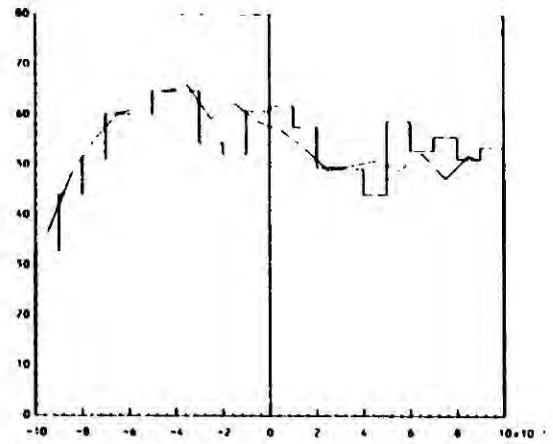

Cos θ^* for $\Lambda\pi^-$ system

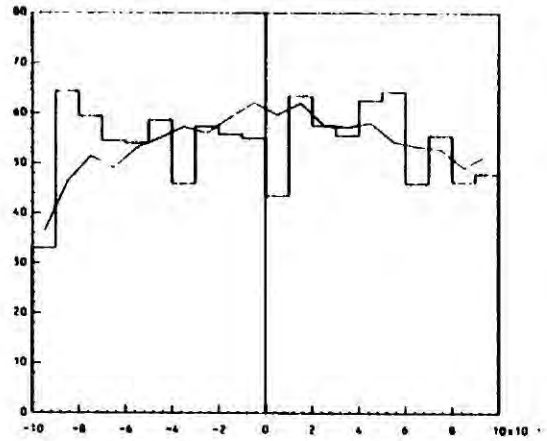

Cos θ^* for $\pi^+\pi^-$ system

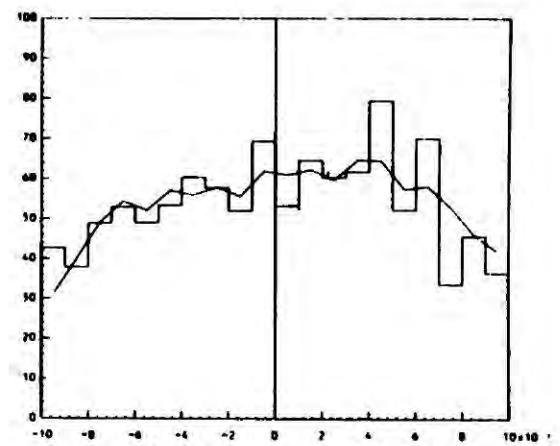

Cos θ^* for $\Lambda\pi^+$ system

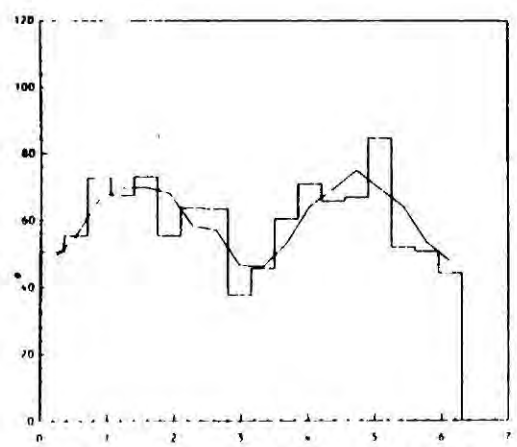

Φ for $\Lambda\pi^-$ system (radians)

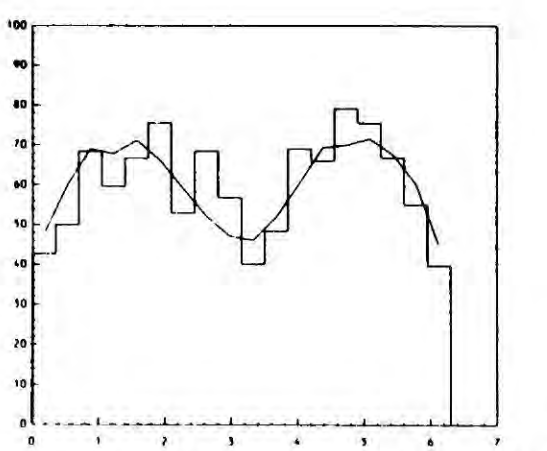

Φ for $\pi^+\pi^-$ system (radians)

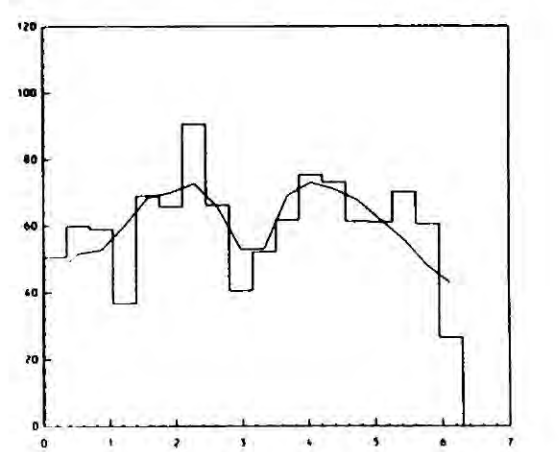

Φ for $\Lambda\pi^+$ system (radians)

Figure 4.7 (Cont'd)

4.6 CONCLUSIONS

Dalitz plots are seen to be dominated by $\Sigma^+(1385)$ and $\Sigma^-(1385)$ production at all incident momenta between 0.720 and 0.860 GeV/c. In addition, structure is seen in the dipion mass spectrum. This effect is most prominent at 0.540 GeV/c, where $\Sigma(1385)$ production does not seem to be an important feature in the Dalitz plot. Kinematic arguments rule out $\Sigma^+(1385)$ / $\Sigma^-(1385)$ interference effects as the origin of a persistent high $\pi^+\pi^-$ mass structure. In the next chapter $\pi\pi$ isobar formation will be invoked to give a satisfactory description of the Dalitz plot density.

CHAPTER 4

REFERENCES

4.1 B. Deller and G. Valladas, Nuovo Cimento, 45A (1966) 559.

4.2 J. Prevost et al, Nucl. Phys. B69 (1974) 246.

4.3 J. Prevost, Thesis, University of Paris,(1974).

4.4 D.A.Evans, Nucl.Phys. B119 (1977) 315.

4.5 W. Cameron et al, Nucl.Phys. B143 (1978) 189.

CHAPTER 5

5.1 INTRODUCTION

In the previous chapter, interference effects were elliminated as the origin of an enhancement observed in the $\pi^+\pi^-$ effective mass for the $\pi^+\pi^-$ Λ final state. This chapter will be devoted to an investigation of the origins of the effect as a final state $\pi^+\pi^-$ interaction.

5.2 GENERAL CONSIDERATIONS OF $\pi\pi$ PHENOMENOLOGY

Prior to invoking any detailed description of the dynamics present in the $\pi^+\pi^-$ system produced in the reaction $k^- p \rightarrow \Lambda\pi^+\pi^-$, the use of simple quantum mechanical arguments can restrict the possible final state interactions.

In terms of isospin, the $\pi^+\pi^-$ system contains I = 2, I = 1 and I = 0 components. However, if one recalls that the initial $k^- p$ system contains only I = 1 and I = 0 components (see section 1.4), then isospin conservationgives the un-normalised wavefunction of the $\pi^+\pi^-$ system, in the isospin basis, as :-

$$\left|\pi^+\pi^-\right> = \sqrt{\frac{1}{2}}\ \left|1, 0\right> + \sqrt{\frac{1}{3}}\ \left|0, 0\right> \qquad (5.1)$$

Bose statistics demand that the wavefunction should be totally symmetric. Since the isotriplet wavefunction is antisymmetric with respect to the interchange of particle labels, the corresponding spatial wavefunction must also be antisymmetric to give total symmetry of the $\pi^+\pi^-$ wavefunction. Similarly, the isosinglet wavefunction is symmetric and requires a symmetric space wavefunction. The total particle spin of the $\pi^+\pi^-$ system is zero and the imposition of Bose statistics give the following relationships between total angular momentum (J) and isospin (I) :-

I = O : J = O, 2, 4 etc. with even parity

I = 1 : J = 1, 3, 5 etc. with odd parity

The even parity I = J = O system will be designated by 'ε' and the odd parity I = J = 1 system by 'ρ' ; these do not necessarily imply resonant systems.

Watson has proposed [ref. 5.1] an ansatz which may be used to represent final state interations for two particle systems produced in three body hadronic final states. If the $\pi\pi$ system recoils against the Λ with momentum p in the overall centre of mass, then the Watson amplitude is given in terms of the $\pi^+\pi^-$ phase shift $\delta^I_J(q)$ by

$$T = \frac{p^{L'}}{q^{J+1}} \sin\left[\delta^I_J(q)\right] \exp\left[i\,\delta^I_J(q)\right] \qquad (5.2)$$

where L' is the $(\pi^+\pi^-)\Lambda$ relative orbital angular momentum and q is the momentum of each pion in the $\pi^+\pi^-$ rest system. Both p and q are measured in pion mass units. For an incoherently produced $\pi^+\pi^-$ system the contribution to the Dalitz plot intensity is proportional to,

$$|T|^2 = \frac{p^{2L'}}{q^{2J+2}} \cdot \sin^2\left[\delta^I_J(q)\right] \qquad (5.3)$$

Kinematically, the quantities p and q may be expressed in terms of the dipion effective mass $m(\pi\pi)$, together with the π and Λ rest masses (μ and m_Λ) :-

$$p^2 = \frac{(s - (m_\Lambda + m(\pi\pi))^2)\,(s - (m_\Lambda - m(\pi\pi))^2)}{4s\,\mu^2} \qquad (5.4)$$

$$q^2 = \frac{(m^2(\pi\pi) - 4\mu^2)}{4\mu^2} \qquad (5.5)$$

where $\sqrt{s}$ is the total centre of mass energy of the $(\pi\pi)\ \Lambda$ system. Hence, p is a monotonically decreasing function of $m(\pi\pi)$ and q is a monotonically increasing function of $m(\pi\pi)$. The combined barrier factor $\left[p^{2L'}/q^{2J+2} \right]$ leads one to expect an enhancement in the $\pi\pi$ mass spectrum near threshold where $m(\pi\pi) = 2\mu$. To obtain an enhancement near the top of available phase space, where $m(\pi\pi) = \sqrt{s} - m_{\Lambda}$, $\sin^2 \left[\delta^I_J (q) \right]$ must rise faster than q^{2J+2}.

Angular momentum and parity conservation give the allowed s-channel partial wave amplitudes for 'ε' and 'ρ' production, in the $L\ L'\ I(2J)$ notation :-

(i) For 'ε' Λ

SP01 PS01 PD03 etc.

(ii) For 'ρ' Λ

SD11 PP11 PP13 PF13 etc.

Published values of the phase shifts for isoscalar and isovector $\pi\pi$ dynamics [see Refs. 5.2, 5.3 and 5.4] indicate that $\delta^0_0 >> \delta^1_1$ in the region for which $m(\pi\pi) < 0.650\ GeV/c^2$. In fact, at $m(\pi\pi) = 0.500\ GeV/c^2$, which is above the highest dipion effective mass accessible in this experiment,

$$\delta^0_0 = 30^0 \quad \left[\text{1978 P.D.G. Tables reference 5.5} \right]$$

$$\delta^1_1 = 5^0$$

If both 'ρ' Λ and 'ε' Λ systems are produced in relative s-waves :-

$$\frac{|T_\rho|^2}{|T_\varepsilon|^2} = \frac{1}{q^2} \frac{\sin^2 \delta^1_1}{\sin^2 \delta^0_0} \lesssim 5\% \qquad (5.6)$$

Viewed phenomenologically, the small value of δ^1_1 is a consequence of the isovector $\pi\pi$ system being described entirely by ρ(770) formation with a

width of0.150 GeV/c^2, (the low energy tail of this effect being insignificant at 0.500 GeV/c). At higher incident momenta [ref. 5.6], the production of $\rho(770)$ is required to account for structure in the $\pi^+\pi^-$ effective mass distribution.

Further evidence for the isoscalar nature of dynamics in the $\pi^+\pi^-$ system comes from consideration of the reaction $k_L^o p \rightarrow \Lambda\pi^+\pi^o$. Data concerning this reaction has been made available by W.Cameron and is published in reference 5.7. The incident momentum range covered is 0.480 to 0.790 GeV/c, which includes the region where kinematic overlap between $\Sigma^+(1385)$ and $\Sigma(1385)$ bands occurs inside the kinematic boundary of the Dalitz plot. Figure 5.1 shows the $\Lambda\pi^+/\Lambda\pi^o$ Dalitz plot and Figure 5.2 shows the $m^2(\pi^+\pi^o)$ distribution for events in the 0.740 to 0.750 GeV/c interval. Clear $\Sigma^+(1385)$ and $\Sigma^-(1385)$ production is seen, but no structure is evident in the $\pi^+\pi^o$ effective mass distribution. Since the $\pi^+\pi^o$ system produced in the reaction $k_L^o p \rightarrow \Lambda\pi^+\pi^o$ is pure isovectorin nature, the absence of any structure indicates that $\pi\pi$ P-wave systems are not produced; the obvious candidate for such an effect being the $\rho(770)$ vector meson. The dynamics of the $\pi^+\pi^-$ system produced in the reaction $k^- p \rightarrow \Lambda\pi^+\pi^-$ must therefore be isoscalar in origin.

Figure 5.3 shows a fit performed using program EXTRA to the quasi two-body variables $m^2(\pi^+\pi^o)$, $m^2(\Lambda\pi^o)$ and $m^2(\Lambda\pi^+)$ for the $\Lambda\pi^+\pi^o$ final state. Agreement found is reasonable, the value of χ^2 found by normalizing the predictions of Monte-Carlo integration for the final fitted parameters to the data sample are :

$m^2(\Lambda\pi^+)$	: χ^2 =	64	for	26	histogram bins
$m^2(\Lambda\pi^o)$	: χ^2 =	76.37	for	40	histogram bins
$m^2(\pi^+\pi^o)$	: χ^2 =	75.86	for	40	histogram bins

Figure 5.1

Dalitz Plot for the Reaction $K_L^0 p \rightarrow \Lambda \pi^+ \pi^0$

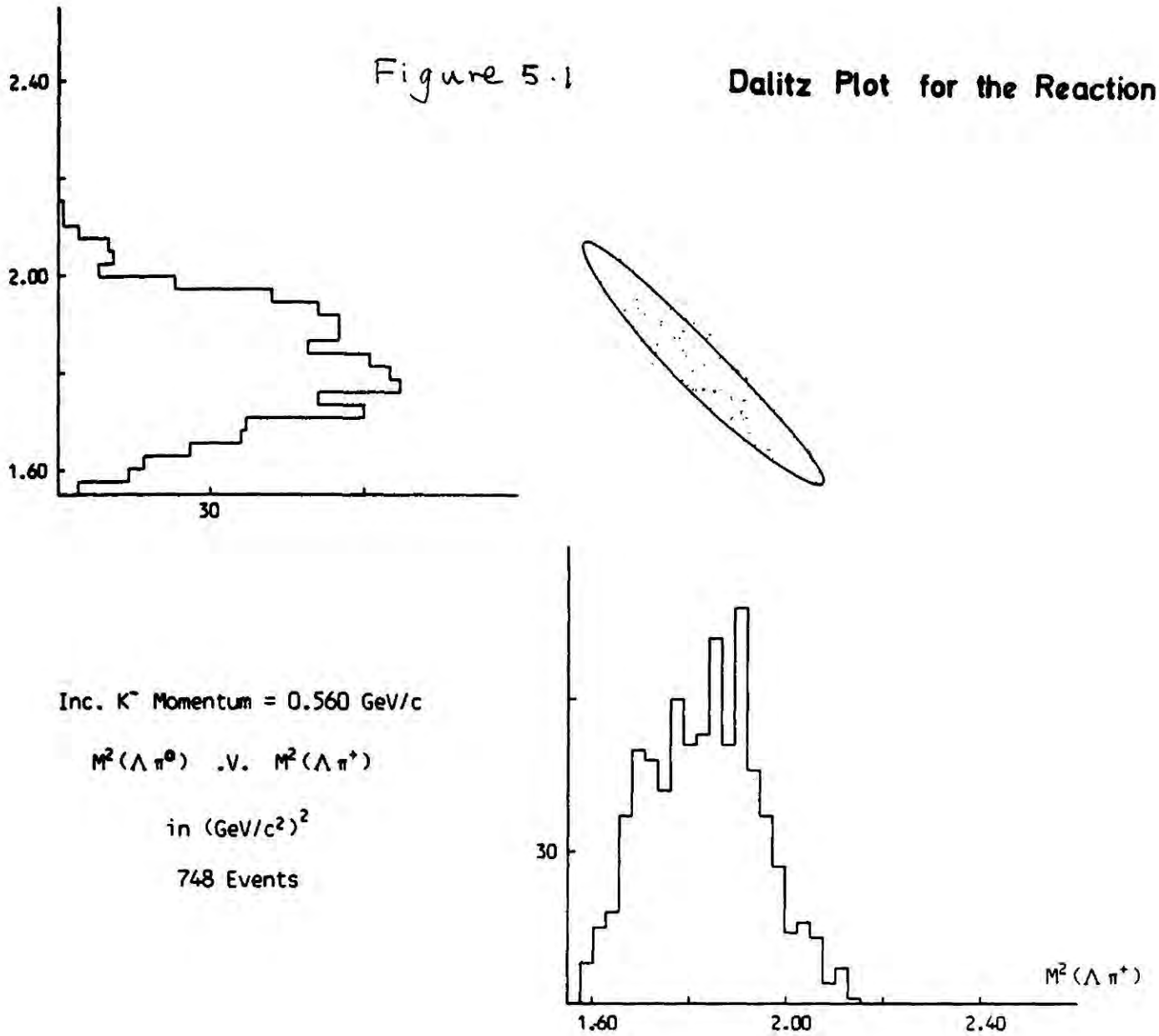

Inc. K^- Momentum = 0.560 GeV/c

$M^2(\Lambda \pi^0)$ .V. $M^2(\Lambda \pi^+)$

in $(GeV/c^2)^2$

748 Events

Dalitz Plot for the Reaction $K_L^0 p \rightarrow \Lambda \pi^+ \pi^0$

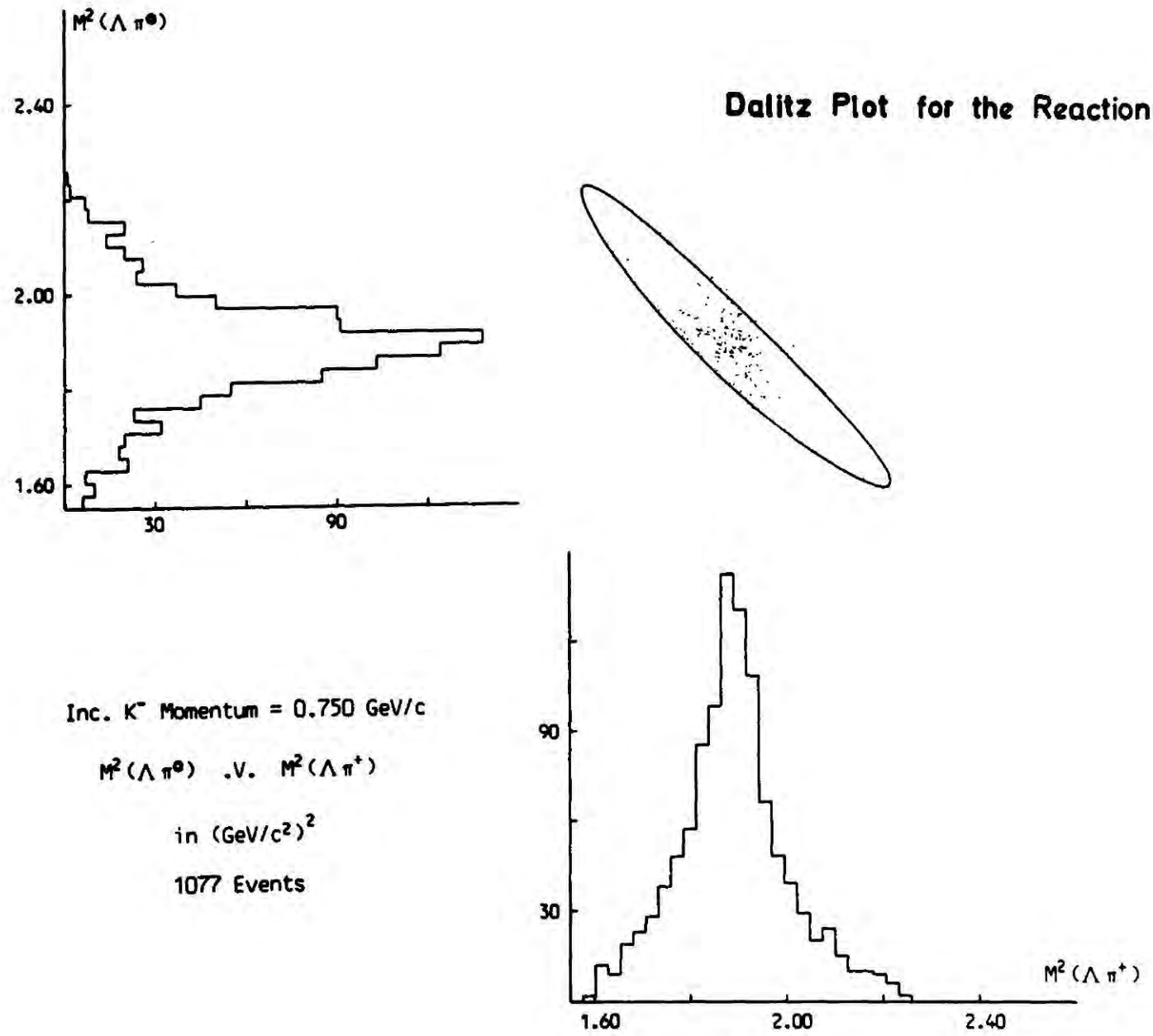

Inc. K^- Momentum = 0.750 GeV/c

$M^2(\Lambda \pi^0)$ .V. $M^2(\Lambda \pi^+)$

in $(GeV/c^2)^2$

1077 Events

Figure 5.1 Cont'd.

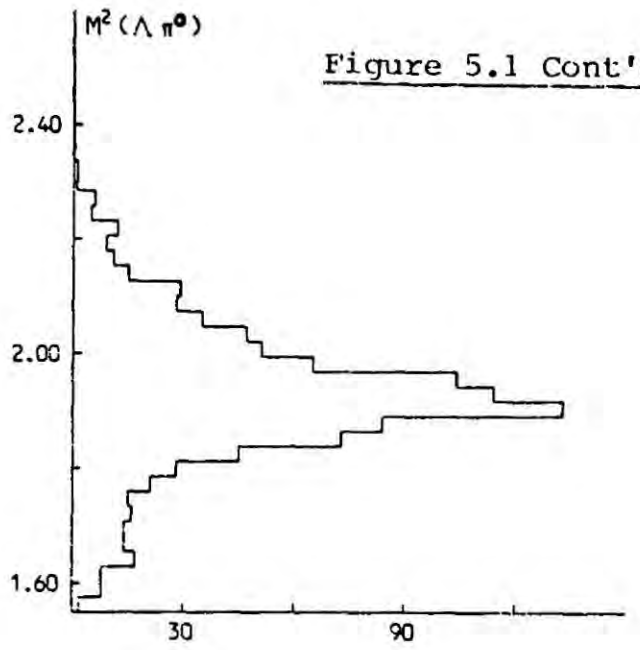

Dalitz Plot for the Reaction $K_L^0 p \rightarrow \Lambda\pi^+\pi^0$

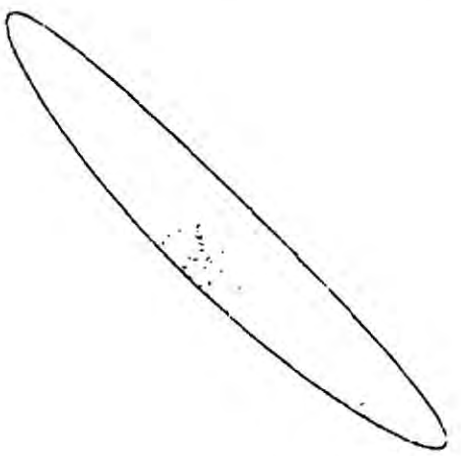

Inc. K^- Momentum = 0.730 GeV/c

$M^2(\Lambda\pi^0)$ .V. $M^2(\Lambda\pi^+)$

in $(GeV/c^2)^2$

1011 Events

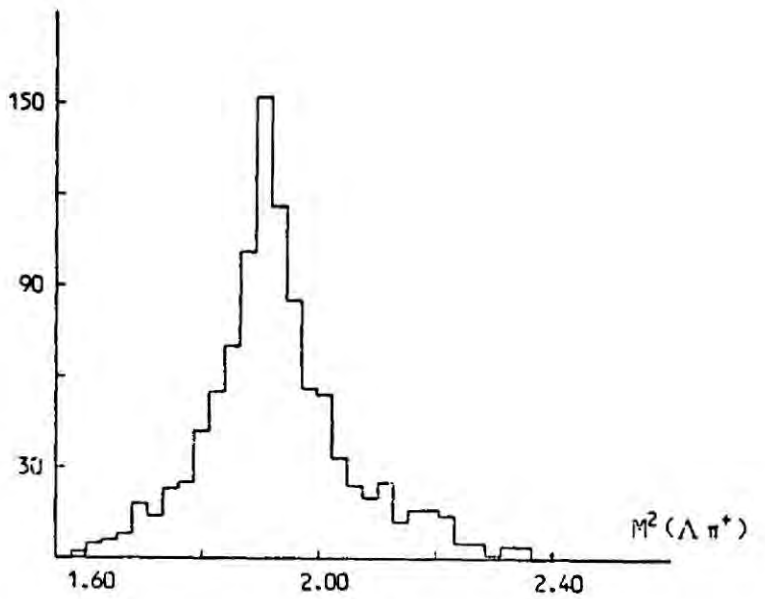

Dalitz Plot for the Reaction $K_L^0 p \rightarrow \Lambda\pi^+\pi^0$

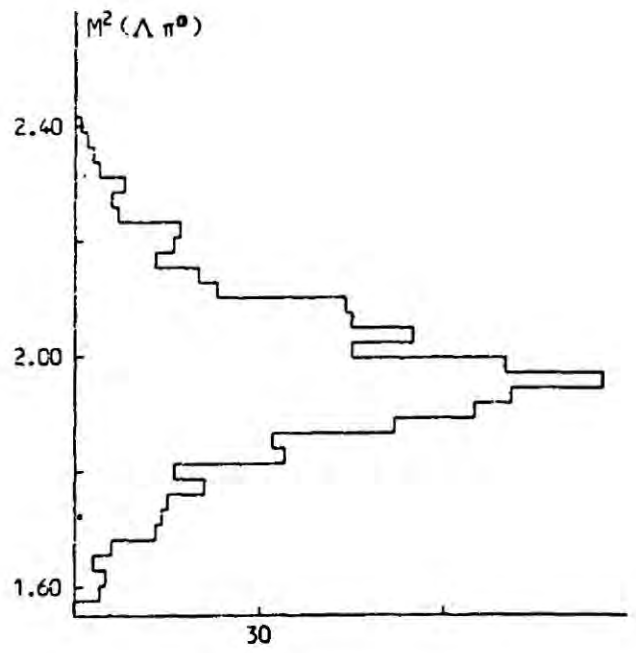

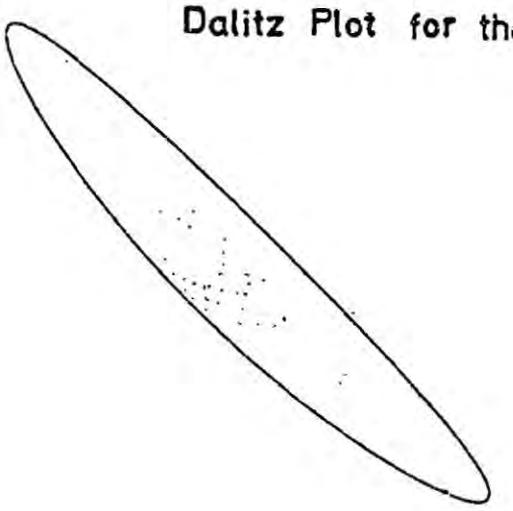

Inc. K^- Momentum = 0.780 GeV/c

$M^2(\Lambda\pi^0)$ .V. $M^2(\Lambda\pi^+)$

in $(GeV/c^2)^2$

816 Events

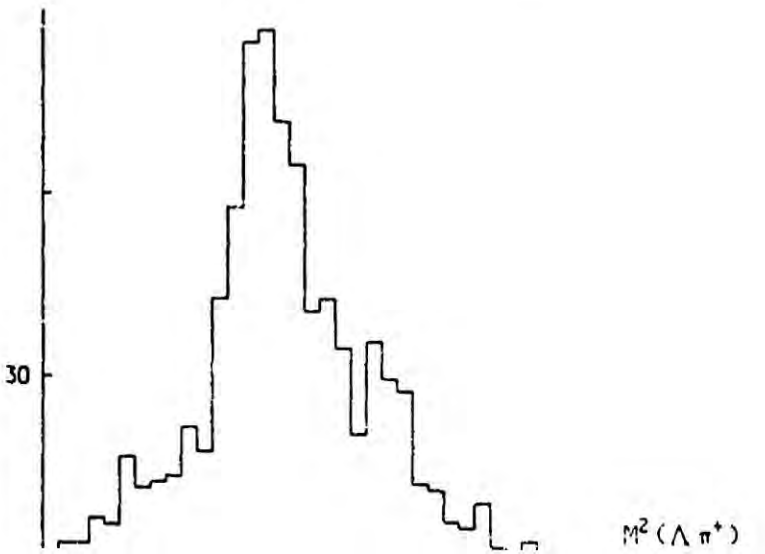

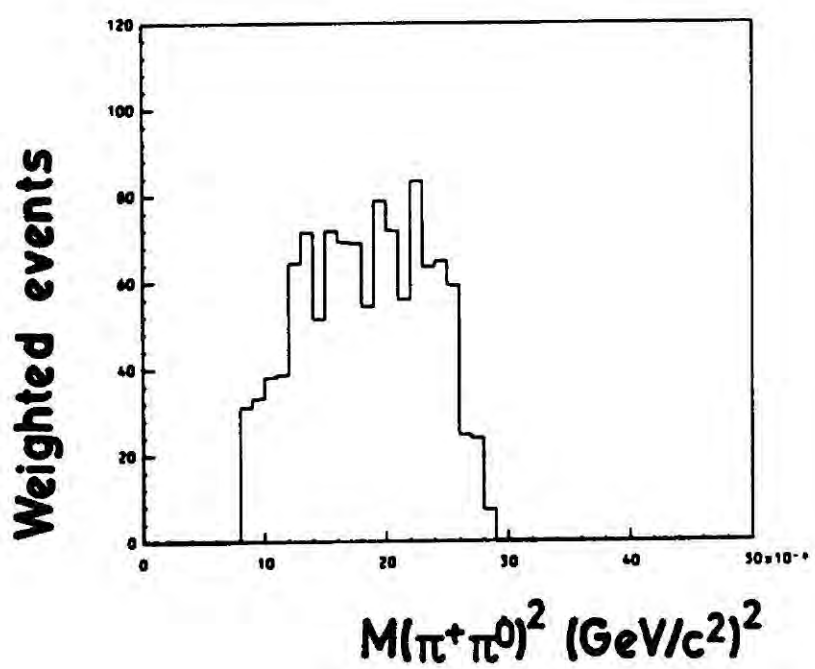

Distribution of $M^2(\pi^+\pi^-)$ for Events Fitting the Reaction $K_L^0 p \rightarrow \Lambda\pi^+\pi^0$

Figure 5.2 : Distributions of $M^2(\pi^+\pi^0)$ for events in the 0.740 to 0.750 GeV/c interval.

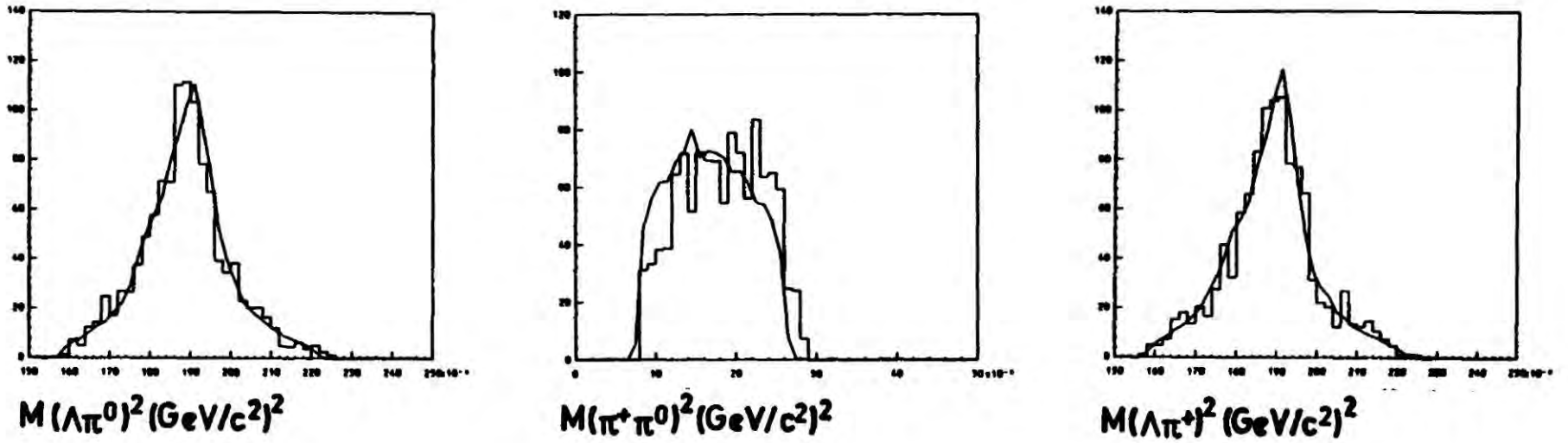

Figure 5.3 : Fit to the quasi-two-body variables of the $\Lambda\pi^+\pi^o$ final state allowing only $\pi\Sigma(1385)$ channels to contribute.

5.3 PARAMETERS OF THE 'ε' CONTRIBUTION

Having found evidence that the final state dynamics in the $\pi^+\pi^-$ system is substantially isoscalar in nature, a paramatrization of this effect is required to account for the quasi two-body variables of the $\Lambda\,\pi^+\pi^-$ final state. A phenomenological framework which permits comparison with previously published work is the effective range approximation. This allows the phase shifts $\delta_J^I(q)$ appearing in the Watson amplitude to contain a dependence on $m(\pi^+\pi^-)$:

$$q^{2J+1}\left[\cot\left(\delta_o^o\right)\right] = \frac{1}{a_o^o} + \frac{1}{2}\,r\,q^2 \qquad (5.7)$$

The isoscalar scattering length a_o^o is measured in units of inverse pion mass, μ^{-1}. A more generally valid expression for δ_o^o is given by the Taylor expansion

$$\delta_o^o = a_o^o\,q + b_o^o\,q^3 + \ldots\ldots \qquad (5.8)$$

The phase shifts paramatrized in this way, together with the Watson amplitude for an s-wave $'\varepsilon'\Lambda$ system, have been used to account for the $\pi^+\pi^-$ effective mass structure. Breit-Wigner forms have been used to describe $\Sigma^+(1385)$ and $\Sigma^-(1385)$ production in $\Lambda\pi^+$ and $\Lambda\pi^-$ effective masses The contributions of $\Sigma(1385)$ production to the $\pi^+\pi^-$ effective mass distribution have been determined by integrating these Breit-Wigner functions over the kinematically accessible ranges of $m^2(\Lambda\,\pi^+)$ and $m^2(\,\Lambda\pi^-)$ for each $m^2(\pi^+\pi^-)$ bin. It was shown in section 4.2 that the available $\pi^+\pi^-$ phase space grows rapidly over the incident momentum range of this experiment. To take account of this fact in the fitting procedure, the integration of $\Sigma(1385)$ contributions over available $\Lambda\pi$ phase space has been performed at each incident momentum represented by the data and the Watson amplitude has been used to weight the distribution of Lorentz invariant phase space

for the $\pi^+\pi^-$ system.

A minimum chi-squared method has been used to fit the corrected number of events in each $m^2(\pi^+\pi^-)$ bin. The free parameters were the total fraction of $\Sigma(1385)$ production present, the fraction of 'ε' contribution and the phase shift constants a_o^o and b_o^o. For the final fit the minimum value of χ^2 was found to be 33.7 for four free parameters 32 fitted $m^2(\pi^+\pi^-)$ bins. The value of a_o^o was found to be consistent with zero $\left[0.0 \pm 0.04\right]$ whilst b_o^o was found to be 0.10 ± 0.04. Figure 5.4 shows the result of the final fit to the data. Terms in the polynomial expansion for $\delta(q)$ (equation 5.8) of order greater than 3 were not used since their inclusion did not appreciablyimprove the quality of the fit to the data.

5.4 DISCUSSION OF $\pi\pi$ INTERACTIONS

In the previous section, the scattering length associated with isoscalar $\pi\pi$ final state interactions was shown to be consistent with zero. This section will be devoted to a discussion of this statement concerning the nature of the low energy $\pi^+\pi^-$ system.

Previous studies of $\pi\pi$ systems have been based mainly on data from two sources :-

(i) The k_4^e decay modes of the k mesons

$$k^+ \rightarrow e^+\nu_e \quad \pi^+\pi^- \tag{5.9}$$

$$k^- \rightarrow e^-\bar{\nu}_e \quad \pi^+\pi^- \tag{5.10}$$

The kinematics of these processes dictates the range of $\pi\pi$ masses studied to be confined to the threshold region $0.280 < m(\pi\pi) < 0.400$ GeV/c^2. Extraction of $\pi\pi$ phase shifts requires the weak interaction effects of the $e\nu_e$ vertex [see Fig.5.5] to be factored using the known V-A nature of the charged weak current. When this has been performed, the only remaining final state dynamics are the strong interactions of the $\pi\pi$ system. An

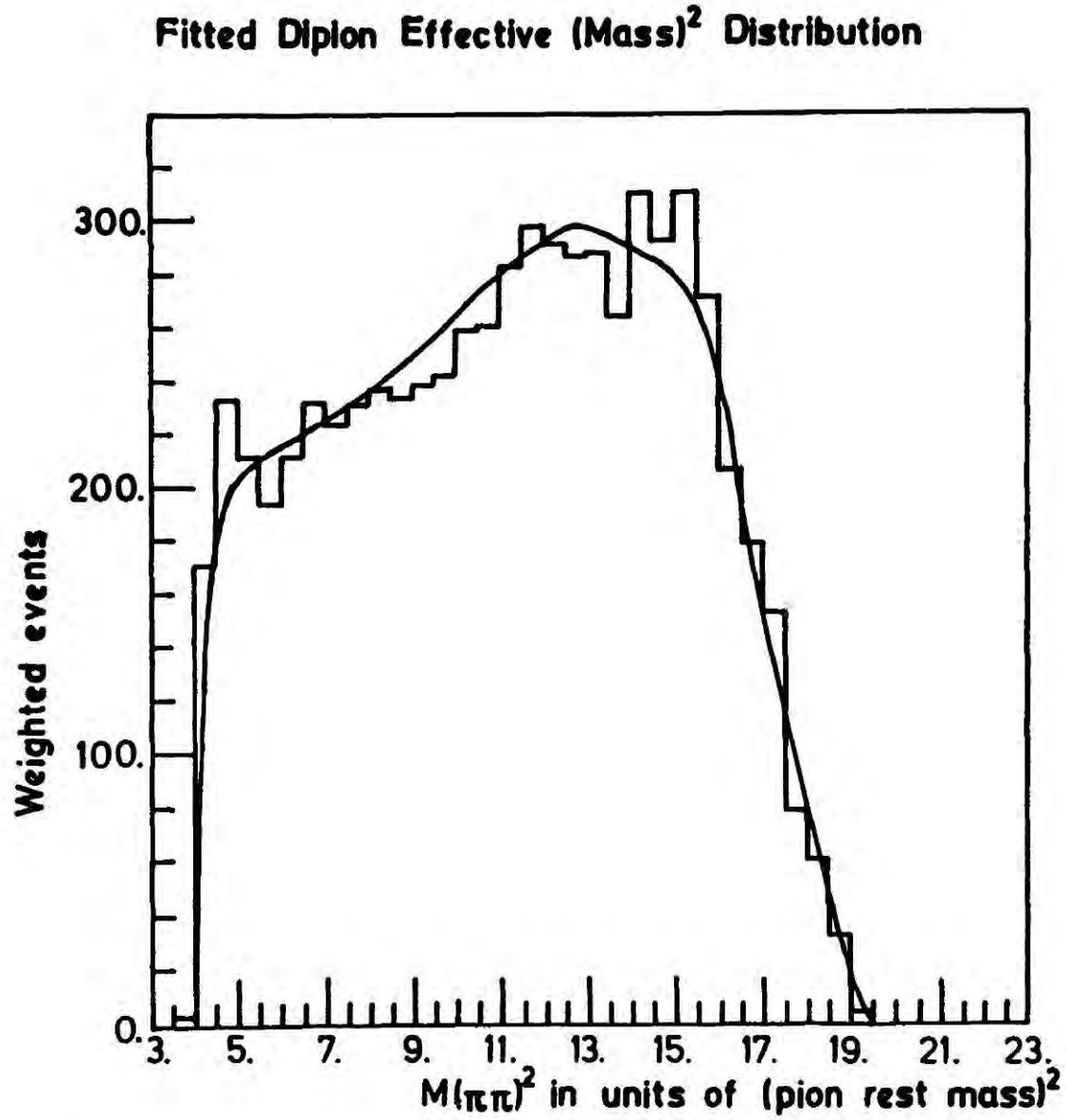

Figure 5.4 : Results of a fit to the $M^2(\pi^+\pi^-)$ distribution for events fitting the reaction $k^- p \to \Lambda\pi^+\pi^-$.

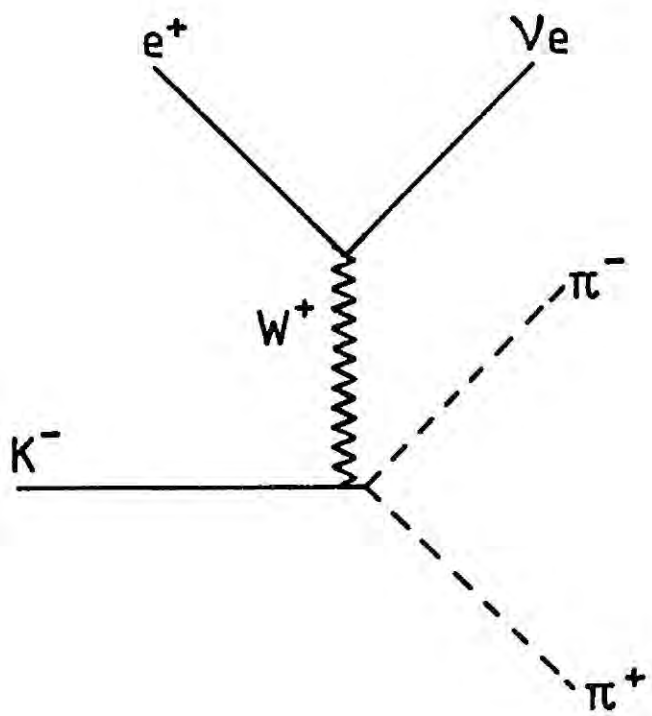

Feynman Diagram for the K_4^e Decay

Figure 5.5 : The k_4^e decay mode.

example of such a study is presented by Zylbersteyn et al in reference 5.8.

(ii) One pion exchange processes explore regions of higher dipion effective mass. Grayer et al [reference 5.9], for example, have studied the $\pi^+\pi^-$ system produced peripherally in the reaction $\pi^- p \rightarrow \pi^+\pi^- n$ at 17 GeV/c incident momentum. The method used to extract $\pi\pi$ phase shift involves extrapolation of the momentum transfer, -t, to the pion mass pole and paramatrizing the angular distribution for decay of the $\pi\pi$ system by expansions of spherical harmonics. Partial wave expansions are then used to relate amplitudes, expressed in terms of phase shifts by the Watson ansatz, to experimentally determined moments of the spherical harmonics.

Analysis of the phase shifts obtained from these experiments indicates that I = J = 1 dynamics is explained entirely by $\rho(770)$ formation with a scattering length $a_1' = 0.039$ [see e.g. Pennington, reference 5.2]. The situation for the I = J = 0 is more complicated. Figure 5.6 shows compilation of $\pi\pi$ isoscalar phase shifts given in the 1978 Particle Data Group Tables [reference 5.5]. Data below 0.4 GeV/c^2 comes from k_4^e decay studies and the data from above 0.5 GeV/c^2 comes from one pion exchange processes. A gap exists in the data between 0.4 GeV/c^2 and 0.5 GeV/c^2. The curves represent fits to the phase shifts by Basdevant [see reference 5.3] using fixed-t dispersion relations. Near threshold, the solutions fall into two categories, the 'up' and 'down' solutions which are illustrated in Figure 5.7. 'Up' solutions are typified by scattering lengths in the region of 0.2, the 'down' solutions have scattering lengths close to zero. Whilst the data above 0.5 GeV/c^2 are compatible with scattering lengths in the range $-0.06 < a_o^o < 0.58$, which accommodates 'up' and 'down' structure, the k_4^e data of Zylbersteyn are only compatible with 'up' solutions.

Phase shifts expected from the values of a_o^o and b_o^o quoted in the previous section are shown in Figure 5.8 and represent a 'down' type solution.

Fits to the I=J=0 $\pi\pi$ phase shift data by Basdevant

Figure 5.6

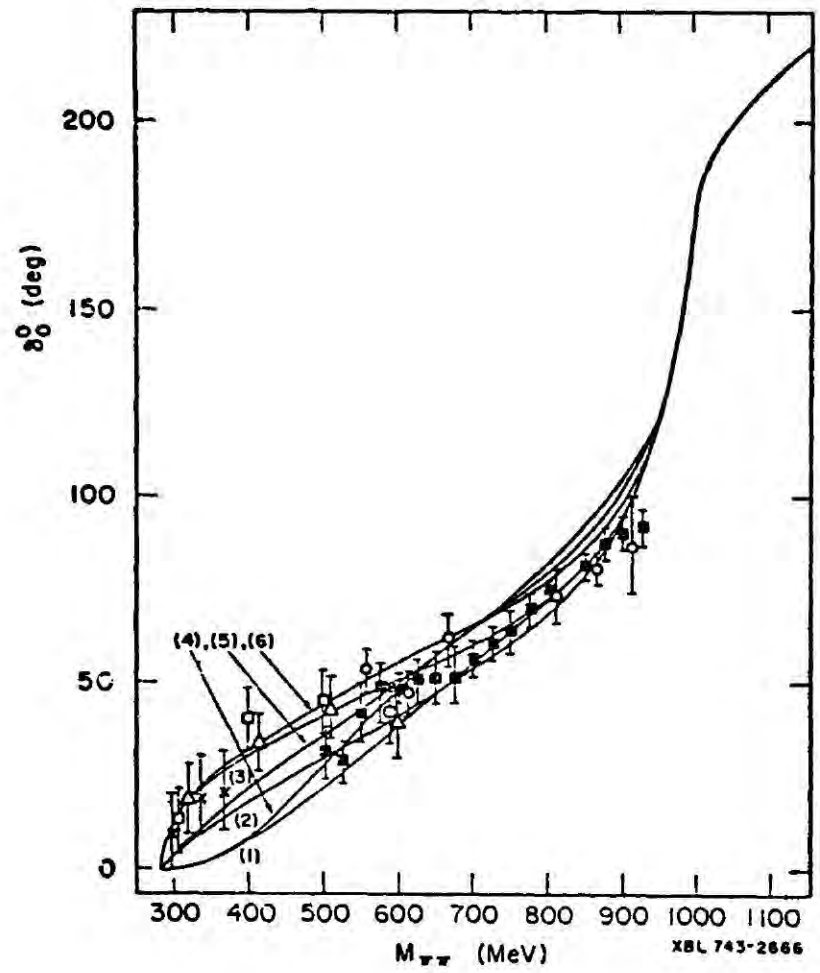

In figures 5.6,5.6b and 5.6c, the fits labelled by 1), 2) and 3) have the following values of a_0^0

1) $a_0^0 = -0.06$

2) $a_0^0 = 0.16$

3) $a_0^0 = 0.58$

Figure 5.6a is taken from the 1978 Particle Data Group Tables, figures 5.6b and 5.6c are taken from Basdevant (reference 5.3). The data shown in figure 5.6b is that of Baton et al (phys. Letts 33B(1970)525), the data shown in figure 5.6c is that of Zylbersteyn (reference 5.8).

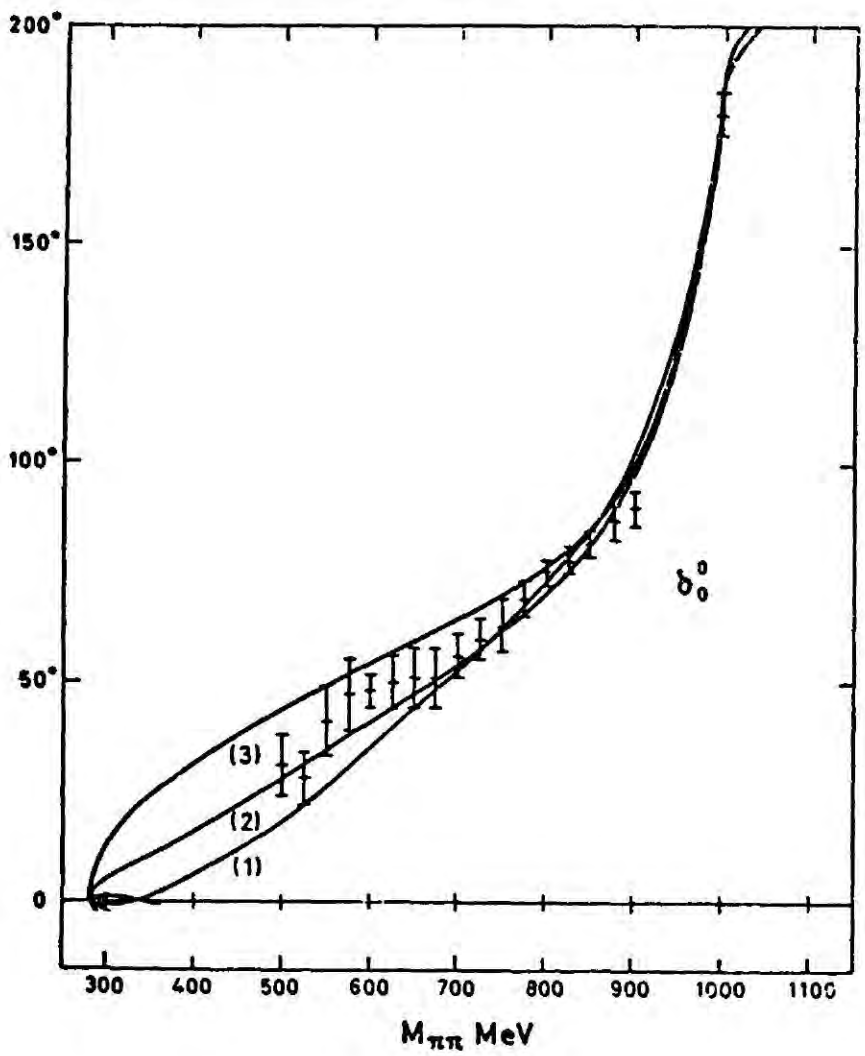

Figure 5.6b

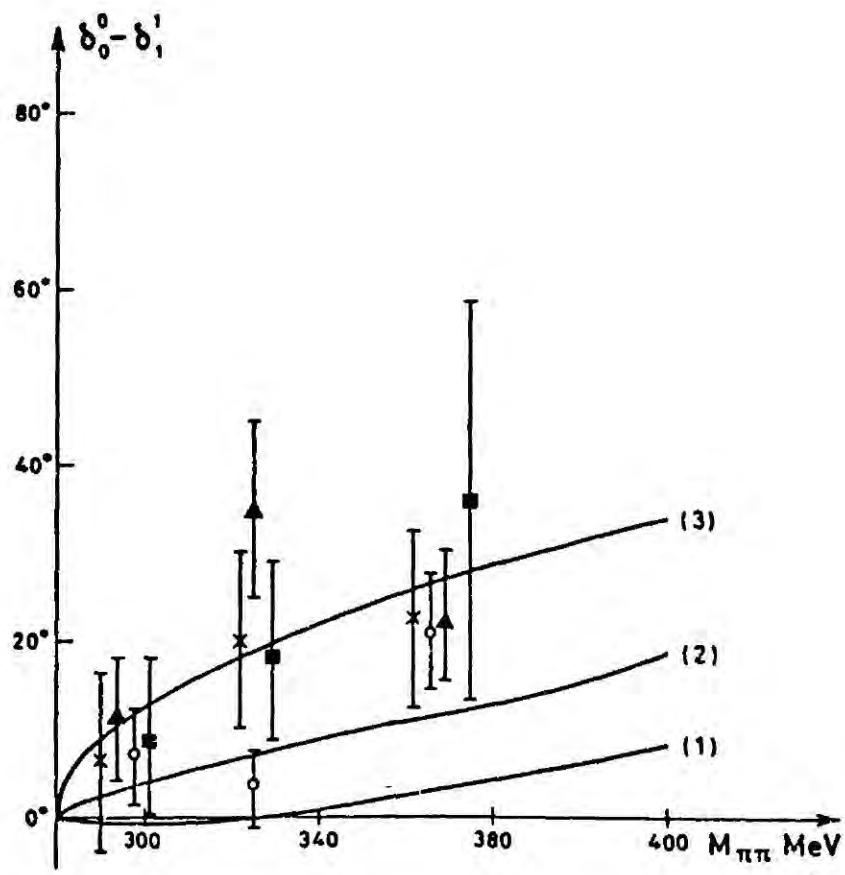

Figure 5.6c

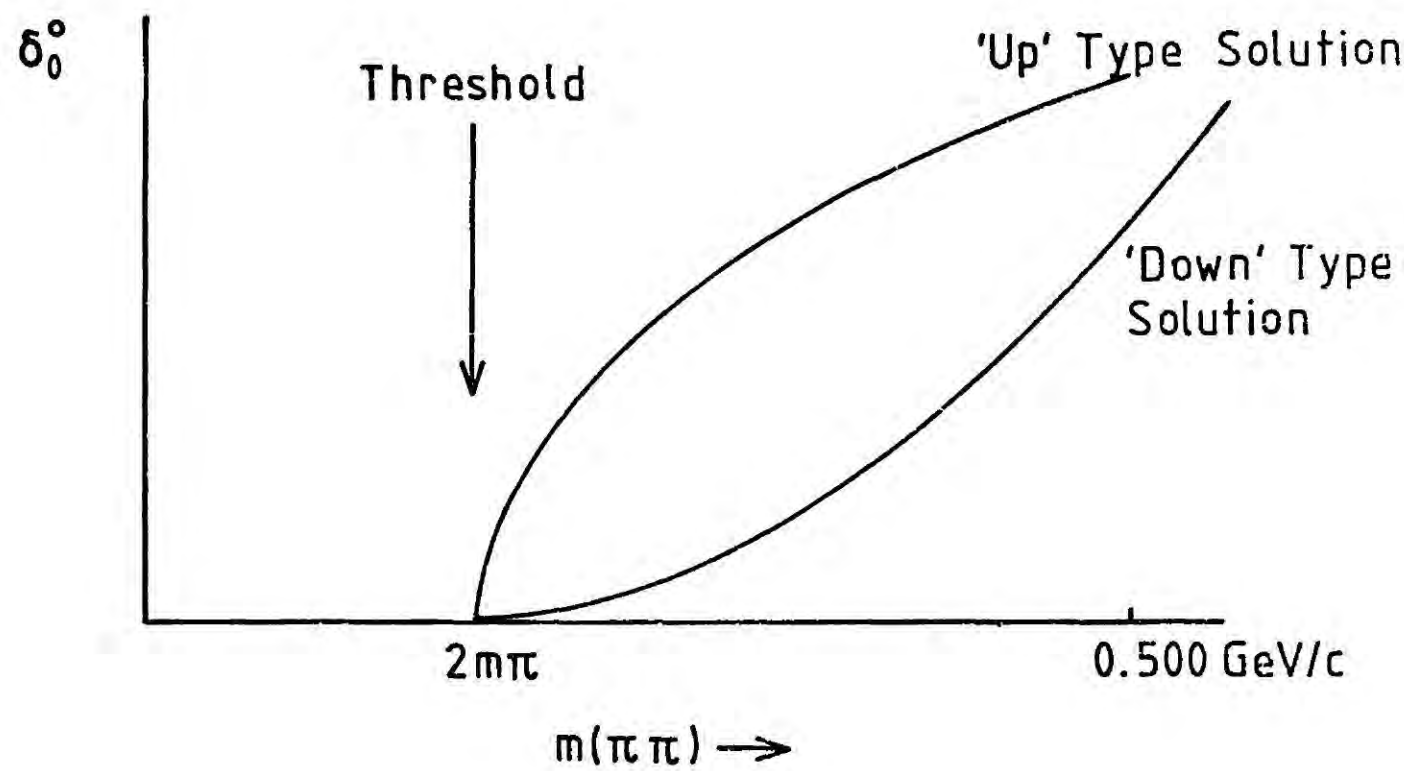

Phase Shift for 'Up' and 'Down' Solutions

Figure 5.7 : Phase shifts for 'Up' and 'Down' Solutions.

Fig. 5.8 : The $I=J=0$ $\pi\pi$ Phase Shifts Deduced From the Fitted Form of the Watson Amplitude

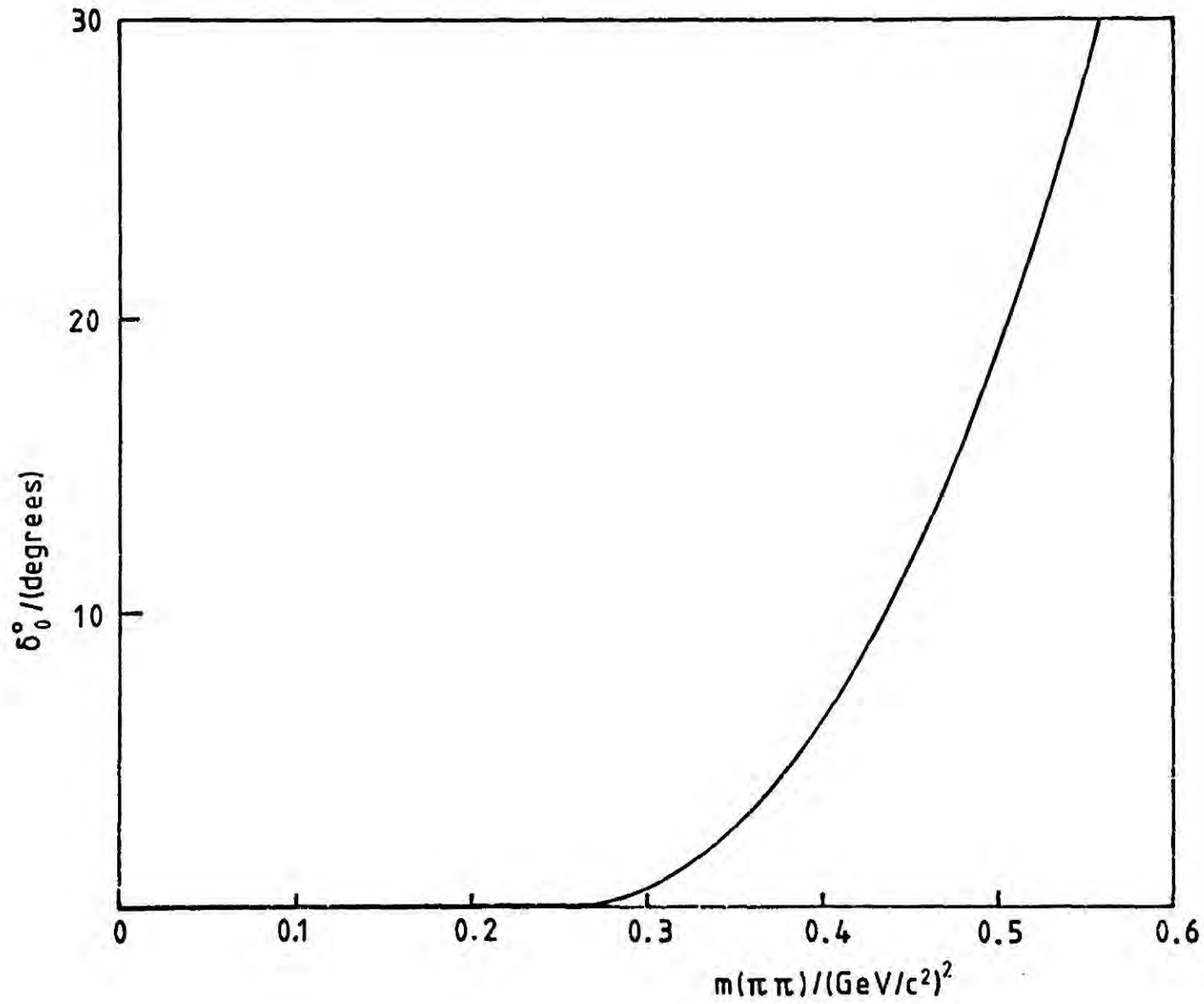

Similar conclusions have been reached by Jones et al [reference 5.10] concerning the nature of final state $\pi\pi$ interactions in the reaction $\pi^- p \rightarrow \pi^+ \pi^- n$ at 0.415 GeV/c incident momentum. As such this reaction is analogous to the reaction $\bar{k} N \rightarrow \Lambda\pi\pi$, being dominated by the formation of $\pi\Delta(1236)$ isobars, the $\Delta(1236)$ having $J^p = 3/2^+$. No significant structure is seen in the $\pi^- \pi^o$ effective mass for the reaction $\pi^- p \rightarrow \pi^- \pi^o p$ and the high $\pi^+ \pi^-$ mass enhancement seen in the $\pi^+ \pi^- n$ final state is deduced to be isoscalar in origin. Scattering lengths in the range $-0.06 < a_o^o < 0.03$, which represent down type solutions, are quoted. Both Arndt et al [reference 5.11] and the SLAC-L.B.L. isobar analyses [reference 5.12] of the $\pi N \rightarrow \pi\pi N$ reactions agree that εN production is important near threshold, the dominant s-channel partial wave amplitude being the PS11.

It therefore seems evident that the $\pi^+ \pi^-$ systems produced in the reactions $k^- p \rightarrow \Lambda \pi^+ \pi^-$ and $\pi^- p \rightarrow \pi^+ \pi^- n$ are dominated by very similar isoscalar final state interactions, which are non-resonant, in the $\pi^+ \pi^-$ system. The treatment of final state interactions using the Watson amplitudes requires that they be narrow and resonant in nature. Since this is clearly not the case for the 'ε' $\pi\pi$ s-wave, there is no validity in assuming that the description found for $\pi\pi$ phase shifts should be identical with those from k_4^e and one pion exchange processes. However, the origin of the 'ε' effect is not the primary objective of this thesis, the paramatrizations willbe used to give complete account of quasi two-body variables for the $\Lambda \pi^+ \pi^-$ final state and extract $\pi\, \Sigma(1385)$ contributions.

5.5 FORMULATION OF THE 'ε' EFFECT IN TERMS OF QUASI-TWO BODY VARIABLES

In order to extract the $\pi^+ \Sigma^-(1385)$, $\pi^- \Sigma^+(1385)$ and 'ε' Λ quasi two-body final states from the reaction $k^- p \rightarrow \Lambda \pi^+ \pi^-$, the paramatrization of isoscalar $\pi^+ \pi^-$ dynamics must be incorporated into the density function $F(\vec{x})$ given by equation 3.23. This is defined as a sum of channel density

functions for each contributing quasi two-body process :-

$$F(\vec{x}) = \sum_{j=1} \alpha_j f_j(\vec{x}) \tag{5.11}$$

where $$f_j(\vec{x}) = \frac{1}{Z_j} B(m_j^2)\, W(\Theta,\phi,\Theta^*) \tag{5.12}$$

For the $\pi\Sigma(1385)$ processes, $B(m_j^2)$ is a Breit-Wigner of the $\Lambda\pi$ effective masses and $W(\Theta,\phi,\Theta^*)$ is a joint angular distribution for production and decay of the $\Sigma(1385)$ quasi two-body system. To modify $f_j(\vec{x})$ to describe 'ε' production, given in terms of the Watson amplitude, the following features are noted :-

(i) The 'ε' decay angular distribution is isotropic

$$W(\Theta,\phi) = \frac{1}{4\pi} \tag{5.13}$$

(ii) Since only s-wave 'ε' Λ final states were included in the Watson amplitude which was fitted to the $\pi^+\pi^-$ effective mass distribution, the only admissible s-channel partial wave amplitude is PSOl. If the production angular distribution is paramatrized by :-

$$\frac{d\sigma}{d\Omega} = 2\pi\lambda^2 \sum_{\ell=o} A_\ell P_\ell(\cos\Theta^*) \tag{5.14}$$

Equation 3.9 leads one to expect an isotropic angular distribution for production of the 'ε' system and only Ao is non-vanishing.

(iii) The Breit-Wigner function $B(m_j^2)$ must be replaced by the

Watson amplitude

$$\left|T_\varepsilon\right|^2 = \frac{1}{q^2} \cdot \sin^2 \left[\delta_J^I (q) \right] \qquad (5.15)$$

subject to the correct normalization.

The complete channel density function can now be written :-

$$f_{\pi\pi} (m(\pi\pi), \cos\Theta^*, \Theta, \phi) = \frac{1}{Z} \cdot \frac{1}{4\pi} \left|T_\varepsilon\right|^2 \qquad (5.16)$$

and the normalization condition

$$1 = \int f_{\pi\pi} (\vec{x}) \, d\, p \, H \qquad (5.17)$$

gives

$$Z = \int_{4\mu 2}^{(\sqrt{s}-m_\wedge)^2} d\, m^2(\pi\pi) \left| T_\varepsilon \right|^2 \frac{p}{4\sqrt{s}} \cdot \frac{q}{4m(\pi\pi)} \qquad (5.18)$$

5.6 RESULTS OF QUASI-TWO BODY ANALYSIS

The Dalitz plot density was refitted including the 'ε' effect using program EXTRA. Free parameters used were the fraction of 'ε' Λ, $\pi^+\Sigma^-$ (1385) and $\pi^-\Sigma^+$ (1385) channels present and the coefficients A_ℓ, B_ℓ C_ℓ and D_ℓ for the $\pi\Sigma$ (1385) production angular distributions. To decide the maximum order for ℓ in equation 3.18, fits were attempted with various values of cut-offs until the highest coefficient was found to be consistent with zero for $\pi^+\Sigma^-$(1385) and $\pi^-\Sigma^+$(1385) channels at all energies. The maximum order of expansion chosen was 5.

Figure 5.9 shows the refitted set of quasi two-body variables for events in the 0.820 to 0.840 GeV/c incident momentum bin. Two features are evident on comparison with the previous fit to the data, which does not contain

Results of Quasi Two Body Analysis for $k^-p \rightarrow \Lambda\pi^+\pi^-$ at 0.830 GeV/c Incident Momentum

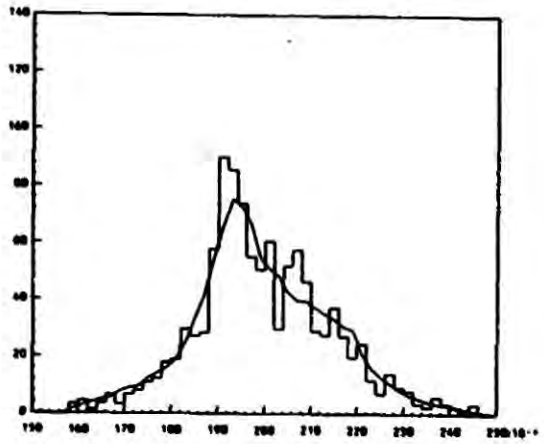

$M(\Lambda\pi^-)^2$ $(GeV/c^2)^2$

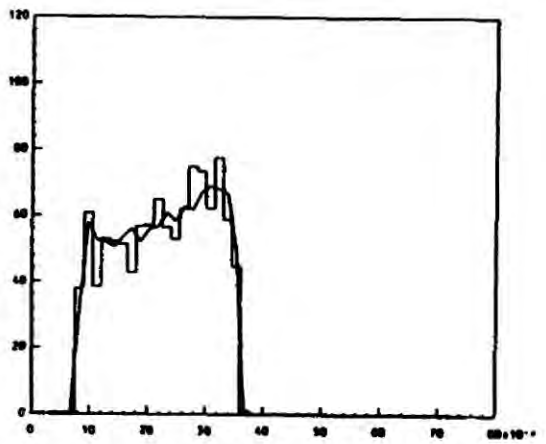

$M(\pi^+\pi^-)^2$ $(GeV/c^2)^2$

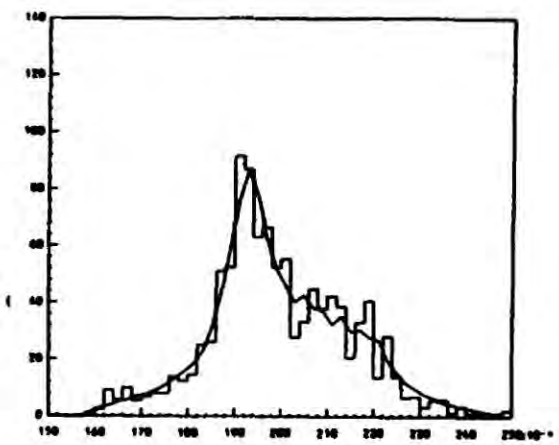

$M(\Lambda\pi^+)^2$ $(GeV/c^2)^2$

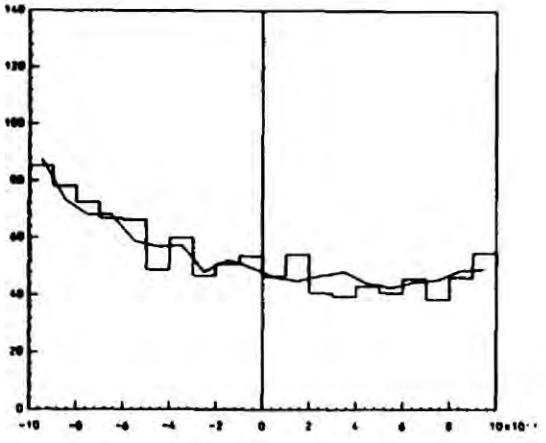

Cos θ for $\Lambda\pi^-$ system

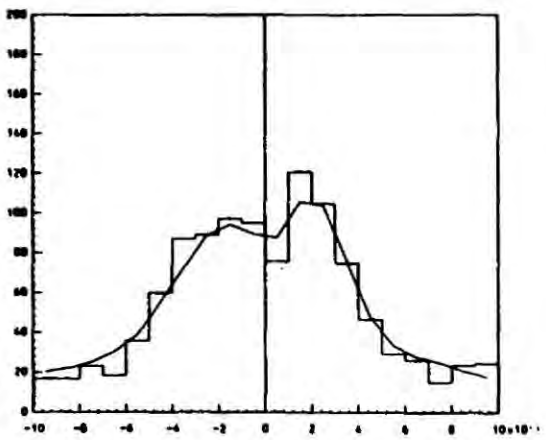

Cos θ for $\pi^+\pi^-$ system

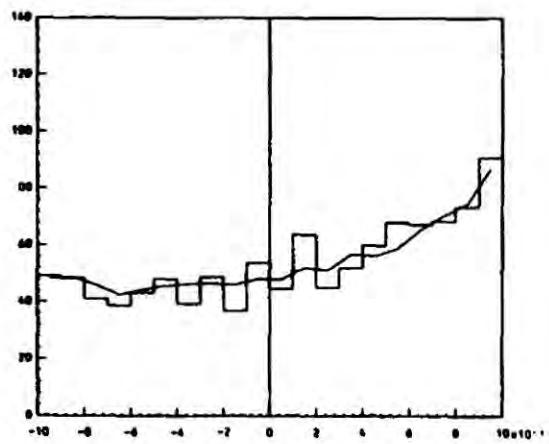

Cos θ for $\Lambda\pi^+$ system

Figure 5.9 : Quasi-two body analysis of the reaction $k^-p \rightarrow \Lambda\pi^+\pi^-$, including the 'ε'Λ channel, in the 0.830 GeV/c incident momentum bin.

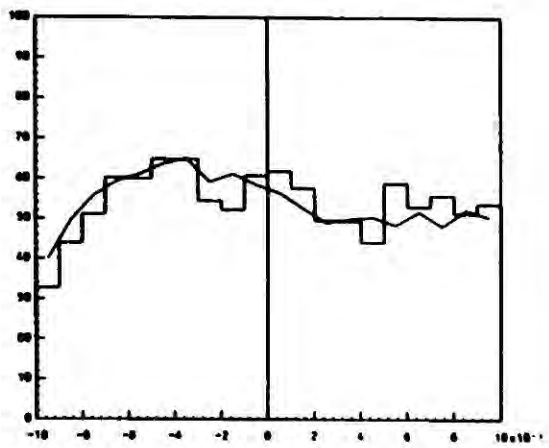

Cos θ* for $\Lambda\pi^-$ system

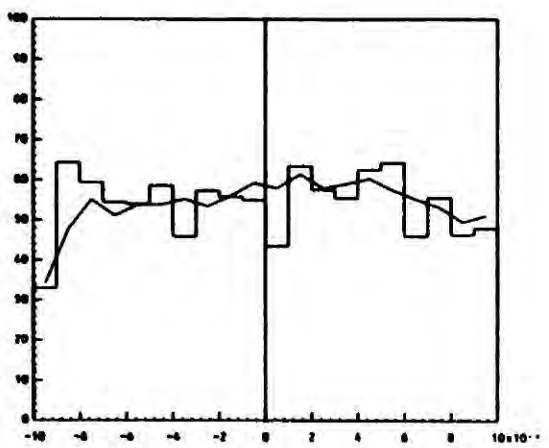

Cos θ* for $\pi^+\pi^-$ system

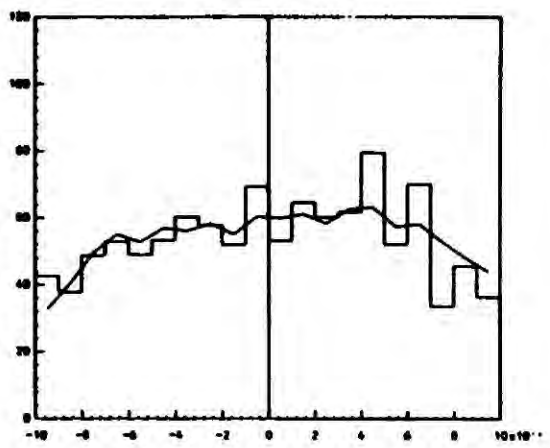

Cos θ* for $\Lambda\pi^+$ system

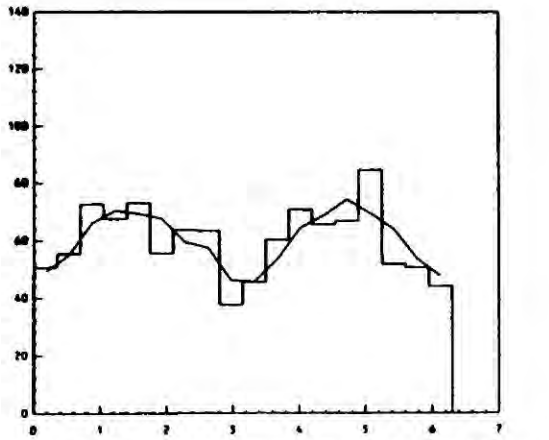

Φ for $\Lambda\pi^-$ system (radians)

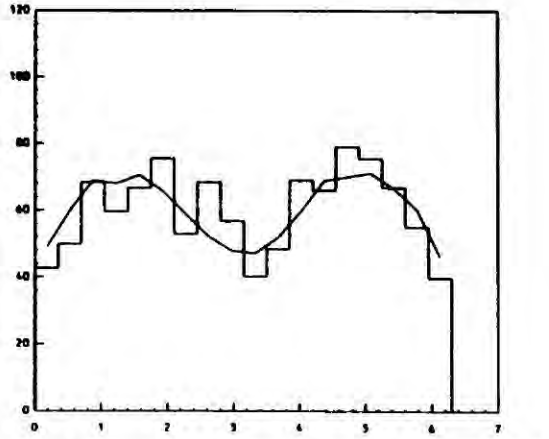

Φ for $\pi^+\pi^-$ system (radians)

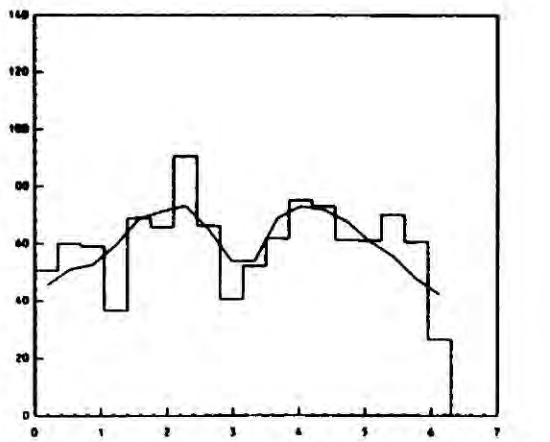

Φ for $\Lambda\pi^+$ system (radians)

Figure 5.9 (Cont'd).

the ε effect [figure 4.5].

(i) A good acount of the $\pi^+\pi^-$ system effective mass is given. The previous fit to the data had a χ^2 value of 69.5 for 28 histogram bins fitted whilst inclusion of the ε effect reduced this value to 40.1.

(ii) The peaking of cosΘ distribution for the $\Lambda\pi^-$ system at -1.0 and the $\Lambda\pi^+$system at + 1.0 are now well described. The improvements in fitted quantities are summarized in Table 5.1.

The stability of the A, B, C and D coefficients to the form taken for the isoscalar $\pi^+\pi^-$ dynamics has been investigated by comparing the results with and without the inclusion of the ε effect. Table 5.2 gives the values of the coefficients obtained for the $\pi^+\Sigma^-$ (1385) final state in the 0.840 to 0.860 GeV/c incident momentum bin. Clearly, the two sets of coefficients agree well within the errors of determination.

Values of the A, B, C and D coefficients found, together with the errors of determination are given in Table 5.3 for πΣ (1385) channels. Correlations exist between the errors in determination for the coefficients and the channel fractions. Errors in coefficients are calculated assuming that the channel fractions are known exactly ; this is clearly not the case. B. Franek has performed Monte-Carlo investigations which indicate that the coefficient errors from EXTRA need to be scaled by a factor of 1.5 [ref. 5.13] . The features of this data for the πΣ (1385) channels will be discussed in the next chapter.

Fractions of the various channels extracted from the ππΛ final state, together with the cross-section for the reaction $k^-p \rightarrow \pi^+\pi^-\Lambda$, as a function of momentum are given in Table 5.4. The fraction of 'ε'Λ present grows throughout the momentum interval and accounts for between 10% and 20% of the Dalitz plot density. T.S.T. data available in the 0.500 to 0.580 GeV/c range has also been analysed in terms of quasi two-body variables. Results of an extraction of πΣ (1385) and ε Λ channels

System	χ^2 per 20 histogram bins with ε	χ^2 per 20 histogram bins without ε
$\Lambda\pi^+$	10.73	38.4
$\Lambda\pi^-$	9.76	36.9

TABLE 5.1 : Improvement in fitted cosθ distributions due to inclusion of the 'ε'Λ channel.

	A_1	A_2	A_3	A_4
With ε	- .084	- .467	.321	0.028
Without ε	- .102	- .444	.304	0.054
Error	$\pm$0.06	$\pm$ .220	$\pm$ .100	$\pm$ 0.110
	B_1	B_2	B_3	B_4
With ε	-.144	-0.056	0.250	- 0.184
Without ε	-.145	-0.032	0.219	- 0.139
Error	$\pm$0.037	$\pm$0.051	$\pm$0.063	$\pm$ 0.073
	C_1	C_2	C_3	C_4
With ε	.194	-0.0176	-0.075	-0.007
Without ε	.181	-0.0210	-0.066	-0.007
Error	$\pm$0.03	$\pm$0.019	$\pm$0.016	$\pm$0.014
		D_2	D_3	D_4
With ε		0.029	-0.003	0.003
Without ε		0.018	0.002	0.004
Error		$\pm$0.012	$\pm$0.006	$\pm$0.004

TABLE 5.2 : Effect on coefficients of ε Λ contribution

INCIDENT MOMENTUM (GEV/C)	A0	A1/A0	A2/A0	A3/A0	A4/A0	A5/A0
0.7300	0.7780	-.3926	-.3207	-.0901	-.3514	0.2900
	+/-0.0380	+/-0.1530	+/-0.1905	+/-0.2216	+/-0.2679	+/-0.2982
0.7500	0.6917	0.6688	-.1615	-.1839	-.0180	0.4694
	+/-0.0220	+/-0.0895	+/-0.1257	+/-0.1537	+/-0.1745	+/-0.1899
0.7700	0.7588	0.5022	-.3162	0.0771	-.1882	0.1237
	+/-0.0240	+/-0.0859	+/-0.1135	+/-0.1350	+/-0.1556	+/-0.1758
0.7900	0.8078	0.3875	-.3046	0.2106	-.1320	0.0111
	+/-0.0300	+/-0.0892	+/-0.1173	+/-0.1374	+/-0.1600	+/-0.1803
0.8100	0.8672	0.0567	-.4058	0.1373	-.1368	0.2122
	+/-0.0340	+/-0.0929	+/-0.1188	+/-0.1458	+/-0.1598	+/-0.1824
0.8300	0.8334	-.1146	-.2998	0.5024	-.1375	-.1534
	+/-0.0300	+/-0.0963	+/-0.1249	+/-0.1440	+/-0.1685	+/-0.1812
0.8500	0.8383	-.0842	-.4668	0.3211	0.0286	-.0797
	+/-0.0330	+/-0.0945	+/-0.1267	+/-0.1553	+/-0.1780	+/-0.1871
0.8700	0.8581	-.2544	-.3258	0.1873	-.4197	0.1261
	+/-0.0625	+/-0.0912	+/-0.1150	+/-0.1314	+/-0.1571	+/-0.1755
0.9100	1.0320	0.0578	-.1659	0.4787	-.1716	-.0478
	+/-0.0464	+/-0.0551	+/-0.0705	+/-0.0899	+/-0.0940	+/-0.1058
0.9500	1.1836	-.0013	-.3082	0.2761	-.3206	-.0489
	+/-0.0282	+/-0.0271	+/-0.0353	+/-0.0417	+/-0.0475	+/-0.0506
0.9600	1.0442	-.1056	-.1481	0.3890	-.6014	-.0942
	+/-0.0481	+/-0.0807	+/-0.0944	+/-0.1222	+/-0.1330	+/-0.1468
0.9900	1.0519	0.1478	-.3888	0.2185	-.4135	-.4004
	+/-0.0729	+/-0.0798	+/-0.1032	+/-0.1232	+/-0.1440	+/-0.1600
1.0050	1.1269	0.1387	-.0598	0.2193	-.3816	-.1422
	+/-0.0552	+/-0.0864	+/-0.1059	+/-0.1258	+/-0.1423	+/-0.1630
1.0450	1.2313	0.3065	0.2995	0.4251	-.3005	-.5053
	+/-0.0486	+/-0.0742	+/-0.0903	+/-0.1076	+/-0.1250	+/-0.1380
1.0850	1.2006	0.5524	0.3102	0.2218	-.4153	-.0735
	+/-0.0503	+/-0.0762	+/-0.0930	+/-0.1136	+/-0.1289	+/-0.1422
1.1250	1.1687	0.5639	0.3617	-.0549	-.4196	-.1283
	+/-0.0464	+/-0.0764	+/-0.0928	+/-0.1115	+/-0.1244	+/-0.1400
1.1650	1.0756	0.6068	0.2405	0.1002	-.4186	-.4005
	+/-0.0418	+/-0.0718	+/-0.0884	+/-0.1061	+/-0.1207	+/-0.1343
1.2050	1.0440	0.7663	0.2596	-.2529	-.4454	-.2768
	+/-0.0423	+/-0.0719	+/-0.0895	+/-0.1077	+/-0.1231	+/-0.1344
1.2450	0.9576	0.7353	0.2739	-.0437	-.5835	-.3511
	+/-0.0351	+/-0.0692	+/-0.0835	+/-0.0996	+/-0.1137	+/-0.1259
1.2850	0.8733	0.8205	0.2977	-.1335	-.5874	-.2036
	+/-0.0310	+/-0.0695	+/-0.0844	+/-0.1040	+/-0.1168	+/-0.1333
1.3200	0.8543	0.8200	0.7538	-.0892	-.7371	-.3683
	+/-0.0345	+/-0.0860	+/-0.0972	+/-0.1147	+/-0.1323	+/-0.1511
1.3550	0.8648	0.8146	1.3808	0.4460	-.3764	-.3162
	+/-0.0725	+/-0.2184	+/-0.2483	+/-0.2891	+/-0.3256	+/-0.3572
1.4620	0.7889	0.6881	0.9451	-.0225	-.6582	-.2120
	+/-0.0351	+/-0.1146	+/-0.1278	+/-0.1529	+/-0.1797	+/-0.2017
1.5140	0.6248	0.6070	0.7688	0.2139	-.7844	0.2005
	+/-0.0380	+/-0.1561	+/-0.1750	+/-0.2086	+/-0.2535	+/-0.2915
1.5460	0.6591	0.5553	1.0631	-.0624	-.8264	-.1791
	+/-0.0351	+/-0.1394	+/-0.1485	+/-0.1743	+/-0.2109	+/-0.2424
1.6060	0.6638	0.6903	1.2575	0.7788	0.0398	0.5611
	+/-0.0482	+/-0.2000	+/-0.2424	+/-0.2718	+/-0.3312	+/-0.3639
1.6530	0.5136	0.8463	1.2119	0.7375	-.2934	-.1164
	+/-0.0279	+/-0.1543	+/-0.1819	+/-0.2021	+/-0.2394	+/-0.2764
1.7050	0.4939	0.5704	0.9986	0.8278	-.0521	-.4297
	+/-0.0346	+/-0.1968	+/-0.2384	+/-0.2739	+/-0.3274	+/-0.3548
1.7410	0.4326	0.8878	1.3121	0.9783	0.0332	-.2278
	+/-0.0303	+/-0.2106	+/-0.2612	+/-0.2874	+/-0.3235	+/-0.3567
1.8000	0.3174	0.9312	1.3128	0.9290	-.4108	-.7936
	+/-0.0295	+/-0.2745	+/-0.3193	+/-0.3523	+/-0.4453	+/-0.5233
1.8430	0.2577	0.5470	1.3137	0.6795	0.4231	0.5493
	+/-0.0249	+/-0.2963	+/-0.3792	+/-0.4413	+/-0.4775	+/-0.5411

TABLE 5.3a: Coefficient data for the quasi-two body process $k^- p \to \pi^+ \Sigma^-(1385)$

INCIDENT MOMENTUM (GEV/C)	B0/A0	B1/A0	B2/A0	B3/A0	B4/A0	B5/A0
0.7300	0.2320	0.0126	-.3561	-.0635	0.0726	0.1029
	+/-0.0566	+/-0.0926	+/-0.1129	+/-0.1380	+/-0.1673	+/-0.1877
0.7500	0.2245	0.0940	-.0406	0.1295	0.1332	0.1532
	+/-0.0319	+/-0.0579	+/-0.0768	+/-0.0937	+/-0.1060	+/-0.1158
0.7700	0.2927	0.1355	-.0127	0.0504	-.1420	0.1027
	+/-0.0309	+/-0.0554	+/-0.0706	+/-0.0846	+/-0.0968	+/-0.1083
0.7900	0.3045	0.0315	-.2009	0.1048	-.0779	-.1385
	+/-0.0309	+/-0.0534	+/-0.0694	+/-0.0829	+/-0.0952	+/-0.1092
0.8100	0.2606	-.0483	-.1349	-.0089	-.0874	0.0885
	+/-0.0344	+/-0.0556	+/-0.0726	+/-0.0879	+/-0.0958	+/-0.1101
0.8300	0.1557	-.1401	-.1432	0.2904	-.2183	0.0228
	+/-0.0353	+/-0.0587	+/-0.0741	+/-0.0872	+/-0.1006	+/-0.1071
0.8500	0.1746	-.1433	-.0561	0.2528	-.1835	-.0209
	+/-0.0366	+/-0.0576	+/-0.0775	+/-0.0945	+/-0.1093	+/-0.1194
0.8700	0.2372	-.2734	-.1058	0.2600	-.0883	-.1022
	+/-0.0399	+/-0.0584	+/-0.0665	+/-0.0779	+/-0.0914	+/-0.1041
0.9100	0.1897	-.2229	-.0499	0.2491	-.1912	0.0187
	+/-0.0222	+/-0.0337	+/-0.0403	+/-0.0495	+/-0.0542	+/-0.0596
0.9500	0.2359	-.2091	-.0844	0.1466	-.0983	0.0414
	+/-0.0126	+/-0.0173	+/-0.0207	+/-0.0253	+/-0.0281	+/-0.0310
0.9600	0.2642	-.1936	-.1020	0.2011	-.2455	-.0505
	+/-0.0286	+/-0.0480	+/-0.0566	+/-0.0757	+/-0.0835	+/-0.0900
0.9900	0.2313	-.2509	-.2074	0.1943	-.0683	-.0394
	+/-0.0375	+/-0.0542	+/-0.0635	+/-0.0785	+/-0.0905	+/-0.1052
1.0050	0.2940	-.1623	-.2114	0.0847	-.1591	0.0795
	+/-0.0300	+/-0.0529	+/-0.0647	+/-0.0770	+/-0.0867	+/-0.0991
1.0450	0.2519	-.0588	-.0789	0.1271	-.0295	-.1680
	+/-0.0237	+/-0.0448	+/-0.0550	+/-0.0661	+/-0.0755	+/-0.0837
1.0850	0.2059	-.0376	-.1758	0.0176	0.0235	0.1876
	+/-0.0251	+/-0.0473	+/-0.0561	+/-0.0679	+/-0.0773	+/-0.0843
1.1250	0.2265	-.1126	-.1028	-.0560	0.0535	0.0988
	+/-0.0253	+/-0.0487	+/-0.0593	+/-0.0702	+/-0.0783	+/-0.0873
1.1650	0.2693	-.0301	-.2411	-.0908	0.0172	-.0006
	+/-0.0240	+/-0.0452	+/-0.0547	+/-0.0653	+/-0.0746	+/-0.0833
1.2050	0.2726	0.0699	-.1344	-.1834	-.0572	-.1197
	+/-0.0243	+/-0.0465	+/-0.0553	+/-0.0669	+/-0.0770	+/-0.0834
1.2450	0.2350	0.1028	-.1047	-.1142	-.0847	-.1318
	+/-0.0231	+/-0.0438	+/-0.0504	+/-0.0609	+/-0.0713	+/-0.0776
1.2850	0.2301	0.1423	-.0818	-.1354	-.1304	-.0696
	+/-0.0235	+/-0.0434	+/-0.0505	+/-0.0619	+/-0.0710	+/-0.0799
1.3200	0.2236	0.0948	-.0533	-.0752	-.1677	-.1060
	+/-0.0263	+/-0.0539	+/-0.0603	+/-0.0687	+/-0.0815	+/-0.0913
1.3550	0.2433	-.0984	0.2332	0.0635	-.3077	-.1083
	+/-0.0581	+/-0.1334	+/-0.1548	+/-0.1712	+/-0.1927	+/-0.2132
1.4620	0.2975	0.1806	0.0935	-.0955	-.2449	-.2154
	+/-0.0333	+/-0.0721	+/-0.0808	+/-0.0929	+/-0.1099	+/-0.1224
1.5140	0.3281	0.0570	0.0596	-.0282	-.3695	0.0477
	+/-0.0458	+/-0.0981	+/-0.1075	+/-0.1248	+/-0.1532	+/-0.1746
1.5460	0.3454	0.0657	0.2574	-.0425	-.3852	0.0593
	+/-0.0400	+/-0.0901	+/-0.0981	+/-0.1110	+/-0.1359	+/-0.1556
1.6060	0.3346	0.1587	0.3371	0.2362	0.0248	0.2132
	+/-0.0518	+/-0.1204	+/-0.1445	+/-0.1558	+/-0.1922	+/-0.2129
1.6530	0.2596	0.0575	0.1.74	0.1341	-.0434	0.0875
	+/-0.0406	+/-0.0899	+/-0.1069	+/-0.1122	+/-0.1380	+/-0.1631
1.7050	0.3006	0.0322	0.3006	0.2866	-.0322	-.3419
	+/-0.0574	+/-0.1255	+/-0.1535	+/-0.1747	+/-0.2027	+/-0.2141
1.7410	0.1969	0.0951	0.1378	0.3313	-.3041	-.4184
	+/-0.0599	+/-0.1342	+/-0.1662	+/-0.1823	+/-0.2004	+/-0.2142
1.8110	0.2178	0.0925	0.1179	0.1212	-.4275	-.6378
	+/-0.0789	+/-0.1726	+/-0.1957	+/-0.2044	+/-0.2593	+/-0.3046
1.8471	0.2561	0.1096	0.3195	0.0871	0.3150	-.3291
	+/-0.0752	+/-0.1745	+/-0.2275	+/-0.2639	+/-0.2796	+/-0.3156

TABLE 5.3a Cont'd

INCIDENT MOMENTUM (GEV C)	C1/A0	C2/A0	C3/A0	C4/A0	C5/A0
0.7300	0.3195 +/-0.0699	-.0082 +/-0.0570	-.0103 +/-0.0473	-.0033 +/-0.0384	-.0088 +/-0.0349
0.7500	0.1443 +/-0.0390	0.0290 +/-0.0276	-.0558 +/-0.0225	0.0028 +/-0.0203	-.0001 +/-0.0186
0.7700	0.1729 +/-0.0368	-.0320 +/-0.0269	-.0187 +/-0.0227	0.0383 +/-0.0183	0.0001 +/-0.0171
0.7900	0.1850 +/-0.0369	0.0004 +/-0.0271	-.0185 +/-0.0229	0.0127 +/-0.0200	-.0302 +/-0.0174
0.8100	0.1960 +/-0.0406	-.0161 +/-0.0279	-.0753 +/-0.0225	-.0099 +/-0.0206	-.0024 +/-0.0180
0.8300	0.1754 +/-0.0415	-.0565 +/-0.0299	-.0565 +/-0.0253	0.0062 +/-0.0216	-.0302 +/-0.0195
0.8500	0.1937 +/-0.0439	-.0176 +/-0.0294	-.0759 +/-0.0242	-.0072 +/-0.0219	-.0283 +/-0.0210
0.8700	0.2567 +/-0.0452	-.0446 +/-0.0279	-.0671 +/-0.0233	-.0425 +/-0.0200	-.0267 +/-0.0171
0.9100	0.1568 +/-0.0232	-.0550 +/-0.0160	0.0048 +/-0.0130	0.0329 +/-0.0121	0.0056 +/-0.0102
0.9500	0.1162 +/-0.0115	-.0367 +/-0.0083	-.0199 +/-0.0067	0.0069 +/-0.0057	-.0213 +/-0.0052
0.9600	0.0671 +/-0.0295	0.0058 +/-0.0235	-.0314 +/-0.0185	-.0158 +/-0.0168	0.0008 +/-0.0148
0.9900	0.1162 +/-0.0326	-.0427 +/-0.0247	0.0072 +/-0.0198	0.0016 +/-0.0171	-.0037 +/-0.0151
1.0050	0.0863 +/-0.0302	0.0147 +/-0.0244	0.0141 +/-0.0207	0.0046 +/-0.0177	-.0046 +/-0.0157
1.0450	0.0967 +/-0.0250	0.0059 +/-0.0212	0.0069 +/-0.0167	-.0120 +/-0.0144	-.0406 +/-0.0130
1.0850	0.0964 +/-0.0259	0.0148 +/-0.0221	0.0105 +/-0.0174	0.0114 +/-0.0157	-.0068 +/-0.0140
1.1250	0.1001 +/-0.0253	0.0016 +/-0.0216	0.0003 +/-0.0173	-.0154 +/-0.0152	-.0139 +/-0.0133
1.1650	0.0979 +/-0.0249	0.0222 +/-0.0214	0.0300 +/-0.0171	-.0213 +/-0.0147	-.0215 +/-0.0132
1.2050	0.1449 +/-0.0259	0.0541 +/-0.0218	0.0340 +/-0.0172	-.0157 +/-0.0152	-.0236 +/-0.0136
1.2450	0.1882 +/-0.0249	0.0709 +/-0.0210	0.0361 +/-0.0170	-.0103 +/-0.0145	-.0134 +/-0.0129
1.2850	0.1452 +/-0.0250	0.1380 +/-0.0212	0.0368 +/-0.0166	-.0408 +/-0.0149	-.0266 +/-0.0129
1.3200	0.1297 +/-0.0266	0.1642 +/-0.0248	0.0426 +/-0.0208	-.0160 +/-0.0177	-.0263 +/-0.0156
1.3550	0.0452 +/-0.0604	0.1532 +/-0.0589	0.0120 +/-0.0540	0.0165 +/-0.0465	-.0235 +/-0.0429
1.4620	0.1078 +/-0.0318	0.1196 +/-0.0315	0.0915 +/-0.0261	0.0178 +/-0.0212	0.0050 +/-0.0193
1.5140	0.0526 +/-0.0472	0.0987 +/-0.0442	0.0404 +/-0.0352	-.0021 +/-0.0292	0.0471 +/-0.0262
1.5460	0.1100 +/-0.0382	0.0738 +/-0.0393	0.0428 +/-0.0327	0.0053 +/-0.0265	0.0038 +/-0.0235
1.6060	-.0397 +/-0.0548	0.0490 +/-0.0551	0.0273 +/-0.0494	-.0053 +/-0.0422	-.0218 +/-0.0390
1.6530	-.0117 +/-0.0396	0.1526 +/-0.0416	0.0085 +/-0.0369	0.0788 +/-0.0319	0.0411 +/-0.0275
1.7050	-.0352 +/-0.0554	0.1138 +/-0.0531	0.0148 +/-0.0450	-.0015 +/-0.0384	0.0276 +/-0.0343
1.7410	-.0189 +/-0.0524	0.0790 +/-0.0523	-.0485 +/-0.0508	0.0282 +/-0.0445	0.0534 +/-0.0392
1.8000	0.0393 +/-0.0650	0.0949 +/-0.0690	0.0937 +/-0.0638	0.1274 +/-0.0519	0.0405 +/-0.0460
1.8430	-.1800 +/-0.0859	0.1065 +/-0.0824	-.0768 +/-0.0752	-.0093 +/-0.0702	0.0001 +/-0.0601

Table 5.3a Cont'd

INCIDENT MOMENTUM (GEV/C)	D2/A0	D3/A0	D4/A0	D5/A0
0.7300	-.0471 +/-0.0297	-.0010 +/-0.0156	-.0035 +/-0.0102	0.0070 +/-0.0071
0.7500	0.0130 +/-0.0160	0.0078 +/-0.0084	0.0085 +/-0.0054	0.0022 +/-0.0039
0.7700	0.0247 +/-0.0164	0.0046 +/-0.0084	0.0013 +/-0.0054	-.0038 +/-0.0039
0.7900	0.0378 +/-0.0165	0.0121 +/-0.0084	0.0090 +/-0.0056	0.0006 +/-0.0039
0.8100	0.0250 +/-0.0179	0.0044 +/-0.0087	0.0133 +/-0.0056	-.0002 +/-0.0042
0.8300	0.0175 +/-0.0172	0.0095 +/-0.0090	-.0001 +/-0.0058	-.0041 +/-0.0042
0.8500	0.0293 +/-0.0186	-.0005 +/-0.0093	0.0051 +/-0.0058	0.0022 +/-0.0040
0.8700	-.0168 +/-0.0151	0.0078 +/-0.0081	0.0027 +/-0.0053	0.0001 +/-0.0037
0.9100	0.0374 +/-0.0092	0.0146 +/-0.0049	0.0063 +/-0.0031	0.0016 +/-0.0023
0.9500	0.0550 +/-0.0051	0.0068 +/-0.0025	0.0018 +/-0.0016	-.0022 +/-0.0012
0.9600	0.0729 +/-0.0138	-.0022 +/-0.0079	0.0049 +/-0.0048	0.0049 +/-0.0034
0.9900	0.0725 +/-0.0160	0.0184 +/-0.0079	-.0047 +/-0.0047	-.0046 +/-0.0035
1.0050	0.0645 +/-0.0140	0.0018 +/-0.0077	0.0036 +/-0.0050	-.0014 +/-0.0036
1.0450	0.0513 +/-0.0108	0.0095 +/-0.0063	0.0032 +/-0.0042	0.0033 +/-0.0030
1.0850	0.0399 +/-0.0112	0.0030 +/-0.0065	0.0062 +/-0.0043	0.0055 +/-0.0030
1.1250	0.0514 +/-0.0112	0.0108 +/-0.0066	0.0105 +/-0.0044	0.0070 +/-0.0032
1.1650	0.0362 +/-0.0110	0.0055 +/-0.0064	0.0063 +/-0.0042	0.0032 +/-0.0030
1.2050	0.0396 +/-0.0112	0.0053 +/-0.0066	0.0034 +/-0.0042	0.0020 +/-0.0030
1.2450	0.0246 +/-0.0103	-.0051 +/-0.0062	0.0059 +/-0.0041	0.0030 +/-0.0029
1.2850	0.0393 +/-0.0106	-.0050 +/-0.0065	0.0079 +/-0.0042	0.0020 +/-0.0030
1.3200	0.0324 +/-0.0109	-.0034 +/-0.0072	0.0113 +/-0.0049	0.0050 +/-0.0035
1.3550	0.0065 +/-0.0207	-.0129 +/-0.0149	0.0099 +/-0.0111	-.0015 +/-0.0082
1.4620	0.0156 +/-0.0126	-.0082 +/-0.0087	0.0001 +/-0.0062	-.0001 +/-0.0044
1.5140	-.0069 +/-0.0183	-.0016 +/-0.0122	-.0025 +/-0.0085	0.0009 +/-0.0059
1.5460	-.0133 +/-0.0140	-.0080 +/-0.0104	-.0134 +/-0.0073	-.0036 +/-0.0051
1.6060	-.0112 +/-0.0192	-.0078 +/-0.0128	-.0194 +/-0.0099	-.0043 +/-0.0073
1.6530	0.0155 +/-0.0145	0.0038 +/-0.0107	-.0031 +/-0.0081	0.0060 +/-0.0060
1.7050	0.0140 +/-0.0235	-.0374 +/-0.0147	-.0114 +/-0.0107	-.0062 +/-0.0076
1.7510	0.0215 +/-0.0191	-.0168 +/-0.0130	0.0029 +/-0.0099	0.0001 +/-0.0076
1.8011	-.0162 +/-0.0267	-.0393 +/-0.0196	-.0033 +/-0.0152	-.0154 +/-0.0107
1.8431	-.0220 +/-0.0263	-.0100 +/-0.0175	-.0105 +/-0.0129	-.0116 +/-0.0105

TABLE 5.3a Cont'd

INCIDENT MOMENTUM (GEV/C)	A0	A1/A0	A2/A0	A3/A0	A4/A0	A5/A0
0.7300	0.4878	-.2595	-.0739	0.4261	0.1912	0.4539
	+/-0.0240	+/-0.1737	+/-0.2343	+/-0.2778	+/-0.3206	+/-0.3394
0.7500	0.5376	0.1257	0.1653	0.3792	0.3362	0.3480
	+/-0.0170	+/-0.1089	+/-0.1480	+/-0.1672	+/-0.1928	+/-0.2069
0.7700	0.4818	-.1683	0.1617	0.3316	-.0390	-.0554
	+/-0.0160	+/-0.1146	+/-0.1428	+/-0.1667	+/-0.1916	+/-0.2184
0.7900	0.5396	-.0811	-.2400	-.1790	-.1884	0.1250
	+/-0.0200	+/-0.1045	+/-0.1325	+/-0.1587	+/-0.1737	+/-0.1922
0.8100	0.7092	0.0181	-.3528	-.2832	-.0627	0.2575
	+/-0.0280	+/-0.1016	+/-0.1323	+/-0.1526	+/-0.1784	+/-0.1970
0.8300	0.7138	0.1149	-.5190	-.1892	-.2979	0.1426
	+/-0.0260	+/-0.0963	+/-0.1191	+/-0.1552	+/-0.1721	+/-0.1906
0.8500	0.6526	0.0598	-.2738	-.2739	-.2296	0.0316
	+/-0.0260	+/-0.1114	+/-0.1406	+/-0.1689	+/-0.2022	+/-0.2050
0.8700	0.7172	-.2249	-.4683	-.1710	-.1916	0 4942
	+/-0.0572	+/-0.0976	+/-0.1334	+/-0.1449	+/-0.1820	+/-0.1956
0.9100	0.7073	-.1294	-.1598	-.3105	-.3080	0.0799
	+/-0.0382	+/-0.0687	+/-0.0874	+/-0.1014	+/-0.1116	+/-0.1289
0.9500	0.8051	-.0456	-.1295	-.0982	-.4280	0.0322
	+/-0.0232	+/-0.0350	+/-0.0437	+/-0.0525	+/-0.0613	+/-0.0673
0.9600	0.6680	0.0124	0.0480	-.4948	-.4433	0.0872
	+/-0.0338	+/-0.1008	+/-0.1215	+/-0.1399	+/-0.1615	+/-0.1809
0.9900	0.5428	0.1436	0.1419	-.3874	-.6743	-.1067
	+/-0.0528	+/-0.1272	+/-0.1556	+/-0.1821	+/-0.2235	+/-0.2253
1.0050	0.6349	0.0697	0.6014	-.4492	-.4316	-.2017
	+/-0.0353	+/-0.1257	+/-0.1456	+/-0.1772	+/-0.2039	+/-0.2262
1.0450	0.7750	0.1482	0.8894	-.6567	-.6988	0.0238
	+/-0.0340	+/-0.1017	+/-0.1103	+/-0.1312	+/-0.1519	+/-0.1701
1.0850	0.6156	0.2070	1.2067	-.7809	-.5020	-.1798
	+/-0.0300	+/-0.1211	+/-0.1340	+/-0.1689	+/-0.1974	+/-0.2218
1.1250	0.6531	0.2614	0.9976	-.7930	-.4554	-.2695
	+/-0.0299	+/-0.1127	+/-0.1269	+/-0.1544	+/-0.1815	+/-0.2000
1.1650	0.6637	0.1708	0.8548	-.5551	-.4603	-.0024
	+/-0.0290	+/-0.1029	+/-0.1165	+/-0.1414	+/-0.1569	+/-0.1742
1.2050	0.6417	0.0819	0.7428	-.6143	-.4423	0.1319
	+/-0.0291	+/-0.1029	+/-0.1178	+/-0.1426	+/-0.1623	+/-0.1783
1.2450	0.6919	0.4633	0.6376	-.4071	-.4716	-.0696
	+/-0.0274	+/-0.0880	+/-0.1014	+/-0.1261	+/-0.1452	+/-0.1574
1.2850	0.6749	0.3022	0.5695	-.5955	-.4716	0.0671
	+/-0.0256	+/-0.0855	+/-0.0988	+/-0.1212	+/-0.1373	+/-0.1544
1.3200	0.6770	0.6428	0.3731	-.4909	-.8527	-.3846
	+/-0.0292	+/-0.0914	+/-0.1014	+/-0.1183	+/-0.1374	+/-0.1556
1.3550	0.7206	1.1282	0.6217	-.9177	-.4021	0 1150
	+/-0.0640	+/-0.2025	+/-0.2507	+/-0.3177	+/-0.3529	+/-0.4048
1.4620	0.6150	0.6806	0.6536	-.4928	-.5549	-.1366
	+/-0.0299	+/-0.1232	+/-0.1416	+/-0.1701	+/-0.2053	+/-0.2268
1.5140	0.6076	0.7121	0.5980	-.7329	-.0607	0.3421
	+/-0.0377	+/-0.1527	+/-0.1917	+/-0.2314	+/-0.2706	+/-0.2990
1.5460	0.6468	0.7249	0.3203	-.6694	-.4215	0.2173
	+/-0.0352	+/-0.1259	+/-0.1526	+/-0.1816	+/-0.2065	+/-0.2342
1.6060	0.6048	0.6216	0.1965	-.8881	0.2498	1 1558
	+/-0.0459	+/-0.1750	+/-0.2377	+/-0.2709	+/-0.3011	+/-0.3190
1.6530	0.6235	0.6874	-.2566	-.8988	0.2606	0.5912
	+/-0.0318	+/-0.1018	+/-0.1440	+/-0.1636	+/-0.1862	+/-0.2075
1.7050	0.6024	0.6391	-.2422	-.5759	0.6679	0.6009
	+/-0.0402	+/-0.1404	+/-0.2110	+/-0.2110	+/-0.2409	+/-0.2715
1.7410	0.7049	0.8737	-.2931	-.7260	0.6528	0.8501
	+/-0.0415	+/-0.1169	+/-0.1825	+/-0.2039	+/-0.2343	+/-0.2481
1.8000	0.4853	0.8817	-.2174	-.4928	0.8629	1.1784
	+/-0.0401	+/-0.1712	+/-0.2677	+/-0.3056	+/-0.3349	+/-0.3561
1.8430	0.6847	1.0620	-.0528	-.8678	0.1025	-.0241
	+/-0.0500	+/-0.1491	+/-0.2111	+/-0.2388	+/-0.2785	+/-0.3050

TABLE 5.3b : Coefficient data for the quasi-two body process $k^- p \rightarrow \pi^- \Sigma^+ (1385)$

INCIDENT MOMENTUM (GEV/C)	B0/A0	B1/A0	B2/A0	B3/A0	B4/A0	B5/A0
0.7300	0.1619 +/-0.0606	-.0842 +/-0.1015	0.0025 +/-0.1428	0.0951 +/-0.1702	-.1125 +/-0.1995	-.0625 +/-0.2044
0.7500	0.1631 +/-0.0341	0.1053 +/-0.0627	-.0233 +/-0.0873	0.1161 +/-0.0987	0.2243 +/-0.1110	0.0759 +/-0.1200
0.7700	0.1392 +/-0.0356	0.0649 +/-0.0637	-.0209 +/-0.0804	0.0280 +/-0.0951	0.0869 +/-0.1074	-.0442 +/-0.1226
0.7900	0.1930 +/-0.0370	0.3038 +/-0.0615	-.2566 +/-0.0800	-.0415 +/-0.0967	0.0341 +/-0.1074	-.0534 +/-0.1153
0.8100	0.2479 +/-0.0367	0.1501 +/-0.0605	-.2479 +/-0.0802	-.0871 +/-0.0959	0.0127 +/-0.1106	0.2443 +/-0.1170
0.8300	0.2175 +/-0.0376	0.0970 +/-0.0582	-.2945 +/-0.0706	-.1672 +/-0.0938	0.1140 +/-0.1037	0.0355 +/-0.1122
0.8500	0.3136 +/-0.0396	0.1248 +/-0.0664	-.3069 +/-0.0824	-.1941 +/-0.1010	-.0498 +/-0.1215	0.1015 +/-0.1218
0.8700	0.1994 +/-0.0424	0.0978 +/-0.0644	-.3654 +/-0.0895	0.1576 +/-0.0969	0.0921 +/-0.1140	-.3357 +/-0.1237
0.9100	0.3279 +/-0.0333	0.0764 +/-0.0404	-.2639 +/-0.0549	-.1683 +/-0.0614	-.0250 +/-0.0663	0.1065 +/-0.0793
0.9500	0.2897 +/-0.0167	0.1487 +/-0.0220	-.2281 +/-0.0282	-.0920 +/-0.0334	-.0079 +/-0.0370	-.0259 +/-0.0421
0.9600	0.2744 +/-0.0338	0.2218 +/-0.0591	-.2264 +/-0.0712	-.2424 +/-0.0843	-.0297 +/-0.0983	0.0505 +/-0.1078
0.9900	0.2434 +/-0.0531	0.1710 +/-0.0778	-.0047 +/-0.0946	-.1634 +/-0.1097	-.0808 +/-0.1278	0.1211 +/-0.1461
1.0050	0.1860 +/-0.0390	0.2003 +/-0.0740	-.2661 +/-0.0889	-.1411 +/-0.1085	-.0392 +/-0.1246	-.0664 +/-0.1393
1.0450	0.2183 +/-0.0307	0.3567 +/-0.0615	-.2086 +/-0.0698	-.1142 +/-0.0821	-.2971 +/-0.0966	0.0533 +/-0.1090
1.0850	0.2055 +/-0.0336	0.4131 +/-0.0706	-.0617 +/-0.0826	-.1816 +/-0.1003	-.3145 +/-0.1160	0.0240 +/-0.1305
1.1250	0.2352 +/-0.0329	0.3600 +/-0.0680	-.0474 +/-0.0813	-.1287 +/-0.0968	-.1460 +/-0.1127	-.1385 +/-0.1230
1.1650	0.2459 +/-0.0308	0.3150 +/-0.0618	-.1755 +/-0.0730	-.2476 +/-0.0863	-.3319 +/-0.0965	-.1146 +/-0.1059
1.2050	0.2210 +/-0.0313	0.3142 +/-0.0630	-.0547 +/-0.0749	-.2040 +/-0.0891	-.2194 +/-0.1009	0.0052 +/-0.1093
1.2450	0.2841 +/-0.0271	0.3582 +/-0.0538	0.0994 +/-0.0641	-.1841 +/-0.0782	-.1056 +/-0.0907	-.1450 +/-0.0963
1.2850	0.2821 +/-0.0266	0.3006 +/-0.0525	-.0577 +/-0.0628	-.2322 +/-0.0757	-.1180 +/-0.0850	-.0257 +/-0.0959
1.3200	0.3480 +/-0.0301	0.4054 +/-0.0578	0.0664 +/-0.0650	-.2210 +/-0.0761	-.2689 +/-0.0890	-.1715 +/-0.0965
1.3550	0.3527 +/-0.0634	0.3719 +/-0.1265	0.0382 +/-0.1442	-.6206 +/-0.1879	-.2750 +/-0.2183	-.2436 +/-0.2463
1.4620	0.4076 +/-0.0373	0.3731 +/-0.0787	0.1672 +/-0.0935	-.0768 +/-0.1103	-.3296 +/-0.1320	-.0182 +/-0.1444
1.5140	0.3998 +/-0.0463	0.1503 +/-0.0961	0.0430 +/-0.1211	-.5609 +/-0.1440	-.0780 +/-0.1739	0.2818 +/-0.1979
1.5460	0.4231 +/-0.0394	0.3115 +/-0.0797	-.0143 +/-0.0937	-.5142 +/-0.1114	-.4519 +/-0.1281	0.0234 +/-0.1441
1.6060	0.4658 +/-0.0573	0.3276 +/-0.1133	-.1037 +/-0.1476	-.6333 +/-0.1659	-.1768 +/-0.1947	0.2476 +/-0.2057
1.6530	0.4412 +/-0.0392	0.3342 +/-0.0647	-.2602 +/-0.0923	-.6351 +/- 0.1038	0.0493 +/-0.1220	0.1328 +/-0.1337
1.7050	0.4980 +/-0.0525	0.2942 +/-0.0933	-.2562 +/-0.1335	-.3571 +/-0.1360	0.2055 +/-0.1552	0.2188 +/-0.1776
1.7410	0.3776 +/-0.0454	0.2399 +/-0.0754	-.3249 +/-0.1103	-.3980 +/-0.1264	0.2852 +/-0.1435	0.3454 +/-0.1544
1.8000	0.3381 +/-0.0650	0.2143 +/-0.1108	-.1624 +/-0.1677	-.4304 +/-0.1838	0.1216 +/-0.2015	0.3135 +/-0.2185
1.9430	0.4557 +/-0.0535	0.4645 +/-0.0940	-.0701 +/-0.1292	-.4914 +/-0.1440	0.0131 +/-0.1775	-.0271 +/-0.1907

Table 5.3b Cont'd

INCIDENT MOMENTUM (GEV/C)	C1/A0	C2/A0	C3/A0	C4/A0	C5/A0
0.7300	0.0558 +/-0.0786	0.0051 +/-0.0515	-.0344 +/-0.0438	-.0080 +/-0.0377	0.0316 +/-0.0335
0.7500	0.1309 +/-0.0395	0.0039 +/-0.0302	0.0409 +/-0.0270	-.0301 +/-0.0237	-.0078 +/-0.0223
0.7700	0.0940 +/-0.0366	0.0348 +/-0.0318	-.0173 +/-0.0267	-.0103 +/-0.0235	0.0195 +/-0.0204
0.7900	0.1649 +/-0.0458	0.0288 +/-0.0345	-.0168 +/-0.0273	0.0344 +/-0.0239	-.0222 +/-0.0210
0.8100	0.1069 +/-0.0432	-.0098 +/-0.0312	0.0177 +/-0.0277	-.0136 +/-0.0220	-.0239 +/-0.0194
0.8300	0.1353 +/-0.0415	0.0697 +/-0.0304	-.0290 +/-0.0225	-.0114 +/-0.0207	0.0086 +/-0.0183
0.8500	0.0928 +/-0.0427	0.1061 +/-0.0303	-.0144 +/-0.0267	-.0331 +/-0.0236	-.0249 +/-0.0230
0.8700	0.0849 +/-0.0419	0.0472 +/-0.0299	0.0084 +/-0.0261	0.0063 +/-0.0206	0.0124 +/-0.0182
0.9100	0.0647 +/-0.0239	0.0031 +/-0.0183	0.0340 +/-0.0160	-.0272 +/-0.0141	0.0192 +/-0.0130
0.9500	0.0752 +/-0.0130	0.0355 +/-0.0102	0.0196 +/-0.0083	-.0245 +/-0.0072	-.0103 +/-0.0064
0.9600	0.1015 +/-0.0351	0.0708 +/-0.0287	-.0026 +/-0.0236	-.0314 +/-0.0204	0.0141 +/-0.0180
0.9900	0.0736 +/-0.0460	0.0914 +/-0.0368	0.0221 +/-0.0297	-.0231 +/-0.0252	0.0107 +/-0.0235
1.0050	0.0100 +/-0.0341	0.0539 +/-0.0324	0.0225 +/-0.0269	-.0025 +/-0.0221	0.0340 +/-0.0200
1.0450	0.0522 +/-0.0262	0.0989 +/-0.0258	0.0583 +/-0.0214	0.0209 +/-0.0181	-.0051 +/-0.0162
1.0850	-.0001 +/-0.0323	0.0994 +/-0.0329	-.0055 +/-0.0277	0.0224 +/-0.0238	0.0114 +/-0.0219
1.1250	0.0090 +/-0.0298	0.1153 +/-0.0295	0.0601 +/-0.0249	0.0156 +/-0.0214	0.0291 +/-0.0193
1.1650	-.0905 +/-0.0274	0.1044 +/-0.0275	-.0206 +/-0.0235	0.0418 +/-0.0205	0.0081 +/-0.0180
1.2050	-.0737 +/-0.0290	0.0872 +/-0.0279	-.0341 +/-0.0233	0.0519 +/-0.0201	0.0007 +/-0.0182
1.2450	-.0704 +/-0.0275	0.0314 +/-0.0253	-.0243 +/-0.0201	0.0322 +/-0.0177	0.0389 +/-0.0159
1.2850	-.0802 +/-0.0270	-.0094 +/-0.0242	-.0408 +/-0.0190	0.0308 +/-0.0170	0.0296 +/-0.0154
1.3200	-.0258 +/-0.0297	-.0169 +/-0.0262	-.0409 +/-0.0212	0.0580 +/-0.0174	-.0059 +/-0.0153
1.3550	0.0262 +/-0.0655	0.0477 +/-0.0581	-.0558 +/-0.0507	-.0033 +/-0.0490	-.0362 +/-0.0415
1.4620	-.0671 +/-0.0370	0.0040 +/-0.0323	0.0416 +/-0.0256	0.0506 +/-0.0212	0.0122 +/-0.0194
1.5140	-.0874 +/-0.0458	-.0371 +/-0.0409	-.0145 +/-0.0326	0.0273 +/-0.0302	-.0197 +/-0.0282
1.5460	-.0145 +/-0.0418	-.0097 +/-0.0351	0.0169 +/-0.0281	0.0569 +/-0.0246	0.0126 +/-0.0215
1.6060	-.0211 +/-0.0505	0.0130 +/-0.0365	0.0043 +/-0.0336	0.0251 +/-0.0333	0.0137 +/-0.0316
1.6530	-.0148 +/-0.0394	-.0240 +/-0.0289	-.0304 +/-0.0262	0.0137 +/-0.0230	0.0141 +/-0.0194
1.7050	0.0456 +/-0.0485	-.0137 +/-0.0328	-.0004 +/-0.0334	0.0089 +/-0.0277	0.0303 +/-0.0250
1.7410	0.0458 +/-0.0459	0.0519 +/-0.0305	0.0351 +/-0.0301	0.0381 +/-0.0260	0.0302 +/-0.0238
1.8000	0.0355 +/-0.0660	0.0694 +/-0.0384	0.0642 +/-0.0357	0.0091 +/-0.0317	-.0270 +/-0.0305
1.8430	0.0150 +/-0.0489	0.0275 +/-0.0419	0.0824 +/-0.0355	0.0547 +/-0.0352	0.0695 +/-0.0314

Table 5.3b Cont'd

INCIDENT MOMENTUM (GEV/C)	D2/A0	D3/A0	D4/A0	D5/A0
0.7300	0.0120 +/-0.0310	0.0060 +/-0.0152	0.0233 +/-0.0094	0.0104 +/-0.0066
0.7500	0.0291 +/-0.0160	-.0048 +/-0.0083	0.0078 +/-0.0057	-.0015 +/-0.0042
0.7700	0.0588 +/-0.0162	-.0176 +/-0.0090	0.0058 +/-0.0061	0.0013 +/-0.0045
0.7900	0.0130 +/-0.0183	0.0135 +/-0.0093	-.0005 +/-0.0063	-.0018 +/-0.0045
0.8100	0.0492 +/-0.0188	0.0111 +/-0.0095	0.0022 +/-0.0060	0.0022 +/-0.0044
0.8300	0.0546 +/-0.0182	-.0079 +/-0.0095	-.0006 +/-0.0055	0.0062 +/-0.0040
0.8500	0.0581 +/-0.0200	0.0037 +/-0.0106	0.0116 +/-0.0069	0.0036 +/-0.0045
0.8700	0.0638 +/-0.0185	-.0143 +/-0.0094	0.0028 +/-0.0064	0.0023 +/-0.0047
0.9100	0.0894 +/-0.0124	-.0065 +/-0.0057	0.0057 +/-0.0038	-.0004 +/-0.0029
0.9500	0.0683 +/-0.0063	0.0027 +/-0.0031	0.0040 +/-0.0019	0.0004 +/-0.0014
0.9600	0.0652 +/-0.0158	0.0160 +/-0.0089	0.0064 +/-0.0059	0.0049 +/-0.0042
0.9900	0.0521 +/-0.0195	0.0136 +/-0.0111	0.0180 +/-0.0073	0.0081 +/-0.0055
1.0050	0.0753 +/-0.0160	0.0215 +/-0.0101	0.0194 +/-0.0065	0.0056 +/-0.0047
1.0450	0.0553 +/-0.0115	0.0162 +/-0.0079	0.0207 +/-0.0054	0.0000 +/-0.0039
1.0850	0.0088 +/-0.0125	0.0193 +/-0.0090	0.0024 +/-0.0061	0.0054 +/-0.0044
1.1250	0.0331 +/-0.0126	0.0303 +/-0.0085	0.0106 +/-0.0058	0.0030 +/-0.0041
1.1650	0.0502 +/-0.0119	0.0321 +/-0.0078	0.0019 +/-0.0052	0.0018 +/-0.0039
1.2050	0.0478 +/-0.0127	0.0240 +/-0.0080	-.0072 +/-0.0054	-.0033 +/-0.0039
1.2450	0.0180 +/-0.0112	0.0171 +/-0.0071	-.0036 +/-0.0047	0.0013 +/-0.0034
1.2850	0.0081 +/-0.0115	0.0227 +/-0.0071	-.0008 +/-0.0046	0.0009 +/-0.0034
1.3200	0.0197 +/-0.0127	0.0127 +/-0.0080	0.0052 +/-0.0054	-.0015 +/-0.0038
1.3550	0.0148 +/-0.0259	0.0301 +/-0.0173	0.0075 +/-0.0109	0.0027 +/-0.0081
1.4620	0.0136 +/-0.0156	0.0031 +/-0.0104	0.0152 +/-0.0070	0.0045 +/-0.0048
1.5140	0.0130 +/-0.0193	0.0054 +/-0.0116	0.0040 +/-0.0079	0.0043 +/-0.0056
1.5460	0.0005 +/-0.0168	-.0133 +/-0.0101	-.0008 +/-0.0069	0.0002 +/-0.0051
1.6060	0.0667 +/-0.0267	0.0013 +/-0.0145	0.0115 +/-0.0092	-.0107 +/-0.0072
1.6530	0.0302 +/-0.0189	0.0027 +/-0.0095	-.0009 +/-0.0059	-.0020 +/-0.0045
1.7050	0.0736 +/-0.0261	0.0052 +/-0.0117	-.0108 +/-0.0090	-.0130 +/-0.0065
1.7410	0.0729 +/-0.0239	0.0209 +/-0.0111	0.0036 +/-0.0073	-.0068 +/-0.0054
1.8000	0.0818 +/-0.0319	0.0401 +/-0.0142	0.0073 +/-0.0099	-.0010 +/-0.0075
1.8439	0.0984 +/-0.0265	0.0164 +/-0.0137	-.0059 +/-0.0097	0.0013 +/-0.0069

TABLE 5.3b Cont'd

Incident Momentum (GeV/c)	Number of Events	Fraction of $\pi^+\Sigma^-(1385)$	Fraction of $\pi^-\Sigma^+(1385)$	Fraction of 'ε' Λ	$\sigma(k^-p \to \Lambda\pi^+\pi^-)$ (mb)
0.750	841	0.516 $\pm$.016	0.401 $\pm$.015	0.083 $\pm$.005	2.99 $\pm$.11
0.770	890	0.537 $\pm$.012	0.341 $\pm$.014	0.122 $\pm$.007	2.99 $\pm$.10
0.790	899	0.485 $\pm$.012	0.324 $\pm$.014	0.191 $\pm$.010	3.35 $\pm$.12
0.810	871	0.461 $\pm$.014	0.377 $\pm$.014	0.162 $\pm$.008	3.60 $\pm$.13
0.830	944	0.439 $\pm$.014	0.376 $\pm$.014	0.185 $\pm$.008	3.46 $\pm$.12
0.850	871	0.456 $\pm$.016	0.355 $\pm$.013	0.188 $\pm$.011	3.20 $\pm$.11

TABLE 5.4 : Channel fractions for the reaction $k^-p \to \Lambda\pi^+\pi^-$ as a function of incident momentum.

are shown in Figure 5.10. Since the distributions are not corrected for the losses described in Chapter 2, it is unreasonable to make any very strong conclusions regarding this data. However, the $m^2(\pi^+\pi^-)$ and $\cos\Theta$ distributions are well described. In particular, the fit to the $\pi^+\pi^-$ distribution is rather impressive since this data was not used to determine the values of a_o^c and b_c^o. At these incident momenta the Dalitz plot is dominated by $\pi\pi$ s-wave effects, 60% of the Dalitz plot density coming from the 'ε'Λ channel.

5.7 CONCLUSIONS

Throughout the incident momentum range of this experiment, an enhancement observed at high dipion masses in the $\pi\pi\Lambda$ final state is found to be well described by an effect paramatrized as an s-wave $\pi\pi$ final state interaction (ε). Previous studies show that the 'ε' effect also plays an important role in the reaction $\pi^- p \rightarrow \pi^+\pi^- n$ near threshold. Inclusion of such an effect, together with $\pi\Sigma(1385)$ quasi two-body processes, allows a good account to be given of the quasi two-body variables. Furthermore at lower momenta, in the 0.500 to 0.580 GeV/c range, which is devoid of confirmed resonance formation in the s-channel, the 'ε' effect dominates the Dalitz plot. This observation is in accordance with the observed dominance of the I = 0 cross-section found by Prevost and the large non-resonant $\varepsilon\,\Lambda$ DP03 amplitude found by Mast in the $\Lambda(1520)$ region.

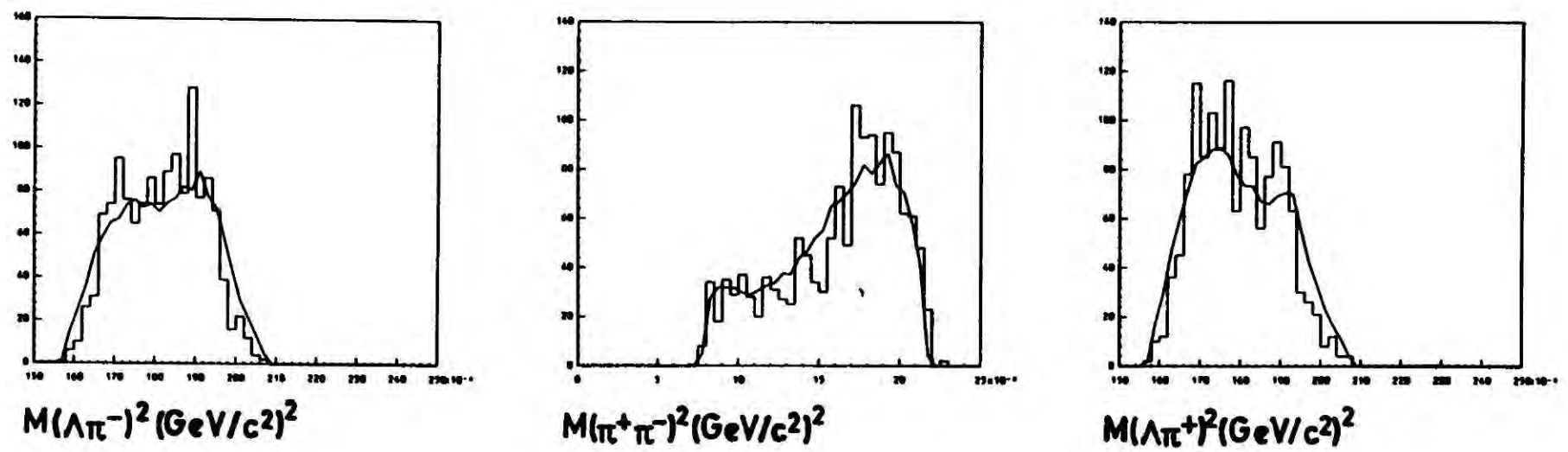

Figure 5.10 : Results of quasi-two body analysis of the reaction $k^- p \to \Lambda\pi^+\pi^-$ in the 0.500 to 0.580 GeV/c incident momentum bin.

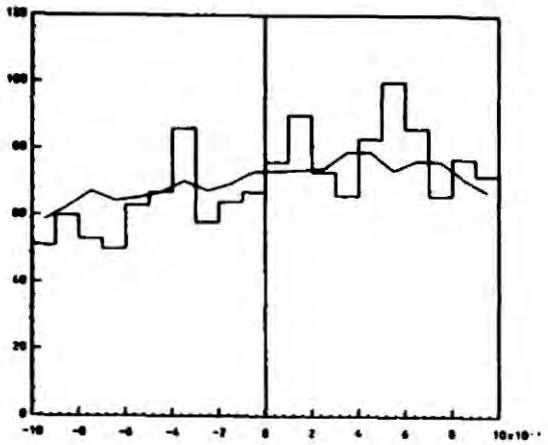

Cos θ^* for $\Lambda\pi^-$ system

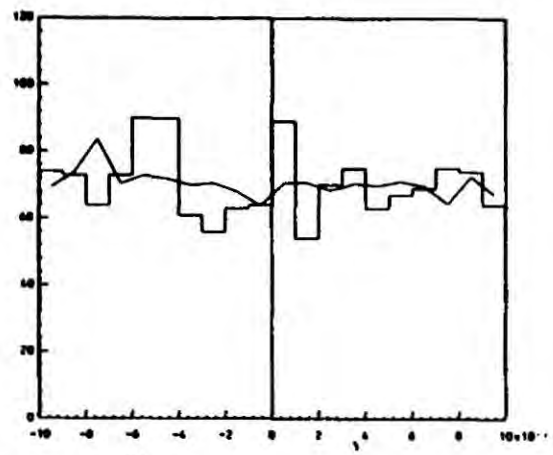

Cos θ^* for $\pi^+\pi^-$ system

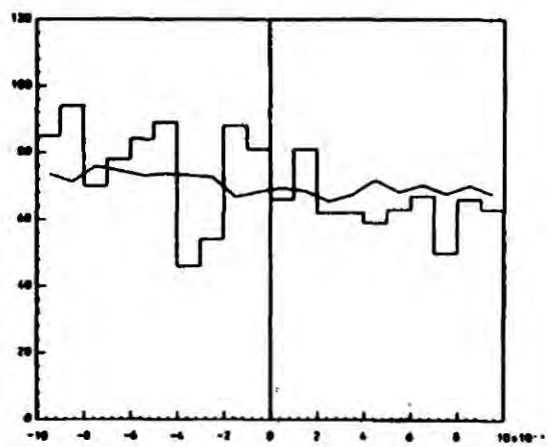

Cos θ^* for $\Lambda\pi^+$ system

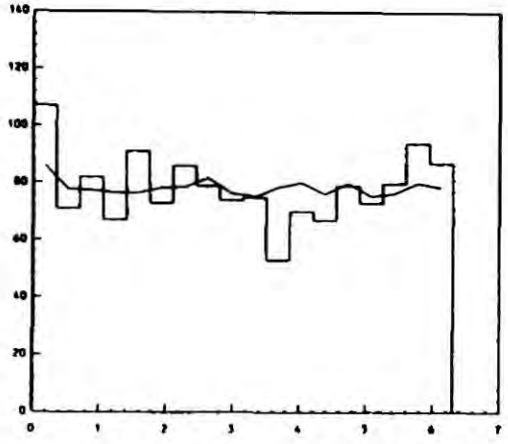

Φ for $\Lambda\pi^-$ system (radians)

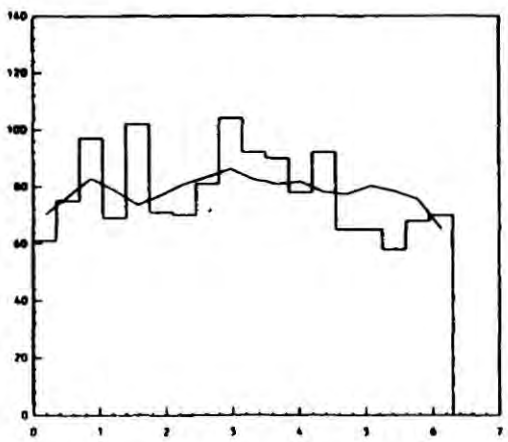

Φ for $\pi^+\pi^-$ system (radians)

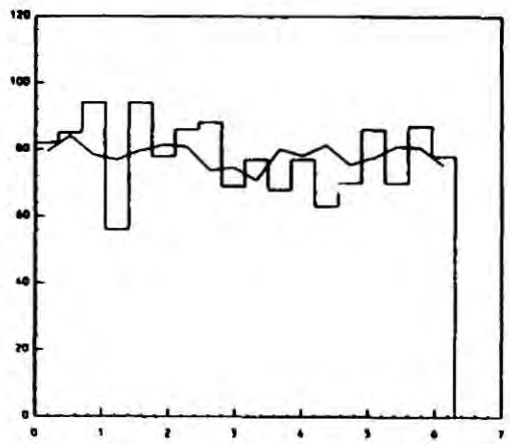

Φ for $\Lambda\pi^+$ system (radians)

Figure 5.10 Cont'd.

CHAPTER 5

REFERENCES

5.1 K.M.Watson, Phys. Rev. 85 (1952) 852.

5.2 M.R.Pennington, Tallahassee Conference Proceedings (1973) page 89.

5.3 J.L.Basdevant et al, Nucl.Phys. B72 (1974) 413.

5.4 P. Estabrooks, Phys. Rev. D19 (1979) 2678.

5.5 Particle Data Group Tables.

5.6 W. Cameron et al, Nucl.Phys. B143 (1978) 189.

5.7 L. Bertanza et al, Nucl.Phys. B110 (1976) 1 and W.Cameron, Private communication.

5.8 A. Zylbersteyn et al, Phys. Letts 38B (1972) 457.

5.9 Greyer et al, Nucl.Phys. B76 (1974) 365.

5.10 J.A.Jones et al, Nucl.Phys B83 (1974) 93.

5.11 R.A.Arndt et al, Phys. Rev. D20 (1979) 651.

5.12 R.S. Longacre et al, Phys. Rev. D17 (1978) 1795.

5.13 R. Stern, Ph.D. Thesis, University of London (unpublished).

CHAPTER 6

6.1 INTRODUCTION

In Chapter three of this thesis it was shown that the A_ℓ, B_ℓ, C_ℓ and D_ℓ coefficients for the reactions $k^- p \to \pi^+\Sigma^-(1385)$ and $k^- p \to \pi^-\Sigma^+(1385)$ could be related to the corresponding set of s-channel partial wave amplitudes. Each of the coefficients is expressed as the real part of a sum of products of partial wave amplitudes (equations 3.10 and 3.12). Traditionally, the extraction of these complex amplitudes follows one of two programs :-

(i) Energy independent solution of the set of coupled bilinear equations implied by the expressions for $d\sigma/d\Omega$ and $\rho_{mm'}\, d\sigma/d\Omega$. Due to the problems associated with the large number of ambiguities present for such a set, a systematic procedure for generating all ambiguous solutions at each energy analysed is required. The method of Barrelet Zeros is most widely used for this purpose.

(ii) Paramatrization and fitting of coefficient data by simple energy dependent forms for the s-channel partial wave amplitudes. Resonant amplitudes are described by Breit-Wigner forms and non-resonant amplitudes by simple polynomials. Few parameters are used to describe data globally over as large an energy range as possible.

Of the two methods, the Barrelet Zero analyses are least model dependent, involving only the selection of the highest angular momentum entering the analysis and the criteria for imposing energy continuity on the various ambiguous solutions. Implementation of this method requires rather precise coefficient data. Since the statistical sensitivity of the data obtained for the $\pi\Sigma(1385)$ channels is low, an energy dependent method of analysis will be pursued.

In outline, this chapter will contain a qualitative description of the $\pi\Sigma(1385)$ final state data,together with an energy independent investigation in the Survey-81 region. Additionally, a full energy dependent partial wave analysis will be performed over the entire energy range for which data is available. A review of Y^* states in the energy range of this analysis has been given in Section 1.3, the parameters of the states given in Table 1.1 will be used as input to the energy dependent partial wave analysis.

Only the A_ℓ, B_ℓ, C_ℓ and D_ℓ coefficients will be used in this analysis. Polarization data, obtained using the weak decay of the Λ^o, will not be used since this is of low statistical sensitivity and increases computer storage space unacceptably.

6.2 DATA FOR THE $\pi\Sigma(1385)$ QUASI TWO-BODY CHANNELS

Figures 6.1 and 6.2 show the total available data sample for the $\pi^+\Sigma^-(1385)$ and $\pi^-\Sigma^+(1385)$ final states as a function of incident momentum. Each coefficient is normalized by the quantity

$$Ao = \frac{\sigma}{4\pi\lambda\!\!\!^{-2}} \cdot \alpha_i \qquad i = 1,2 \qquad (6.1)$$

where σ is the partial cross-section for the reaction $k^- p \rightarrow \Lambda\pi^+\pi^-$, $\lambda\!\!\!^-$ is the wavenumber of the incident k^- in the overall centre of mass and the α_i are fractions of $\pi^+\Sigma^-(1385)$ and $\pi^-\Sigma^+(1385)$ channels extracted from the $\Lambda\pi^+\pi^-$ final state by the program EXTRA. In addition to the Survey-81 data, which covers the 0.730 to 0.850 GeV/c interval, the following data has been used :-

(i) Previously published data given in reference 6.1,which covers the 0.960 to 1.850 GeV/c range. This represents the result of two separate Hydrogen Bubble Chamber exposures, the method used to extract $\pi^+\Sigma^-(1385)$ and $\pi^-\Sigma^+(1385)$ quasi two-body final states is essentially identical to that described in Chapter Five of this thesis. A partial wave analysis of this data has been performed and is described in reference 6.1.

(ii) Rather high statistics data in the narrow 0.850 to 1.000 GeV/c interval. Results for the $\Lambda\pi^+\pi^-$ final states are unpublished ; however, details

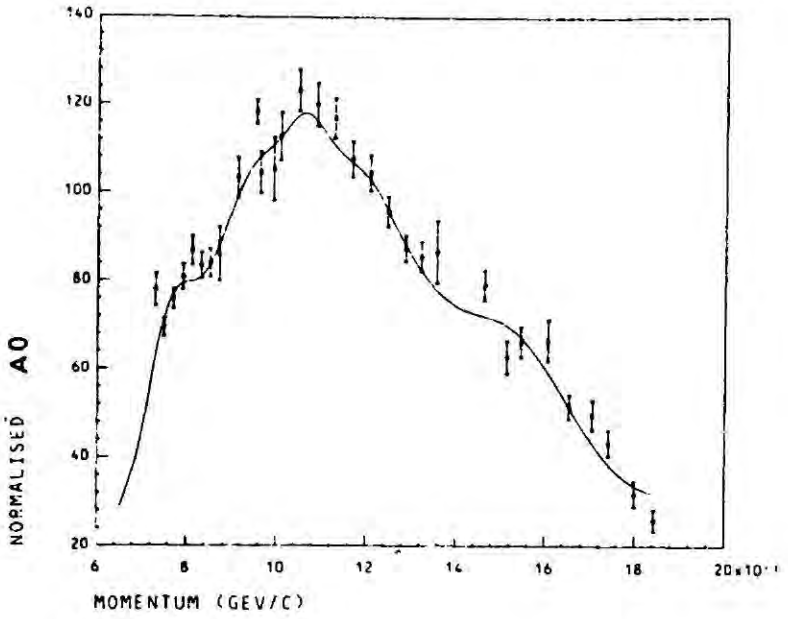

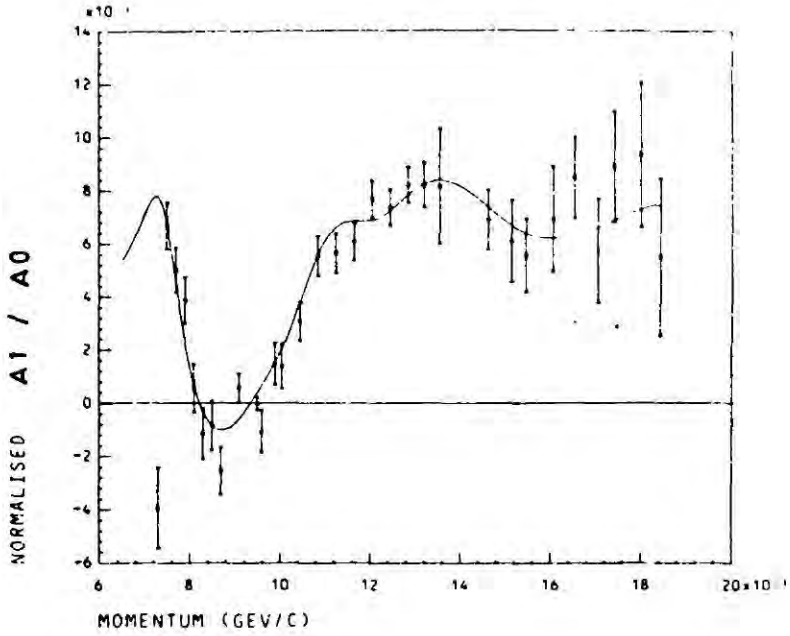

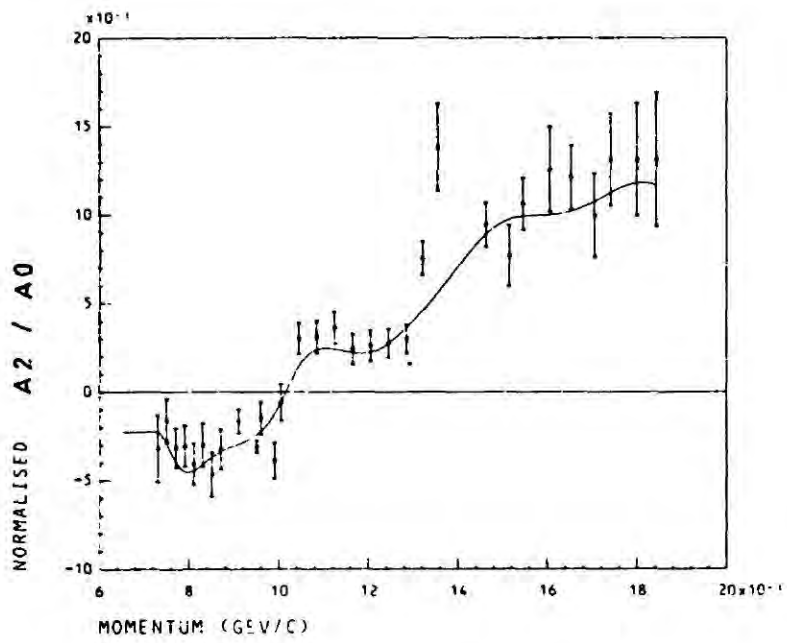

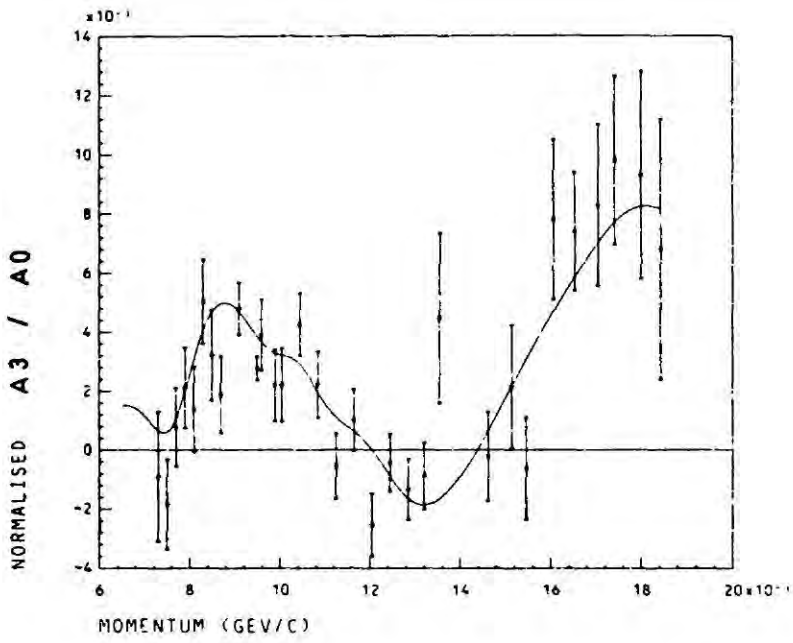

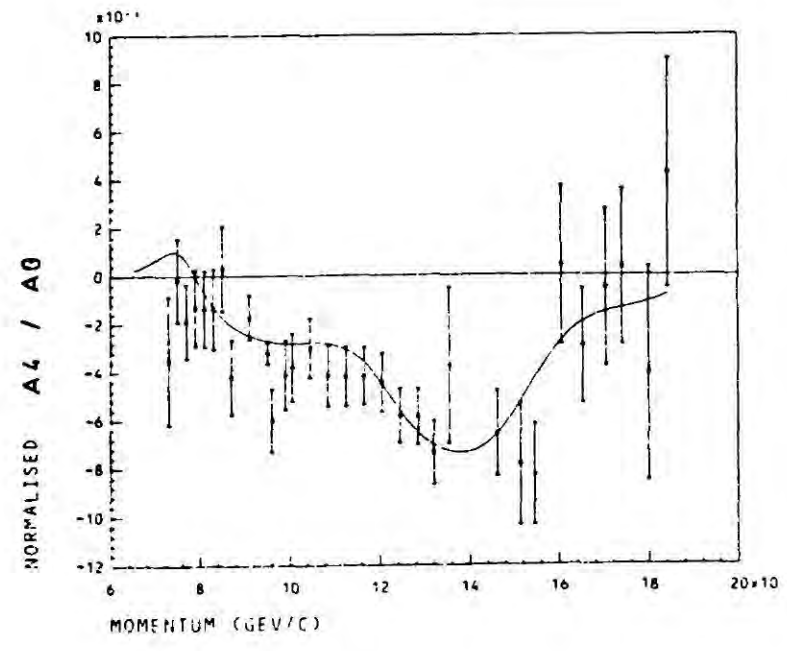

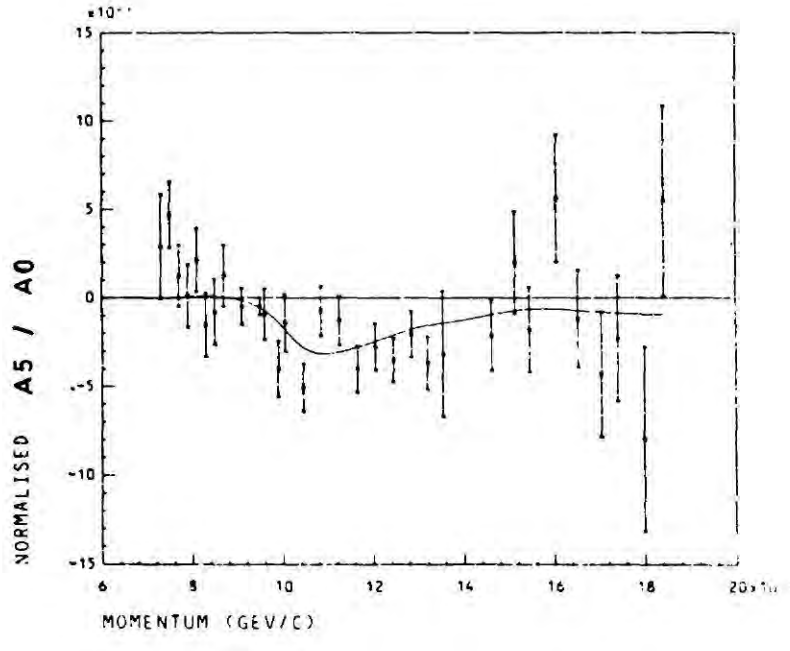

Fig. 6.1 Results of Partial Wave Analysis For The $\pi^+\Sigma^-(1385)$ Channel

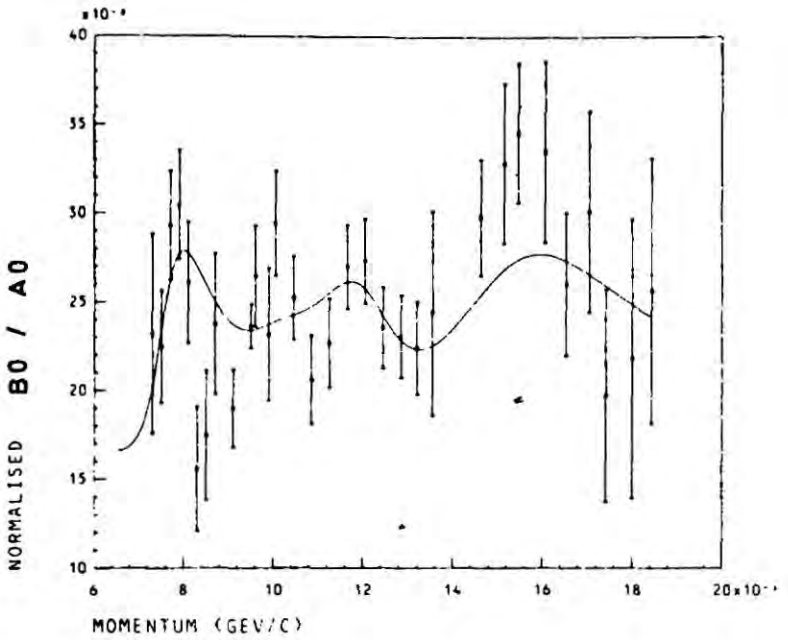

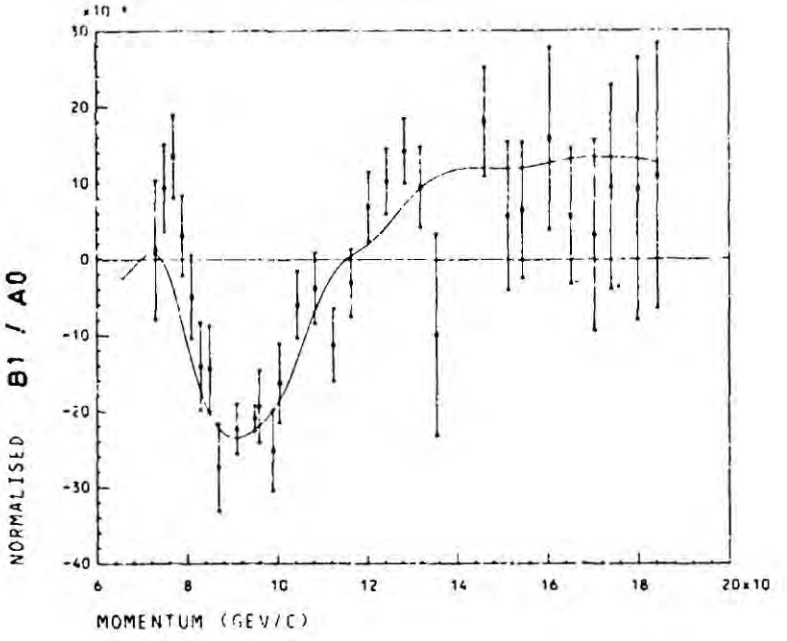

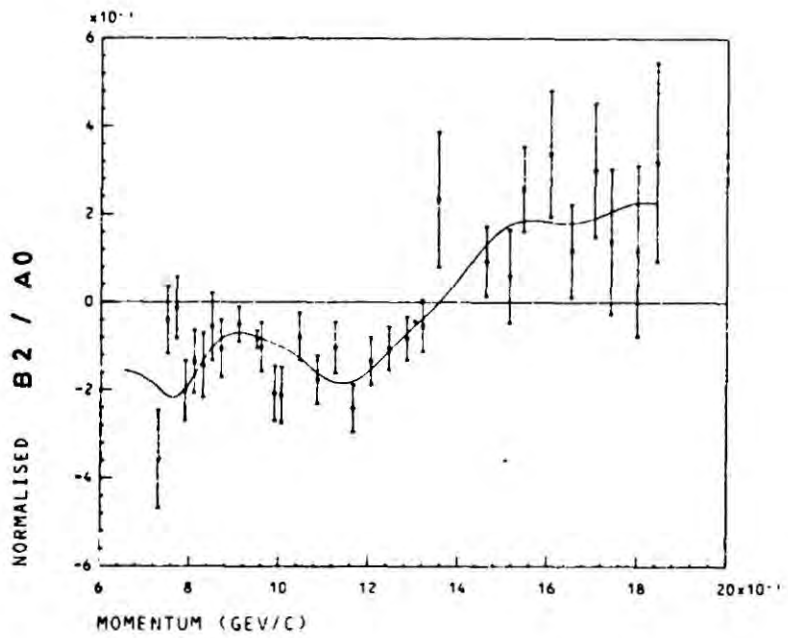

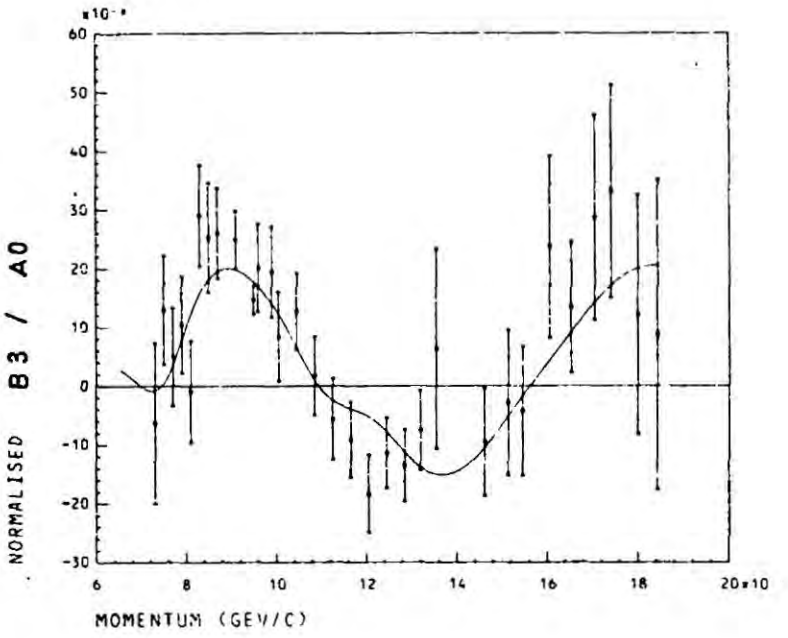

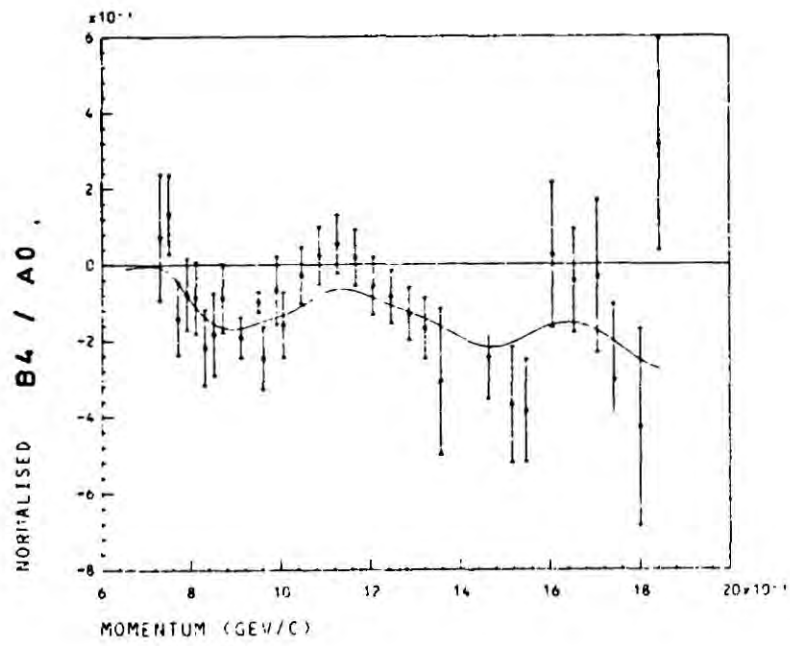

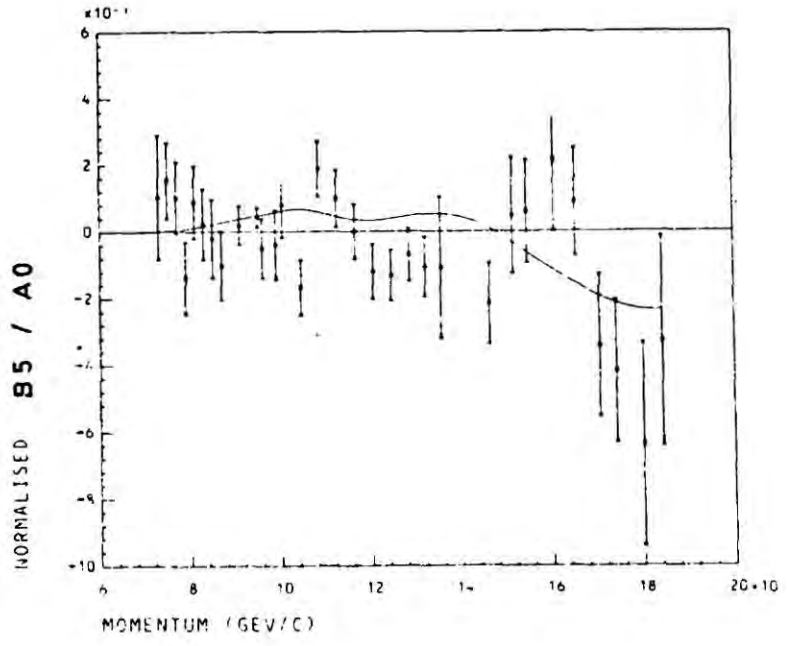

Fig. 6.1cont. Results of Partial Wave Analysis For The $\pi^+\Sigma^-(1385)$ Channel

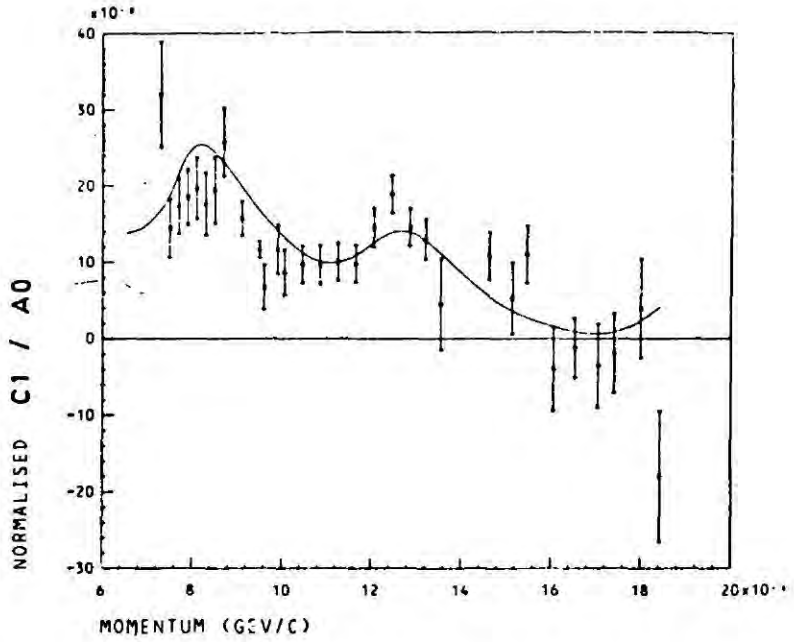

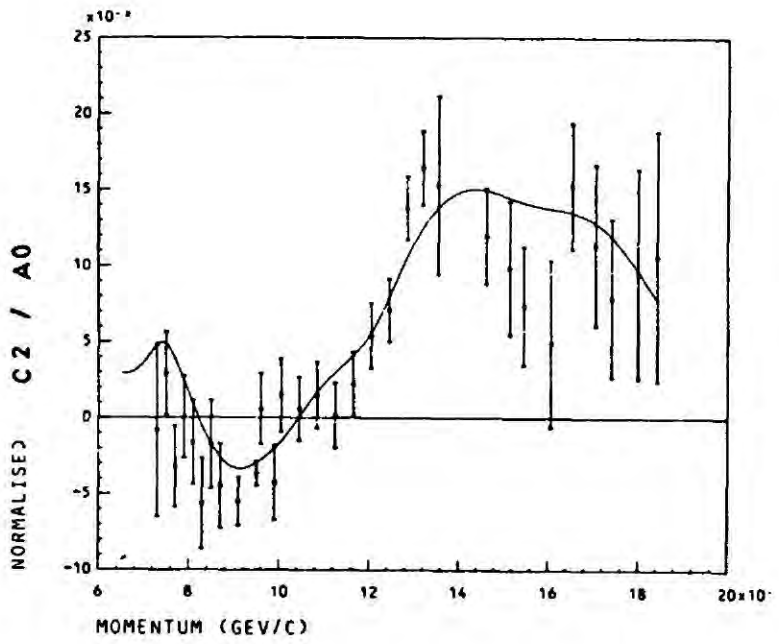

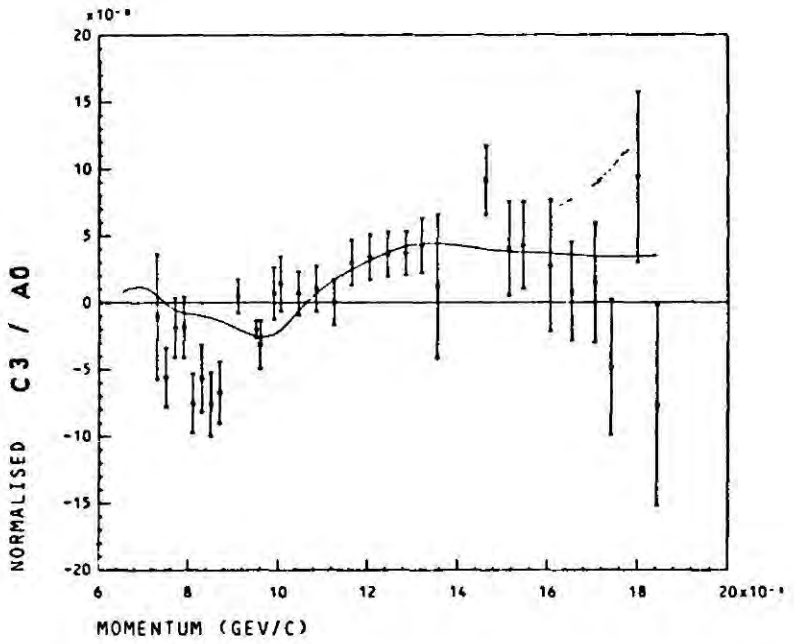

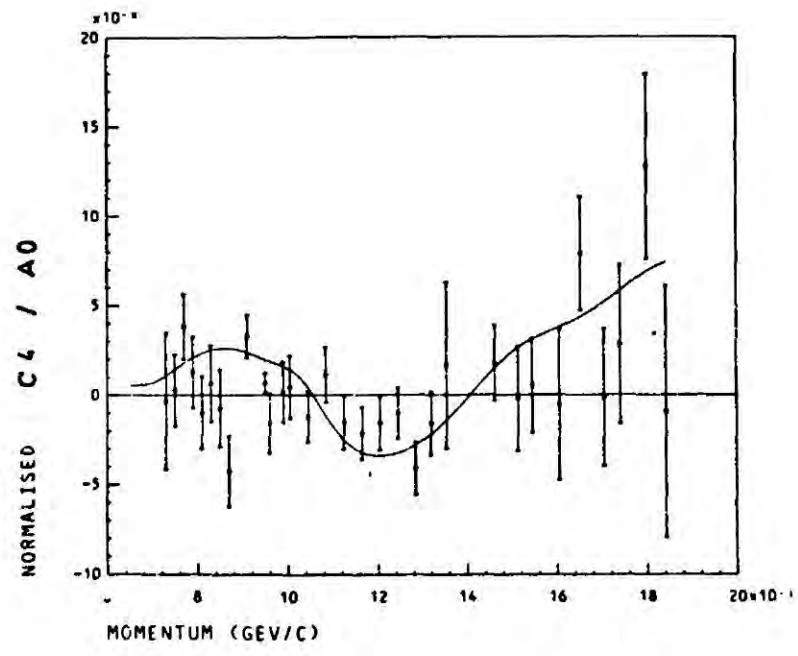

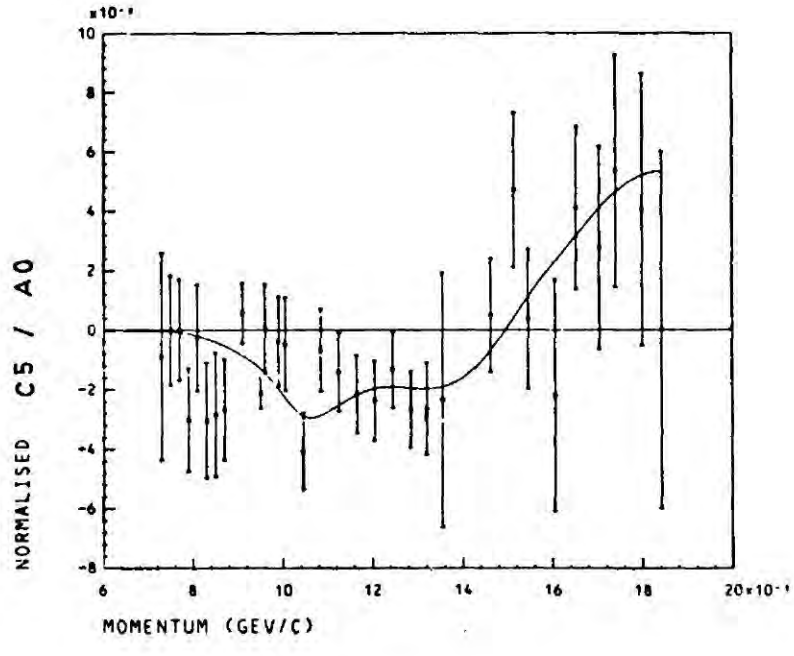

Fig. 6.1 cont. Results of Partial Wave Analysis For The $\pi^+\Sigma^-(1385)$ Channel

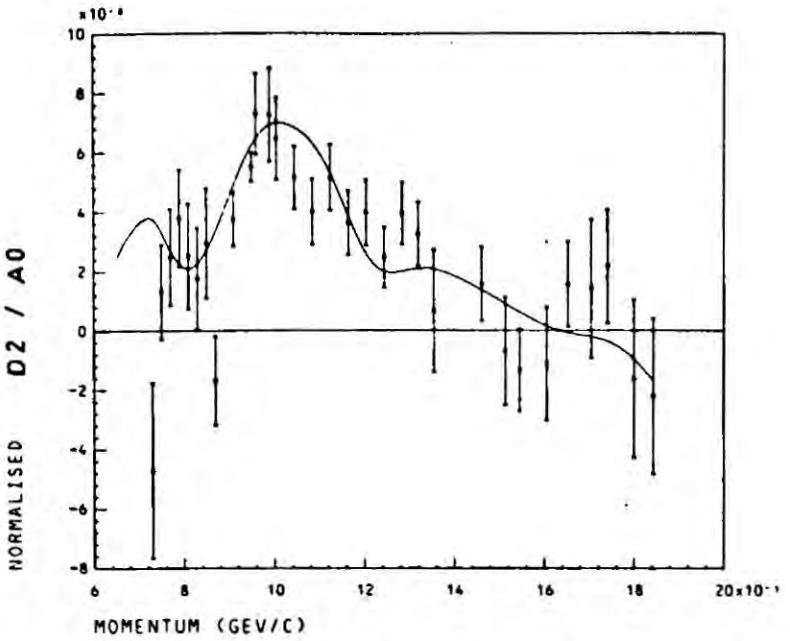

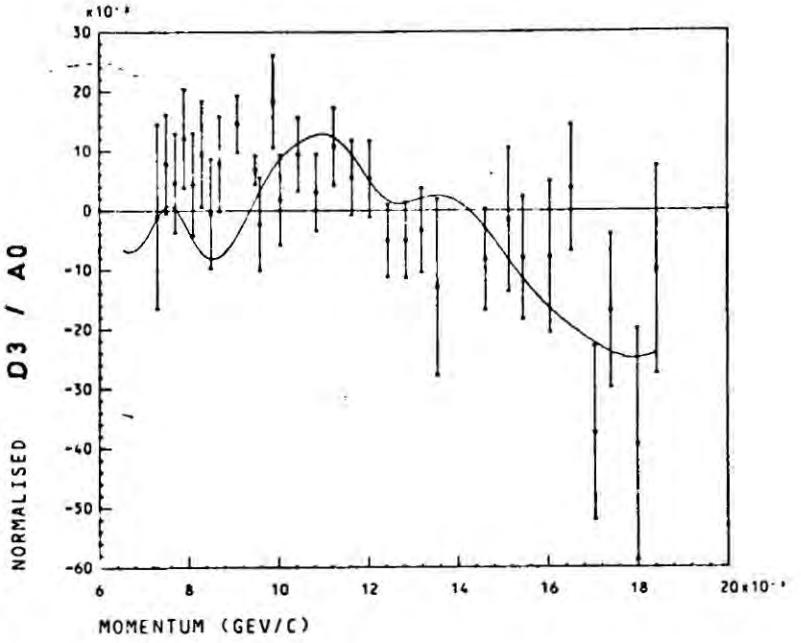

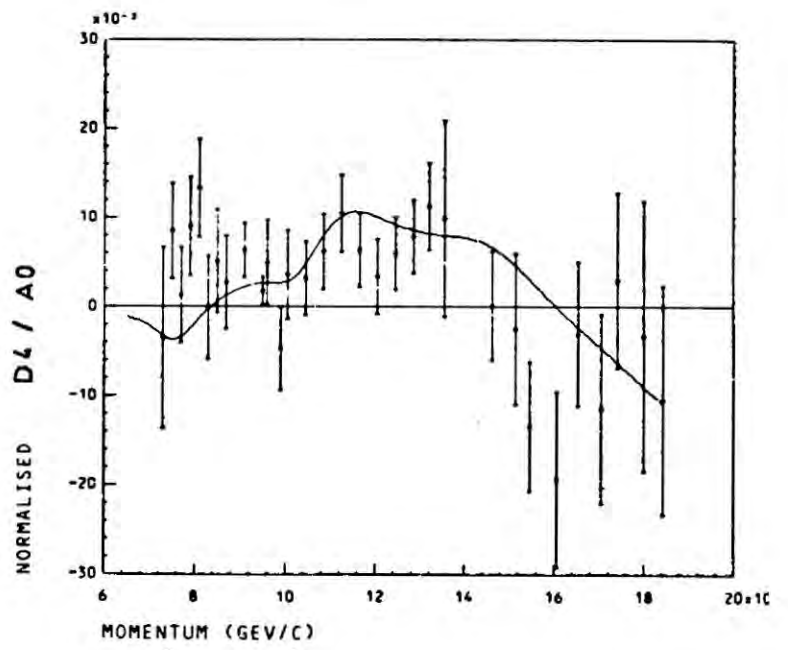

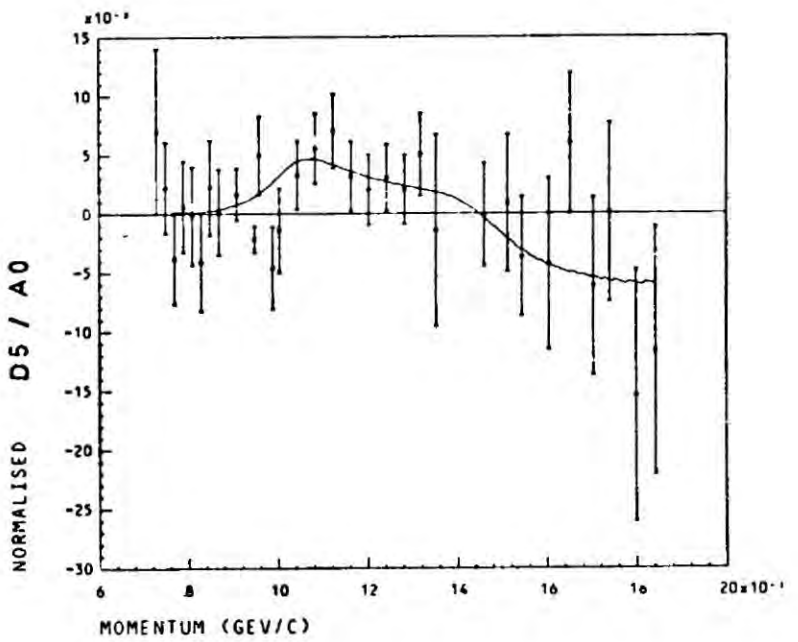

Fig. 6.1 cont. Results of Partial Wave Analysis For The $\pi^+\Sigma^-(1385)$ Channel

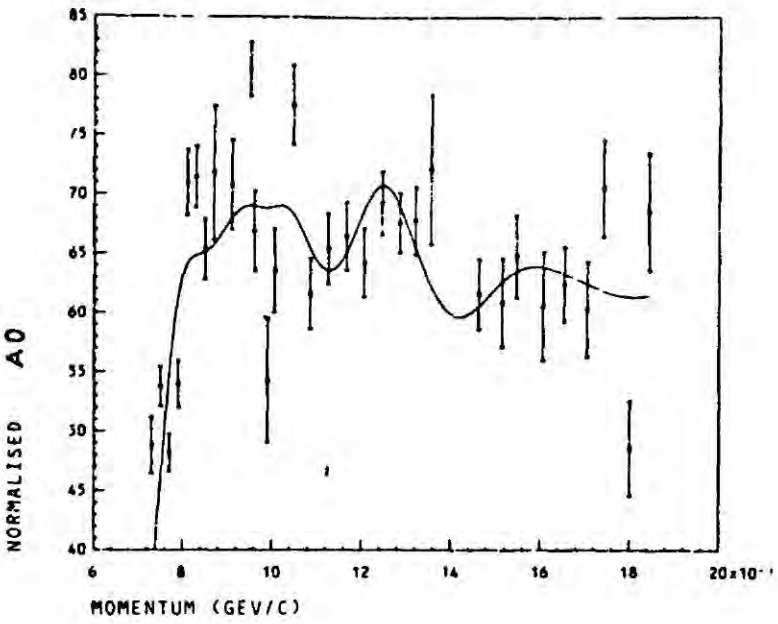

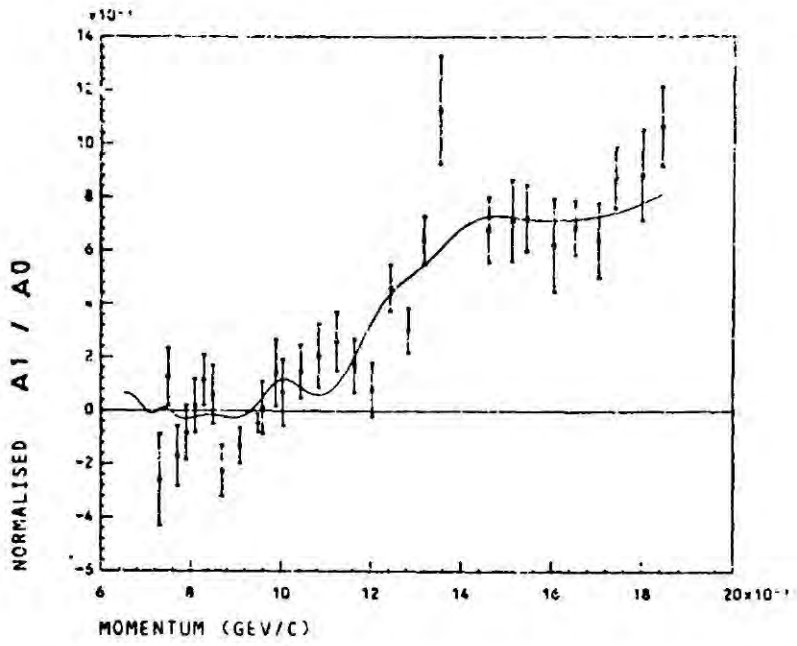

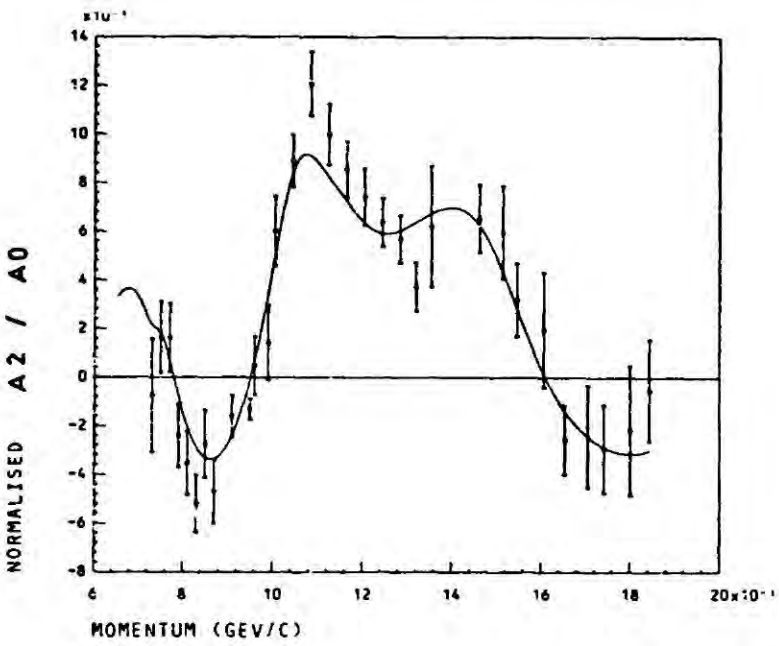

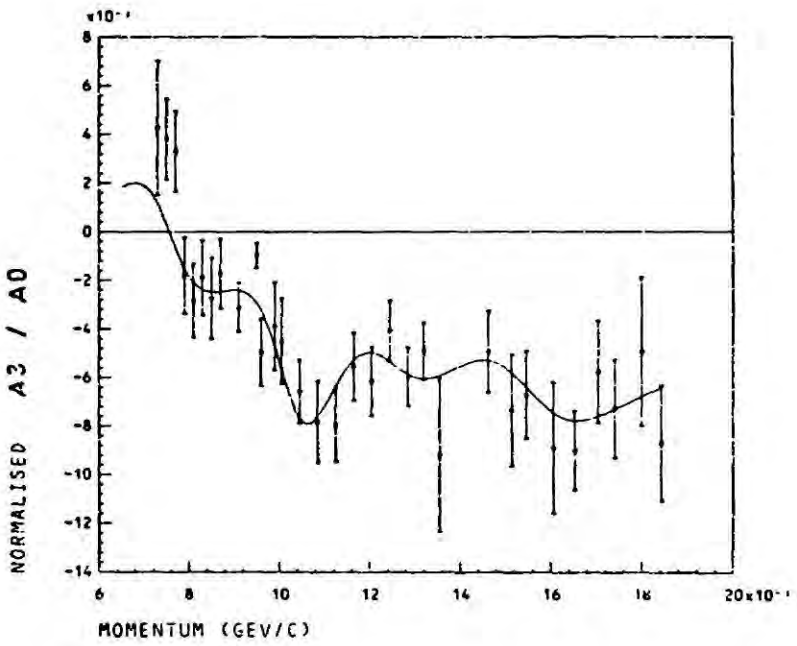

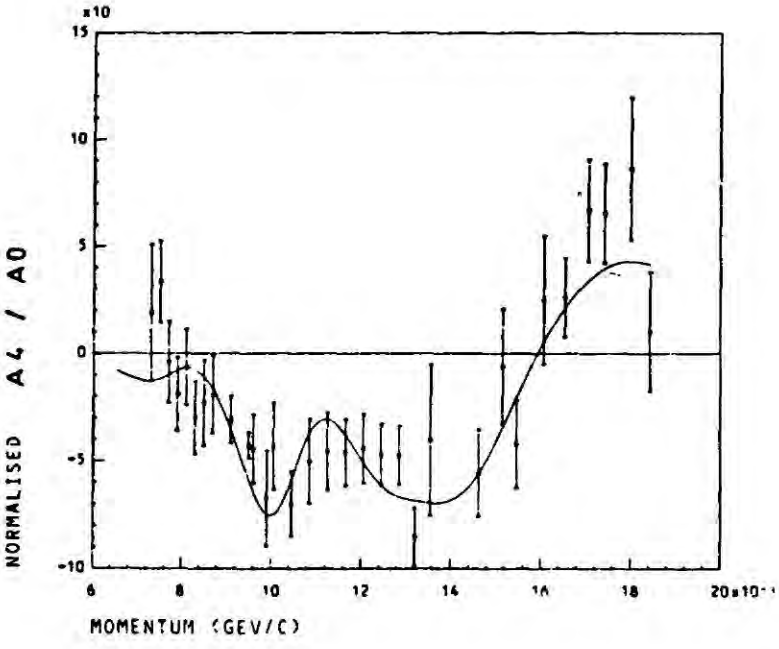

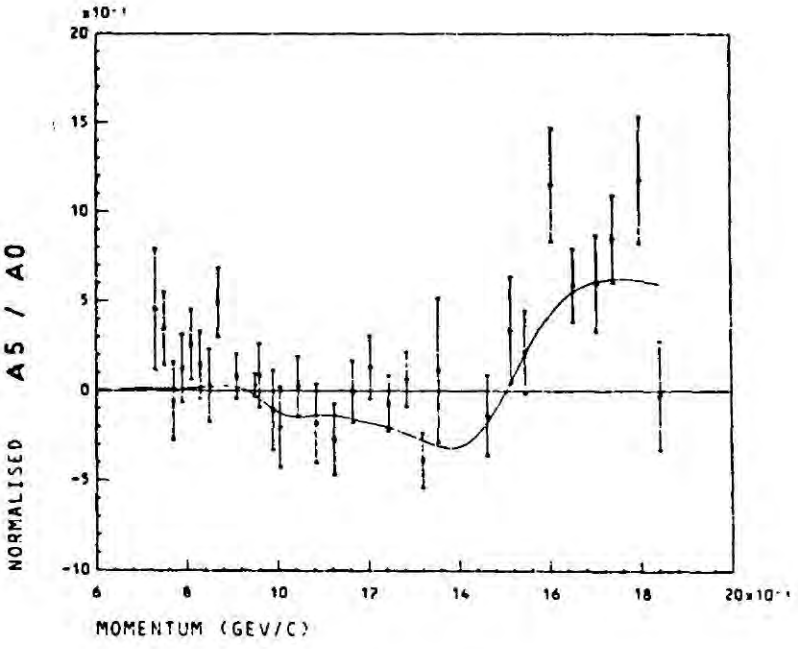

Fig. 6.2 Results of Partial Wave Analysis For The $\pi^{-}\Sigma^{+}(1385)$ Channel

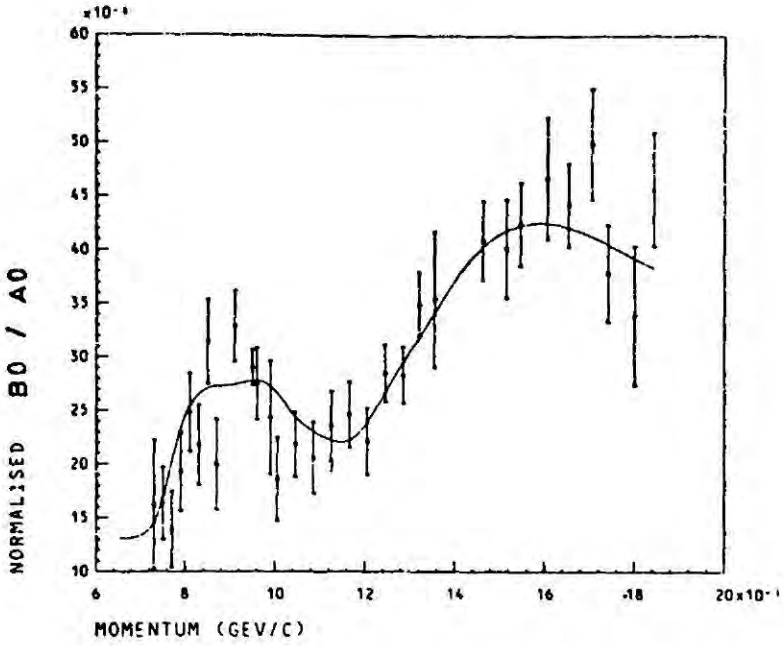

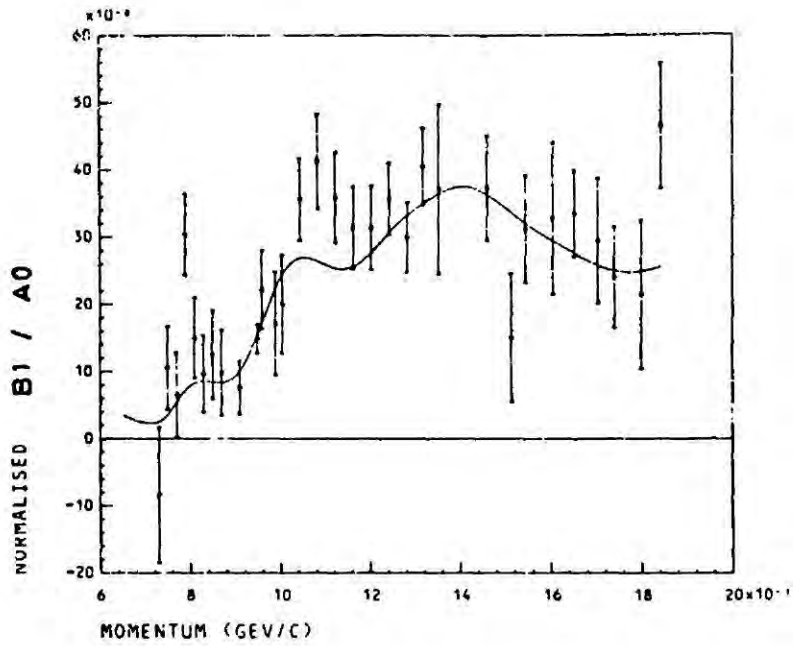

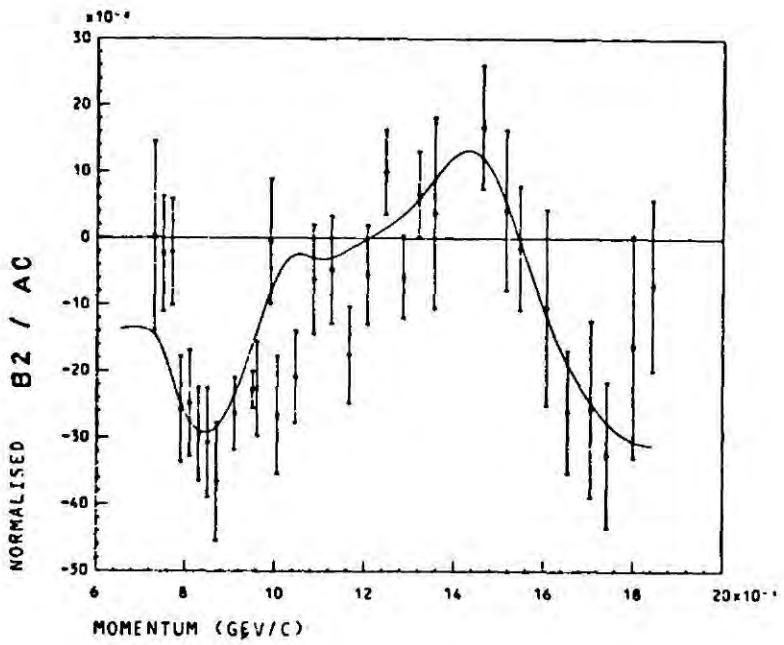

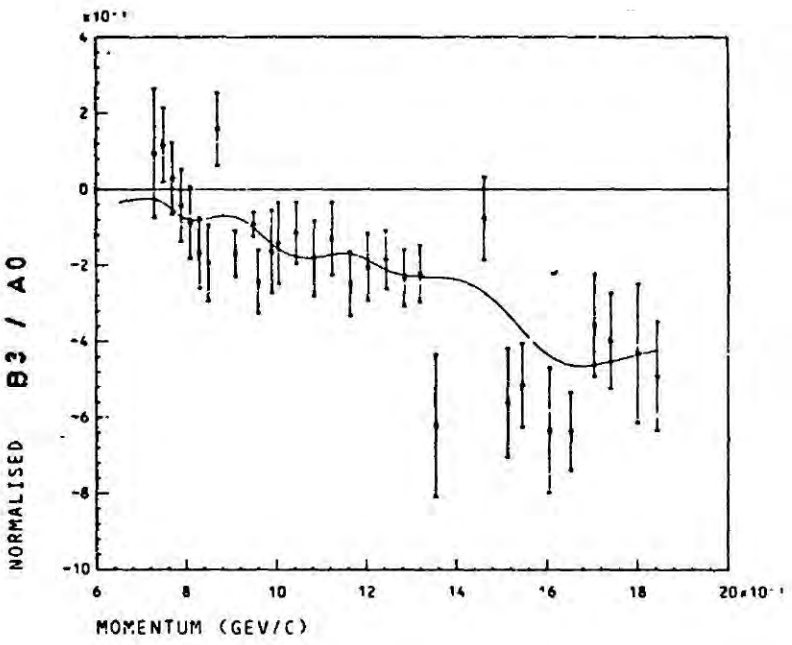

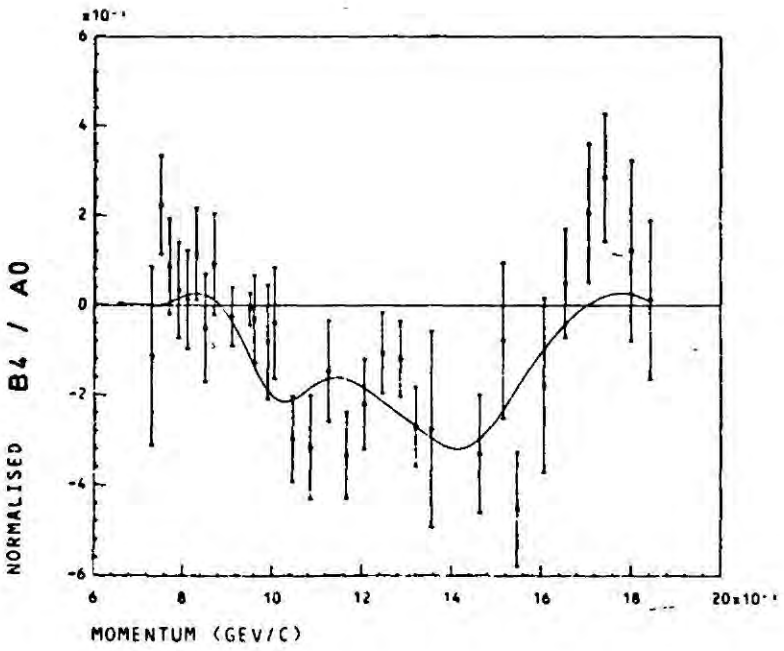

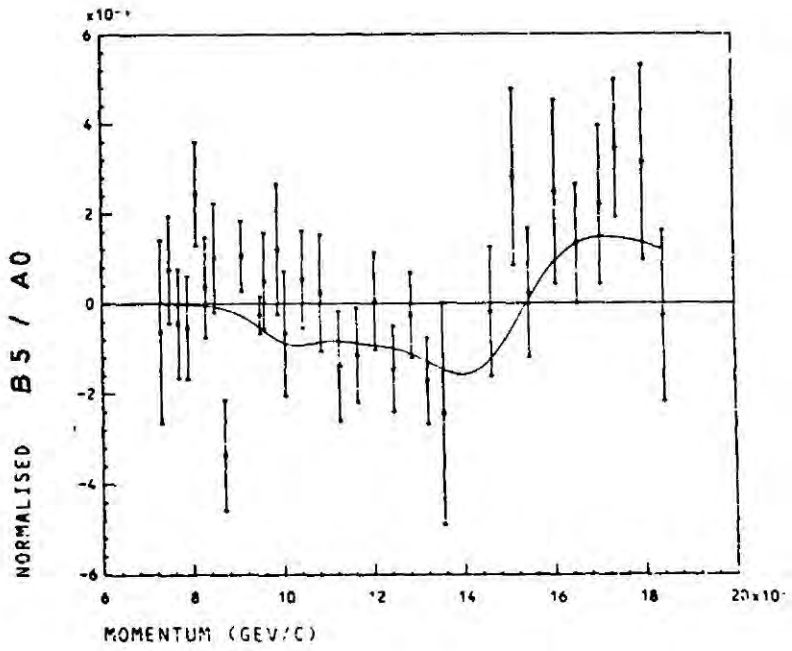

Fig. 6.2 cont. Results of Partial Wave Analysis For The $\pi^- \Sigma^+(1385)$ Channel

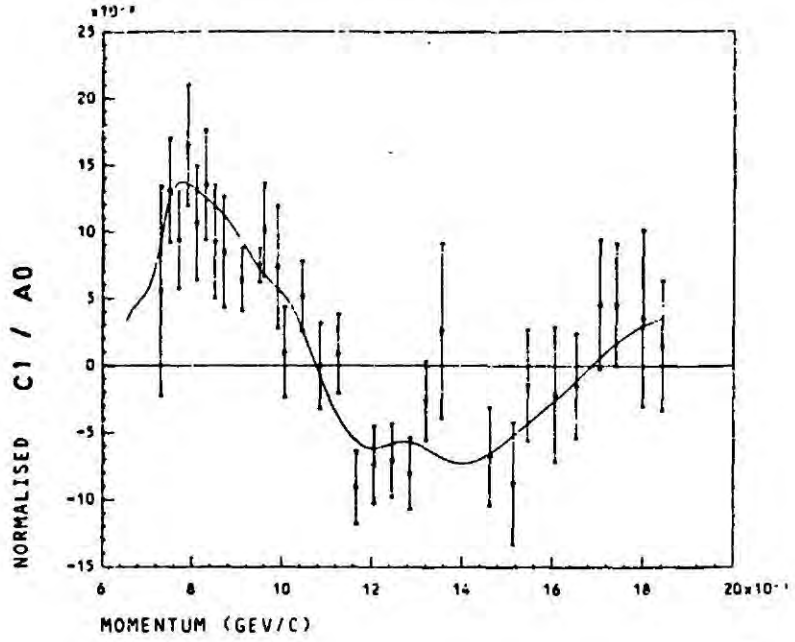

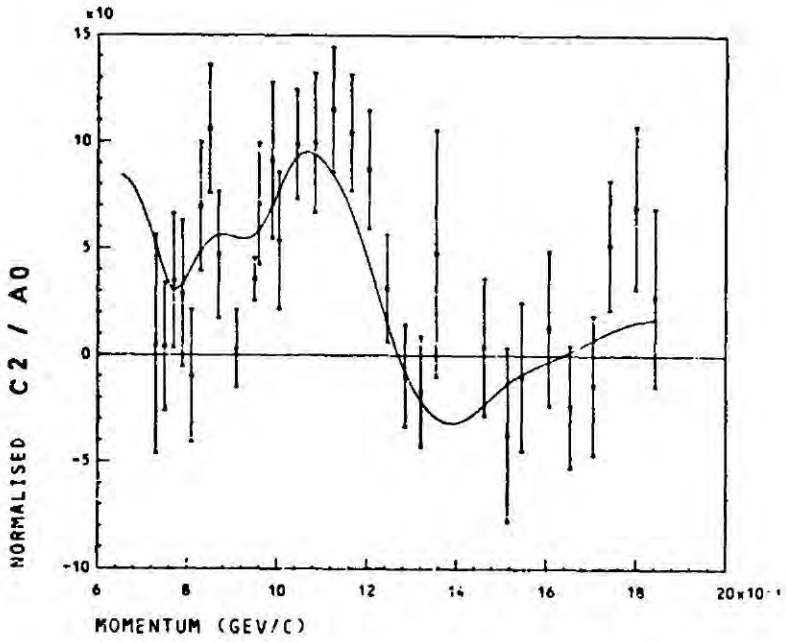

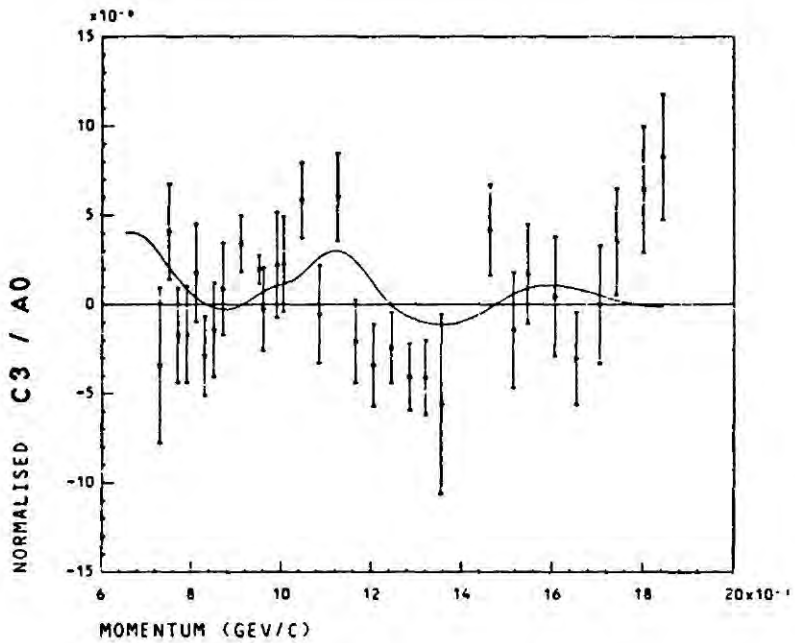

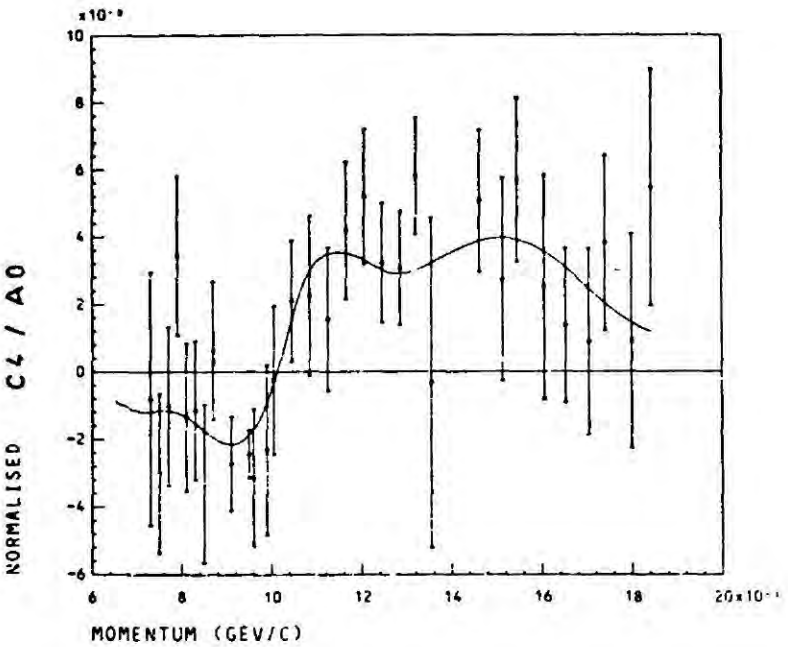

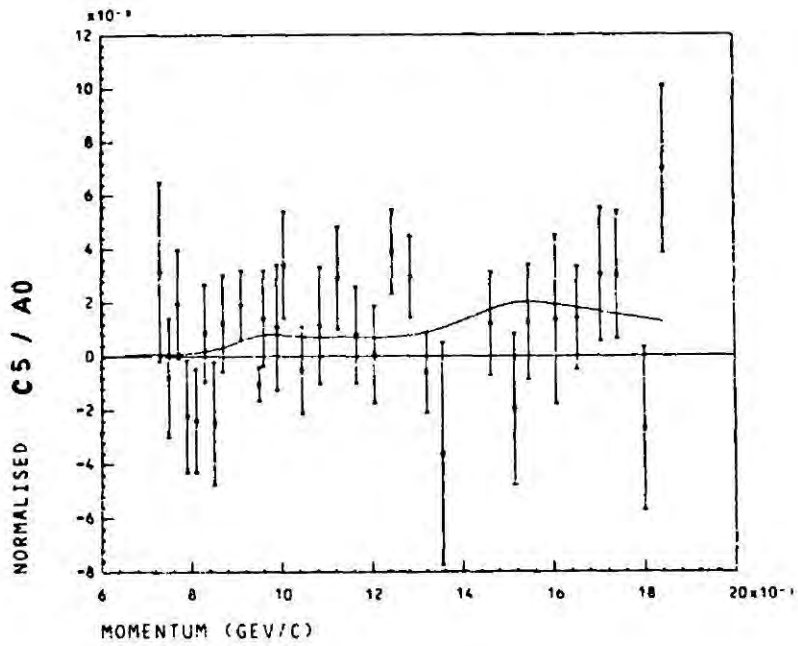

Fig. 6.2 cont. Results of Partial Wave Analysis For The $\pi^- \Sigma^+(1385)$ Channel

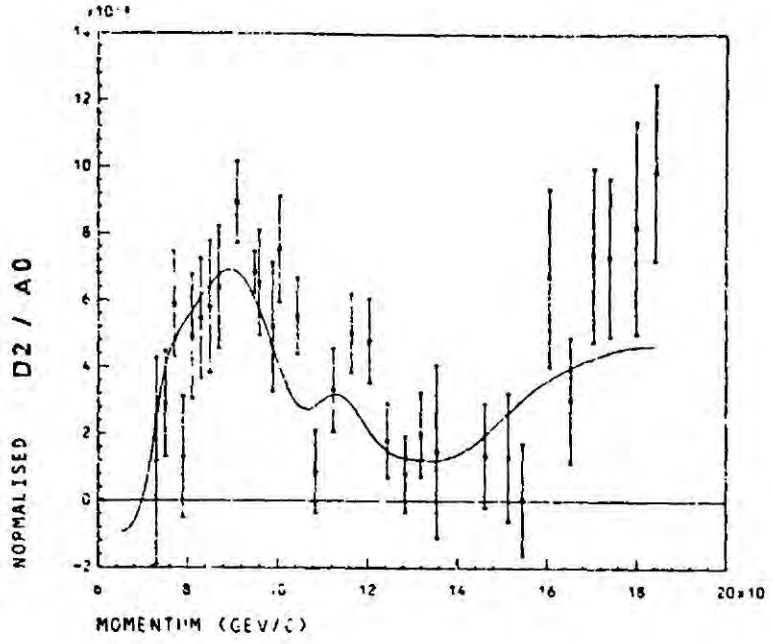

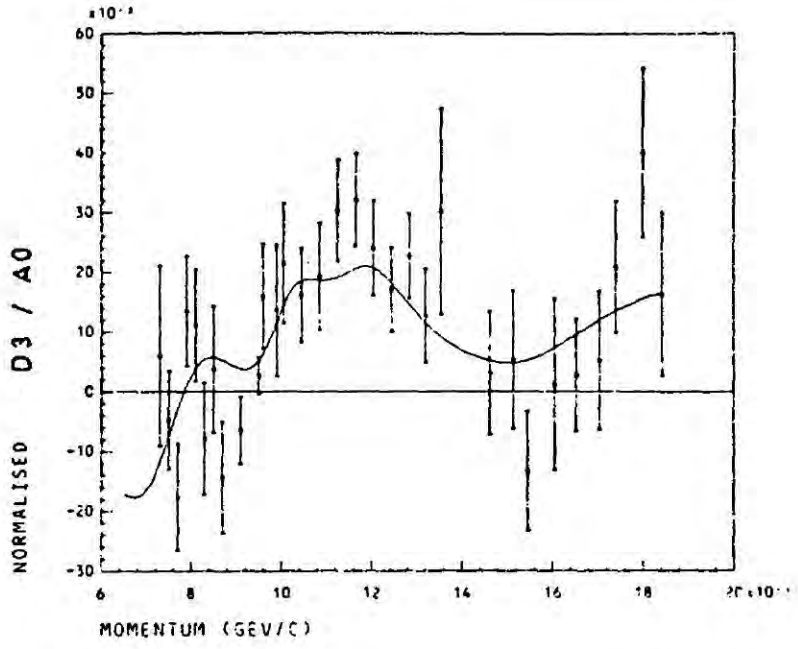

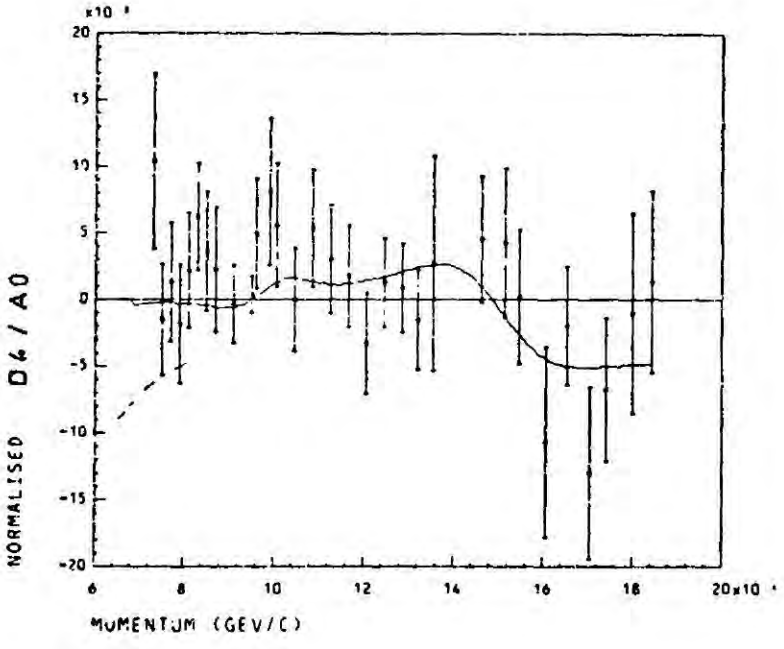

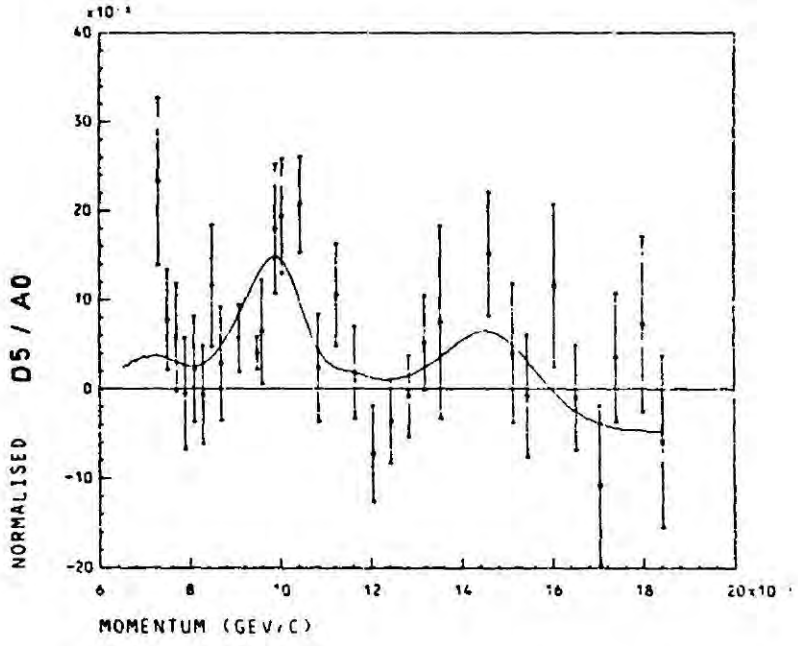

Fig. 6.2 cont. Results of Partial Wave Analysis For The $\pi^- \Sigma^+(1385)$ Channel

of the experimental method and data for the two-body final states from the same experiment are described in reference 6.2.* The method used to extract the $\pi\Sigma(1385)$ quasi two-body final states is based on a maximum likelihood fitting of the Dalitz plot density (given by equation 3.18). Reference 6.3 gives details of this method of analysis and checks performed on the consistency of the results with those obtained by program EXTRA.

The entire data set used is listed in Table 5.3. Data sets for different experiments join smoothly ; there are no apparent discontinuities between different experiments. The cross-sections for production of $\pi^+\Sigma^-(1385)$ and $\pi^-\Sigma^+(1385)$ channels, which are expressed in terms of Ao [figures 6.1 and 6.2], substantially reflect the structures seen in the $\Lambda\pi^+\pi^-$ partial cross-section [see Figure 2.13]. Both cross-sections show a shoulder between 0.750 and 0.800 GeV/c corresponding to the complex region of S01(1670), D13(1670) and D03(1690) formation. Above 0.900GeV/c, the $\pi^+\Sigma^-(1385)$ channel is dominant [see Figure 6.1], a clear enhancement is seen in the 1.00 to 1.30 GeV/c interval where D15(1765), D05(1830) and F05(1815) formation is anticipated to occur. Above 1.30 GeV/c, the $\pi^+\Sigma^-(1385)$ cross-section falls rapidly, [see Figure 6.2] displaying a shoulder at about 1.60 GeV/c, where the spin 7/2 F17(2030) and G07(2100) states have been reported. The $\pi^-\Sigma^+$ (1385) cross-section is less structured and becomes comparable with that for the $\pi^+\Sigma^-(1385)$ channel only above 1.50 GeV/c. Due to their broadness, it is impossible to identify states of particular spin-parity with structures in the cross-sections. To identify the angular momentum content of the s-channel, the coefficient data must be examined.

6.3 QUALITATIVE CONSIDERATIONS OF THE COEFFICIENT DATA

Equations 3.10 and 3.12 allow the coefficient, C_L , which paramatrize $d\sigma/d\Omega$ and $\rho_{mm'}\, d\sigma/d\Omega$ to be expanded in terms of the partial wave

* This is the so-called Survey-3 experiment.

amplitudes $T^{J_1,}_{L_1\ L_1}$ and $T^{J_2,}_{L_2\ L_2}$

$$C_L = \sum_{|J_1-J_2|\leq L\leq J_1+J_2} \xi \quad \mathrm{Re}\left\{ T^{J_1,*}_{L_1\ L_1}\ T^{J_2,}_{L_2\ L_2} \right\} \tag{6.2}$$

where the sum runs over the variables indicated for equation 3.12 and ξ contains the appropriate Clebsch-Gordan coefficients. For the physical $\pi^+\Sigma^-$ (1385) and $\pi^-\Sigma^+$(1385) channels, each of the s-channel partial waves contains admixtures of I = 0 and I = 1 components, dictated by SU(2) isospin Clebsch-Gordan coefficients. Thus, the product $\mathrm{Re}\left\{ T^{J_1,*}_{L_1\ L_1}\ T^{J_2,}_{L_2\ L_2} \right\}$ may be evaluated in terms of pure isospin amplitudes :-

$$\begin{aligned}
\mathrm{Re}\left[T^{J_1,*}_{L_1\ L_1}\ T^{J_2,}_{L_2\ L_2} \right] = & \frac{1}{4}\left\{ \mathrm{Re}\ S(1)\mathrm{Re}\ T(1) + \mathrm{Im}\ S(1)\ \mathrm{Im}\ T(1) \right\} \\
& + \frac{1}{6}\left\{ \mathrm{Re}\ S(0)\mathrm{Re}\ T(0) + \mathrm{Im}\ S(0)\ \mathrm{Im}\ T(0) \right\} \\
& \pm \frac{1}{2\sqrt{6}}\left\{ \mathrm{Re}\ S(1)\mathrm{Re}\ T(0) + \mathrm{Im}\ S(1)\ \mathrm{Im}\ S(0) \right\} \\
& \pm \frac{1}{2\sqrt{6}}\left\{ \mathrm{Re}\ S(0)\mathrm{Re}\ T(1) + \mathrm{Im}\ S(0)\ \mathrm{Im}\ T(1) \right\}
\end{aligned} \tag{6.3}$$

where S(1)/S(0) and T(1)/T(0) correspond to the pure I = 1/pure I = 0 parts of the partial waves $T^{J_1,}_{L_1L_1}$ and $T^{J_2,}_{L_2L_2}$ respectively. The $^+/_-$ signs relate to $\pi^+\Sigma^-$ (1385) and $\pi^+\Sigma^-$(1385) channels. Terms representing the interference of amplitudes with identical isospin appear with the same sign in each final state, interference of different isospin appear with opposite

signs. Only if different isospin amplitudes are orthogonal, i.e. $\pi/2$ out of phase in the Argand plot, should coefficients and cross-sections in different channels be identical.

On evaluation of the Clebsch-Gordan coefficients and angular momentum factors, ξ , Ao may be expressed in terms of the permitted s-channel partial waves which were described in Chapter One of this thesis :-

$$Ao = |SD1|^2 + |PP1|^2 + 2|PP3|^2 + 2|PF3|^2$$

$$+ 2|DS3|^2 + 2|DD3|^2 + \ldots\ldots (2J+1)|T_{LL}^{'J}|^2 \qquad (6.4)$$

Hence, differences in structures observed in the channel cross-sections are due to interferences of partial waves of different isospin but identical angular momentum content. An example of such an effect is the enhancement of the $\pi^+\Sigma^-(1385)$ cross-section between 1.0 and 1.3 GeV/c where FO5(1815)-F15(1915) and DO5(1830)-D15(1765) interferences occur.

Turning to the coefficient data, the following observations can be made concerning the partial wave expansions given by equation 3.10 and 3.12 for $\pi\Sigma(1385)$ final states :-

(i) Even -L coefficients are formed as a sum of products of like-parity amplitudes ; odd -L coefficients are formed as a sum of products of unlike-parity amplitudes.

(ii) The total angular momenta of amplitudes which may appear in products for a coefficient of given order L are limited by :-

$$|J_1 - J_2| \leq L \leq J_1 + J_2 \qquad (6.5)$$

(ii) The B_L coefficients, which paramatrize $\rho_{33}(\cos\theta^*)d\sigma/d\Omega$, do not contain $J = \frac{1}{2}$ amplitudes.

The most structured coefficients are :-

(i) For the $\pi^+\Sigma^-(1385)$ final state, A_1, A_3, B_1 and B_3 in the 0.70 to 1.10 GeV/c interval [see Figure 6.1].

(ii) For the $\pi^-\Sigma^+(1385)$ final state, A_2 and B_2 in the 1.0 GeV/c region (see Figure 6.2).

Since the structure observed in the 0.70 to 1.10 GeV/c region appears most pronounced in the $\pi^+\Sigma^-(1385)$ odd-coefficient data and is common to both A_1 and B_1 [see Figure 6.1], it is due to interferences of different-isospin, unlike-parity, amplitudes. Regarding this not as one structure, but as two different effects centred on 0.80 GeV/c and 1.0 GeV/c respectively, the s-channel dynamics can be considered as a sum of $J^P = 5/2^-$ and $J^P = 3/2^-$ resonant amplitudes interfering with common, non-resonant, $J^P = 3/2^+$ amplitudes. Clearly, the D03(1690) and D15(1775) are good candidates for such resonances. Alternative models which involve $J^P = 5/2^+$ resonances require a greater number of non-resonant amplitudes.

The structures present in both A_2 and B_2 can clearly be interpreted in several ways. In terms of the approximations used to explain the structures in A_1 and B_1, these may be accounted for by the following terms which appear in the partial wave expansion implied by equation 6.2 :-

(i) $|DS3|^2$, $|DD3|^2$, Re $(DD3^* . DS3)$ for the $J^P = 3/2^-$ D03(1690) and D13(1670) resonant amplitudes in the 0.80 GeV/c region.

(ii) $|DD5|^2$, $|DG5|^2$, Re $(DD5^* DG5)$ for the $J^P = 5/2^-$ D05(1830) and D15(1775) resonant amplitudes in the 1.0 GeV/c region.

(iii) $|FP5|^2$, $|FF5|^2$, Re $(FP5^* . FF5)$ for the $J^P = 5/2^+$ F05 and F15 resonant amplitudes in the 1.0 GeV/c region.

Different-isospin interference effects are clearly present since similar structures are not seen in the $\pi^-\Sigma^+(1385)$ data. Interferences of different spin resonances, represented by terms of the form Re $\left[DS3^* \; DD5 \right]$ will

also contribute in the region of overlap between DO3(1690) and D15(1775). Since terms of the form $|DS3|^2$ and $|DD3|^2$ do not contribute to the L = 4 coefficients, an indication of the onset of J = 5/2 s-channel dynamics is given by terms of the form $|DD5|^2$ and $Re(DS3^* DD5)$. Inspection of these L = 4 coefficients indicate such effects become important above 0.85 GeV/c.

Spin 7/2 resonance structures are indicated by the L = 6 coefficients $[A_6, B_6, C_6$ and $D_6]$, to which purely spin 5/2 resonance contributions, from terms such as $|FP5|^2$, $|DD5|^2$, do not occur. Resonance terms such as $|GD7|^2$ and $|FF7|^2$ together with interference terms such as $Re[FF5^* FF7]$ and $Re[DD5^* GD7]$ will determine the onset of J = 7/2 effects. Inspection of Figures 6.1 and 6.2 reveals that the L = 6 coefficients are consistent with zero below 1.35 GeV/c and show structure at 1.60 GeV/c, i.e. in the region of the F17 (2030) and GO7(2100) states.

Hence, much of the resonance structure obscurred in the $\pi\Sigma(1385)$ channel cross-sections, due to the widths of states formed in the s-channel, are evident in the coefficient data. A more quantitative approach will now be attempted to determine which partial waves are most significant in the low-energy Survey 81 region.

6.4 QUANTITATIVE INVESTIGATION OF THE L = 3 COEFFICIENTS

Given the evidence presented in the previous section that J = 5/2 amplitudes are not significant in the 0.730 to 0.850 GeV/c range of Survey 81, it is possible to extract more direct information concerning the J = 3/2 partial waves from the L = 3 coefficients in an energy independent manner. For each of the two $\pi\Sigma(1385)$ channels, the four L = 3 coefficients are determined by the following mixed-isospin partial wave products :-

$$P_1 = Re[PP3^* DS3] \qquad P_2 = Re[PF3^* DS3]$$
$$P_3 = Re[PP3^* DD3] \qquad P_4 = Re[PF3^* DD3]$$

the relationships being :-

$$A_3/Ao = 0.0\ P_1 - 5.367\ P_2 - 3.22\ P_3 + 4.293\ P_4 \quad (6.6)$$

$$B_3/Ao = -0.805\ P_1 - 0.268\ P_2 - 0.805\ P_3 - 0.268\ P_4 \quad (6.7)$$

$$C_3/Ao = 0.310\ P_1 - 0.155\ P_2 - 0.155\ P_3 - 0.310\ P_4 \quad (6.8)$$

$$D_3/Ao = -0.077\ P_1 - 0.155\ P_2 + 0.155\ P_3 - 0.077\ P_4 \quad (6.9)$$

Unique analytical solution of these four simultaneous linear equations is possible in terms of the products P_1, P_2, P_3 and P_4, given the values of A_3, B_3, C_3 and D_3 at each energy. An additional check on the validity of the assumption concerning the smallness of higher spin-amplitudes comes from the condition that $B_1 = -B_3$ provided $J \geq \frac{5}{2}$ amplitudes are ignored. Figure 6.3 shows the quantity $(B_1 + B_3)/A_o$, as a function of incident momentum, for both $\pi\Sigma(1385)$ final states, which is consistent with zero below 0.900 GeV/c. The curve represents the prediction for this quantity from a partial wave analysis described later in this chapter.

Figures 6.4 and 6.5 show the products P_1, P_2, P_3 and P_4 as a function of incident momentum, for $\pi^+\Sigma^-(1385)$ and $\pi^-\Sigma^+(1385)$ final states. For both channels, the products P_1 and P_3 are most significant and are structured over the Survey-81 incident momentum range. This indicates that strong resonant couplings of the DO3(1690) and Dl3(1670) states may be anticipated to both DS3 and DD3 waves. The dominant $J^P = 3/2^+$ non-resonant amplitudes is the PP3 partial wave.

6.5 THE PARAMATRIZATION OF AMPLITUDES

The energy dependent partial wave analysis of the coefficient data has been undertaken using the now standard program APPLE developed at the Saclay Laboratory and modified by the Imperial College/Rutherford Laboratory Collaboration. In its present form, this program has been extensively used for the analysis of several two-body and quasi-two-body final states of $\bar{k}N$ interactions. Details of the energy dependent paramatrizations and the

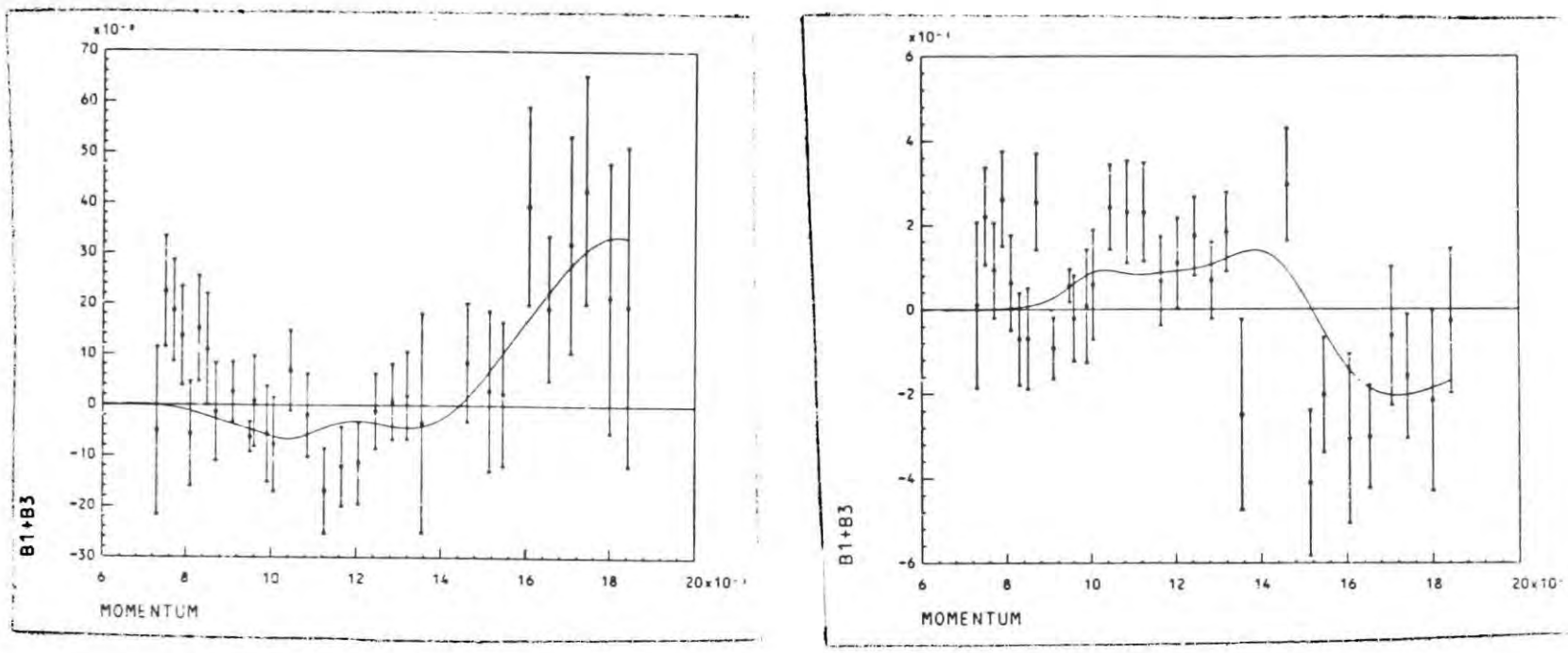

Fig. 6.3 The Quantity $B_1 + B_3$ as a Function of Incident Momentum

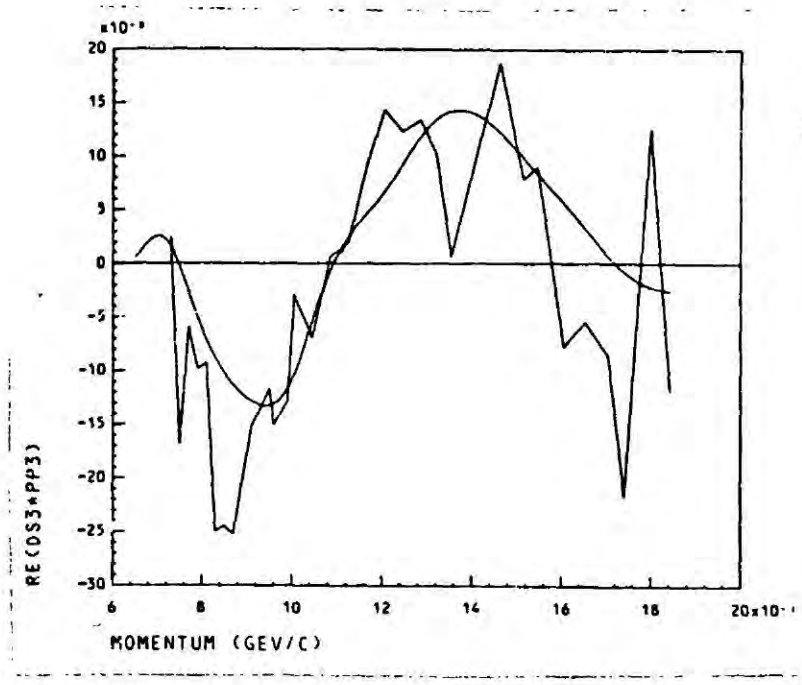

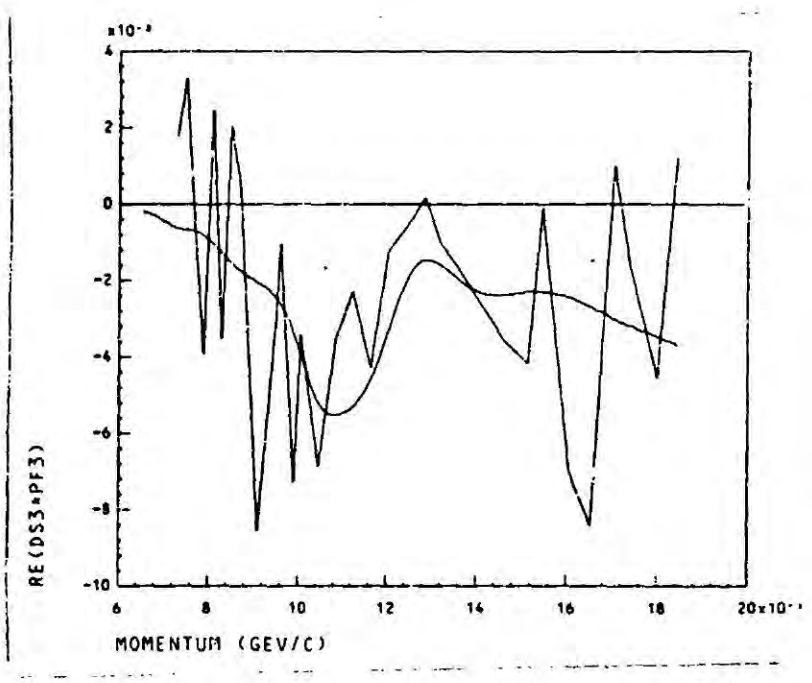

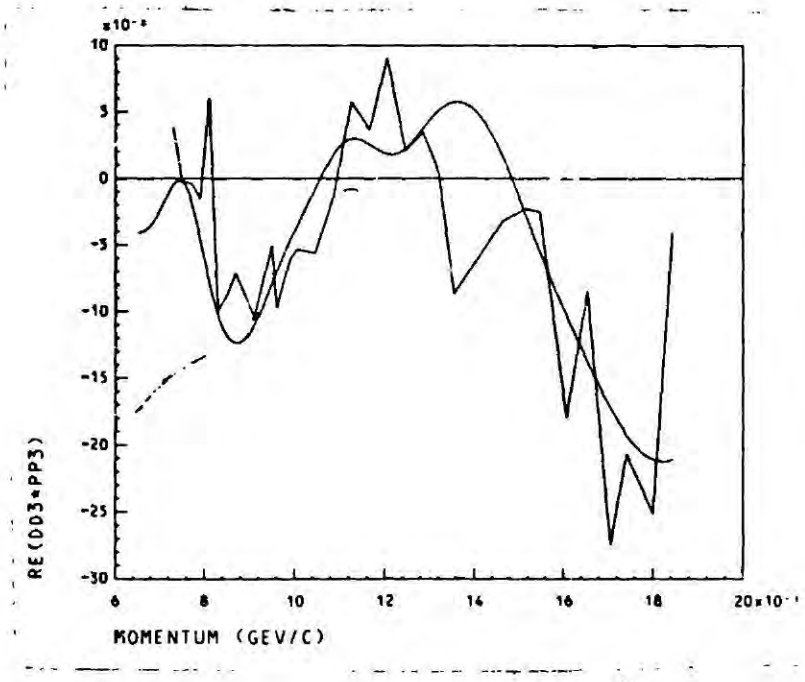

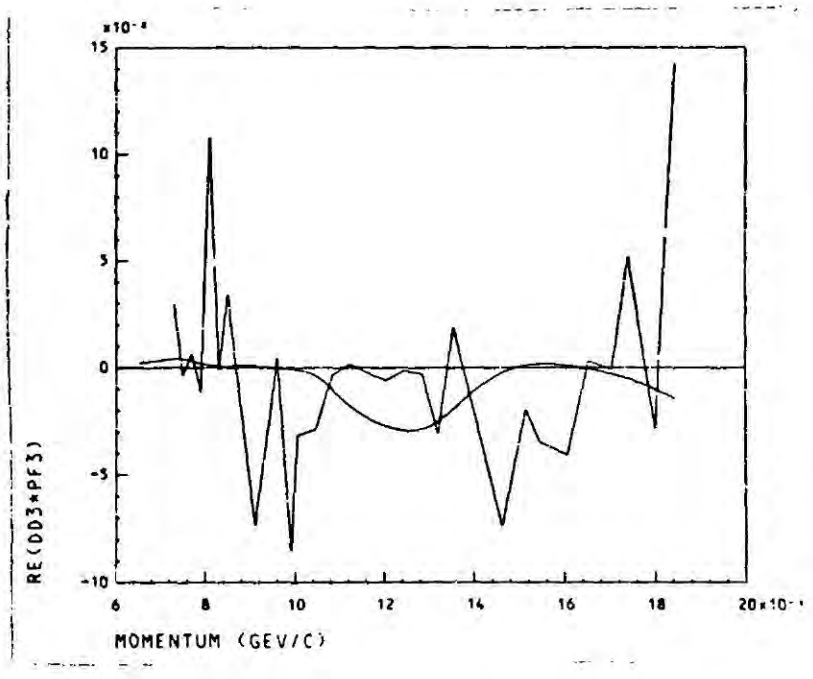

Fig. 6.4 Mixed-Isospin Partial Wave Products For The $\pi^+\Sigma^-(1385)$ Channel

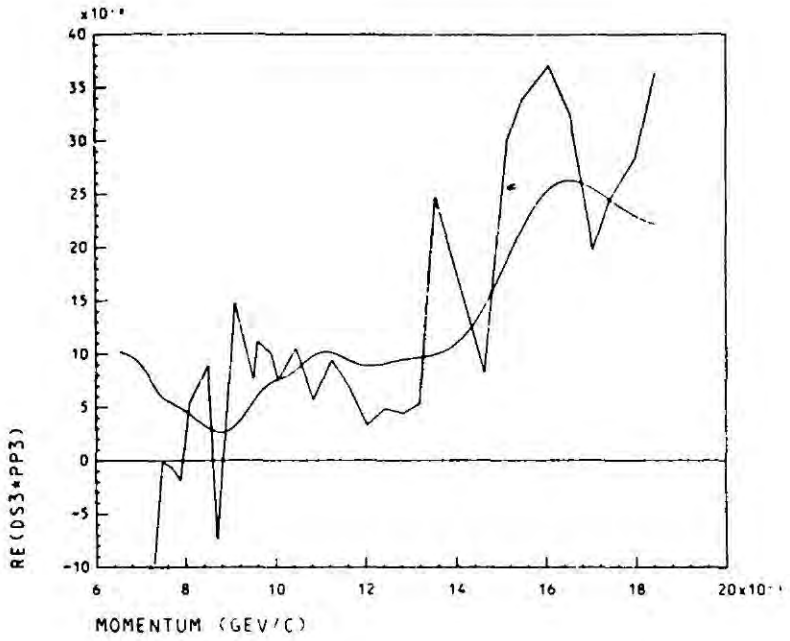

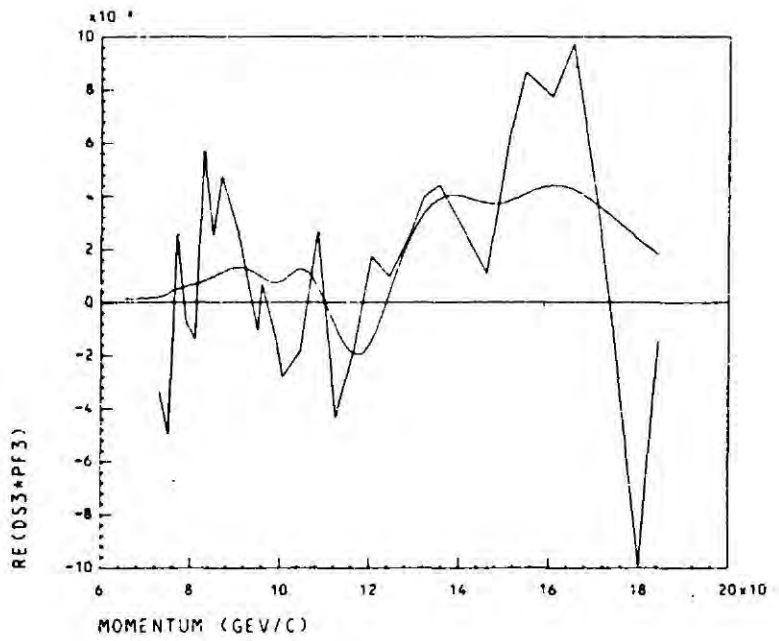

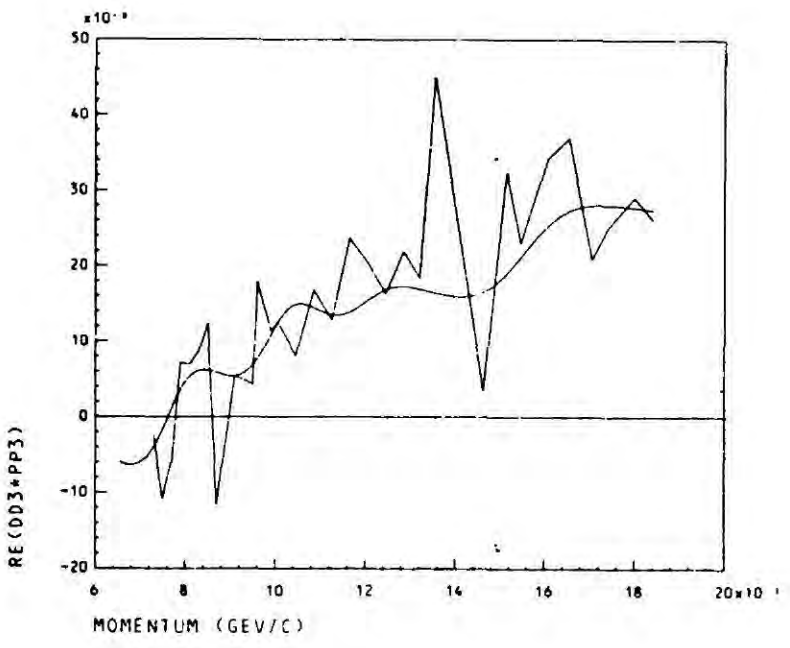

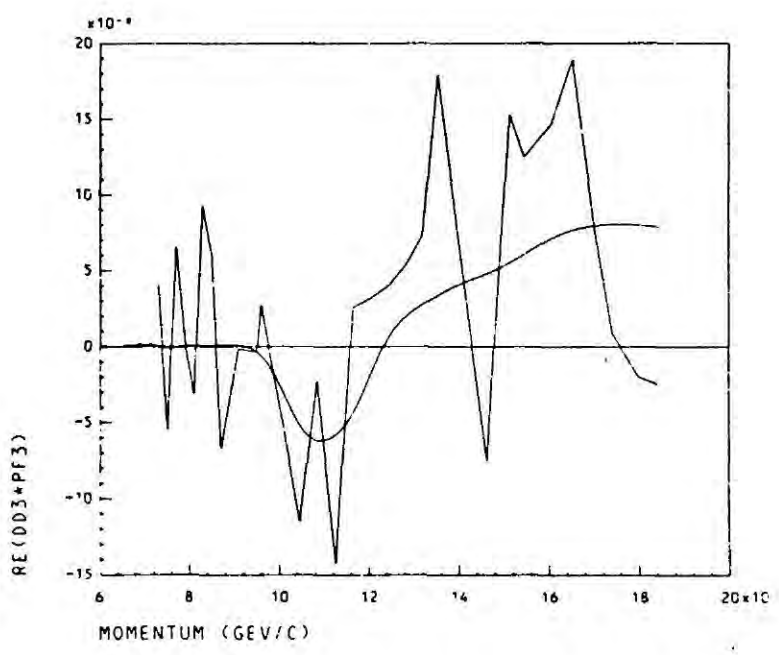

Fig. 6.5 Mixed-Isospin Partial Wave Products For The $\pi^- \Sigma^+(1385)$ Channel

method of analysis used are given in references 6.1,6.3 and 6.4.

In principle, each amplitude may contain a sum of resonant and non-resonant parts. Resonant amplitudes are represented by non-relativistic Breit-Wigner forms :-

$$T_R = \frac{t}{\varepsilon - i} \cdot e^{i\phi} \qquad (6.10)$$

where ϕ represents a rotation of the resonant amplitude in the Argand plane, t is the amplitude at resonance and

$$\varepsilon = \frac{2(E_R - E)}{\Gamma(E)} \qquad (6.11)$$

Energy dependence of the full width, $\Gamma(E)$, is represented by Blatt and Wiesskopf barrier factors $\nu_\ell(kr)$, expressed in terms of the incoming orbital angular momentum ℓ and the incident centre of mass momentum k :-

$$\Gamma(E) = \Gamma(E_R) \frac{k\, \nu_\ell(kr)}{k_k\, \nu_\ell(k_R r)} \cdot \frac{E_R}{E} \qquad (6.12)$$

where E_R and k_R are the values of centre of mass energy, E, and k evaluated at the position of the resonance. The functions $\nu_\ell(kr)$ are evaluated in terms of the effective range of the strong interaction r, which is taken to be 1 Fermi, and are listed in Table 6.1.

Assuming that the partial widths in the elastic and $\pi\Sigma(1385)$ channels, Γ_e and Γ_i, have identical energy dependence, then the amplitude at resonance, t, has the energy independent value :-

$$t = \sqrt{\frac{\Gamma_i(E_R)\ \Gamma_e(E_R)}{\Gamma^2(E_R)}} \qquad (6.13)$$

Non-resonant background amplitudes were chosen to have the form

$$T_B = \sqrt{B_\ell B_{\ell'}} \quad R(E') \exp\left[i \Theta (E') \right] \tag{6.14}$$

where $R(E')$ and $\Theta(E')$ are Legendre polynomial expansions

$$R(E') = \sum_{m=0}^{M} a_m P_m (E') \tag{6.15}$$

$$\Theta(E') = \sum_{n=0}^{N} b_n P_n (E') \tag{6.16}$$

N and M being the maximum orders of expansion. These are expressed in terms of the normalized energy variable :-

$$E' = \frac{2E - E_{max} - E_{min}}{E_{max} - E_{min}} \tag{6.17}$$

where E_{max} is the maximum energy of the fitted range and E_{min} is the lowest energy. When $E = E_{max}$, $E' = +1$ and when $E = E_{min}$, $E' = -1$. Barrier effects, which depend on the incident and final state angular momenta , ℓ and ℓ', are represented in terms of the energy dependent factor $\sqrt{B_\ell B_{\ell'}}$,

$$B_\ell = \frac{k}{k_{max}} \cdot \frac{E_{max}}{E} \cdot \frac{\nu_\ell (kr)}{\nu_\ell (k_{max} r)} \tag{6.18}$$

where k_{max} is the centre of mass momentum for the initial state evaluated at the maximum energy of the analysis. An identical expression exists for $B_{\ell'}$ in terms of the final state momentum q.

The barrier factors, used in the expressions for the full width and the background amplitudes, ensure that the partial waves embody energy dependence which is in accordance with the results of potential theory. Such energy

L	$\nu_L(R)$
0	1
1	$R^2/(1 + R^2)$
2	$R^4/(9 + 3\,R^2 + R^4)$
3	$R^6/(225 + 45\,R^2 + 6\,R^4 + R^6)$
4	$R^8/(11025 + 1575\,R^2 + 135\,R^4 + 10\,R^6 + R^8)$

TABLE 6.1 : Blatt and Weisskopf barrier factors

behaviour suppresses higher angular momentum background amplitudes and the low energy tails of rather wide resonances near threshold for the $\pi\Sigma(1385)$ channel.

Free parameters used in fitting the $\pi\Sigma(1385)$ channels will be t and ϕ for each resonance in each partial wave, together with the background parameters required. Masses and widths of states will be constrained to the values given in Tables 1.1 and 1.2. Fitting of parameters is performed using a minimum χ^2 method.

6.6 DEVELOPMENT OF PARTIAL WAVE SOLUTIONS

Two rather different methods have been used to develop energy dependent solutions for the partial wave amplitudes. Firstly, the previously published $\pi\Sigma(1385)$ solution has been extended in energy, so as to preserve those structures already described in reference 6.1. Secondly, a new solution has been developed in order to exploit the proximity of the S01(1670), D13(1670) and D03(1690) states, which constrain the behaviour of the lower angular momentum amplitudes. In addition, the strong interference effects discussed in Section 6.4 will determine the low energy behaviour of the PP3 amplitude.

6.6.a The Extended Energy Range Solution

The previous partial wave analysis [reference 6.1] of the $\pi\Sigma(1385)$ channels, performed by the RL/IC group, covers the centre of mass energy range 1775 to 2170 MeV. Couplings of the established P03(1900), D05(1830), D15(1775), F05(1820), F15(1906) and F17(2040) states were observed to the permitted partial waves. In addition, evidence was seen for the less well established S01(1825), D13(1920) and F05(2100) states. Non-resonant backgrounds were found necessary in all amplitudes with $J \leq 5/2$, the exceptions being SD01, FP05 and FF05. Final results of this analysis are given in Table 6.2.

In order to extend the energy range of this analysis and include new

data, the following procedure was adopted :-

(i) All resonant amplitudes previously found were fixed and the solution reconverged with the background amplitudes free. As expected, the quality of the fit was rather poor, no account being given of the structures in the 0.800 GeV/c region.

(ii) Resonant amplitudes for the well established S01 (1670), D13(1670) and D03(1690) states were introduced into the permitted partial waves and the solution reconverged with backgrounds and resonant amplitudes free. This solution gave a χ^2 of 1930 for 1561 degrees of freedom.

(iii) An attempt was then made to reconverge this solution with the addition of various less well established states. Firstly, the P11(1675) and P11(1870) states were added to the PP11 amplitude giving an improved χ^2 of 1857 for 1559 degrees of freedom. The P11(1675) showed a strong resonant signal, while the P11(1870)had a less pronounced resonant amplitude. Addition of the D03(1815) and F15(2130) states resulted in neither an appreciable decrease in χ^2 nor did they show strong resonant amplitudes.

The final solution has a χ^2 per degree of freedom of 1.19. Masses and widths of states used, together with the final resonant amplitudes, are given in Table 6.2. Inclusion of new data has not appreciably changed the resonant amplitudes found previously. In particular, the Survey 3 data in the 0.870 to 1.00 GeV/c interval, which covers the low energy tail of the D15(1775), has not affected its couplings to DD15 or DG15 partial waves. Large resonant amplitudes in both DD03 and DS03 partial waves for the D03(1690) indicate that this state is responsible for coefficient structures in the 0.800 GeV/c region.

6.6.b The New Solution

Structure seen in the $\pi^+\chi^-$ (1385) A_1 and B_1 coefficients [see figures 6.1 and 6.2] was shown in Section 6.4 to be consistent with the interference of a strong $J^p = 3/2^+$ background amplitude with $J^p = 3/2^-$

resonant amplitudes due to s-channel formation of D13(1670) and DO3(1690) states. Hence, the presence of narrow resonances in the Survey-81 region can place constraints on the lower angular momentum partial waves, which previously contained no stable resonant structure. In order to exploit this fact,an entirely new solution has been developed. This not only includes the new data described in Section 6.2, but makes use of the improved parameters available for some of the poorly confirmed states described in Section 1.3.

Clearly, one very important feature of an acceptable energy dependent partial wave solution is that it should contain as little arbitrary structure and as few free parameters as possible. To observe this criteria, the following procedure has been adopted to fit cross-sections and coefficient data for the $\pi\Sigma(1385)$ channels.

(i) A fit to the data was performed including only the well established states listed in Table 1.1. No background amplitudes were included and the only free parameters were the amplitudes at resonance in each permitted partial wave for the following states : SO1(1670), PO3(1896), DO3(1690), D13(1670), DO5(1823), D15(1775), FD5(1820), F15(1930), F17(2040)and GO7(2110). However the quality of fit was poor, χ^2 having a value of 7365 for 1609 degrees of freedom.

(ii) Those states which are described as poorly established in Table 1.1 were then introduced, i.e. SO1(1810), S11(1768), S11(1925), PO1(1580), PO1 (1850), P11(1670), P11(1870), D13(1920), FO5(2115) and F15(2060). With all resonant amplitudes free, an improved value of χ^2 = 4584 for 1597 degrees of freedom was obtained. As such, no account was given for the structures seen in the $\pi^+\Sigma^-(1385)$ B_1, A_3, B_3, C_3 or D_3 coefficients and the $\pi^-\Sigma^+(1385)B_2$ coefficient in the 0.700 to 1.200 GeV/c range. Coefficients which do not involve interference between amplitudes of different J^P, i.e. Ao and Bo, were moderately well described.

(iii) To overcome the difficulties described previously, background amplitudes were introduced. A systematic method, economical on computer time, was used to investigate the importance of various non-resonant amplitudes. All of the resonant amplitudes for 4* and low-* states were fixed at the values found in (ii) above. Then, for each partial wave in turn, fits were performed with the parameters of an N = M = O background (as defined by equation 6.14) free. On the basis of χ^2 per degree of freedom, background amplitudes were found necessary in all amplitudes with $J \lesssim 5/2$. With resonance parameters still fixed, a multi-background fit was performed, with two parameter backgrounds free to vary in each amplitude with $J \lesssim 5/2$. A subsequent fit with background and resonant amplitude free to vary gave a value $\chi^2 = 2451$ for 1557 degrees of freedom. The advantage of this method was to preserve as much resonant structure as possible in the amplitudes.

(iv) Although accounting for most of the major trends and structures in the coefficient data, the fit developed in Stage (iii) above did not describe the full magnitude of structures in the $\pi^+\Sigma^-(1385)$ B_1, B_3 or C_3 and the $\pi^-\Sigma^+(1385)$ B_2 coefficients. A second iteration was performed to ascertain whether inclusion of N = M = 1 backgrounds (as defined by equation 6.14) were required in particular partial waves. All resonant and background parameters were fixed. On a wave by wave basis, identical to Stage (iii), the parameters of N = M = 1 backgrounds were allowed to vary. Again, on the basis of improved χ^2 per degree of freedom higher order backgrounds were found necessary in PPO1, PPO3, PP13, DSO3 and FP15 amplitudes. A fit with all parameters free to vary gave a value of $\chi^2 = 1862$ for 1533 degrees of freedom.

(v) Several of the amplitudes fitted contained two resonances, in order to relax the condition that Breit-Wigner amplitudes should be purely imaginary at their resonance masses, the phases, ϕ, were allowed to vary in

various waves. Freedom of phase was permitted for the following resonant amplitudes : SDO1(1670), SDO1(1810), SD11(1768), SD11(1925), DS13(1670), DD13(1670), DS13(1920), DD13(1920), FFO5(1820), FFO5(2115), FF15(1930) and FF15(2060).

Also, particularly small resonant FP15(1930) and FP15(2060) amplitudes were set to zero. This final solution gave a χ^2 per degree of freedom =1.14 Fitted resonance parameters are given in Table 6.2 and Argand diagrams for the partial wave amplitudes are shown in figure 6.6. Curves superimposed on the coefficient data, shown in figures 6.1 and 6.2, represent the results of the final 'New Solution'. Structures in the 0.700 to 1.200 GeV/c interval are well accounted for in all coefficients. In particular, the fitted $J \geq 5/2$ effects are negligible below 0.85 GeV/c, supporting the approximations made in calculating the interference terms between $J^P = 3/2^-$ and $J^P = 3/2^+$ amplitudes. Furthermore, the dominant $J^P = 3/2^+$ amplitude is, as anticipated, the PP13. Most prominent of all the resonant amplitudes fitted is the DDO3(1690) and substantial DD15(1775), DDO5(1830) and FPO5(1820) partial waves were also found.

6.7 COMPARISON OF RESULTS

In this section a comparison of the fitted amplitudes found in the solutions ,described in Sections 6.6.a and 6.6.b (referred to as FIT B and FIT A respectively) ,will be given. This is undertaken to assess the stability and significance of various structures found.

Amplitudes at resonance of each state fitted are given in Table 6.2 for FIT A,FIT B and the solution published by the Imperial College/Rutherford Laboratory collaboration. Agreement between the larger fitted amplitudes is good. Smaller amplitudes are less stable, as are those for less well established states. In fact, the fluctuations of amplitudes in Table 6.1 probably represent the errors in determination of the resonant amplitudes more than real ambiguities between solutions. Amplitudes with magnitudes

State	Mass (MeV)	Width (MeV)	Partial Wave	Resonant Amplitude			
				FIT A (Sect.6.6b)	FIT B (Sect.6.6.a)	RL/IC (Ref 6.1)	CHS (Ref6.5)
S01(1670)	1670	35	SD01	- 0.10	- 0.10	-	- 0.18
S01(1810)	1810	215	SD01	- 0.10	- 0.08	- 0.06	-
S11(1750)	1768	105	SD11	0.19	-	-	0.18
S11(1925)	1925	200	SD11	0.22	-	-	-
P01(1580)	1588	187	PP01	- 0.18	-	-	-
P01(1870	1830	150	PP01	small	-	-	0.18
P11(1670)	1673	140	PP11	small	0.12	-	-
P11(1870)	1870	140	PP11	- 0.07	- 0.05	-	-
P03(1900)	1896	104	PP03	0.11	0.06	+(small)	-
			PF03	0.15	0.12	0.13	-
D03(1690)	1690	62	DS03	0.10	0.07	-	0.27
			DD03	0.21	0.21	-	-
D13(1670)	1670	60	DS13	- 0.07	0.03	-	0.11
			DD13	0.05	0.07	-	-
D13(1920)	1920	215	DS13	- 0.07	- 0.07	- 0.07	-
			DD13	0.03	0.03	+(small)	-
D05(1820)	1823	90	DD05	- 0.13	- 0.14	- 0.14	0.13
			DG05	+(small)	+(small)	+(small)	-
D15(1775)	1775	120	DD15	0.15	0.17	0.18	0.20
			DG15	+(small)	+(small)	+(small)	-
F05(1820)	1820	50	FP05	0.13	0.14	0.17	0.21
			FF05	- 0.07	-(small)	- 0.07	-
F05(2115)	2115	190	FP05	- 0.10	- 0.05	- 0.07	-
			FF05	- 0.05	+(small)	+(small)	-
F15(1930)	1930	120	FP15	0.0	-(small)	+(small)	-
			FF15	- 0.05	0.0	- 0.04	-
F15(2060)	2060	225	FP15	0.0	0.0	-	-
			FF15	- 0.04	- 0.05	-	-
F17(2040)	2040	165	FF17	- 0.13	0.0	- 0.15	-
			FH17	small	0.0	(small)	-
G07(2110)	2110	190	GD07	small	0.0	-	-
			GG07	small	0.0	-	-

TABLE 6.2 : Amplitudes at resonance for the states in the various analyses described in the text
(small amplitudes are those with magnitudes less than 0.03 and those magnitudes 0.0 have been set to zero).

less than 0.03 have been regarded as small and are unstable in sign.

The largest stable amplitudes found in both FIT A and FIT B are those for the DD wave coupling of the D03(1690). Consistent large amplitudes are also found for the D05(1775) and D05(1830) states. Clearly, these values reflect the fact that the most prominent structures in the coefficients are present between 0.700 and 1.200 GeV/c.

Although the paramatrizations of the $J^P = 1/2^-$ and $J^P = 1/2^+$ amplitudes are somewhat different in the various solutions, the fitted values do follow the same approximate forms in the Argand diagrams. An example of such behaviour is the SD11 amplitude. Starting from the amplitudes obtained for FIT A, the N = M = 0 background plus resonant amplitudes for S11(1750) and S11(1925) were replaced by an N = M = 1 background. A value of χ^2 = 1811 for 1535 degrees of freedom was found. The SD11 amplitude described a counterclockwise loop in the Argand diagram, similar to that of Figure 6.6 , without the cusp effect seen at 1850 MeV. However, on the basis of χ^2 per degree of freedom, this alternative paramatrization is clearly not as successful as that containing more resonant structure.

Of the $J^P = 3/2^+$ amplitudes, the PP13 is consistently found to be dominant and structured, whilst the PF13 is small and nearly negligible in the Survey-81 energy region. In all three solutions, the P03(1900) is found to couple strongly to the PF03 amplitude. However, both FIT A and FIT B require a substantial non-resonant PP03 amplitude, which is presumably constrained by the interference required at low energy with the resonant D03(1690) amplitudes.

Despite the presence of the D13(1670) in DS13 and DD13 partial waves, resonant amplitudes of the D13(1920) have not been affected. Consistency is seen for the DS13(1920) resonant amplitudes in all three solutions. However, the small DD13 amplitude is rather fluctuant, stable amplitudes for D13(1670) and D13(1920) states coupling to this partial wave cannot be

found, there being a substantial background amplitude in this wave.

Parameters of the $J^P = 5/2^-$ partial waves are well defined, couplings to the final state D-wave being much greater than those to the final state G-wave.

Results for the $J^P = 5/2^+$ sector are less satisfactory. Both FO5(1820) and FO5(2115) have substantial resonant amplitudes in the FPO5 partial wave, but decouple from the FFO5 partial wave. No resonant structure was required in the FP15 partial wave. Consistent couplings of the F15(1930) and F15(2060) states to the FF15 partial wave were not obtained, although it seems clear that these amplitudes are small and negative.

Finally, a strong FF17(2040) amplitude was found to be responsible for structure in the L = 6 coefficients, no FH17(2040) amplitude being required. Couplings of the GO7(2110) were found to be consistently small.

6.8 CONCLUSIONS

New data for the $\pi^+\Sigma^-(1385)$ and $\pi^-\Sigma^+(1385)$ channels shows strong evidence for formation of $J^P = 3/2^-$ s-channel resonances. This data is compatible with data previously published and used by the Rutherford Laboratory/Imperial College collaboration in a partial wave analysis. Combining both sets of data, the energy range of this analysis has been extended. Structures found previously are unaffected and a particularly strong coupling of the DO3 (1690) state to the DDO3 partial wave is observed. Starting afresh, a new partial wave solution has been found. The features of this solution are essentially identical to those previously published (reference 6.1) and again find a strong DDO3(1690) resonant amplitude. Dominant features of the data are explained in terms of DDO3(1690), DD15(1775) DDO5(1830) and FPO5(1820) resonant amplitudes. Lesser resonant amplitudes for DSO3(1690), DD13(1690), SDO1(1670), DS13(1920), FPO5(2115) and FF15(2060) are also found to be stable. Less well established states, which couple to the PP11, PPO1 and SD11 partial waves, are wide and are not observed with consistent parameters. The forms found for these partial waves may be

replaced by completely non-resonant backgrounds.

Results of the partial wave analysis performed by the C.H.S. Group (reference 6.5) are also given in Table 6.2. As stated in Chapter One, only the lower outgoing angular momenta were included for each J^P sector by this analysis. However, similar conclusions are drawn as to the signs and magnitudes of all the established resonances. In agreement with this work, the dominant structure is found to be the DO3(1690), but this is found in the DSO3 and not the DDO3 partial wave. The most important disagreement between the analyses concerns the sign of the large DD15 amplitude.

CHAPTER 6

REFERENCES

6.1 W. Cameron et al, Nucl.Phys. B143 (1978) 189.

6.2 W. Cameron et al, Rutherford Laboratory Report RL-80-073, (1980).

6.3 R.A.Stern, Ph.D. Thesis, University of London (unpublished).

6.4 G. Gopal et al, Nucl.Phys. B119 (1977) 362.

6.5 J. Prevost et al, Nucl.Phys. B69 (1974) 246.

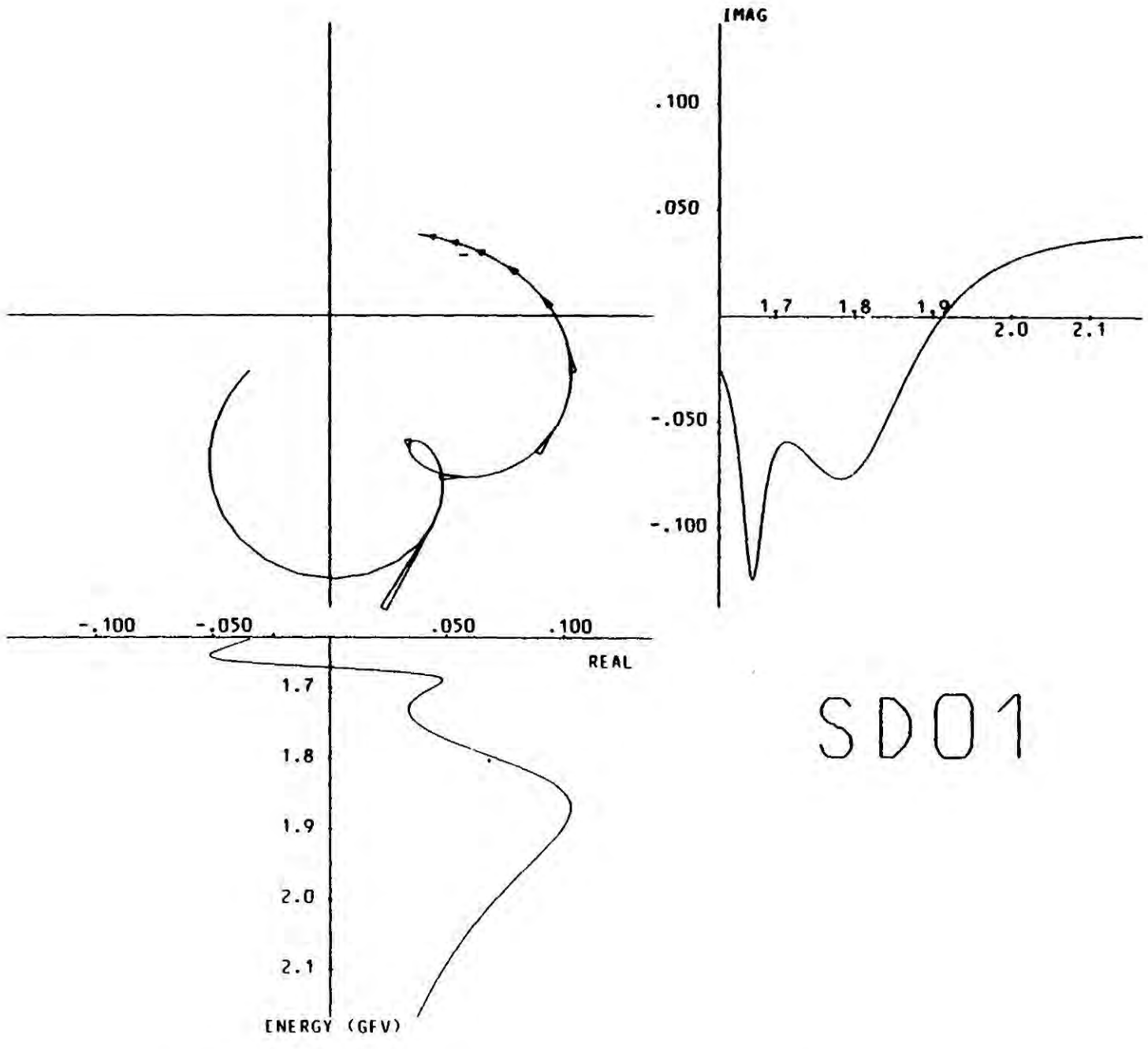

FIGURE 6.6 : Argand Diagrams for the Fitted Partial Wave Amplitudes.

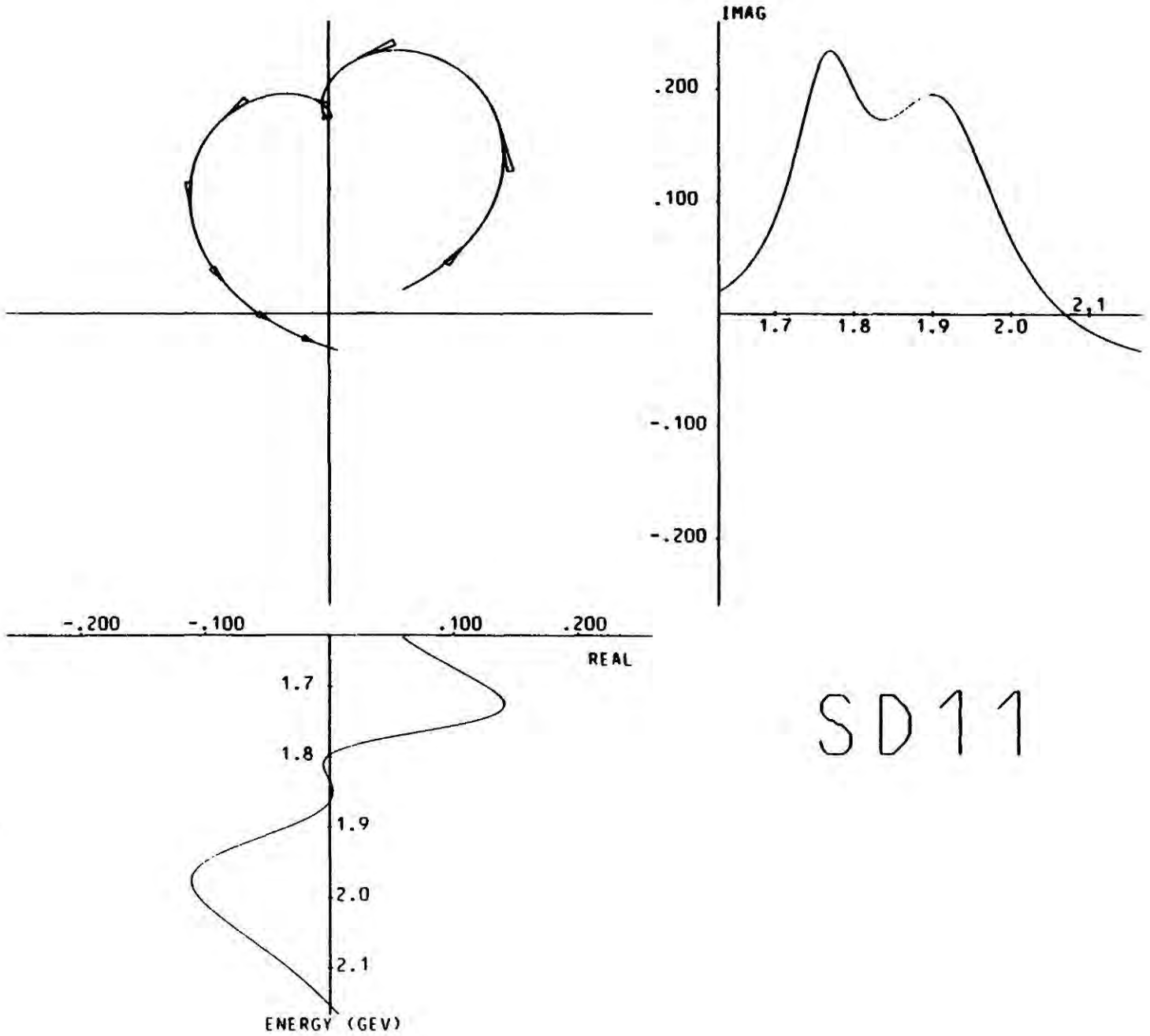

Figure 6.6 Cont'd

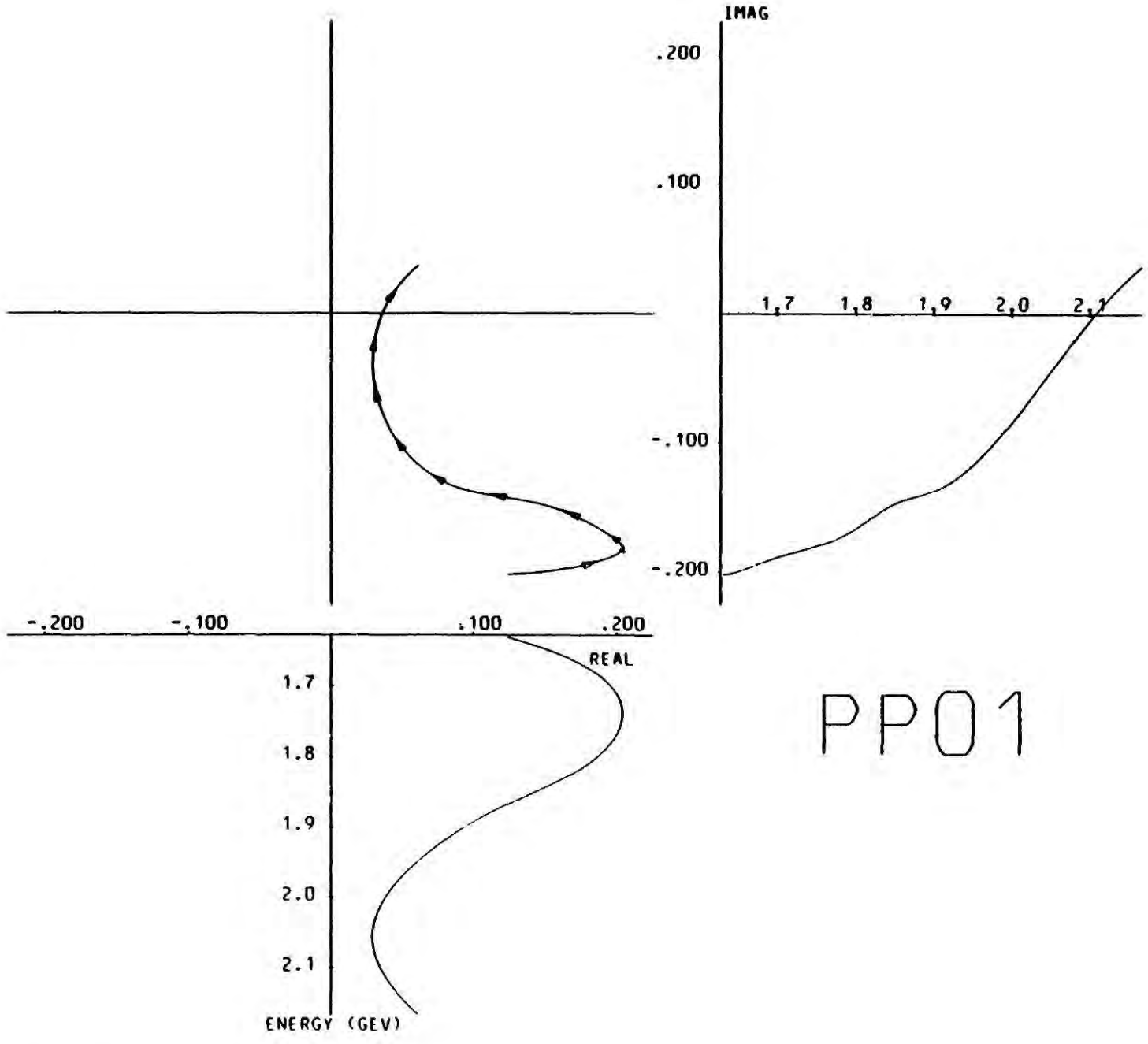

Figure 6.6 Cont'd

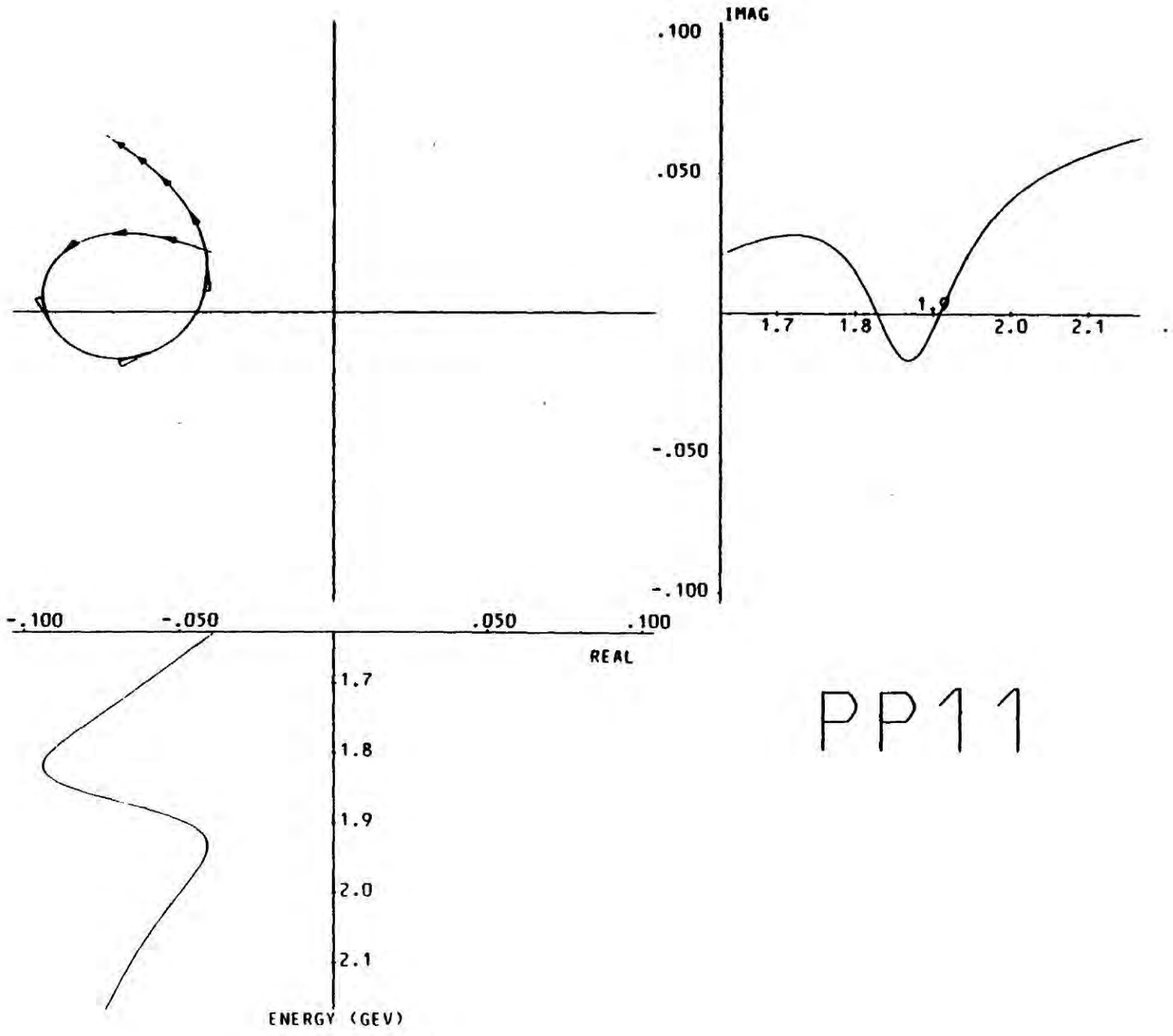

Figure 6.6 Cont'd

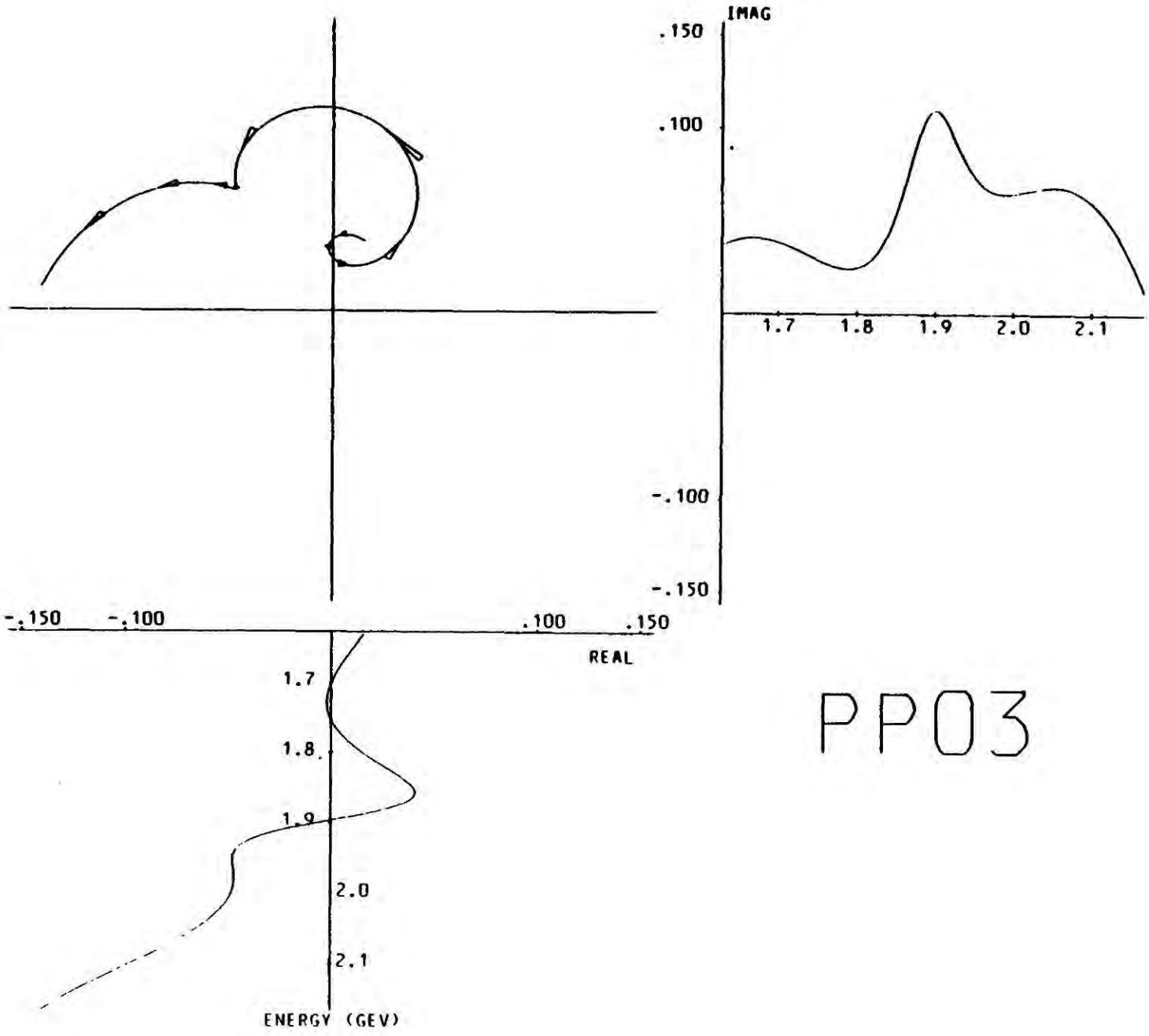

Figure 6.6 Cont'd

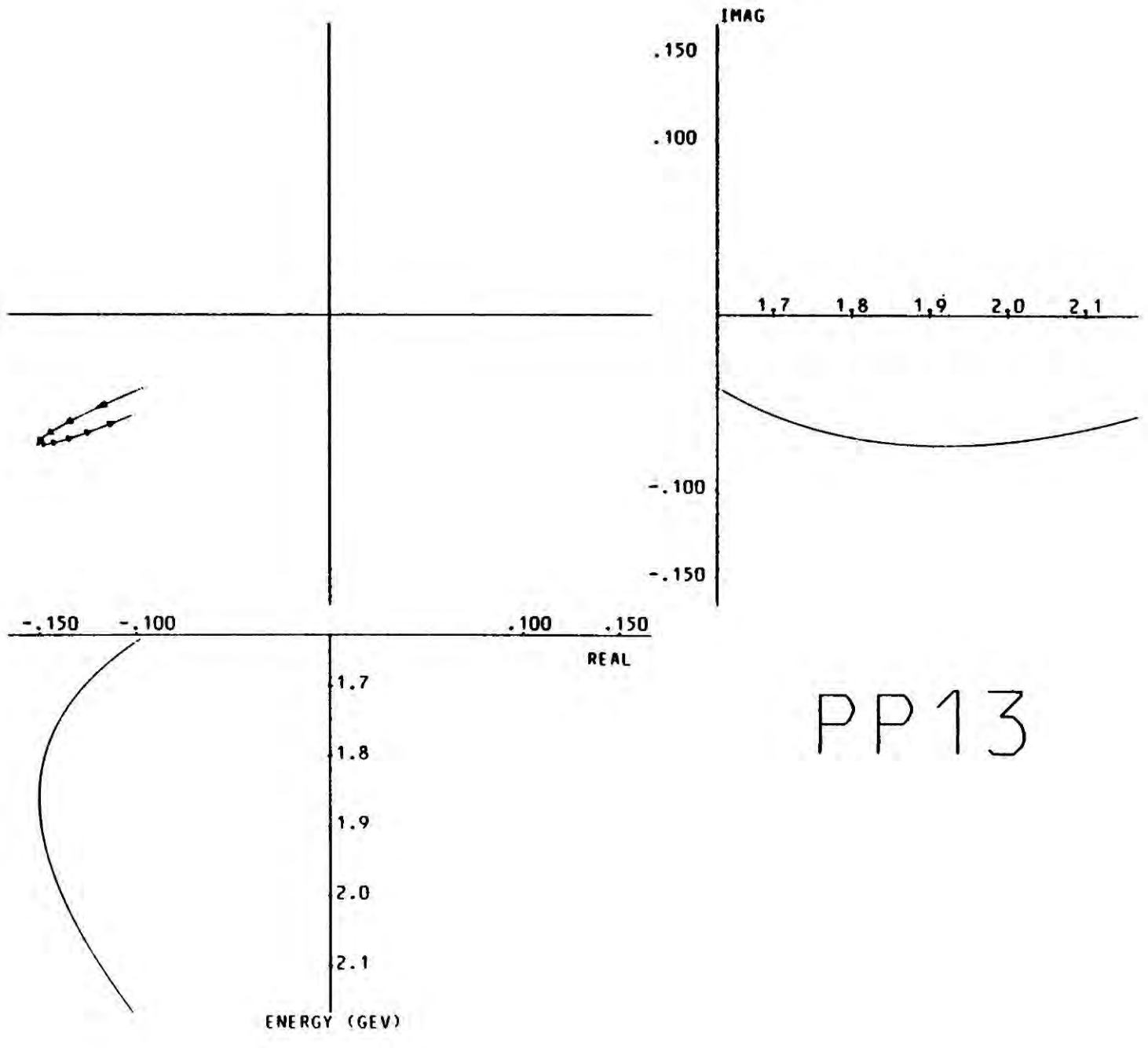

Figure 6.6 Cont'd

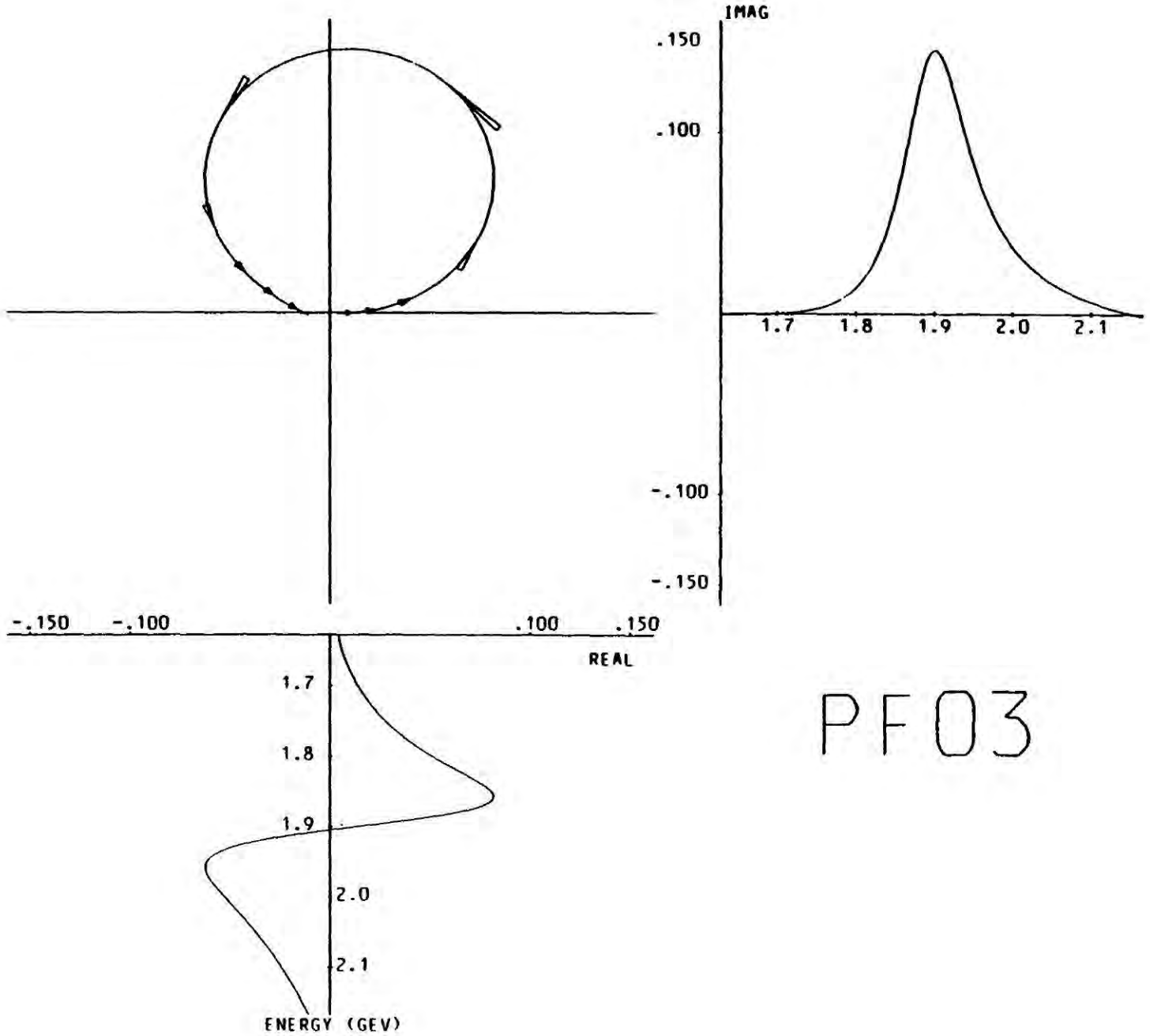

Figure 6.6 Cont'd

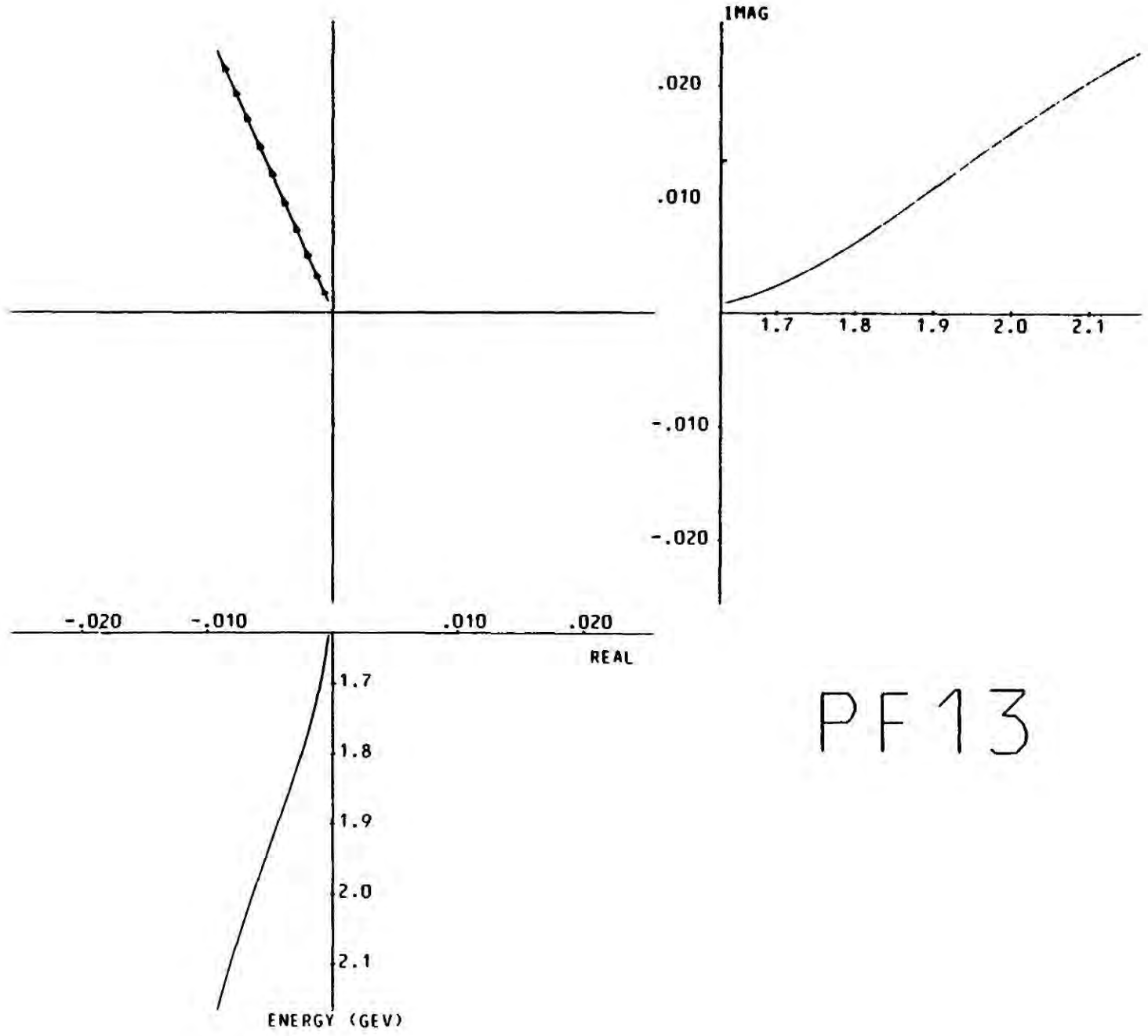

Figure 6.6 Cont'd

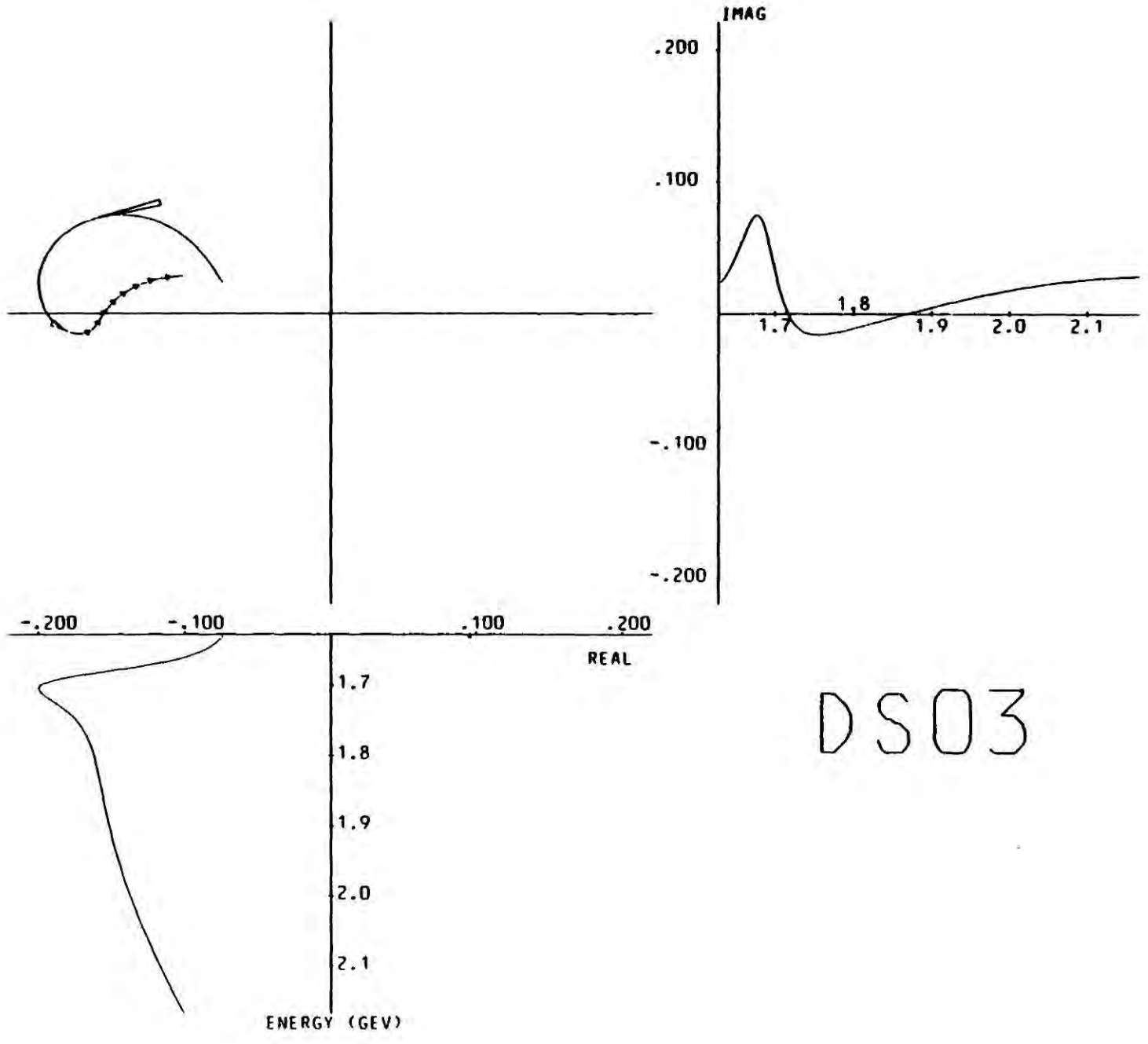

Figure 6.6 Cont'd

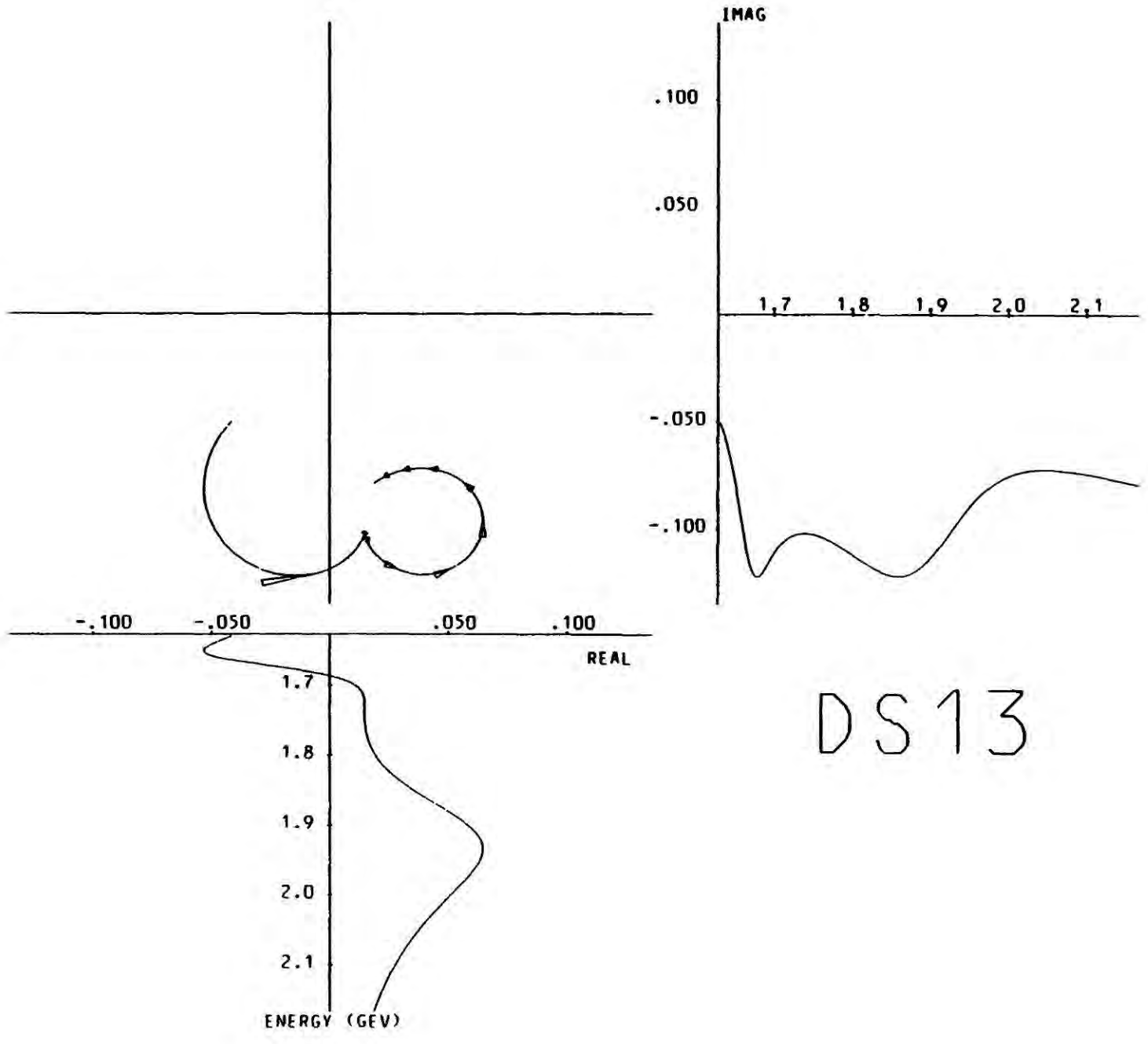

Figure 6.6 Cont'd

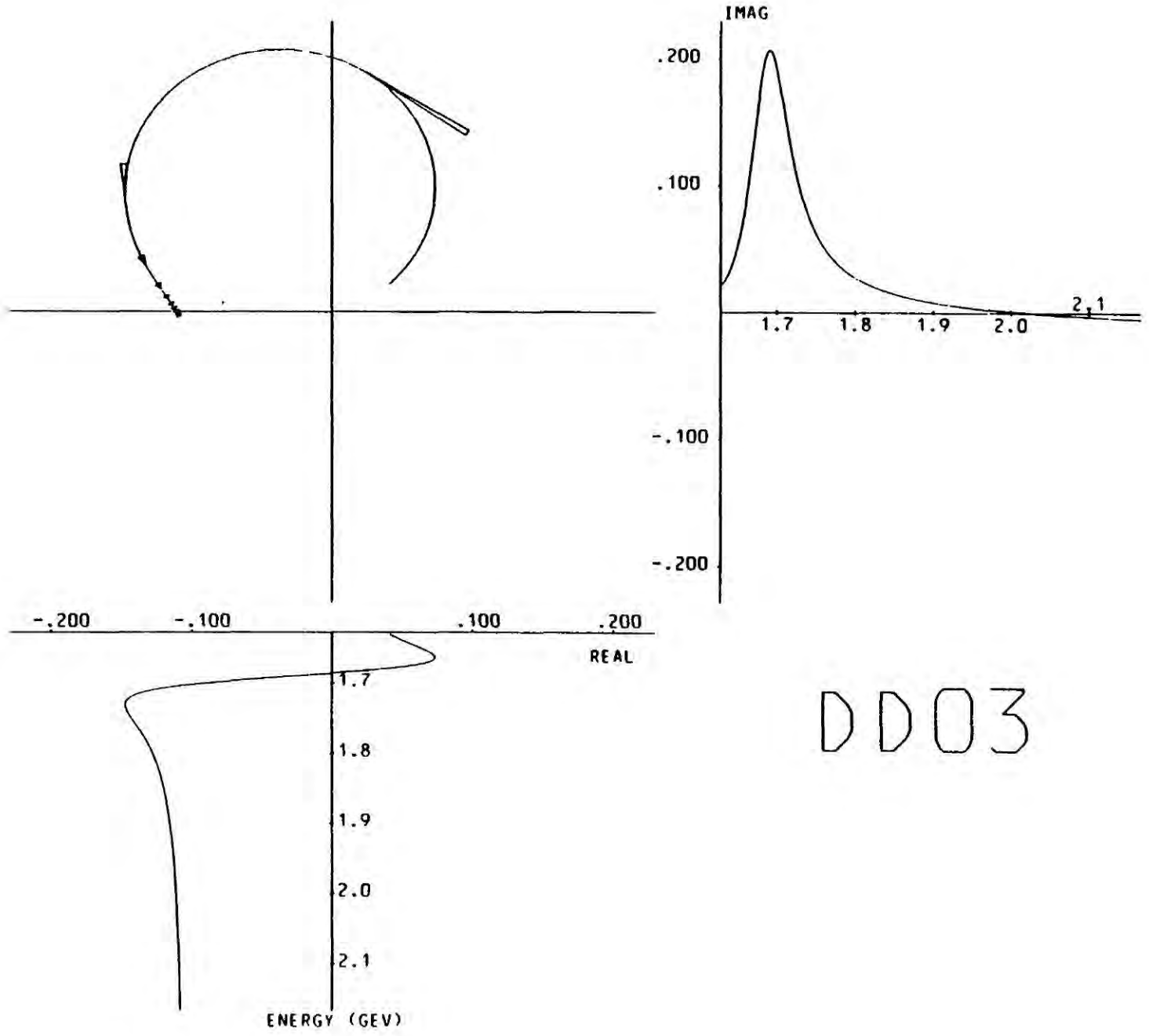

Figure 6.6 Cont'd

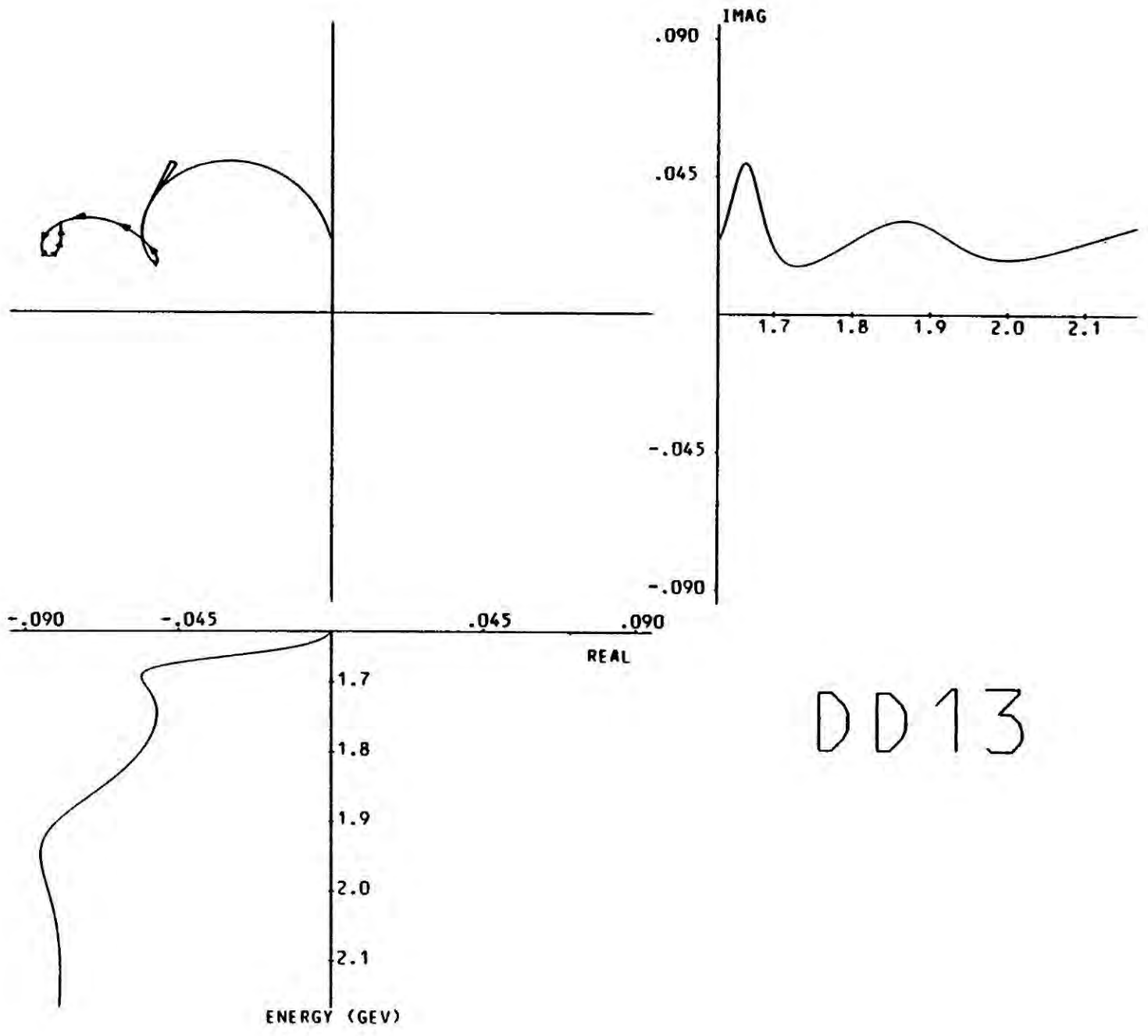

DD13

Figure 6.6 Cont'd

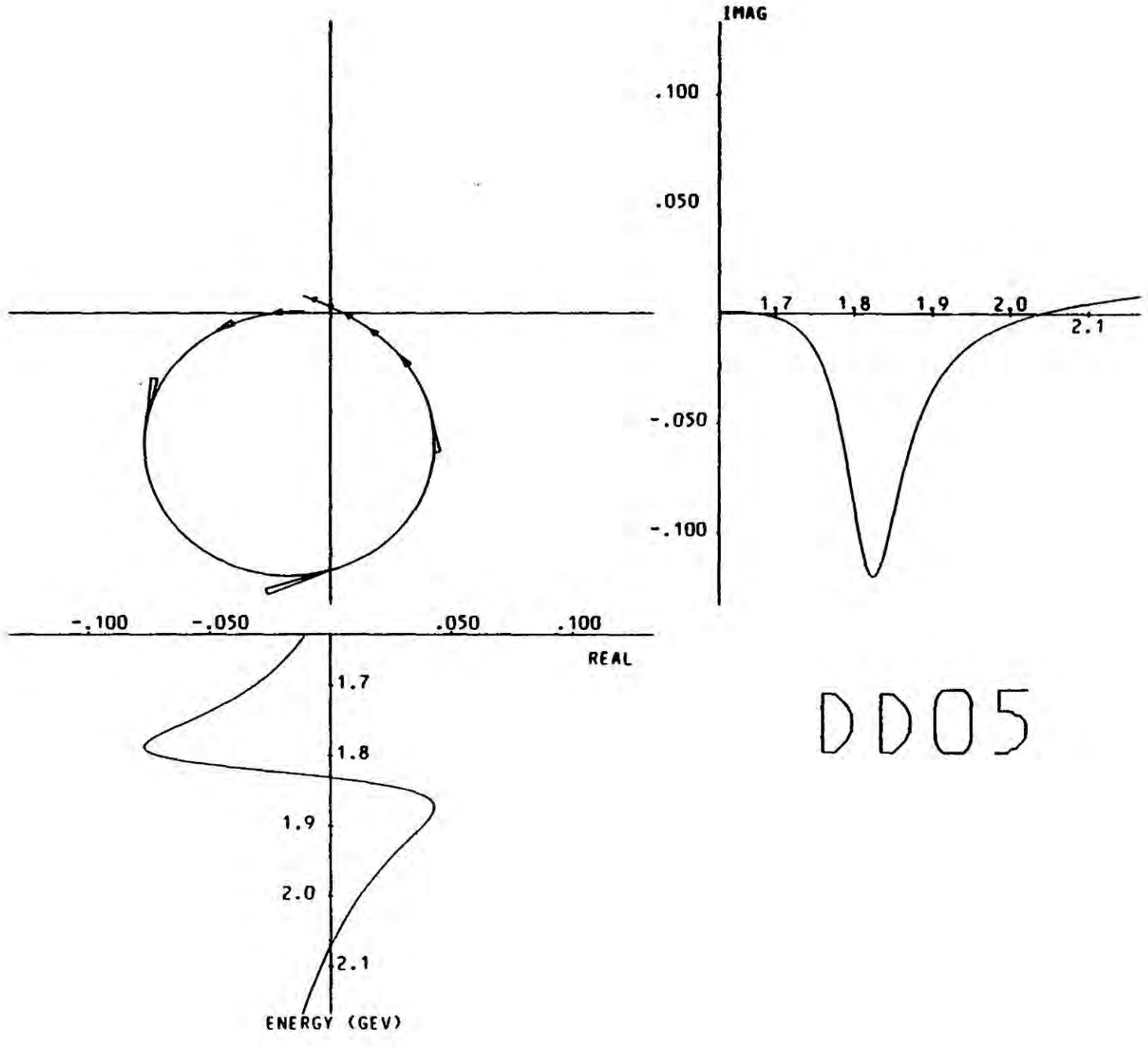

Figure 6.6 Cont'd

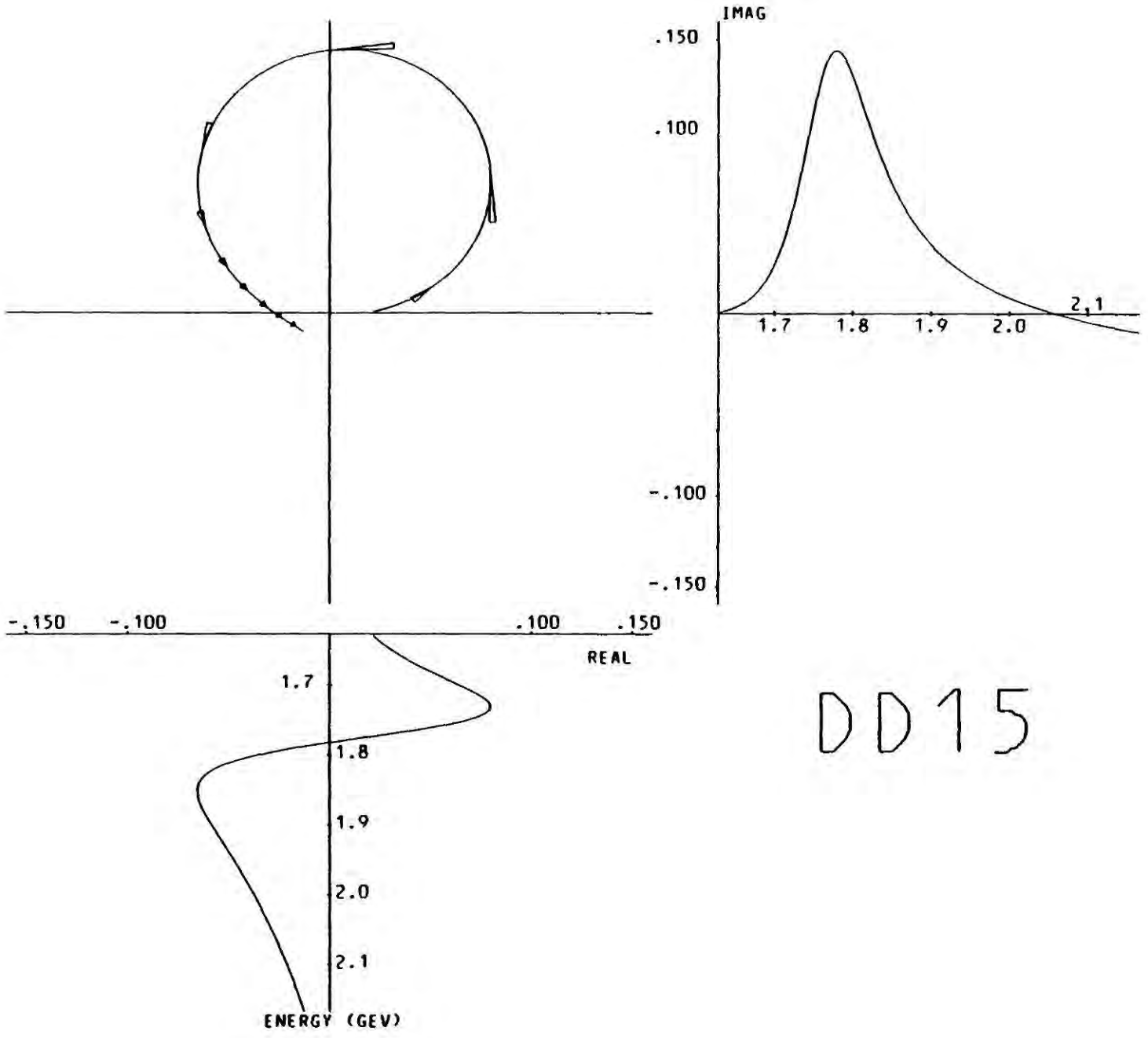

DD15

Figure 6.6 Cont'd

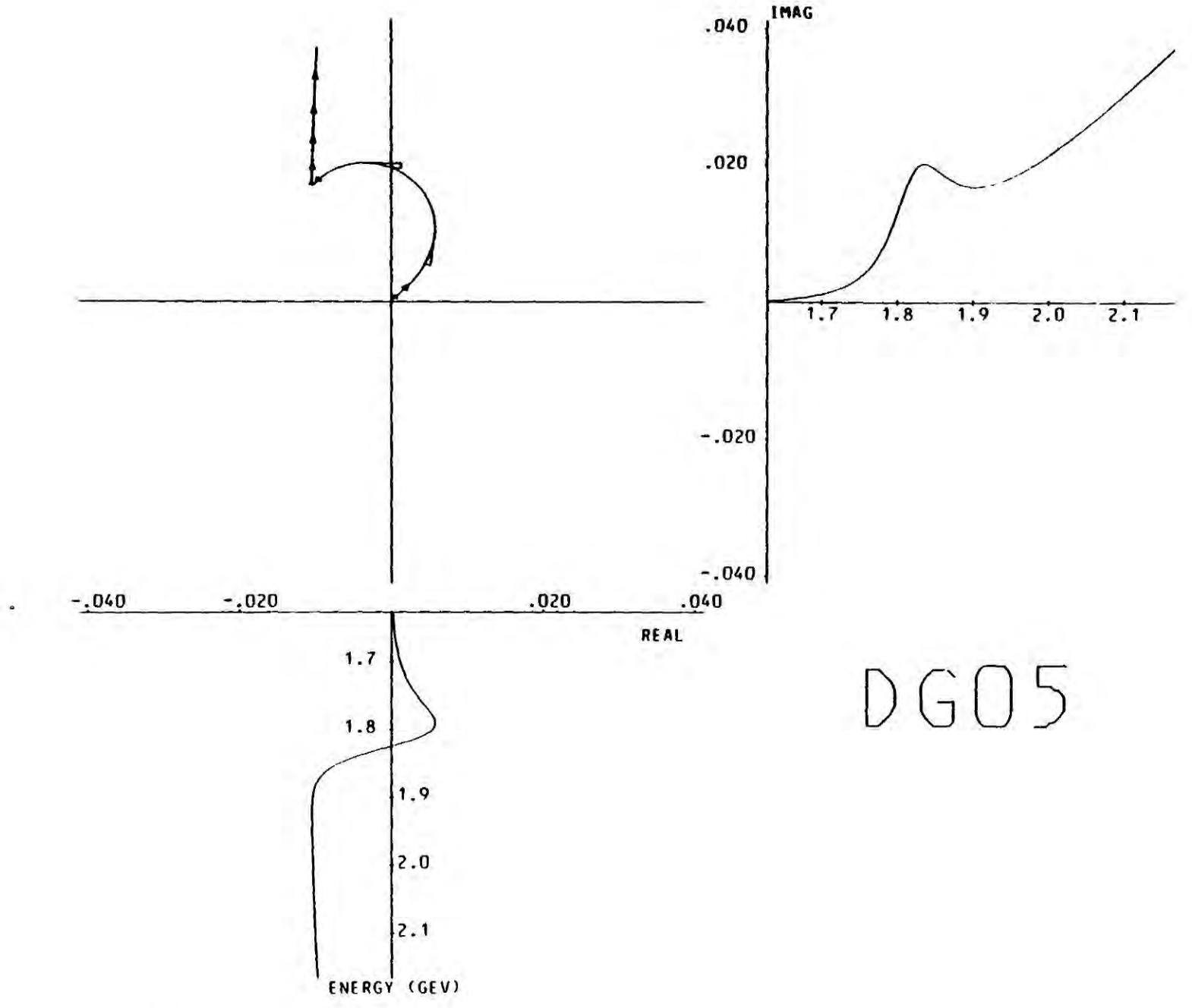

Figure 6.6 Cont'd

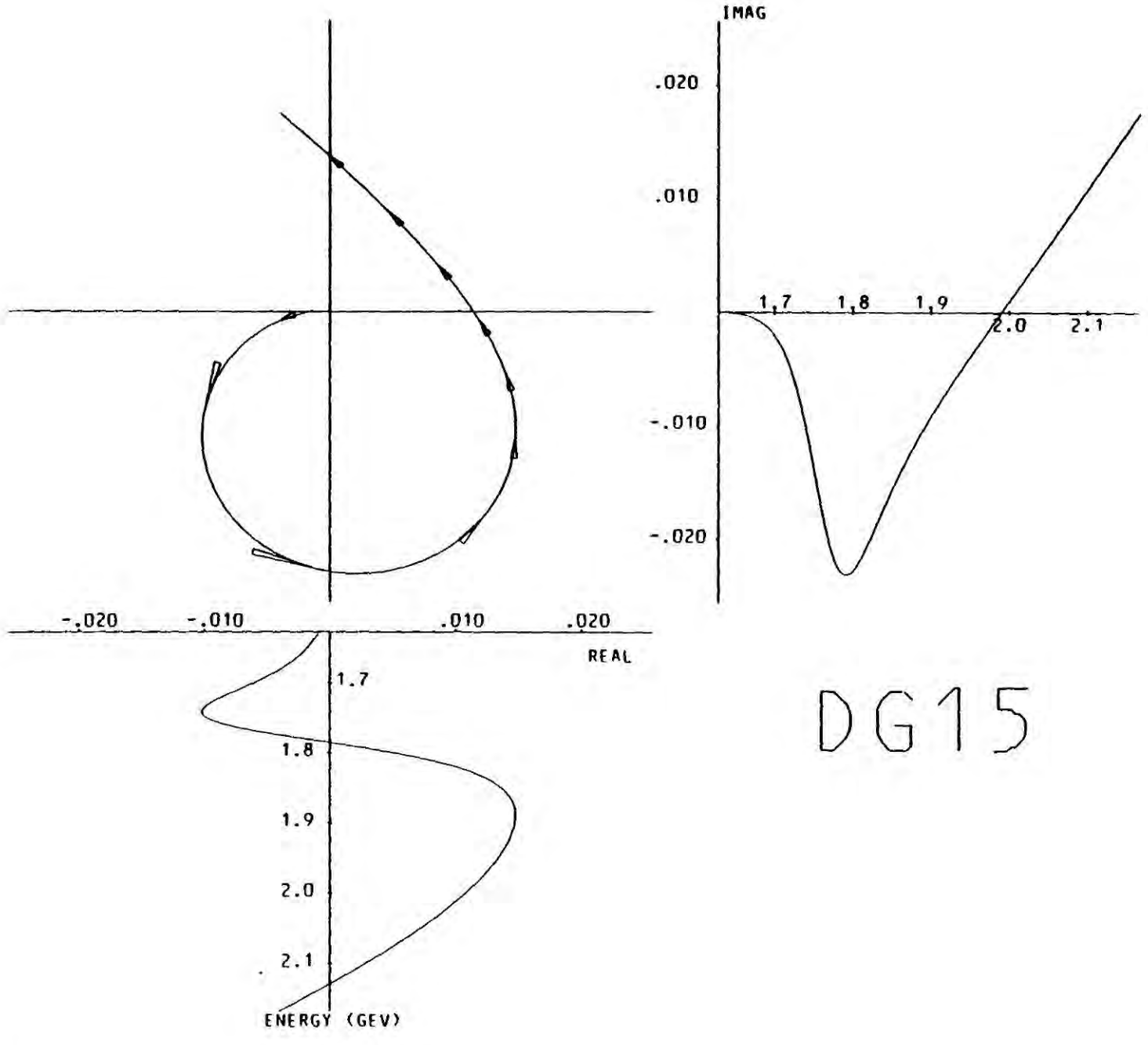

Figure 6.6 Cont'd

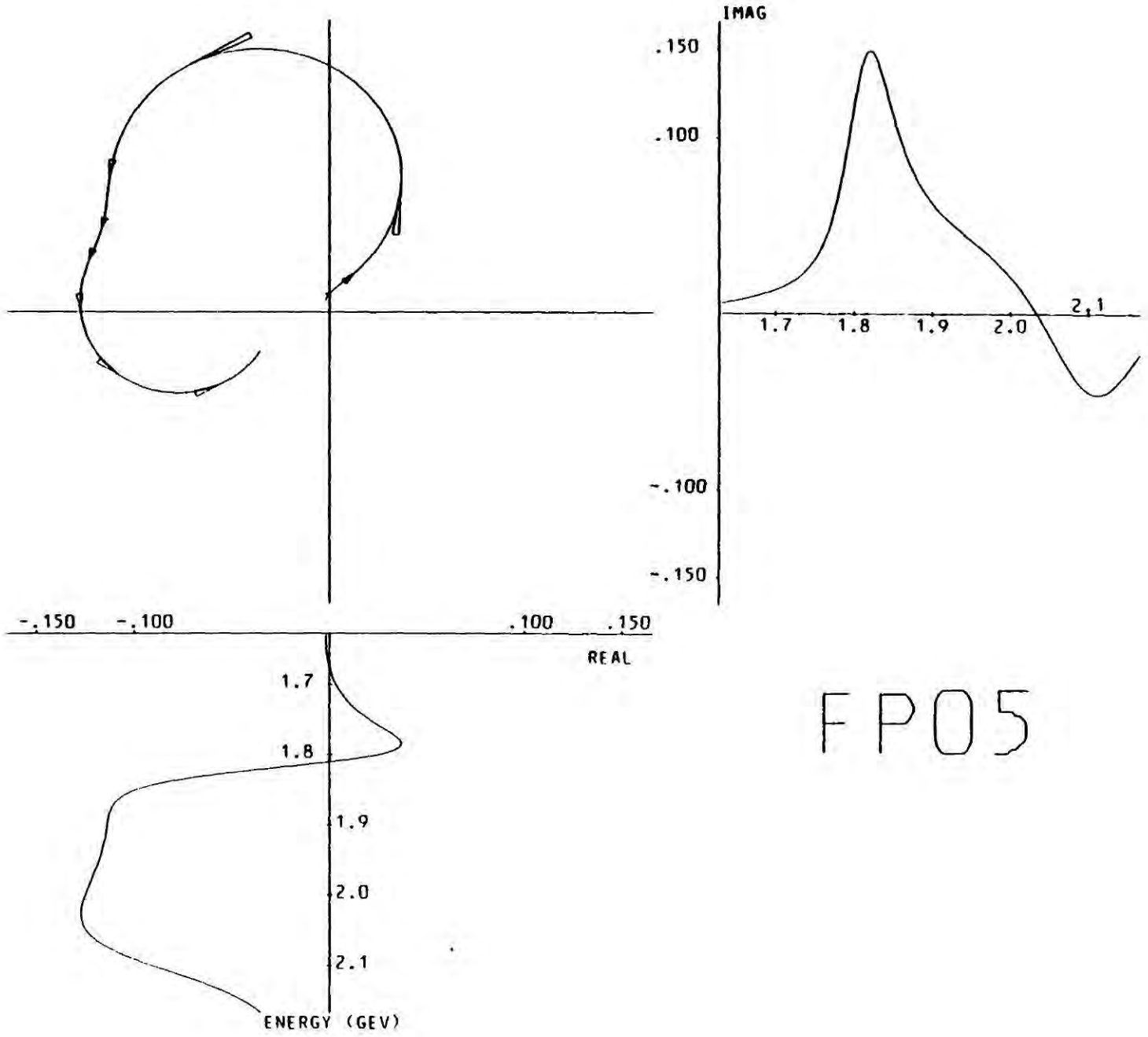

Figure 6.6 Cont'd

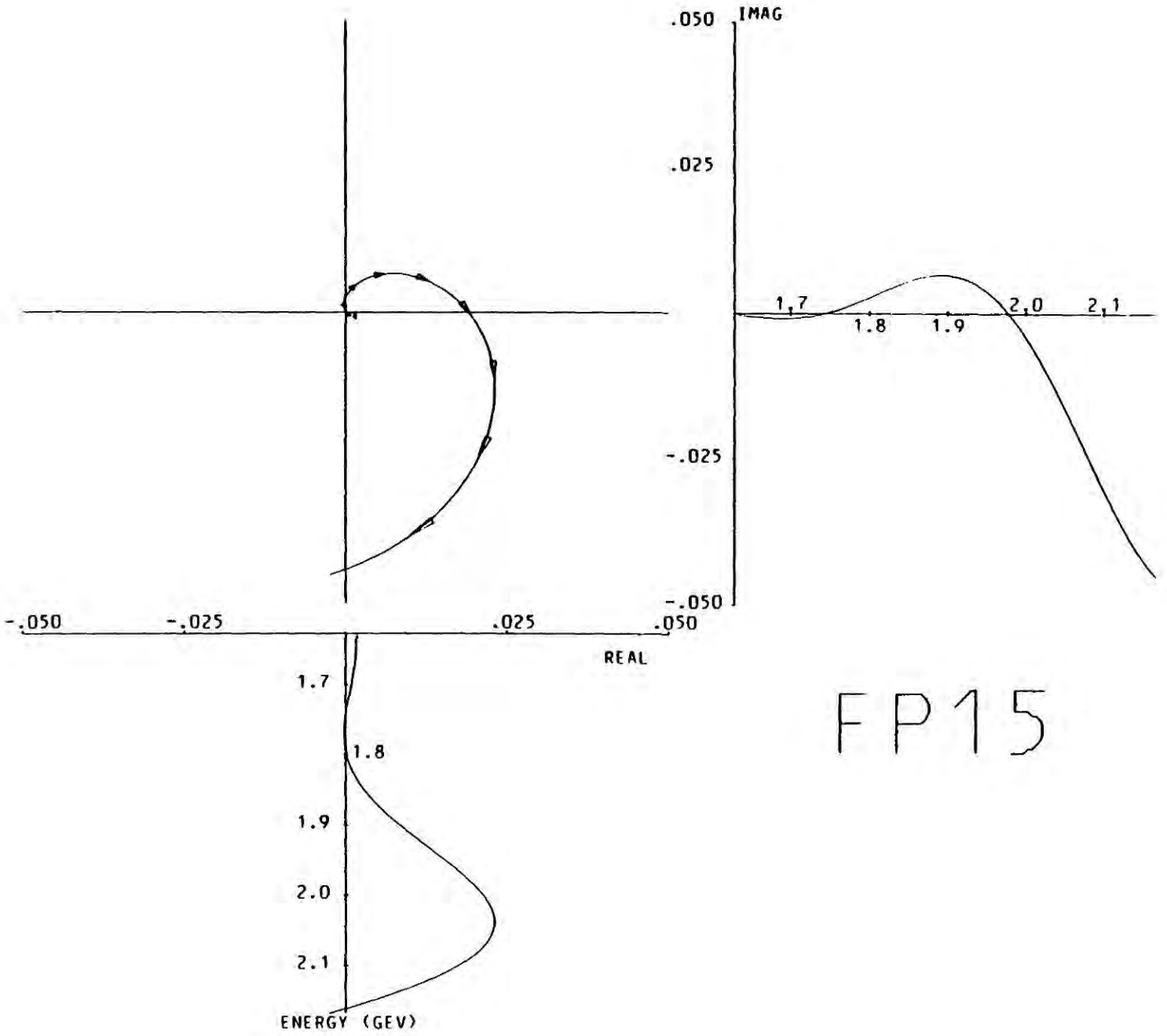

Figure 6.6 Cont'd

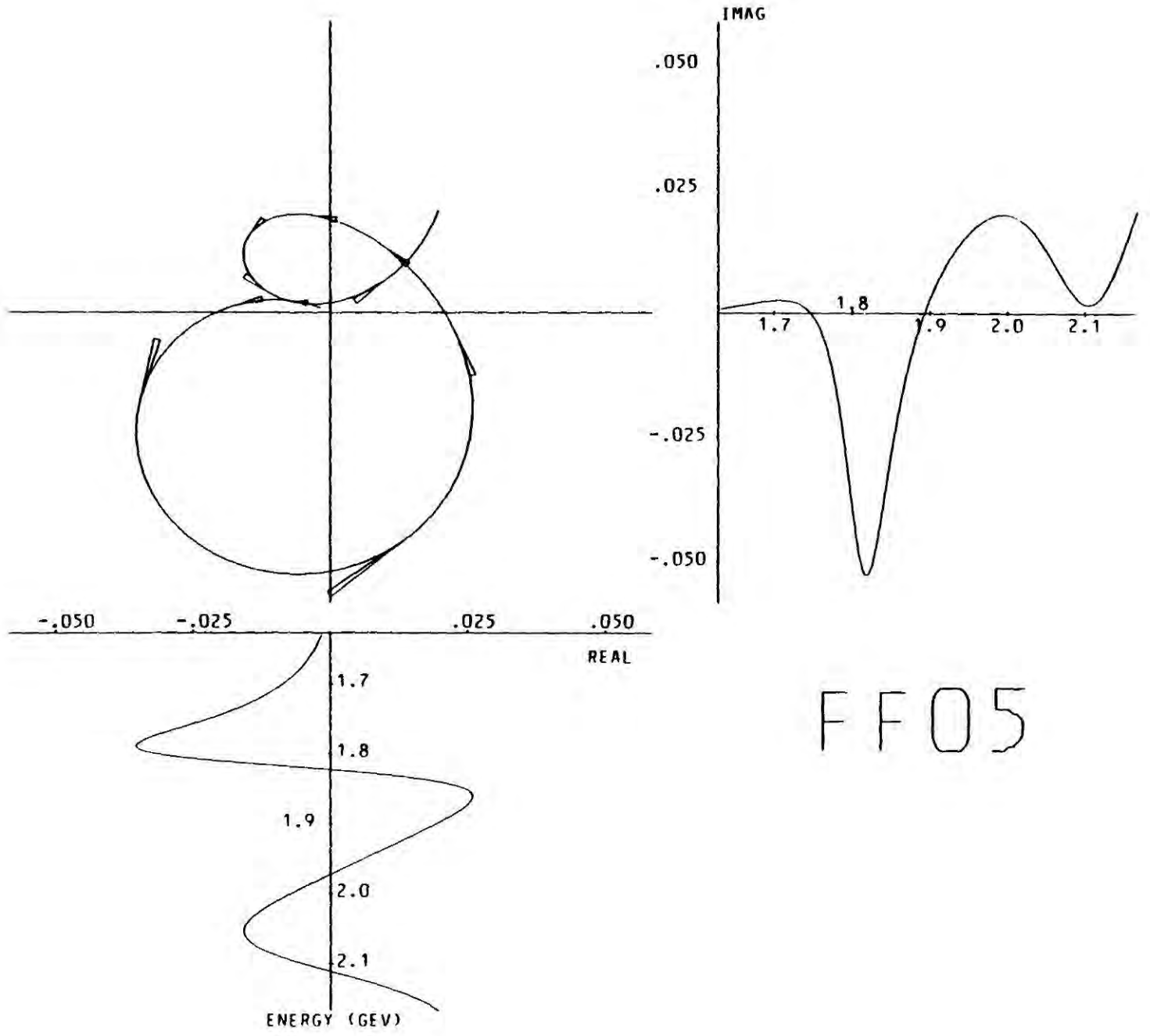

Figure 6.6 Cont'd

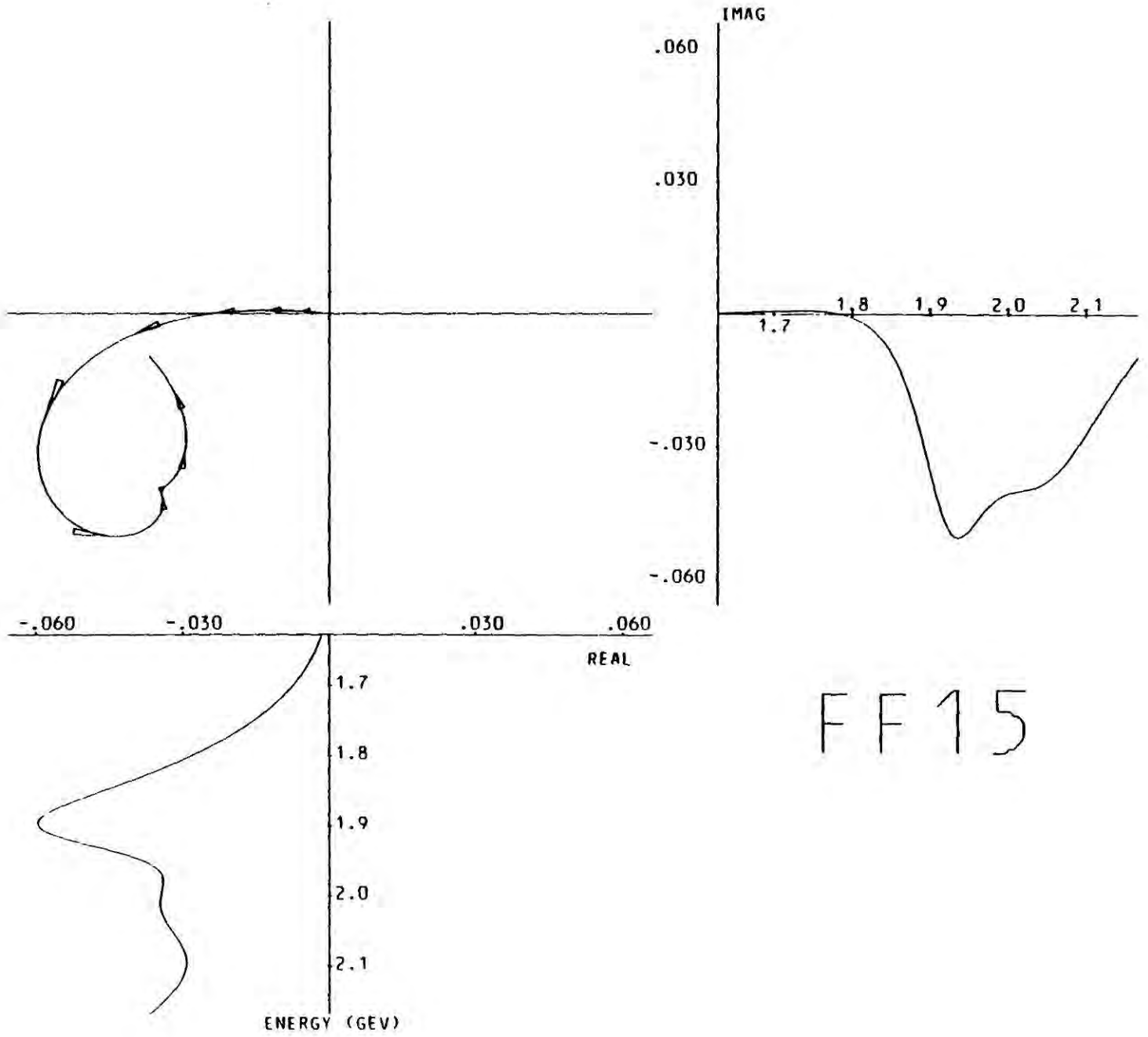

Figure 6.6 Cont'd

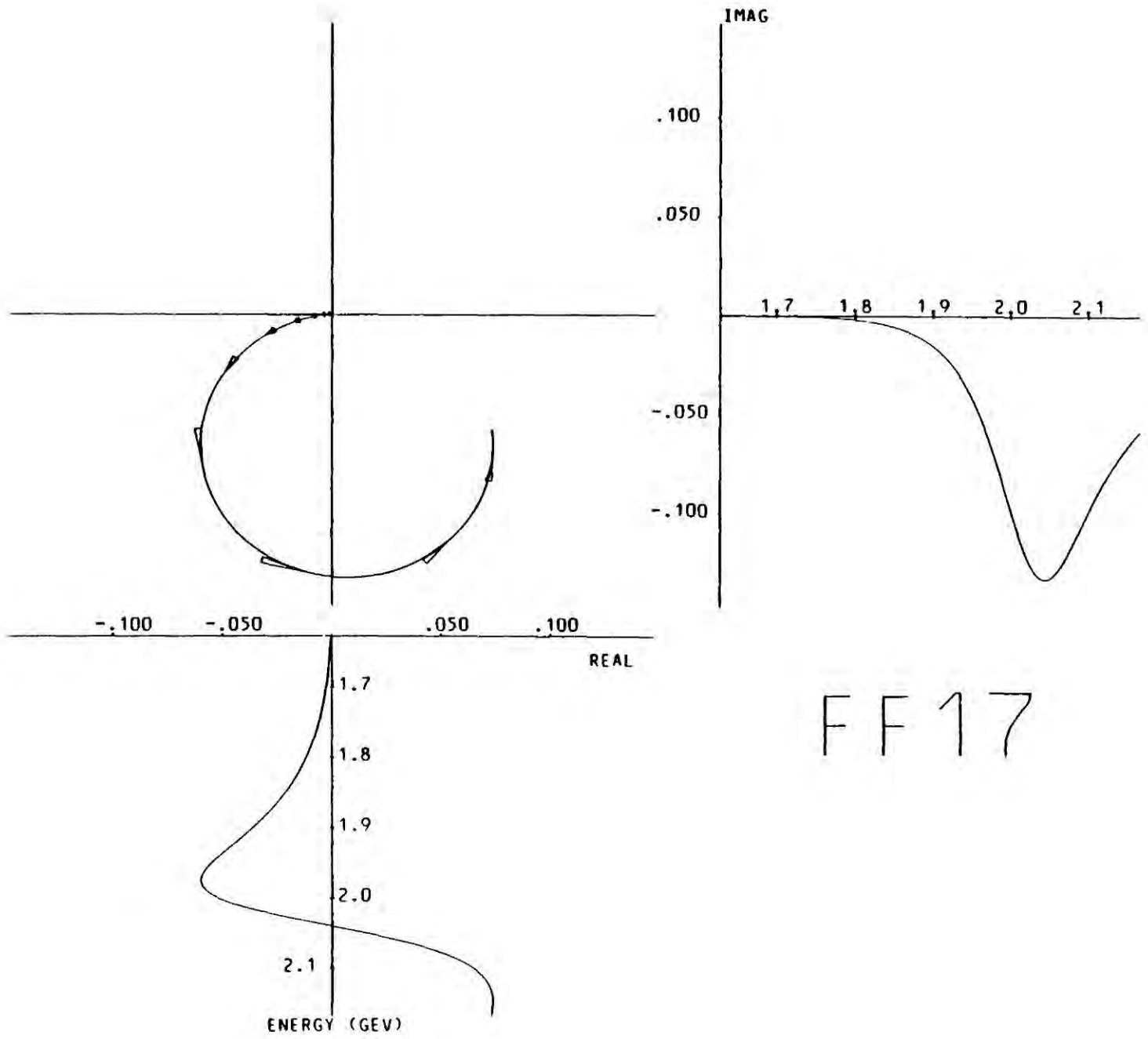

Figure 6.6 Cont'd

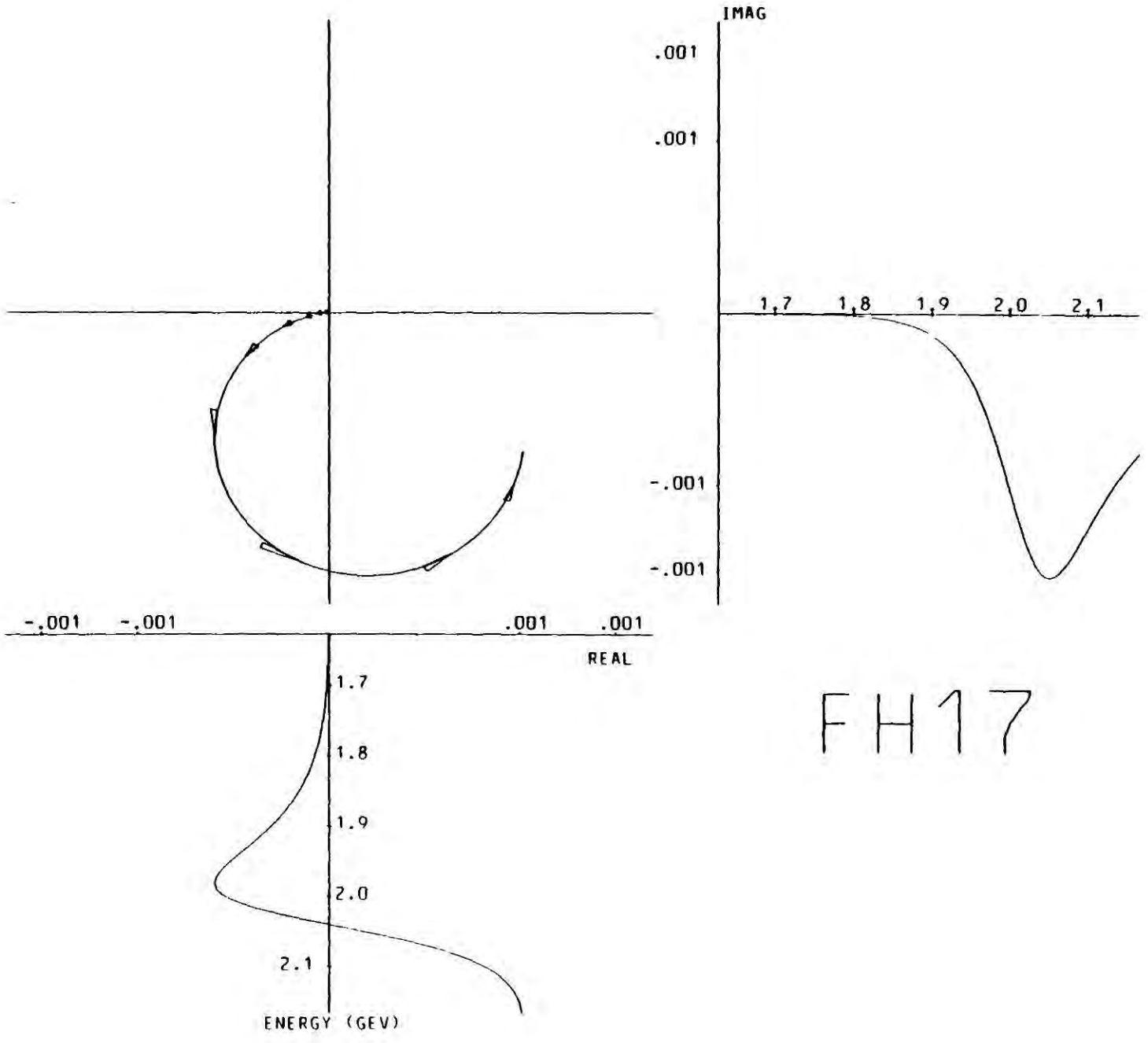

Figure 6.6 Cont'd

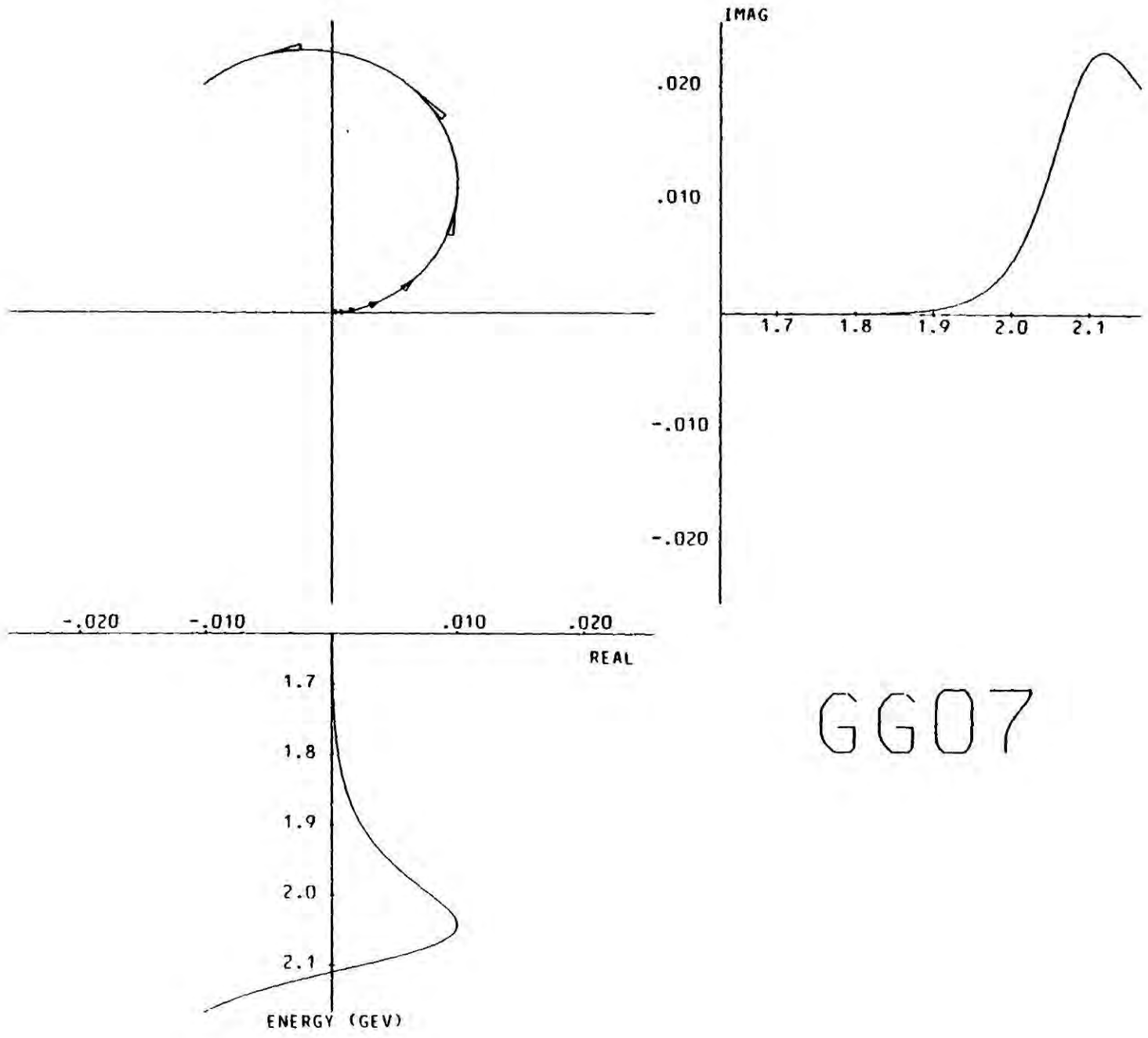

Figure 6.6 Cont'd

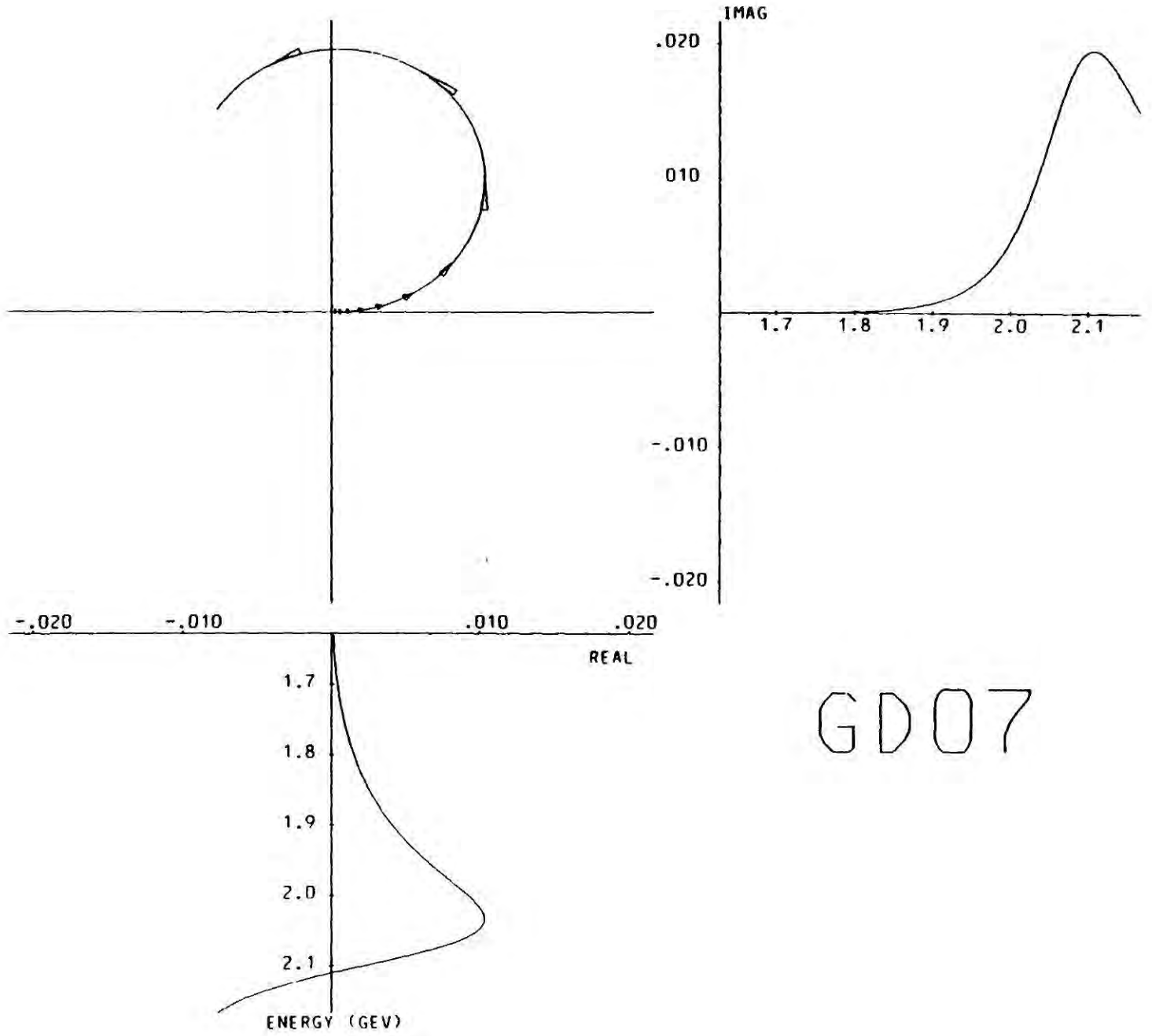

Figure 6.6 Cont'd

CHAPTER 7

7.1 INTRODUCTION

From the point of view of particle symmetries, the reaction $\bar{k}\,N \to \pi\Sigma(1385)$ is interesting for two reasons :-

(i) In terms of SU(3), the reaction is inelastic and is represented by :-

$$\tilde{8} \otimes \tilde{8} \to \tilde{8} \otimes \tilde{10} \qquad (7.1)$$

Ordinary two body final states of $\bar{k}N$ interactions only probe the SU(3) elastic reaction :-

$$\tilde{8} \otimes \tilde{8} \to \tilde{8} \otimes \tilde{8} \qquad (7.2)$$

Since,

$$\tilde{8} \otimes \tilde{8} = \tilde{1} \oplus \tilde{8}_F \oplus \tilde{8}_D \oplus \tilde{10} + \tilde{10}^* \oplus 27 \qquad (7.3)$$

and

$$\tilde{8} \otimes \tilde{10} = \tilde{8} + \tilde{10} + \tilde{27} + \tilde{35} \qquad (7.4)$$

then, as a consequence of the fact that baryons belong to $\tilde{1}$, $\tilde{8}$ and $\tilde{10}$ representations of SU(3) only, just two amplitudes are required to describe couplings of baryon resonances to $\pi\Sigma(1385)$ or $\pi\Delta(1232)$ final states, while four amplitudes are required to describe couplings to the two-body πN, $\bar{k}N$, $\pi\Lambda$ and $\pi\Sigma$ final states. It is also clear that isoscalar $\tilde{1}$ members (i.e. Λ's) may not couple to $\pi\Sigma(1385)$ channels, since $\tilde{8} \otimes \tilde{10} \not\ni \tilde{1}$.

(ii) As described in Section 1.2, each J value of the s-channel can couple to two final state orbital angular momenta, provided $J > \frac{1}{2}$. Within SU(6), states with negative parity can be accommodated within the

$\left[70,1^-\right]$ supermultiplet. All S and D wave decays of states belonging to this supermultiplet are described in terms of just two reduced partial wave amplitudes. Hence, for example, the partial decay widths for the DO3(1690) seen in DSO3 and DDO3 partial waves are related. Similarly, the decays of excited positive parity states, which are assigned to the $\left[56,\ 2^+\right]$ supermultiplet are determined by universal P and F wave amplitudes.

Configuration mixing between the Λ(1520) and Λ(1690) may be calculated within the SU(3) framework using the Gell-Mann/Okubo mass formula (ref7.1) and the ratio between s-wave partial widths for $\pi\Sigma$ (1385) decays. The two mixing angles found are in disagreement. This feature has been known for a long time. In Section 7.2, it will be shown that the new Λ(1690) amplitudes found in Chapter Six of this thesis do not resolve this problem. Additional mixings, possible within SU(6)w schemes, will be shown in Section 7.6b to account for the inconsistency in SU(3) mixing angles and are constrained by the relative strengths D and S wave $\pi\Sigma$ (1385) amplitudes for the Λ(1690).

Sections 7.6a and 7.6b will be concerned with the predictions of SU(6)w models concerning other resonant amplitudes found in Chapter Six of this thesis.

7.2 SU(3) IMPLICATIONS

Although the observed hadronic quantum numbers are accommodated within irreducible representations of SU(3), it is clear that substantial symmetry breaking effects are present. Baryonic masses for members of the $J^P = 3/2^+$ decuplet and $J^P = \frac{1}{2}^+$ nonet show splittings which depend systematically on strangeness. This effect has been accounted for by the Gell-Mann/Okubo mass formula.

For baryons, which belong to a particular irreducible representation of SU(3) labelled by μ (e.g. octet, singlet, decuplet) and which

have charge like quantum numbers labelled by ν(i.e. specified N,Δ,Σ,Λ etc), masses are generated by an operator O, which transforms as a singlet under SU(3) :-

$$M(\mu,\nu) = \langle \mu\nu \,|O|\, \mu\nu \rangle \tag{7.5}$$

Applying the Wigner-Eckart theorem

$$M(\mu,\nu) = C^{\mu\ 1\ \mu}_{\nu\ \ O\ \ \nu} \langle \mu \,|O|\, \mu \rangle \tag{7.6}$$

In an unbroken symmetry, the Clebsch-Gordan coefficients $C^{\mu\ 1\ \mu}_{\nu\ \ O\ \ \nu}$, which are products of SU(3) isoscalar factors and SU(2) isospin factors, are all equal to unity and the masses for all members of a particular irreducible representation are degenerate. To introduce symmetry breaking effects, O is allowed to transform as a sum of singlet and octet parts under SU(3) :-

$$O = O^1 + O^8 \tag{7.7}$$

Gell-Mann and Okubo [reference 7. 10] have shown that the following mass formulae hold under this assumption :-

(i) for decuplets

$$M(\Omega) - M(\Xi^*) = M(\Xi^*) - M(\Sigma) = M(\Sigma^*) - M(\Delta)$$

i.e. equal-mass splittings (7.8)

(ii) for octets :-

$$\frac{M(N) + M(\Xi)}{2} = \frac{M(\Sigma) + 3M(\Lambda)}{4} \tag{7.9}$$

A further consequence of the form taken for O is the mixing of singlet and octet isoscalar states, since :-

$$\langle 8 \mid O^{1} \mid 1 \rangle = 0 \quad \text{as } \tilde{8} \otimes \tilde{1} \not\subset \tilde{1} \tag{7.10}$$

$$\langle 8 \mid O^{8} \mid 1 \rangle \neq 0 \quad \text{as } \tilde{8} \otimes \tilde{8} \subset \tilde{1} \tag{7.11}$$

An example of two such states are the DO3(1690) and DO3(1520), for which a mass-mixing matrix can be defined :-

$$\tilde{M} = \begin{pmatrix} \langle 1 \mid O \mid 1 \rangle & C^{1}_{\hat{8}\,\hat{8}} \langle 8 \mid O^{8} \mid 1 \rangle \\ C^{8}_{\hat{8}\,\hat{1}} \langle 1 \mid O^{8} \mid 8 \rangle & \langle 8 \mid O \mid 8 \rangle \end{pmatrix} \tag{7.12}$$

When no symmetry breaking effects are present (i.e. when $O^{8} = 0$), since $C^{8}_{\hat{1}\,\hat{1}} = 0$ and $C^{1}_{\hat{1}\,\hat{8}} = 0$, the mixing matrix is diagonal with mass eigenvalues $\langle 1 \mid O \mid 1 \rangle$ and $\langle 8 \mid O^{1} \mid 8 \rangle$. When symmetry breaking terms are present, diagonalization of this matrix gives the mixed octet-singlet physical wavefunctions as eigenvectors and the physical masses as eigenvalues. Writing :-

$$\mid DO3(1520) \rangle = \sin\theta \mid 1 \rangle + \cos\theta \mid 8 \rangle$$

$$\mid DO3(1690) \rangle = \cos\theta \mid 1 \rangle - \sin\theta \mid 8 \rangle$$

gives the mixing angle, θ, in terms of the mass eigenvalues, m(1690) and m(1520),

$$\cos^{2}\theta = \frac{m_{8} - m(1520)}{m(1690) - m(1520)} \tag{7.13}$$

where $m_{8} = \langle 8 \mid O \mid 8 \rangle$

A value for the unmixed octet member mass, m_8, may be deduced from the Gell-Mann/Okubo mass formula :-

$$m_8 = \frac{1}{3}\left[2\,M(N) - 2M(\Xi) - M(\Sigma)\right] \qquad (7.14)$$

The members of the $J^P = 3/2^-$ octet are taken to be N(1520), Σ(1580) and Ξ(1830), the masses being taken from the 1980 Particle Data Group Tables. Possible uncertainty is associated with the values since the Σ(1580) is a poorly observed state and a definitive $J^P = 3/2^-$ determination has not been made for the Ξ states. However, a value $\theta = 20^\circ$ is found.

SU(3) is also a vertex symmetry for baryon resonance decays. Potential theory allows the partial width for such decays to be written as :

$$\Gamma_\ell = G^2 \; k \; B_\ell(k) \cdot \frac{M_N}{M_R} \qquad (7.15)$$

In this expression, G is a sum of products of SU(3) Clebsch-Gordan coefficients and SU(3) invariant amplitudes for the decaying resonance to couple to the observed final state. As an example, consider the decay $\Lambda(1690) \rightarrow \pi\Sigma(1385)$:

$$G = \left[\cos\theta \; C^{8\;\;10\;\;1}_{\pi\quad\Sigma\quad\Lambda} - \sin\theta \; C^{8\;\;10\;\;8}_{\pi\quad\Sigma\quad\Lambda}\right] g_{10} \qquad (7.16)$$

where g_{10} is the universal amplitude for $J^P = 3/2^-$ octet members coupling to SU(3) $\tilde{8} \otimes \tilde{10}$ final states. Dependence on the orbital angular momentum of the final state particles, ℓ , is embodied in the barrier factor $B_\ell(k)$, which is expressed in terms of the centre of mass decay momentum k. A form which corresponds to the more rigorous Blatt and Wiesskopf barrier

penetration factors in the limit k r → o is chosen [see Chapter Six] :-

$$B_\ell(kr) = \left(\frac{k}{M_N}\right)^\ell \qquad (7.17)$$

where M_N is the nucleon mass and r is the radius of the strong interaction(= 1fm).

Since $\tilde{8} \otimes \tilde{10} \not\subset \tilde{1}$, i.e. $C^{8\ 10\ 1}_{\pi\ \Sigma\ \hat{}} = 0$, only the $\hat{8}$ component of DO3(1520) and DO3(1690) may couple to the $\pi\Sigma$ (1385) final state.

Hence,

$$G\left[\Lambda(1520)\right] = C^{8\ 10\ 8}_{\pi\ \Sigma\ \hat{}} \cos 0\ g_{10} \qquad (7.18)$$

$$G\left[\Lambda(1690)\right] = -C^{8\ 10\ 8}_{\pi\ \Sigma\ \hat{}} \sin 0\ g_{10} \qquad (7.19)$$

and for S-wave decays to $\pi\Sigma(1385)$:-

$$\mathrm{Tan}^2\ 0 = \frac{k_{1690}}{k_{1520}} \cdot \frac{\Gamma_{DSO3(1520)}}{\Gamma_{DSO3(1690)}} \cdot \frac{M_{(1520)}}{M_{(1690)}} \qquad (7.20)$$

Using the values for the elasticity (= 0.23) and total width(= 63 MeV) for the $\Lambda(1690)$. given in reference 7.1, the values of the S-wave amplitude at resonance for FIT A and FIT B given in Table 7.1 indicate that the corresponding partial width lays in the range $1.3 \lesssim \Gamma_{DSO3\ (1690)} \lesssim 2.7$ MeV/c^2. Mast et al quote a value of the $\Lambda(1690)$ S-wave partial width as 1.4 ± 0.6 MeV/c^2 and have found the $\Lambda(1520)$ centre of mass decay momentum, averaged over the $\Sigma(1385)$ width to be, $k_{1520} = 25$ MeV/c. From this data, values of the mixing angle in the range $64^o \lesssim 0 \lesssim 72^o$ are found.

As such, $t_{DSO3}(1690)$ is subject to large errors of determination. Unfortunately, it has not been possible to perform error analyses for the

partial wave solutions discussed. However, the resonant amplitudes found for the $\Lambda(1690)$ appear stable to the method used to develop the solutions, this provides some confidence in the values quoted in this thesis. Whatever the errors in $t_{DSO3}(1690)$, they would not accommodate a value of $\Gamma_{DSO3}(1690) = 93$ MeV/c^2, required to obtain agreement with the Gell-Mann/Okubo mass formula. Furthermore, Plane et al [reference 7.2] perform an SU(3) analysis of partial widths for Λ, Σ and N $J^P = 3/2^-$ octet decays into two and quasi-two body final states using the expression for the partial width given by equation 7.16. A value $\theta = 25^o \pm 6^o$ is found, which is compatible with the value expected from the mass formula and is constrained by the decay widths observed to $\bar{k}N$ and $\pi\Sigma$ final states. Hence, the value of θ found from the study of $\pi\Sigma(1385)$ final states is too large to be accommodated within the SU(3) multiplet structure of the $J^P = 3/2^-$ states. In the next section, higher symmetries which embody particle spin and have a richer multiplet structure will be invoked to account for this result.

7.3 THE $SU(6)_W \otimes O(3)$ VERTEX SYMMETRY

In $SU(6)_W \otimes O(3)$ schemes, baryons are constructed of three spin $-\frac{1}{2}$ quarks with relative orbital angular momentum $\vec{L}$. Baryon spin is formed as a vector sum, $\vec{J} = \vec{L} + \vec{S}$, where $\vec{S}$ is the total quark spin. The fermionic wavefunction of each baryon must be totally antisymmetric and the SU(6) wavefunctions formed by the combination of three fundamental $\tilde{6}$ representations are either symmetric (S), antisymmetric (A) or of mixed symmetry (M), according to :-

$$\tilde{6} \otimes \tilde{6} \otimes \tilde{6} = \tilde{20}\ A \oplus \tilde{70}\ M \oplus \tilde{70}\ M + \tilde{56}\ S \qquad (7.21)$$

Hence, if N is the SU(6) representation and P the parity of states, baryons may be assigned to the following supermultiplets, in the $[N, L^P]$ notation

$$[56, 0^+] = {}^2 8_1 \oplus {}^4 10_3 \qquad (7.22)$$

$$[70,\ 1^-] = {}^4 8_5 \oplus {}^4 8_3 \oplus {}^4 8_1 \oplus {}^2 8_3 \oplus {}^2 8_1 \oplus {}^2 10_3 \oplus {}^2 10_1 \oplus {}^2 1_3 \oplus {}^2 1_1 \qquad (7.23)$$

$$[56,2^+] = {}^4 10_7 \oplus {}^4 10_5 \oplus {}^4 10_3 \oplus {}^4 10_1 \oplus {}^2 8_5 \oplus {}^2 8_3 \qquad (7.24)$$

where the ${}^{2s+1} M_J$ notation has been used to give the composition of supermultiplets in terms of SU(3) representations. It is also possible to construct $[20,\ 1^+]$ and $[70,\ 0^+]$ and $[70,\ 2^+]$ supermultiplets.

As a vertex symmetry, this scheme as it stands fails. Decays such as $\Delta \longrightarrow p\pi$ are forbidden on the grounds of angular momentum conservation. To overcome this difficulty, the static quark spin of SU(6) is replaced by dynamic W-spin of $SU(6)_w$. The replacement of SU(6) by $SU(6)_w$ for decay processes is described in a review by Rosner [reference 7.3].

With an $SU(6)_w \otimes O(3)$ vertex symmetry, the decays of excited $[70,\ 1^-]$ and $[56,2^+]$ baryons to psuedoscalar $[35,0^-]$ meson plus ground - state $[56,\ 0^+]$ baryon, are described in terms of one amplitude per supermultiplet, since :-

$$\tilde{35} \otimes \tilde{56} = \tilde{56} \oplus \tilde{70} \oplus \tilde{700} \oplus \tilde{1134} \qquad (7.25)$$

Hence, for the $[70,1^-]$ supermultiplet S and D wave decay amplitudes are related; for the $[56,2^+]$ states P and F wave amplitudes are related. These constraints prove too stringent to accommodate the observed decay rates, so they are relaxed. Two different theoretical explanations have been proposed to account for such breaking of the $SU(6)_w$ symmetry. For states belonging to the $[70,1^-]$ supermultiplet, Hey et al [reference 7.4] perform an analysis motivated by the Melosh transform, while Faiman and Plane [reference 7.5] justify their analysis in terms of L-broken $SU(6)_w \otimes O(3)$. Both of these approaches are discussed in the review by

Rosner [reference 7.3] .

In the minimal supermultiplet scheme, it has been possible to assign all negative parity Y^* states observed (see Table 1.1) with the exception of the GO7(2100) in the $[70,1^-]$ supermultiplet. All ground state baryons may be assigned to the $[56,0^+]$ supermultiplet, the remaining positive parity states, with the exception of the excited PO1 states, are assigned to the $[56,2^+]$ supermultiplet. Figures 7.1 and 7.2 show the assignments of states and the mixings possible within the $[70,1^-]$ and $[56,2^+]$ supermultiplets respectively. The $\Lambda(1690)$ is now formed by three way mixing between the $\Lambda^2 8_3$, $\Lambda^4 8_3$ and $\Lambda^2 1_3$ states, for which three mixing angles are required. Mixing parameters required for the states, indicated in Figures 7.1 and 7.2, are determined in one of two ways :-

(i) Phenomenological fitting of decay width data.

(ii) Explicit quark model calculations.

These approaches will be discussed in Sections 7.4 and 7.5.

7.4 PHENOMENOLOGICAL MIXING MODELS

Although somewhat different in theoretical motivation, the Hey et al [HLC] and Faiman/Plane [FP] analyses of $[70,1^-]$ supermultiplet decay states are identical in phenomenological content. If G is replaced by a sum of products $SU(6)_w$ isoscalar factors and mixing parameters, partial widths may be calculated for the mixed states shown in Figure 7.1 using equation 7.16. As an example, consider the D wave

SU(3) Multiplet	Σ States	Λ States
$^4 8_5$	D15(1770)	DO5(1830)
$^2 10_3$	D13(1580)	
	⋮	
$^4 8_3$	D13(1940)	DO3(unseen)
	⋮	⋮
$^2 8_3$	D13(1670)	DO3(1690)
		⋮
$^2 1_3$		DO3(1520)
$^2 10_1$	S11(1750)	
	⋮	
$^4 8_1$	S11(unseen)	SO1(1670)
	⋮	⋮
$^2 8_1$	S11(1925)	SO1(1810)
		⋮
$^2 1_1$		SO1(1402)

Figure 7.1 : Predominant $SU(6)_w$ assignments and possible mixings (indicated by dashed lines) for Y^* members of the $[\bar{70},1^-]$ supermultiplet.

SU(3) Multiplet	Σ States	Λ States
$^4 10_7$	F17(2030)	
$^4 10_5$	F15(2060)	
	⋮	
$^2 8_5$	F15(1930)	F05(1820)
$^4 10_3$	P13(unseen)	
	⋮	
$^2 8_3$	P13(unseen	P03(1900)
$^4 10_1$	P11(1673 or 1870)	

Figure 7.2 : Assignment of states to the $\left[56,2^+\right]$ supermultiplet.

partial widths of the $\Lambda(1690)$ couplings to $\pi\Sigma$ (1385) :-

$$G(\ell = 0) = \left\{ -\frac{\sqrt{15}}{5} \left[-4\frac{\sqrt{6}}{9} \cdot M_{21} \quad -2\frac{\sqrt{15}}{9} M_{22} \right] + 0 \quad M_{23} \right\} g_S$$

$$G(\ell = 2) = \left\{ -\frac{\sqrt{15}}{5} \left[-5\frac{\sqrt{6}}{9} \cdot M_{22} \quad +2\frac{\sqrt{15}}{9} M_{22} \right] + 0 \quad M_{23} \right\} g_D$$

SU(3) factor for $\tilde{8} \to \tilde{8} \otimes \tilde{10}$

SU(3) factor for $\tilde{1} \to \tilde{8} \otimes \tilde{10} = 0$

$SU(6)_w$ factor $^4 8_3 \to \pi\Sigma(1385)$

$SU(6)_w$ factor $^2 8_3 \to \pi\Sigma(1385)$ (7.26)

In this expression g_S and g_D are universal S and D wave decay amplitudes for the $[\underline{70},1^-]$ supermultiplet and M_{21}, M_{22}, M_{23} are the admixtures of $\Lambda^4 8_3$, $\Lambda^2 8_3$ and $\Lambda^2 1_3$ in the $\Lambda(1690)$, the $\Lambda(1690)$ wave function being :

$$|\Lambda(1690)> = M_{21} |\Lambda^4 8_3> + M_{22} |\Lambda^2 8_3> + M_{23} |\Lambda^2 1_3>$$

If Γ_e is the partial width in the elastic channel and Γ_c the partial width of a state in another particular channel, both calculated according to the prescription above, then if the total partial width of the state, Γ , is known, comparison may be made with data for amplitudes as resonance in different partial waves,

$$t = \sqrt{\frac{\Gamma_e \Gamma_c}{\Gamma^2}}$$

The mixing angles (which determine M_{21} etc.) and decay amplitudes

are treated as free parameters in a fit to all measured resonant amplitudes for N, Δ, Λ and Σ states in the $[\bar{7}0,1^-]$. Predictions therefore exist from both FP and HLC models for the resonant amplitudes of negative parity Y^* states to the $\pi\Sigma$ (1385) channels. These amplitudes are given in Table 7.1 for comparison with the values found in Chapter Six of this thesis.

Hey et al perform a similar fit to decay rates for $[\bar{5}6,2^+]$ members in terms of P and F wave amplitudes, g_p and g_f. All states are assumed to be unmixed. Results are given in Table 7.2.

In both the HLC and FP analyses, the ground state baryons are assumed to be pure $[\bar{5}6,0^+]$ members and the psuedoscalar mesons pure $[\bar{3}5,0^-]$ members.

7.5 THE ISGUR-KARL MODEL

Mixing angles and partial decay widths, which were fitted by the models described in the previous section, can be calculated together with the masses of states in explicit quark models. Isgur and Karl (and latterly Konuik) [references 7.6 and 7.7] have constructed such a model which embodies many of the phenomenological aspects of quantum chromodynamics, i.e. the currently favoured asymptotically free field theory of the strong interaction. Interquark forces should therefore be two body in nature and exhibit features reminiscent of vector-gluon exchange. Although the strong coupling constant becomes large at the distance scales encountered in hadron spectroscopy, great success has been achieved in predicting charmonium properties using the vector-gluon - photon analogy.

The model of Isgur and Karl contains the following elements :

(i) A harmonic oscillator potential. This predicts a basic spectrum of states and reproduces long range confining effects of the inter-quark potential. Wave functions for unmixed states of $SU(6)_W \otimes O(3)$ may be written in the orthogonal eigenmodes of the harmonic oscillator basis. A form of this model has been investigated by Horgan and Dalitz [reference 7.8].

State	Partial Wave	Measured Width (MeV/c^2)	Experiment		Hey et al	Faiman-Plane	Isgur & Karl
			FIT A	FIT B			
S01(1670) S01(1810)	SD01 SD01	36 215	- 0.10 - 0.10	- 0.10 - 0.08	- 0.07 - 0.158	- 0.05 - 0.07	- 0.11 - 0.07
S11(1750) S11(1925)	SD11 SD11	105 200	+ 0.19 + 0.22	- -	+ 0.32 -	- -	- 0.02 + 0.09
D03(1690)	DS03 DD03	62	+ 0.10 + 0.21	+ 0.07 + 0.21	+ 0.27 + 0.08	0.06 0.14	+ 0.38 + 0.15
D13(1670)	DS13 DD13	60	- 0.07 + _.05	+ 0.03 + 0.07	+ 0.07 + 0.04	0.01 0.00	0.03 0.02
D13(1920)	DS13 DD13	215	- 0.07 + 0.03	- 0.07 + 0.03	- 0.10 + 0.02	- -	- 0.22 - 0.03
D05(1830)	DD05 DG05	90	- 0.13 + 0.01	- 0.14 -	+ 0.0 -	- -	- 0.13 -
D15(1775)	DD15 DG15	120	+ 0.15 - 0.02	+ 0.17 -	+ 0.12 -	0.12 -	0.16

TABLE 7.1 : Amplitudes at resonance for the $[70,1^-]$ states

State	Partial Wave	Measured Width (MeV/c^2)	Experiment		Hey et al		Isgur et al	
			FIT A	FIT B	ELASTICITY		ELASTICITY	
P01(1588)	PP01	187	- 0.18	-	-	-	0.16	- 0.06
P01(1850)	PP01	150	small	small	-	-	0.14	0.12
P11(1673)	PP11	140	small	0.12		+ 0.03†	0.01	0.01
P11(1870)	PP11	140	- 0.07	- 0.05			0.04	0.04
P03(1900)	PP03	104	0.11	+small	0.28	+ 0.06	0.52	- 0.001
	PF03		0.15	+ 0.12		- 0.13		- 0.08
F15(1930)	FP15	120	small	small	0.03	- 0.03	0.01	- 0.007
	FF15		- 0.05	- 0.04		+ 0.02		0.005
F05(1823)	FP05	90	0.12	+ 0.15	0.58	0.23	0.45	0.11
	FF05		- 0.07	- 0.05		- 0.11		- 0.04
F05(2115)	FP05	190	- 0.10	- 0.06			0.02	- 0.03
			- 0.05	small				0.06
F17(2040)	FF17	70	- 0.13	- 0.15	0.17	- 0.11	0.04	0.10
	FH17		small	small	-	-	-	-

† only one P11 state exists in this analysis.

TABLE 7.2 : Amplitudes at resonance for the $[56,2^+]$ states.

(ii) A hyperfine interaction between quark pairs. This simulates the magnetic dipole - magnetic dipole interaction of electrodynamics. As such, this represents the chromodynamic effects of vector-gluon exchanges. The consequences of this interaction will be briefly discussed for the states of the $[70,1^-]$ [reference 7.6] .

If $\vec{r}$ is the radius vector between two quarks of spin $\vec{S}_1$ and $\vec{S}_2$, then the hyperfine interaction is written as :-

$$H_{HYP} = A \left[\left(\frac{8\pi}{3}\right) \vec{S}_1 . \vec{S}_2 \; \delta^3 (\vec{r}) + \frac{1}{r^3} \left(3 \vec{S}_1 . \hat{r} . \vec{S}_2 . \hat{r} - \vec{S}_1 . \vec{S}_2 \right) \right] \qquad (7.27)$$

Baryons are thought of as being made up of three pairs of quarks. One unit of orbital angular momentum resides in one pair and the remaining two pairs exist in relative S-waves. This assignment makes consideration of the quark dynamics relatively simple. The first term in H_{HYP} averages to zero when the relative orbital angular momentum between quark pairs is non-zero, whilst the second term vanishes if quarks are in a relative S-wave. These are referred to as the contact (H_C) and tensor terms (H_T) respectively ; schematically :-

$$H_{HYP} = H_C + H_T \qquad (7.28)$$

Hence in two quark pairs only H_C operates, whilst in the remaining pair only H_T operates.

A mass mixing matrix is constructed, which is similar to that used in deriving the Gell-Mann/Okubo mass formula. Consider the $J^P = 3/2^-$ Λ sector, the elements of this matrix may be written as

$$M_{ij} = < \Lambda^{2S_i + 1} \chi_i \; | \; H \; | \; \Lambda^{2S_j + 1} \chi_j > \qquad (7.29)$$

where S_i and S_j are the total quark spins of the ith and jth states and χ_i and χ_j are the SU(3) representations to which these states belong. The labels i and j run over the $\Lambda^4 8_3$, $\Lambda^2 8_3$ and $\Lambda^2 1_3$ states. Only when the tensor term operates does the $\Lambda^4 8_3$ state mix with $\Lambda^2 8_3$ and $\Lambda^2 1_3$ states. Contact forces only operate when two states have identical total quark spin. Hence $\Lambda^2 8_3 - \Lambda^4 8_3$ and $\Lambda^2 1_3 - \Lambda^4 8_3$ mixings are a measure of the importance of the tensor term.

Matrix elements are calculated in terms of the constant A(determined from the N(940) - Λ(1236) mass splitting) and the u, d and s quark masses. The eigenvalues of the mass-mixing matrix are the physical baryon masses and the eigenvectors correspond to the mixed state wavefunctions.

All the mixings indicated in Figure 7.1 for the $[\bar{70},1^-]$ supermultiplet may be calculated in this way.

In the positive parity sector [reference 7.7] , the hyperfine interaction mixes $[56,0^+]$, $[\bar{70},0^+]$, $[\bar{56},2^+]$, $[70,2^+]$ and $[\bar{20},1^+]$ supermultiplets. Matrix elements are calculated in a similar manner to those for the $[\bar{70},1^-]$ supermultiplet. Qualitatively, this approach has several rather attractive features for the positive parity Y^* states.

As a consequence of SU(6) symmetry, the decay of the $[\bar{70},1^-]$ member $\Lambda^4 8_5$ and $\Lambda^4 8_5 \rightarrow \bar{k}N$ are forbidden if the N state is a pure $^2 8_1$ member of the $[\bar{56},0^+]$ supermultiplet. Hence, the DO5(1830) state is expected to decouple entirely from $\bar{k}N$ formation experiments and have zero amplitudes at resonance in all two body and quasi-two body final states. In the Isgur-Karl model, the $[\bar{56},0^+]$ ground state baryons contain a substantial admixture of $[\bar{70},0^+]$, supermultiplet states [references 7.7 and 7.8] Consequently, couplings of the DO5(1830) to the $\bar{k}N$ channel via $[\bar{70},0^+]$ impurities in the ground state N are allowed. This is a most attractive result since substantial resonant amplitudes are observed for the Λ(1830) in all two-body and quasi two-body final states of $\bar{k}N$ interactions [see Table 1.1] .

According to the specific quark model used by Isgur and Karl [reference 7.6], states in which the orbital angular momentum resides in the non-strange quark pair may not decay into a ground state baryon plus strange meson. Hence, Y^* states belonging to the $[\bar{56},2^+]$ and $[\bar{70},2^+]$ supermultiplets may not couple to $\bar{k}N$, $\bar{k}\,{}^*N$ or $\bar{k}\,\Delta$ channels. In addition, within SU(6), states belonging to the $[\bar{20},1^+]$ supermultiplets are inaccessible to formation experiments since $\tilde{35} \otimes \tilde{56} \not\subset \tilde{20}$. These two results, together with the mixings between supermultiplets, lead to a situation in which large numbers of the positive parity Y^* states are expected to decouple from $\bar{k}$ N formation experiments.

Isgur and Koniuk [reference 7.9] have used the mixing parameters for positive and negative parity states to predict partial widths for decays into each permitted channel. This approach uses an operator motivated by PCAC (Partially Conserved Axial Current Hypothesis) for emission of a psuedo-scalar meson from an excited baryon resonance. Rather complicated momentum dependent decay amplitues are predicted, which depend on only two independent coupling constants for all supermultiplets studied. Simplification of the analysis results from fitting of two reduced momentum independent amplitudes to Δ, N and Y^* decay width data for each of the supermultiplets. Results are given in reference 7.9 and are expressed in terms of the quantities $\sqrt{\Gamma_e}$ and $\sqrt{\Gamma_i}$, resonant amplitudes being calculated from the relationship :-

$$t = \frac{\sigma \sqrt{\Gamma_e} \cdot \sqrt{\Gamma_i}}{\Gamma} \qquad (7.30)$$

where σ is the sign of the decay amplitude to the ith channel whose partial width is Γ_i. Using the measured widthsgiven in Table 1.1, the resonant amplitudes of states have been calculated from the results of this analysis and are given in Tables 7.1 and 7.2.

7.6 DISCUSSION OF RESULTS

Tables 7.1 and 7.2 give the resonant amplitudes of the states, observed in the analyses performed in Chapter Six of this thesis, to each permitted partial wave. For comparison the predictions are given of the Hey et al, Isgur-Koniuk and Faiman-Plane decay analyses. In this section the significance of these results will be discussed.

In Chapter Five, the centre of mass production angles were measured between incoming and outgoing meson systems. Hence, the resonant amplitudes given in Tables 7.1 and 7.2 are expressed in a meson first convention. Results of the HLC analysis are in a baryon first convention and the signs of amplitudes given in reference 7.4 must be reversed for comparison with those found in Chapter Six. Isgur/Koniuk and FP both use the same meson first convention.

7.6.a The Negative Parity States [see Table 7.1] .

Since both HLC and FP assume the ground state N states to be pure $[\bar{5}6,0^+]$ supermultiplet members, zero $\pi\Sigma(1385)$ resonant amplitudes are predicted. Isgur and Koniuk correctly predict the sign and magnitude of the DDO5 amplitude by allowing $[\bar{7}0,0^+]$ impurities in the ground state. For both the D15(1775) and DO5(1830) states, no G wave final state partial wave amplitude can be accommodated within the $[\bar{7}0,1^-]$ supermultiplet. In both FIT A and FIT B (see Table 7.1), G-wave amplitudes consistent with zero were found. All three theoretical analyses are in accordance with the resonant amplitudes for the D15(1775) in the DD15 partial wave found in Chapter Six.

Signs are correctly predicted for the DO3(1690) amplitudes, however the magnitudes seem to be in disagreement. This state will be given special consideration in a later section. All three analyses agree as to the positive signs of the DS13 and DD13 amplitudes of the $\Lambda(1670)$. However, the DD13 wave is found to be rather unstable in partial wave fitting (see

Chapter Six). Uncertainties in both D03(1670) and D03(1920) amplitudes are anticipated to be rather large. In the decay analyses, the D13 resonances are formed by three way mixing between $\Sigma^4 8_3$, $\Sigma^2 8_3$ and $\Sigma^2 10_3$ states. The third physical state is the D13(1580), which is rather poorly established, only the $\pi\Lambda$ amplitude being determined by formation experiments. Isgur and Konuik predict the $\pi\Sigma(1385)$ amplitudes of the D13(1670) to be small, the D13(1920) being the dominant feature of the DD13 partial wave, with a large amplitude (= -0.22). However, the amplitudes found in this experiment (see Table 7.1) are roughly comparable. Since few reliable two body amplitudes have been determined for either the D13(1580) or the D13(1920) by other analyses (see Table 1.1) the three-way mixing angles are strongly constrained by the more reliable date for the D13(1670).

Similar uncertainties in available data exist for the S01 states. The resonance nature of the S01(1405) is subject to some doubt, since it has also been considered as a sub-threshold virtual bound state of the $\bar{k}N$ system, but nonetheless is used in all three decay analyses. Substantial amplitudes have been observed for the S01(1670) in all two-body channels. However, the third member, which is the poorly established $\Lambda(1810)$ state, has not been well observed and was not included by the HLC and FP analyses. Strong $\bar{k}^* N$ amplitudes observed by the RL/IC group [reference 7.10] have subsequently improved the status of this resonance. All three analyses are in good agreement with the value found in this thesis for the S01(1670) amplitude and are also in accordance concerning the signs of the S01(1810) amplitude in the $\pi\Sigma(1385)$ channel, (see Table 7.1).

Most poorly determined of all in the mixing-sectors studied is that for the S11 states. This contains no well established resonance structure. As stated in Chapter Six, the rather wide S11(1750) and S11(1925) states can both be replaced by a single non-resonant background amplitude in the partial wave analysis. Although vast reliance cannot be placed on the parameters determined for this sector by the HLC analysis, signs of the

$\pi\Sigma(1385)$ amplitudes predicted by Isgur/Koniuk and HLC, are in agreement with those found in Chapter Six of this thesis.

7.6.b The DO3(1690) Amplitudes

The resonant amplitudes of the DO3(1690) are an interesting indicator of all three models. Three-way mixing between the $\Lambda(1690)$, $\Lambda(1520)$ and a hitherto unobserved state is expected. Isgur and Karl predict the mass of this missing state to be 1880 MeV. However, such a state was included in the development of FIT B in Chapter Six, but was not required by the data. For these states the mixing matrix may be written :-

$$\begin{pmatrix} \Lambda(1520) \\ \Lambda(1690) \\ \Lambda(1880) \end{pmatrix} = \begin{pmatrix} M_{11} & M_{12} & M_{13} \\ M_{21} & M_{22} & M_{23} \\ M_{31} & M_{32} & M_{33} \end{pmatrix} \begin{pmatrix} \Lambda\,{}^4 8_3 \\ \Lambda\,{}^2 8_3 \\ \Lambda\,{}^2 1_3 \end{pmatrix} \qquad (7.31)$$

Values of the M_{ij} are given in Table 7.3, for each of the three decay models and are determined in terms of three independent Euler angles. Using equation 7.16, together with the appropriate $SU(6)_w$ Clebsch-Gordan coefficients, a measure of the $\Lambda\,{}^4 8_3$ - $\Lambda^2 8_3$ mixing is given by the ratio t_{DS}/t_{DD} for the $\Lambda(1690)$:-

$$\frac{t_{DS}}{t_{DD}} = \frac{1}{k^2} \cdot \left\{ \frac{-\frac{5\sqrt{6}}{9} M_{21} + \frac{2\sqrt{15}}{9} M_{22}}{-\frac{4\sqrt{6}}{9} M_{21} - \frac{2\sqrt{15}}{9} M_{22}} \frac{g_s}{g_D} \right\} \qquad (7.32)$$

In this ratio, g_s and g_D are the reduced S and D wave amplitudes for the $[\underline{70},1^-]$ supermultiplet ; SU(3) isoscalar factors common to both partial waves have been divided out. Given a determination of the ratio g_s/g_d, it

(i) DO3(1520)

	Hey et al	Isgur-Karl	Faiman and Plane	
			Sol.1	Sol.2
M_{11}	-0.04	-0.01	-0.021	-0.015
M_{12}	0.39	0.40	0.430	0.438
M_{13}	0.92	0.91	0.900	0.899

(ii) DO3(1690)

	Hey et al	Isgur-Karl	Faiman and Plane	
			Sol.1	Sol.2
M_{21}	0.0	-0.12	-0.437	-0.436
M_{22}	0.92	0.91	+0.805	+0.806
M_{23}	-0.39	-0.40	-0.401	-0.400

(iii) DO3(unseen)

	Hey et al	Isgur-Karl	Faiman and Plane	
			Sol.1	Sol.2
M_{31}	1.0	0.99	0.899	0.900
M_{32}	0.01	0.11	0.402	0.398
M_{33}	-0.04	-0.04	-0.173	-0.178

TABLE 7.3 : Mixing parameters in the $3^P = 3/2^-$ Λ sector of the $|70,1^-|$ supermultiplet

is possible to calculate $\alpha = M_{21}/M_{22}$, which is a measure of the $\Lambda^4 8_3$ admixture in the $\Lambda(1690)$.

HLC find $g_s/g_D = -0.21$ and FP find gs/gd = - 0.31. Isgur and Koniuk adopt a more complicated approach. Each partial wave amplitude contains a momentum dependent form factor $\exp\left[-\frac{1}{6}\frac{k^2}{\beta^2}\right]$ and an angular momentum barrier factor $\left[k/\beta\right]^{\ell}$. Additional momentum dependence of the amplitudes is predicted by their PCAC based psuedoscalar meson emission operator ; this,however, is suppressed and effective universal partial wave amplitudes are employed :-

$$g_\ell(k) = \tilde{g}_\ell \left[\frac{k}{\beta}\right]^\ell \exp\left[-\frac{1}{6}\frac{k^2}{\beta^2}\right] \qquad (7.33)$$

where $\tilde{g}_\ell$ is a reduced, momentum independent, amplitude found by fitting decay rates. Hence, since k^ℓ is just the angular momentum barrier appearing in equation 7.16, gs/gd is momentum independent and :-

$$\frac{g_s}{g_D} = \frac{\tilde{g}_S}{\tilde{g}_D} \cdot \beta^2 \qquad (7.34)$$

Using the values $\tilde{g}_S = -7$, $\tilde{g}_D = +6$ and $\beta = 0.41$ GeV quoted by Isgur and Koniuk [reference 7.9], the value $g_s/g_D = -0.20$ is found.

The HLC and Isgur/Koniuk values of gs/gd are in good agreement Only FP quote errors on the values of gs and gd, giving $g_s/g_D = 0.31 \pm 0.04$, which is not consistent with the other two values. However, since the data available to HLC and Isgur/Koniuk represents a great improvement on that used by FP, a value $g_s/g_D = 0.2$ will be assumed.

HLC conclude that there is no $\Lambda^4 8_3$ admixture in the $\Lambda(1690)$, which implies

$$\frac{t_{DS}}{t_{DD}} = \frac{(-1)}{k^2} \frac{g_s}{g_D} = +3.44 \qquad (7.35)$$

This result is certainly not in agreement with the value implied by the amplitudes found in Chapter Six of this thesis :-

$$\frac{t_{DS}}{t_{DD}} = 0.5 \quad \text{FIT A} \tag{7.36}$$

$$\frac{t_{DS}}{t_{DD}} = 0.3 \quad \text{FIT B} \tag{7.37}$$

In fact, that $t_{DD} > t_{DS}$ requires a value $\alpha \lesssim -0.36$, which is clearly not satisfied by the Isgur and Karl mixing parameters, which give $\alpha = .013$, but which is in accordance with the value $\alpha = -5.4$ found by FP, who predict $t_{DS}/t_{DD} = 0.43$. Resonant amplitudes found in this experiment lead to a value in the range $-0.70 \lesssim \alpha \lesssim -0.53$.

Clearly, if one accepts that the universal S and D-wave amplitudes are well determined for the $[70,1^-]$ supermultiplet, the ratio t_{DS}/t_{DD} found in this thesis indicates a substantial $\Lambda^4 8_3$ admixture in the $\Lambda(1690)$. What has been attempted here is by no means rigorous, but goes to restore credence in the SU(3) prediction. It is only $\Lambda^2 8_3 - \Lambda^2 1_3$ mixing which is determined by the Gell-Mann/Okubo relationship, while the total $\Lambda^2 8_3$ and $\Lambda^2 8_3$ content of the $\Lambda(1690)$ and $\Lambda(1520)$ resonances is measured by the ratio $\Gamma_{DS}(1690) / \Gamma_{DS}(1520)$.

7.6.c Positive Parity States [See Table 7.2]

In the analysis performed by HLC for the $[56,2^+]$ supermultiplet, all states are unmixed. Ratios of P and F partial wave amplitudes for Y^* states coupling to the $\pi\Sigma(1385)$ channel may therefore given an indication as to the importance of $\Sigma^2 10_5 / \Sigma^4 8_5$ and $\Sigma^2 10_3 / \Sigma^4 8_3$ mixings in the $[56,2^+]$ supermultiplet and the mixings between different positive parity supermultiplets required by Isgur and Karl.

HLC find that $g_P/g_F = +0.24$; using the values $\tilde{g}_P = 11$ and $\tilde{g}_F = 6$, Isgur and Koniuk [reference 7.9] give a value :

$$\frac{g_P}{g_F} = \frac{\tilde{g}_P}{\tilde{g}_F} \cdot k^2 = 0.31 \qquad (7.38)$$

Although somewhat different in structure, the two analyses give values which are in approximate agreement.

Within $SU(6)_w$ the following ratios of P and F wave amplitudes are predicted for unmixed states of the $[56,2^+]$ supermultiplet :-

(i) For FO5 and F15 $^2 8_5$ states

$$\frac{t_{FP}}{t_{FF}} = -\frac{\left\{\frac{\sqrt{30}}{45}\right\}}{\left\{\frac{2\sqrt{5}}{45}\right\}} \cdot \frac{1}{k^2} \cdot \frac{g_P}{g_F} = r_8 \qquad (7.39)$$

(ii) For F15 $^4 10_5$ states

$$\frac{t_{FP}}{t_{FF}} = \frac{\left\{\frac{\sqrt{42}}{45}\right\}}{\left\{16\sqrt{\frac{7}{315}}\right\}} \cdot \frac{1}{k^2} \cdot \frac{g_P}{g_F} = r_{10} \qquad (7.40)$$

(iii) For PO3 $^2 8_3$ states

$$\frac{t_{PP}}{t_{PF}} = -\frac{\left\{\frac{\sqrt{5}}{45}\right\}}{\left\{\sqrt{\frac{5}{15}}\right\}} \cdot \frac{1}{k^2} \cdot \frac{g_P}{g_F} = r \qquad (7.41)$$

The $SU(6)_w$ Clebsch-Gordan coefficients have been taken from Table IV of reference 7.9. Table 7.4 gives the value of k, r_8, r_{10} and r for the PO3(1900), FO5(1823), FO5(2115) and F15(1930) states together with the ratio of P and F partial wave amplitudes calculated for FIT A and FIT B.

Clearly, the relative sign of P and F wave amplitudes is a good indicator of the success of the $SU(6)_w$ model and the degree of mixing present. However, to have any confidence in statement based of the P and F wave amplitudes found in Chapter Six of this thesis (see Table 7.2), it must be clear that the partial wave parameters are stable in the fitting process. It is the case for FO5(2115) and F15(1930) states that one outgoing partial wave is large and stable, whilst the other is small and fluctuates in sign and magnitude depending on the paramatrizations used for the amplitude. The rates t_p/t_F found for the FO5(1823) are consistent with it being a pure $\left[56,2^+\right]$ supermultiplet member. If the relative signs of the $\pi\Sigma$(1385) amplitudes for the F15(1930) were known, this state could clearly be assigned to either the $^4 10_5$ or the $^2 8_5$ representation. Although the FF15 amplitude is found to be stable and negative, no sign is favoured for the FP15 amplitude, which is found to be consistent with zero in Table 7.2. Relative signs for the PO3(1900) and FO5(2115) amplitudes are both in disagreement with $SU(6)_w$ [see Table 7.4]. Stable positive amplitudes are found for the PO3(1900) in both PPO3 and PFO3 partial waves.

Detailed comparison of the amplitudes found for the positive parity structures observed in this thesis with those predicted by Isgur and Konuik is difficult. Because of the plethora of states required in the extensive supermultiplet mixing scheme, it is impossible to assign unambiguously the mass of states with those predicted in Isgur-Karl analysis for the positive parity sector. However, many of the Y^* states predicted are highly inelastic and decouple from $\bar{k}N$ formation experiments, others cluster closely together in mass. Hence amplitudes have been roughly averaged for states close to

State	k (GeV/c)	r_8	r_{10}	r	t_{p/t_F}	
					FIT A	FIT B
P03(1900)	0.428	-	-	- 0.455	+ 0.73	∿ + 0
F05(1823)	0.364	- 2.31	-	-	- 1.7	- 3.0
F05(2115)	0.592	- 0.87	-	-	+ 2.0	∿ 0
F15(1930)	0.451	- 1.505	1.31	-	Undetermined	Undetermined

TABLE 7.4 : Ratios of P and F Wave Amplitudes for Positive Parity States.

the observed structures in Table 7.2.

Five F15 states are predicted, one corresponds in mass to the F15(1930), the rest cluster around 2100 MeV,and one may be associated with the F15(2060). Of the five F05 states, one is predicted to lay discretely in the F05(1830) region while the remaining states are between 2000 and 2160 MeV and are identified with the F05(2100) structure. The P03 sector is a success, seven states are predicted and all but the P03(1900) decouple from the $\bar{k}N$ channel. Unfortunately, only four of the seven P13 states decouple from $\bar{k}N$; no structure,except the P13(1385),exists to be associated with the remaining states. In both the P01 and P11 sectors all but two states decouple from the $\bar{k}N$ critical state, these are identified with the structures given in Table 7.2 .

Comparing amplitudes with those found in Chapter Six of this thesis (see Table 7.2), agreement for the F05(1820) is good; however,the predictions for the remaining states are poor, especially in the $J^P = 1/2^+$ sector. Even with the addition of extra positive parity multiplet the signs of the P03(1900) amplitudes are not correctly predicted. If one inspects the decay amplitudes given in Table IV of reference 7.9, the ratio of P and F wave partial wave amplitudes for the $\Lambda^4 8_3$ member of the $\left[\bar{70},2^+\right]$ is :-

$$\frac{t_P}{t_F} = \frac{\left\{\sqrt{\frac{105}{90}}\right\}}{\left\{4\sqrt{\frac{70}{315}}\right\}} \cdot \frac{1}{k^2} \cdot \frac{g_P}{g_F}$$

i.e. t_P and t_F are of the same sign, since g_P and g_F determined by Isgur and Koniuk are both positive. Hence, depending on the overall sign of t_P and t_F, the problem concerning the relative signs of the P03(1900) can be overcome if it is assigned to the $\left[70,2^+\right]$ supermultiplet.

7.7 CONCLUSIONS

If SU(3) configuration mixing between octet and singlet isoscalar states is invoked, a mixing angle of 20° may be deduced for the $\Lambda(1520)$-$\Lambda(1690)$ using the Gell-Mann-Okubo mass formula. This angle is in conflict with the angle of 70° deduced from the partial widths for $\Lambda(1690)$ and $\Lambda(1520)$ decays to $\pi\Sigma(1385)$ final states, assuming SU(3) as a vertex symmetry for these decays. Consideration of the DSO3 and DDO3 partial wave amplitudes for the $\Lambda(1690)$ indicate that a substantial $\Lambda^4 8_3$ - $\Lambda^2 8_3$ octet mixing occurs, which is permitted in the higher $SU(6)_w \otimes O(3)$ vertex symmetry.

Additionally, predictions concerning the resonant amplitudes of states determined in Chapter Six are considered. Three such analyses exist. Agreement is good for the negative parity states but is poor for the positive parity states. Consideration of the relative signs of the PO3(1900) state P and F wave amplitudes indicates that the values found in this thesis are incompatible with this state being a $[\bar{56},2^+]$ supermultiplet member, but can be be accommodated if it belongs to the $[\bar{70},2^+]$ supermultiplet.

CHAPTER 7

REFERENCES

7.1 T.S. Mast et al, Phys. Rev. D7 (1973)5.

7.2 D.E.Plane et al, Nucl.Phys. B22 (1970) 93.

7.3 J.L. Rosner, Phys. Reports 11 (1974) 189.

7.4 A.J.G.Hey et al, Nucl.Phys. B95 (1975) 516.

7.5 D.Faiman and D.E.Plane, Nucl.Phys B50(1972) 379.

7.6 N.Isgur and G.Karl, Phys. Rev. D18 (1978) 4187.

7.7 N.Isgur and G.Karl, Phys.Rev D19 (1979) 2653.

7.8 R. Horgan and R.H.Dalitz, Nucl.Phys. B66 (1973).

7.9 N.Isgur and R. Koniuk, Phys. Rev.D21 (1980) 1868 and
N. Isgur and R. Koniuk, Phys. Rev. Lett. 44 (1980) 845.

7.10 R.Cashmore, Proceedings Summer School for Young Experimentalists, (1978)Rutherford Laboratory.

CHAPTER 8

8.1 GENERAL CONCLUSIONS

Using the corrected data sample described in Chapter Two of this thesis, channel cross-sections for the reaction $k^- p \to \pi^+\pi^-\Lambda$ over the 0.650 to 0.860 GeV/c incident momentum interval have been determined. The values found are in good agreement with those obtained by 2 previous studies of the same channel [see figure 2.10] . The main feature observed in this data is an abrupt shoulder between 0.650 and 0.750 GeV/c which corresponds to the region of D03(1690), D13(1670) and S01(1670) resonance formation. However, due to the widths of these states, the effects of different resonance are not evident in the cross-section data alone.

Using the same corrected data sample, the Dalitz plot for the $\pi^+\pi^-\Lambda$ final state has been examined. Strong $\Sigma^+(1385)$ and $\Sigma^-(1385)$ production is apparent in the $\Lambda\pi^+$ and $\Lambda\pi^-$ effective-mass combinations at all energies studied [see figure 4.1] . In addition, an enhancement in density at the higher accessible $\pi^+\pi^-$ effective-masses is observed [see figure 4.2] . This effect persists at all incident momenta in the 0.500 to 0.860 GeV/c interval, unormalized data in the lower incident momentum range comes from the T.S.T. experiment [see figures 4.3 and 4.4].

In the incident momentum range studied in the Survey-81 experiment, the kinematic cross-over between $\Sigma^+(1385)$ and $\Sigma^-(1385)$ bands moves across the physical region of the Dalitz plot. Any interference effect between $\Sigma^+(1385)$ and $\Sigma^-(1385)$ bands should be represented by an enhancement at dipion masses corresponding to the $\Sigma(1385)$ overlap, which moves from the lower limit of available $\pi^+\pi^-$ phase space at 0.500 GeV/c to the upper limit at 0.860 GeV/c. The observed enhancement is therefore inconsistent with being the result of an interference effect.

An alternative description of this effect as a final state $\pi\ \pi$ interaction has been attempted. In order to assign quantum numbers to the $\pi\ \pi$

dynamics present, the pure I = 1 reaction $k_L^o p \to \pi^+\pi^o\Lambda$ has been examined. Any final state $\pi\pi$ interaction present in this process must therefore be pure isovector in origin. A satisfactory description of the quasi-two body variables of the $\pi^+\pi^o\Lambda$ final state is given by pure incoherent formation of $\pi^+\Sigma^o$ (1385) and $\pi^o\Sigma^+$ channels. It is concluded therefore, that the final state $\pi\pi$ interaction is pure isoscalar in nature. Using the Watson form for the final state interaction, the I = J = O $\pi\pi$ dynamics has been paramaterized in terms of the corresponding set of phase shifts. Energy dependence of the phase shifts is given by the effective range approximation. In a χ^2 fit to the $\pi^+\pi^-$ effective mass distribution, allowing both $\Sigma^-(1385)$ and $\Sigma^+(1385)$ production, the I = J = O scattering length (a_o^o) has been found to be consistent with zero. This result is at odds with the value of a_o^o found from analyses of k_4^e experiments and $\pi\pi$ scattering deduced from processes in which one pion exchange is dominant. However, the description of final state $\pi\pi$ interactions is in accordance with that for a similar effect seen in isobar analyses of the reaction $\pi N \to \pi\pi N$. This is not surprising, since unlike virtual $\pi\pi$ scattering processes, the $\pi\pi$ systems observed in $\pi\pi N$ and $\pi\pi\pi\Lambda$ channels are not produced peripherally.

Including the paramatrization of the I = J = O $\pi\pi$ dynamics ('ε') contributions to the $\pi^+\pi^-\Lambda$ final state from incoherent addition of $\pi^+\Sigma^-(1385)$, $\pi^-\Sigma^+$ (1385) and 'ε' Λ channels have been extracted. A vastly improved description of quasi-two body variables results from the addition of the 'ε'Λ channel. In addition, a good account of the $\pi^+\pi^-$ effective mass distribution for T.S.T. data in the 0.500 to 0.580 GeV/c interval, which was not used to determine the 'ε' parameters.

Quasi-two-body descriptions of the $\pi^+\Sigma^-(1385)$ and $\pi^-\Sigma^+(1385)$ channels have been extracted and used in an energy dependent partial wave analysis. Qualitative consideration of this data indicates that strong interference between $J^P = 3/2^+$ and $J^P = 3/2^-$ partial wave amplitudes, in the region of the D03(1690) resonance, produces marked structure in the A_1, B_1, A_3, B_3, C_3 and

D_3 coefficients for the $\pi^+\Sigma^-$ (1385) channel [see figure 6.1] . In fact, when combined with previously published data, this new data contains the most prominant feature for the reaction $k^-p \rightarrow \pi\ \Sigma(1385)$. Full energy dependant partial wave analysis, reveals substantial resonant amplitudes of SO1(1670) and D13(1670) states in the permitted partial waves. However, the largest resonant amplitudes are found for the DO3(1690) in DSO3 and DDO3 partial waves. Structures found by a previous analysis of data above 1.740 GeV/c^2 centre of mass energy are not affected by the addition of the new Survey-81 data in the Λ(1690) region [see Table 6.2] . The role of some rather poorly established states has also been considered. However, the stability of the corresponding partial wave amplitudes in the $\pi\Sigma$(1385) channels does not add conclusively to the understanding of these resonances.

Within $SU(6)_w \otimes O(3)$ symmetry schemes, the Λ(1690), Λ (1520) and a hitherto unobserved $J^P = 3/2^-$ Λ state are formed by 3-way mixing between $\Lambda^2 8_3$, $\Lambda\ ^4 8_3$ and $\Lambda\ ^2 1_3$ states in the [$70,1^-$] supermultiplet. Fitting of decay rates by Hey et al [reference 7.4] leads to physical states in which the Λ(1690) and Λ(1520) result almost entirely from $\Lambda\ ^2 8_3 - \Lambda\ ^2 1_3$ mixing, while the unseen member is an almost pure $\Lambda\ ^4 8_3$ state. Similar conclusions are reached by the Q.C.D. motivated quark model of Iggur and Karl. Since the decay $\Lambda^4 8_3 \rightarrow \bar{k}N$ is forbidden in $SU(6)_w$, the unseen state is therefore predicted to be highly inelastic and is not expected to be seen in $\bar{k}N$ formation experiments. The consequence of this mixing scheme for the Λ(1690) is that a large DSO3 $\pi\Sigma$ (1385) amplitude is predicted together with a somewhat smaller DDO3 amplitude. This is in direct conflict with the relative magnitudes of these amplitudes found in Chapter Six of this thesis. That the DDO3 amplitude be dominant, requires a substantial $\Lambda\ ^4 8_3$ admixture in the Λ(1690) and consequently a higher admixture of $\Lambda^2 8_3$ in the unseen state. However, this has the undesirable effect of making the unseen state more elastic. Faiman and Plane [reference 7.5] in their decay rate analysis find substantial $\Lambda\ ^4 8_3 - \Lambda^2 8_3$ mixing and predict Λ(1690) resonant amplitudes which agree

well with those found in this thesis, without predicting unacceptably large amplitudes for the missing state. Using the measured ratio of DSO3 and DDO3 amplitudes found in this thesis, the proportion of $\Lambda^4 8_3$ and $\Lambda^2 8_3$ in the (1690) have been found to be in the approximate ratio 1 : 2.

Using the measured total widths of states given in Table 1.1, the amplitudes at resonance for states observed in the partial wave analysis, given in Chapter Six,have been compared with the predictions of Hey et al, Faiman/Plane and Isgur/Koniuk. The agreement is good for the $[\underline{70},1^-]$ supermultiplet but poor for the $[\underline{56},2^+]$ supermultiplet. In particular, the mixing of positive parity supermultiplets in the Isgur-Karl model, allows non- $[\underline{56},0^+]$ impurities in the ground state and permits the $SU(6)_w$ violating process DO5(1820) $\rightarrow \bar{k}N$, and allows observation of this state in $\bar{k}N$ formation experiments. The predictions for the $\pi\Sigma(1385)$ amplitudes are in good agreement with those found in this thesis.

8.2 OUTLOOK FOR FUTURE WORK

The T.S.T. experiment mentioned in Chapter Two of this thesis explores the 0.800 to 0.600 GeV/c incident momentum range of k^-p interactions. Although devoid of well-confirmed resonance structure, this region may contain the narrow D13(1580) state.

Litchfield, in a re-analysis of the C.H.S. [reference 8.1] pure pure I = 1 $\pi^o\Lambda$ final state data, has found a $J^P = 3/2^-$ state with mass 1582 MeV and width 11 MeV [reference 8.2] . Carroll [reference 8.3] , has performed an isospin separation for total k^-p and k^-d cross-sections between 0.410 and 1.070 GeV/c. Evidence is seen for a pure I = 1 state at 1.583 GeV/c^2 with width 15 MeV/c^2 and a rather small elasticity of 0.06. A study of the $\Lambda\pi^+\pi^-$ system produced in pp collisions at the CERN Intersecting Storage Rings has revealed a state with a mass of 1572 MeV/c^2 and a width of 15 MeV/c^2 [reference 8.4] . Non-confirmation of this state comes from several pure I = 1 $k^o_L p$ experiments.

If such a state exists, what would be the consequences for symmetry schemes? Hey et al have included the D13(1580) in their analysis of decay rates. Within the $[\bar{70},1^{-}]$ three way mixing may occur with the D13(1670) and D13(1920) states. The largest of all resonant amplitudes for the D13(1580) is predicted in the $\pi\Sigma(1385)$ final state S-wave ($t_{DS13} = 0.1$). This is certainly a substantial coupling and such a state should be evident in coefficient data over the 0.500 to 0.600 GeV/c interval from strong $J^P = 3/2^-$ and $J^P = 3/2^+$ amplitude interference effects (c.f. the $\Lambda(1690)$).

Although measurements and data processing for the T.S.T. experiment are still underway, study of the $\Lambda\pi^+\pi^-$ final state will help to refute or confirm the existence of the $\Sigma(1580)$.

CHAPTER 8

REFERENCES

8.1 R. Armenteros et al, Nucl.Phys. B21 (1970) 15.

8.2 P.J.Litchfield, Physics Letters 51B (1974) 509.

8.3 A.S.Carroll et al, Phys. Rev.Letts 37 (1976) 806.

8.4 W.Lockman et al, Saclay preprint DPh PE 78-01(1978).

LIST OF TABLES

LIST OF FIGURES

2.13 Comparison of cross-sections found in this experiment with those found by previous studies of the reaction $k^- p \to \pi^+\pi^-\Lambda$.

Chapter 3 : 3.1 Isobar formation in the reaction $k^- p \to \pi^+\pi^-\Lambda$.

Chapter 4 : 4.1 Dalitz Plots for the reaction $k^- p \to \Lambda\pi^+\pi^-$ as a function of incident momentum in 20 MeV/c bins.

4.2 Distributions of $M^2(\pi^+\pi^-)$ for the reaction $k^- p \to \Lambda\pi^+\pi^-$, with the same binning as Figure 4.1.

4.3 Dalitz plot for the reaction $k^- p \to \Lambda\pi^+\pi^-$, in the 0.500 to 0.580 GeV/c momentum interval.

4.4 Distribution of $M^2(\pi^+\pi^-)$ for events in the Dalitz plot shown in Figure 4.3.

4.5 Distributions of $\cos\Theta$ for the $\Lambda\pi^+$ system as a function of incident momentum with the same binning as Figure 4.1.

4.6 Distribution of $\cos\Theta$ for the $\Lambda\pi^-$ system as a function of incident momentum, with the same binning as Figure 4.1.

4.7 Results of Quasi-two Body Analysis of the reaction $k^- p \to \Lambda\pi^+\pi^-$ in the incident momentum bin centred on 0.830 GeV/c and allowing only pure $\pi\Sigma(1385)$ channels.

Chapter 5 : 5.1 Dalitz plots for the reaction $k_L^o p \to \Lambda\pi^+\pi^o$ as a function of incident momentum.

5.2 Distributions of $M^2(\pi^+\pi^o)$ for events in the 0.740 to 0.750 GeV/c interval.